FEUP Universidade do Porto
Faculdade de Engenharia

SEISMIC RISK ASSESSMENT OF REINFORCED CONCRETE FRAMES WITH MASONRY INFILL

Hossameldeen Mohamed Ahmed Mohamed

A dissertation presented to the Faculty of Engineering of the University of Porto for the Degree of Doctor in Civil Engineering.

Supervisor: Xavier das Neves Romão (Assistant Professor)

Erasmus Mundus

LOT1 FATIMA AL-FIHRI
Erasmus Mundus Fatima Al Fihri Scholarship Program

Acknowledgements

It has been a really fruitful journey full of new experiences both academically and personally. However, as any other experiences in our life, this experience was not free of hard times, it would not have been possible without the contribution and support of the kind people who accompanied me throughout this process. In the following paragraphs, I would like to express my most sincere gratitude and appreciation for those who have helped me in completing this journey.

Firstly, I would like to acknowledge my sincere gratitude to my supervisor, Professor Xavier Romão, for providing the guidelines of the most work I have been done since our first meeting, which put me on the right path and saved a lot of time from me. I also grateful to him for giving me the freedom to pursue independent work and explore things on my own. I am also grateful to him for his skilful supervision, continuous encouragement, and unconditional support during the preparation of this document.

I would also like to express my deep appreciation to colleagues and friends from the Civil Engineering Department, Structural Division at Faculty of Engineering of the University of Porto (FEUP). Among those, I would like to thank Luís Martins, Mário Marques, Miguel Araújo and Nuno Pereira for their valuable help and for the fruitful talks about many ideas addressed in this dissertation. To all my office friends, who I was fortunate to work with them in the same office and who made the working environment very friendly, I would like to express my deep thank to all of them. Finally, I would also like to thank Luís Martins, Tuba Tatar and Despoina Skoulidou for their companionship and friendship which made this experience in a foreign country more pleasant and enjoyable.

I also thank the Erasmus Mundus programme Al Fihri project for the financial support though the PhD grant (ALFI1201678 grant from July 2013- July 2016). In this regard, I also thank all Erasmus Mundus coordination team at the University of Porto and at University of Deusto, especially Ms. Ana Paiva, for their unconditional support. For his support during applying for this grant and his helpful advice, I would like to express my deep appreciation to professor Hany Madkour, coordinator of Al Fihri project at Aswan university. Finally, for their companionship and friendship, I would like to thank all my colleagues in the Erasmus Mundus programmes at the University of Porto. Namely, I would like to thank Mohamed Soliman, Nagwa Arafa, Raina Elemam Ahmed Saeed, and Mohamed Alaa, for their companionship and friendship which made this experience in a foreign country more pleasant and enjoyable.

To my father, brothers and sisters, I would like to thank them for their unconditional encouragement and support. To my wife, Hend, who has never given up on me even in the hardest time which we have experienced during this journey. I am also deeply grateful to her for help in editing some figures in this dissertation.

Finally, it was a long process, which gave me the opportunity to get in touch with several professors, colleagues and people who shared in this work even by a kind word, to those may not be mentioned in these acknowledgements I would like to express deep appreciations.

To my beloved family,

Abstract

Reinforced concrete (RC) infilled frames are one of the most commonly used structural systems in the world, namely in earthquake-prone regions. In most designed buildings, the function of the masonry infill does not exceed its architectural function, i.e. it is not considered as a structural element. However, past earthquakes (e.g. Turkey, 1999, Chania, 2008, Nepal 2015) have caused huge losses in lives and properties, namely in RC infilled buildings, thus showing the vulnerability of these structures. Extensive research has been carried out over the years to study the interaction between the RC frame and its infill wall. Experimental investigations were the first approach to figure out the structural aspects of the interaction between the structure and the infill walls. Experimental tests of masonry infilled RC frames provide a unique tool for researchers to investigate the complex seismic behaviour of this kind of buildings. However, the high cost of these tests has limited the number of experiments that have been conducted so far.

Although the main component of this thesis involves assessing the seismic behaviour of RC frames with masonry infills, a reliable model for the infill wall is still required. Simplified approaches involving macro-models, such as strut-type models, have been used in research, combined with experimental observations, to represent the overall force-displacement relation of this type of structures in computationally efficient models. However, when analysing existing macro-modelling approaches, it was found that their properties need to be established using reliable data. Experimental testing can be seen to be difficult to use on a regular basis to obtain the necessary data to establish the properties of such simplified models due to the high costs usually involved in such procedures. In this context, due to their ability to represent the complex behaviour of masonry infilled structures, including the multiple failure modes that can occur in the infill or in the frame, the developed research proposes the use of the refined finite element models (also known as micro-models) as a proxy for the experimental tests. Using this numerical modelling approach, the data needed to define the properties of simplified models can be obtained at a lower cost. The results that were obtained in this study when using detailed finite element models were seen to provide an acceptable match to the experimental results. The numerical model was able to successfully capture the highly nonlinear behaviour of the physical specimens and predict their overall strength, stiffness and several failure mechanisms.

The research that was carried out also proposes calibration procedures for defining the parameters of different types of simplified infill modelling approaches based on available experimental or numerical data. The reliability of the proposed calibration procedures is evaluated based on available experimental data gathered from the literature. The research also analyses the probabilistic performance of masonry infilled RC frames under seismic loading. As such, the performance of several infilled frames where the infill was modelled using a strut model calibrated using two different sets of data was analysed using nonlinear dynamic analyses. In one set of structures, the parameters of the strut model were calibrated based on experimental data, while in another set of structures these parameters were modelled based on the results obtained from a refined finite element model simulating the experimental data. The experimentally calibrated model is used as a reference to analyse the vulnerability of the selected masonry infilled RC frames and to assess the errors in the probabilistic performance resulting from the numerically calibrated model. Based on this comparison, it was found that the use of numerical data resulting from the detailed finite element models to define the infill parameters of the simplified model leads to adequate probabilistic results that are able to represent the seismic vulnerability of masonry infilled RC structures with sufficient reliability.

Resumo

As estruturas de betão armado (BA) com painéis de alvenaria de enchimento são um dos sistemas estruturais mais utilizados no mundo, inclusivamente em regiões sujeitas a sismos. Na maioria dos edifícios projetados com este sistema estrutural, a função dos painéis de enchimento é essencialmente arquitetónica, não sendo portanto considerados como elementos estruturais. No entanto, observa-se que os sismos do passado (e.g. Turquia, 1999, Chania, 2008, Nepal 2015) causaram perdas significativas, quer em termos de vidas, que em termos das propriedades danificadas, nomeadamente em edifícios de BA com painéis de alvenaria de enchimento, o que mostra a vulnerabilidade destas estruturas. A investigação neste domínio tem se dedicado desde há muito a estudos que têm como objetivo analisar e caracterizar a interação entre a estrutura de BA e o painel de alvenaria de enchimento. Os estudos experimentais foram a primeira abordagem utilizada para entender os aspetos estruturais da interação entre a estrutura de BA e as paredes de enchimento. Este tipo de ensaios experimentais são uma ferramenta única para a investigação que permite representar o comportamento complexo deste tipo de estruturas sob a ação sísmica. No entanto, o custo elevado destes ensaios não permite a sua utilização em larga escala.

Embora a principal componente desta dissertação envolver a avaliação do comportamento sísmico de estruturas de BA com painéis de alvenaria de enchimento, é necessário estabelecer uma abordagem de modelação fiável para o painel de enchimento. Abordagens simplificadas que envolvem macro-modelos, como os modelos baseados em escoras, têm sido usadas na investigação neste domínio, utilizando dados experimentais para representar a relação força-deslocamento global deste tipo de estruturas em modelos computacionalmente eficientes. No entanto, ao analisar as abordagens propostas nos macro-modelos existentes, verificou-se que as suas propriedades precisam de ser estabelecidas com base em dados adequados e fiáveis. Dado que as dificuldades associadas aos ensaios experimentais, nomeadamente os elevados custos envolvidos, não permitem a sua utilização de forma corrente para obter os dados necessários para estabelecer as propriedades dos referidos modelos simplificados, procurou-se uma alternativa eficaz. Neste contexto, devido à sua capacidade de representar o comportamento complexo de estruturas com alvenaria, incluindo os possíveis modos de rotura que podem ocorrer na alvenaria ou no BA, o estudo desenvolvido propõe o uso de modelos refinados de elementos finitos (também conhecidos como micro-modelos) em substituição dos ensaios experimentais. Usando esta abordagem de modelação numérica, os dados necessários para definir as

propriedades dos modelos simplificados podem ser obtidos com custos menores. Os resultados obtidos no estudo desenvolvido com modelos refinados de elementos finitos permitem concluir que esta abordagem numérica tem capacidade para simular os resultados experimentais com fiabilidade aceitável. O modelo numérico foi capaz de capturar com sucesso o comportamento altamente não-linear dos casos de estudo analisados e de prever sua resistência, rigidez e vários mecanismos de rotura.

Os estudos realizados nesta dissertação também propõem procedimentos de calibração para definir os parâmetros de diferentes tipos de modelos simplificados de painéis de alvenaria com base em dados experimentais ou numéricos disponíveis. A fiabilidade dos procedimentos de calibração propostos foi avaliada com base em dados experimentais disponíveis obtidos a partir da literatura. Os estudos realizado também analisam o desempenho probabilístico de estruturas de BA com painéis de alvenaria de enchimento sob ações sísmicas. Neste contexto, foi analisado o desempenho de várias estruturas deste tipo usando análises dinâmicas não-lineares, sendo que os painéis de alvenaria foram modelados usando um elemento de escora cujo comportamento calibrado usando dois conjuntos diferentes de dados. Num conjunto de estruturas, os parâmetros do modelo de escora foram calibrados com base em dados experimentais, enquanto noutro conjunto de estruturas esses parâmetros foram modelados com base nos resultados obtidos a partir de um modelo detalhado de elementos finitos que simulou os dados experimentais. O modelo calibrado experimentalmente foi utilizado como referência para analisar a vulnerabilidade das estruturas de BA com painéis de alvenaria selecionadas e para avaliar os erros no desempenho probabilístico resultante do modelo calibrado com dados numéricos. Com base nessa comparação, verificou-se que a utilização de dados numéricos resultantes de modelos de elementos finitos detalhados para definir os parâmetros de modelos simplificados que simulam o comportamento dos painéis de enchimento permite obter resultados probabilísticos adequados que são capazes de representar a vulnerabilidade sísmica destas estruturas com fiabilidade suficiente.

Contents

Chapter 1.
Introduction

1.1 General Overview

Over decades, reinforced concrete (RC) frame buildings with masonry infills have been widely used to construct commercial, residential and industrial buildings. Such buildings have been mostly designed and constructed following different specifications and codes, usually disregarding the contribution of the masonry for the structural behaviour. However, experiments on the behaviour of masonry infilled RC frames (e.g. see (Mehrabi, 1994, Bergami*, et al.*, 2015, Shan*, et al.*, 2016) among several others) have shown that masonry panels affect both the lateral stiffness and the displacement capacity of a structure. To illustrate these facts, Figure 1.1 and Figure 1.2 show the effect of the infill wall in the lateral strength and lateral displacement capacity determined from ten experimental tests gathered from the literature (Pires, 1990, Mehrabi*, et al.*, 1996, Crisafulli, 1997, Bergami, 2007, Kakaletsis*, et al.*, 2009, Kakaletsis, 2009, Stylianidis, 2012, Sigmund*, et al.*, 2013, Bergami*, et al.*, 2015, Misir, 2015, Basha*, et al.*, 2016, Zhai*, et al.*, 2016). Figure 1.1 shows that a masonry infill wall can increase the lateral strength of the structure up to 350% with respect to the lateral strength of the bare RC frame. On the other hand, Figure 1.2 indicates that infills can reduce the lateral displacement corresponding to maximum strength, which means that infilled RC frames have less displacement capacity in terms of the pre-peak response. As such, existing experimental research demonstrates that infill walls affect the structural behaviour during lateral loading and that such influence should not be neglected.

Furthermore, field evidence gathered from previous earthquakes shows that infill panels can induce several failure mechanisms, due to the interaction between the infill panel and the RC frame. This interaction can then lead to severe damage, as shown in the examples in Figure 1.3 to Figure 1.5.

As can be seen in these figures, the interaction between the infill panels and the RC frames leads to several damage patterns that start from a local damage in the infill panel and then spread to their adjacent RC members (e.g. see Figure 1.3). Moreover, this interaction leads to the development of unusual failure mechanisms such as the one known as the "captive column failure" (Varum, 2003) (Figure 1.4) and, eventually, can also lead to global structure collapse, as shown in Figure 1.5 where a soft-storey failure mechanism was developed. Therefore, based on these facts, the existence of infills leads to a change in the global characteristics of the structure and, consequently, to a change of their failure mechanisms. Hence, the real performance of these structures and their ability to withstand earthquakes must be adequately evaluated. Although, there is a vast body of literature that, over the past decades, tried to fully understand the dynamic response of RC infilled frames, either experimentally or numerically, there are still several aspects of the infill modelling requiring further research efforts.

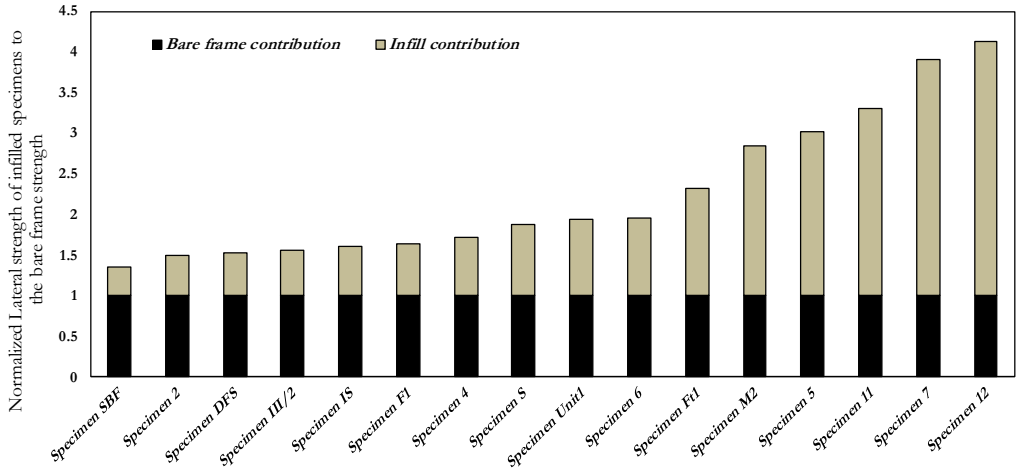

Figure 1.1 Contribution of the infills for the global in-plane response of the infilled RC for several experimental specimens (Pires, 1990, Mehrabi*, et al.*, 1996, Crisafulli, 1997, Bergami, 2007, Kakaletsis*, et al.*, 2009, Kakaletsis, 2009, Stylianidis, 2012, Sigmund*, et al.*, 2013, Bergami*, et al.*, 2015, Misir, 2015, Basha*, et al.*, 2016, Zhai*, et al.*, 2016) *

* The response of the bare frame was obtained from numerical analysis when a given test campaign had no bare frame specimen

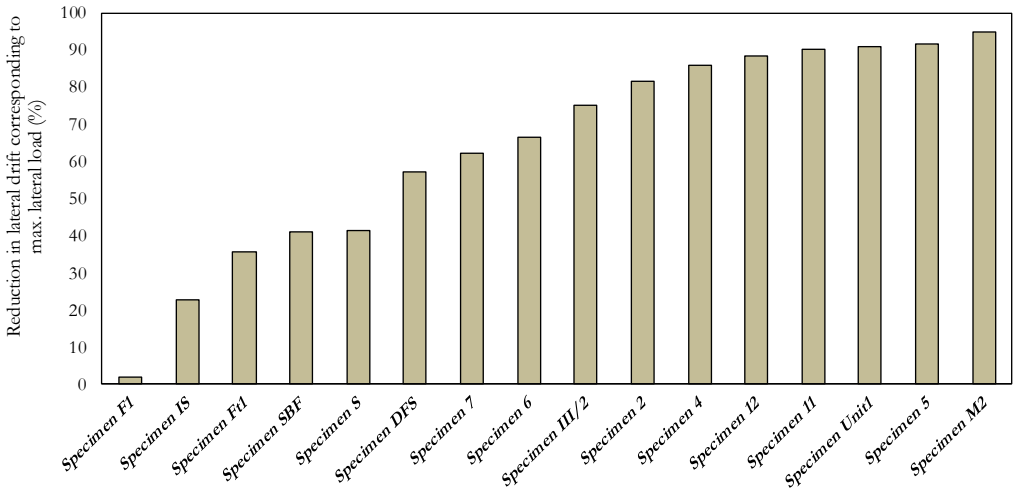

Figure 1.2 Reduction in the lateral displacement capacity corresponding to the maximum lateral strength of infilled RC frames when compared to bare RC frames (Pires, 1990, Mehrabi*, et al.*, 1996, Crisafulli, 1997, Bergami, 2007, Kakaletsis*, et al.*, 2009, Kakaletsis, 2009, Stylianidis, 2012, Sigmund*, et al.*, 2013, Bergami*, et al.*, 2015, Misir, 2015, Basha*, et al.*, 2016, Zhai*, et al.*, 2016).

a) Infill shear and minor frame damages, Nepal earthquake, 2015

b) shear failure in infill and shear failure at the ends of RC column, San Antonio earthquake, 2010 (Velasquez, et al., 2016)

c) Infill shear and frextural frame damages Wenchuan earthquake, 2008 (Li, et al., 2008)

d) Collapsed infill panel with major frame damages Wenchuan earthquake, 2008 (Li, et al., 2008)

Figure 1.3 Damage pattern of masonry infills and RC frames; which varies from minor cracks to major failure

a) Managua earthquake. 1972 (Pradhan, et al., 2012)

b) Northridge earthquake, 1994(Faison, et al., 2004)

c) Düzce earthquake, 1999 (Beyhan, et al., 2011)

Figure 1.4 Captive column failure (short column failure)

a) Northridge earthquake, 1994 (Schierle, 2003) *b) Loma Prieta Earthquake, 1989 (Dean, et al., 2008)* *c) Algeria earthquake, 2003 (NOAA, 2003)* *d) Nepal earthquake, 2015 (Ohsumi, et al., 2016)*

Figure 1.5 Global structural failure due to soft-storey mechanism.

1.2 Objectives

The main objective of this thesis is to assess the probabilistic performance of masonry infilled RC frames under seismic loading using a simple and reliable model for the in-plane response of the infill, with properties adequately defined and calibrated. In this context, this study introduces a comprehensive investigation to define a reliable model for the infill that can be used in probabilistic performance analyses. The use of a single strut element to model the infill, which is based on the original experimental observations made by Polyakov (1956), is found to be the most widespread approach due to its simplicity. However, due to the wide variety of masonry materials, several approaches can be used to calibrate the structural parameters of this equivalent strut (e.g. see (Asteris, *et al.*, 2011a)). Since these different approaches usually lead to different values of the model parameters, the proposed research assesses the reliability of these approaches using available experimental data.

Due to the variability of masonry infills types, configurations, construction technologies and materials across countries, as well as to the significant cost of experimental tests, available experimental data do not cover all the possibilities and requirements. Therefore, alternative approaches need to be established to obtain adequate data to assess the reliability of the referred simplified models and to calibrate their properties. In this context, the use of refined finite element models, which became affordable due to the considerable evolution of computing capabilities, is proposed herein as a proxy for the experimental data. Several refined finite element modelling approaches, which are also known as micro-models, were found in the literature. These models used different techniques which varied in terms of modelling detail and, therefore, in terms of accuracy and computational cost involved. The

proposed research introduces a refined modelling approach that uses the capabilities of the ANSYS software (ANSYS, 2012), therefore enabling the replication of the procedures used herein by other researchers. The proposed modelling approach aims to use the more significant aspects proposed by previous researchers in order to achieve an optimized balance between accuracy and computational cost. This refined modelling approach is meant to be used either as a proxy for the experimental data to assess the reliability of selected empirical expressions defining the parameters of the strut model or to be used to calibrate directly the parameters of the strut models.

The research that was carried out also proposes calibration procedures for defining the parameters of the strut model based on the available experimental or numerical data. The reliability of the proposed calibration procedures is evaluated based on available experimental data gathered from the literature. Finally, as referred before, the current research also aims to analyse and assess the probabilistic performance of masonry infilled RC frames under seismic loading. This study analysed the performance of several infilled frames where the infill was modelled using a strut model calibrated using two different sets of data: in one case the parameters of the strut were calibrated based on experimental data, while in the other case these parameters were modelled based on the results obtained from a refined finite element model simulating the experimental data. The experimentally calibrated model is used as a reference to analyse the vulnerability of the selected masonry infilled RC frames and to assess the errors in the probabilistic performance resulting from the numerically calibrated model. The overall adopted methodology is summarized in the diagram shown in Figure 1.6, where Model R stands for the reference model calibrated using experimental data, Model M stands for the model calibrated using results obtained with a micro-modelling approach, and Model E refers to the model calibrated using empirical expressions.

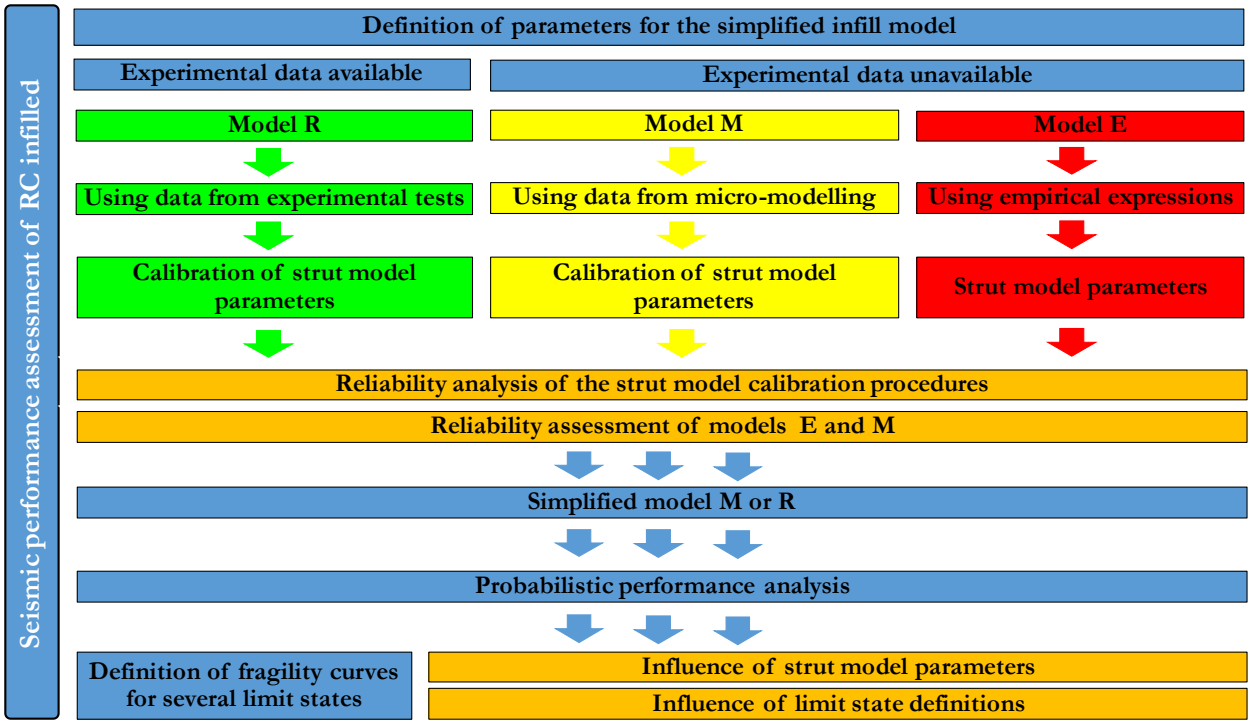

Figure 1.6 Summary of the objectives and of the research methodology considered in the present thesis.

1.3 Thesis Outline

The present thesis analyses the behaviour of masonry infilled RC frames focussing on the infill's in-plane response modelling aspects in order to get reliable performance results. In this context, several aspects of existing infill modelling techniques are addressed in three parts. The first part includes a review of the three main procedures found in the literature to analyse the behaviour of RC frames with masonry infills (experimental tests, refined finite element modelling and simplified modelling) which appears in Chapter 2 and is followed by a comparative review on the use of simplified modelling approaches in Chapter 3. The second part involves the use of a refined finite element modelling approach to simulate the detailed behaviour of infilled frames as an alternative to experimental tests (Chapter 4) and the development of calibration procedures for the parameters of the simplified strut models (Chapter 5). Finally, the last part of the thesis, which corresponds to Chapter 6, addresses the probabilistic performance and vulnerability assessment of several masonry infilled RC frames with infill properties calibrated using experimental and numerical data.

Chapter 2 presents a literature review of past research addressing the in-plane behaviour of masonry infilled RC frames. First, experimental research is presented, followed then by a discussion on existing analytical research on the different modelling approaches that have been used for masonry panels, including micro-modelling and macro-modelling approaches. Chapter 2 also reports some of the in-plane failure modes of masonry infilled RC frames to provide motivation background for the study of the seismic performance of these systems.

Chapter 3 presents a comparative review on the use of single strut elements to model the structural behaviour of infill walls. Besides testing the applicability of several expressions available from the literature to determine the parameters of the model in order to analyse their reliability, this study also aims to assess the reliability of strut models adopted by several norms and standards. Moreover, the possibility of using modified parameters of single strut models to simulate partially infilled frames (i.e. when there are windows and doors in the infill panel) is also addressed.

Chapter 4 presents the refined modelling approaches that were selected to model the different parts of infilled RC frames using the ANSYS software (ANSYS, 2012). The proposed micro-modelling approach is implemented to simulate the monotonic and cyclic behaviour of several masonry infilled RC frame specimens that were previously tested experimentally. The chapter presents the numerical simulation results and their comparison with the experimental results

Chapter 5 reports the calibration procedures that are proposed to optimise the mechanical parameters of single strut elements modelling an infill wall. First, experimental data is used to illustrate the calibration procedures. In case experimental data are unavailable, this chapter also presents the use of results obtained from refined finite element models as a proxy for the experimental data. The use of the calibration procedures is also extended to allow its usage for strut models with special configurations. Finally, this chapter presents a brief analysis of the influence and reliability of strut models when computing local demand represented by shear forces in frame elements.

Chapter 6 presents the probabilistic performance analysis of several 2D frames with different infill panel configurations and different numbers of storeys. The study analyses the differences between the fragility curves of different infilled RC frames for several limits states, focussing particularly on the influence of the type of data that is used to calibrate the parameters of the infill model (i.e. experimental data or numerical data). The chapter presents the performance analysis methodology that was used and details the probabilistic analyses that were performed to establish the limit state fragility curves.

The final chapter briefly presents a summary of the main conclusions and findings of the previous chapters, along with proposals and recommendations for future research on some of the topics addressed in this thesis.

Chapter 2.
Analysis of the in-plane behaviour of masonry infilled RC frames under earthquake loading: a review

2.1 Preface

Reinforced concrete (RC) frames with unreinforced masonry infill wall structures are one of the most common structural systems in countries around the world, including in seismically active regions. Although these infill masonry walls have been constructed as non-structural elements, their behaviour is integrated with that of RC frames during earthquakes. As background for the research reported in the following chapters, the current chapter presents a review of existing research addressing the in-plane structural behaviour and failure modes of masonry infilled RC frames. Subsequently, a review about existing experimental and analytical studies that were conducted on this type of structures is also presented, illustrating the strengths and limitations of each approach.

2.2 In-plane failure modes of RC frames with infills

Understanding the failure mechanism of fully infilled RC frames enhances considerably the understanding of the earthquake-resistant behaviour of infilled frames and improves the comprehension about their modelling, analysis and design. Due to the material inhomogeneity of the

infill panel, the failure mechanisms of masonry infilled frames have a wide variety. However, experimental tests provide valuable information in this regard. Several experimental campaigns have been carried out over time to categorize the individual failure mechanisms of masonry infilled RC frames and to simplify the analysis of this type of structures. A brief summary addressing the more important aspects of the failure mechanisms for RC frames with fully infilled panels and with partially infilled panels (i.e. panels with openings) is thus presented in the following.

Based on tests carried out on twelve half-scale frames, Mehrabi (1994) recognized twenty four different in-plane failure mechanisms for infilled frames. More recently, Stavridis (2009) alternatively categorized in-plane failure according to three main mechanisms as shown in Figure 2.1:

- Diagonal cracking in the infill with column shear failure or, more rarely, plastic hinges in columns. This failure typically occurs in weak/non-ductile frames with strong infills;
- Horizontal sliding of the masonry with flexural or shear failure of the columns. Infill crushing is sometimes observed in these cases. This failure mechanism was observed in weak frames with weak panels and also in strong and ductile frames with weak infill panels;
- Infill corner crushing with flexural failure in the columns. This mechanism is more likely in strong and ductile frames with strong infills.

In the same context, based on a comprehensive review of experimental and analytical research from the past fifty years, El-Dakhakhni*, et al.* (2003) classified the failure mechanisms of infilled frames into five distinct modes illustrated in Figure 2.2. These failure mechanisms are the corner crushing (CC), sliding shear (SS), diagonal compression (DC), diagonal cracking (DK), and frame failure (FF) modes. However, among these five failure mechanisms, CEB (1996) mentions that only the CC and SS modes are of practical importance. Furthermore, the third mode (DC) is said to occur very rarely and requires a high slenderness ratio of the infill to result in out-of-plane buckling of the infill under in-plane loading and, according to (El-Dakhakhni*, et al.*, 2003), most infills are not slender. Asteris*, et al.* (2011a) stated that (DK) should not be considered a failure mode because of the post-cracking capacity of the infill to carry additional load while (FF) is related to the failure of the frame and is particularly important when analysing existing structures that exhibit structural weaknesses.

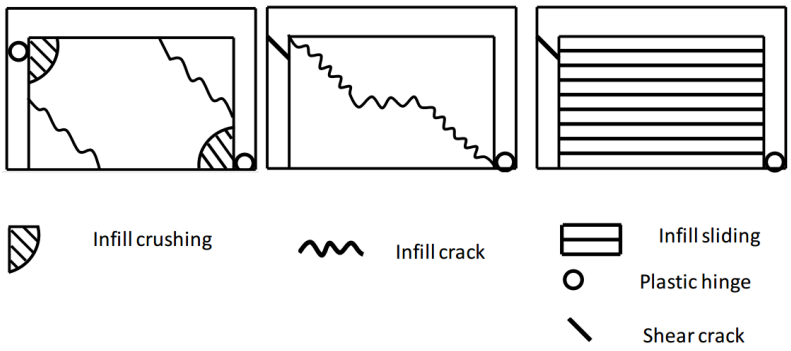

Figure 2.1. Failure mechanisms of infilled frames defined by Stavridis (2009) based on (Mehrabi, 1994)

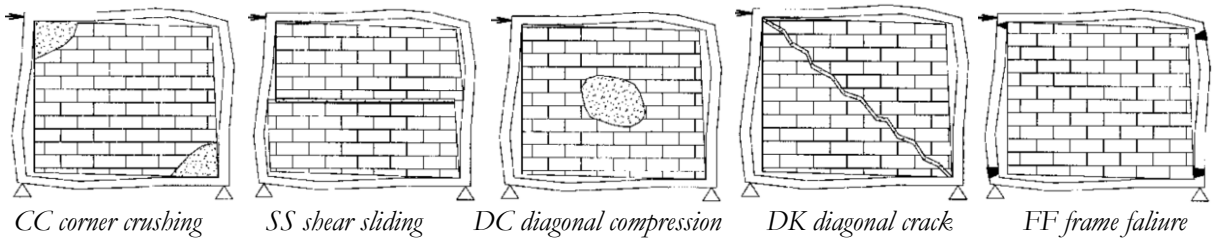

Figure 2.2. Various modes of failure according to (El-Dakhakhni*, et al.*, 2003)

The existence of an opening in the infill panel changes its behaviour and, therefore, its expected failure modes. In order to evaluate the failures modes of partially infilled panels, Asteris*, et al.* (2011c) classified the failure mechanisms for infilled frames with openings according to the type and location of the opening (i.e. door or window). Irrespective of the type of opening, Asteris*, et al.* (2011c) observed a sliding shear failure mode above the opening. They also reported that the presence of an opening across the diagonal of the infill panel eliminates the well-known failure modes of Diagonal Compression (DC) and Diagonal Cracking (DK). Therefore, the opening prevents the infill panel from working as a diagonal bracing (diagonal strut†).

† The diagonal strut formulation is the model representing the infill wall structural behaviour proposed by Polyakov (1956) that will be presented later in this chapter.

2.3 Experimental Research

Experimental investigation is one of most reliable tools that has been used to understand the behaviour of this kind of structure in order to improve comprehension about their modelling, analysis and design. Several experimental campaigns are found in literature that were carried out over six decades. These experimental campaigns studied various aspects of the interaction between the RC frame and the infill panel. However, this section addresses only experimental studies which have analysed the influence of masonry infills on the in-plane behaviour of RC frames. The experimental studies are presented in chronological order.

Polyakov (1956) conducted the earliest experimental studies which tried to clarify the interaction between frames and the wall infills. Polyakov conducted experimental tests on masonry infilled steel frames. One of the main remarks of this study is that the masonry infill wall works as a bracing system for the frame by forming a compression strut. This observation motivated several researchers to use a compression strut as a model for the infill panel which became later one of the main macro-modelling approaches for infills, as presented later in this chapter.

Later, Sachanski (1960) conducted a series of monotonic static tests on a full scale infilled RC frame models in order to calibrate his theoretical approach to assess the contributions of infill walls for the combined stiffness and load distribution of structures. Sachanski used the experimental data to develop a theoretical method to analyse infilled RC frames. This method assumes that there is no separation between the frame and the wall and that the wall has elastic, homogeneous and isotropic behaviour. However, these assumptions may not be entirely realistic.

Holmes (1961) performed several tests on infilled steel frames with full and small sizes subjected to racking and shear loading. This study confirmed the diagonal strut formation theory. Based on his experimental works, Holmes proposed a width of the equivalent strut w equal to one-third of the panel diagonal length in order to compute the maximum strength of the infilled frame. One year later, Stafford-Smith (1962) also tested three steel frames with infills. This study was an extension to the equivalent strut theory proposed earlier by Polyakov (1956) and led to an alternative method to compute the equivalent strut width based on the test results which were used to measure the stiffness of the infill panels.

Fiorato*, et al.* (1970) carried out monotonic tests on twenty-seven RC frames with masonry infills in a 1:8 scale. The specimens had different number of storeys, of bays, of reinforcement arrangement, of gravity loads, of concrete quality and of openings in the walls. They inferred that RC frames with

masonry infills have higher stiffness and strength but less ductility than bare frames. Mainstone (1971) and Mainstone*, et al.* (1972) also confirmed the strut formation in their experiments on full-scale concrete-encased steel frames infilled with masonry panels. They proposed an empirical equation to calculate the effective width of the strut as a function of the relative stiffness of the frame and infill and on the diagonal length of the infill. To develop this empirical equation, they assumed that the effective width of the strut is a function of the diagonal load on the infill at the first diagonal crack, of the thickness and of the crushing stress of the infill (both measured from the experiments). Later, based on tests carried out on 1:3 scale frames representing an eleven-storey RC apartment building of the 1970s, Klingner*, et al.* (1978) concluded that the presence of reinforced infill panels reduces the risk of incremental collapse, compared to that of a bare RC frame.

In the 1980s, Zarnic*, et al.* (1988) performed cyclic tests on twenty eight specimens including bare and infilled RC frames. The specimens had different scales, which were 1:2 and 1:3, infill materials (clay bricks and concrete blocks), types of openings (doors, windows but also solid infills) and also accounted for unreinforced and reinforced walls. They found a significant increase in the strength and stiffness, as well as a significant reduction in the ductility, from the bare to the infilled frames. They also reported severe strength deterioration after the infilled systems reached their ultimate strength and they observed a severe reduction of the stiffness of the infilled frame in the cyclic loading. It is also worth mentioning that this study involved the repair of nine of the specimens using different infill repair techniques (epoxy-grouting and a combination of epoxy-grouting with reinforced cement coating) to investigate the effect of different strengthening approaches.

Later, Pires (1990) tested seven models in a 2:3 scale consisting of one-storey, one-bay RC frames, six infilled with brick masonry walls and one bare frame. The bare frame model was used as a reference for the analysis of the results obtained from the infilled models. The tests involved cyclic horizontal displacements imposed at the level of the beam centreline and vertical forces applied at the top of the columns, in order to represent the effect of the gravity loads. This study also included the analysis of the influence of some parameters on the behaviour of the models, namely those related to model construction procedures, the reinforcement of the frames and the characteristics of the masonry. This study also addressed the influence of the drift on the failure mechanism of the infilled RC frames.

Mehrabi (1994) carried out twelve tests on half scale one-bay one-storey specimens, including two bare frames and frames with different infill conditions in terms of materials, loading procedures and reinforcement arrangement. After the tests, the frames were also repaired to analyse the efficiency

of the repair procedures. These test results have been used widely by researchers to calibrate numerical models due to the comprehensive data available from the tests, including data required for developing refined finite element models and the experimental explanation of the failure mechanisms. These tests also confirmed the increase in stiffness and strength of the infilled frame when compared to the bare frame.

Crisafulli (1997) performed a cyclic lateral loading test for two fully infilled RC frames with a ¾ reduced scale. These two specimens had the same size, materials and the same type of masonry but different reinforcing details. The use of tapered beam-column joints with diagonal reinforcement was addressed in one of these frames. Crisafulli (1997) concluded that the use of strong beam-column joints improves the transfer of the lateral force from the frame to the masonry infill. In addition, the test specimens showed significant pinching effects in their force-displacement responses.

The pseudo-dynamic algorithm presented in (Mosalam*, et al.*, 1998) was used to test a two-bay, two-storey steel frame infilled with unreinforced concrete block masonry to assess the seismic performance of the infilled frame. The global response and the development of crack patterns were similar to the results obtained from static tests conducted in previous studies. Also, Buonopane*, et al.* (1999) performed the same pseudo-dynamic test but on half scale RC frames with two openings in the second storey. It is worth mentioning that, in this study, they observed the development of compression struts for low force levels. However, for higher force levels, the contribution of the diagonal strut decreased and the stress distribution changed due to bed joint sliding at several locations in the wall. This change of the stress path in the infill implies the use of other strut configurations in the modelling rather than just the single diagonal strut, as will be presented in the next sections.

To investigate the influence of the masonry on the strength and stiffness of RC frames, Al-Chaar*, et al.* (2002) tested, under monotonic static loading, one bare frame and four single storey infilled frames with a 1:2 scale with a different number of bays and masonry materials. They confirmed the significant increase in stiffness, residual and ultimate strength from the infilled frame to the bare frame. Also, they mentioned that increasing the number of spans implied an increase of the maximum strength and stiffness of the infilled frame, but the effect is not linear.

Dynamic and static monotonic tests were conducted by Lee*, et al.* (2002) on 1:2 scale masonry infilled non-ductile RC frames with two bays and three storeys. They also observed the significant increase in stiffness, strength and inertial force (due to the added mass) from the infilled frame to the bare frame. They also reported that the deformation capacity of the infilled frame is almost the same as that of the bare frame. However, they concluded that the increase in the inertial force due to the

existence of the infill is lower than the increase in strength, and they also observed a better structural response of the infilled frame in terms of the maximum strength and stiffness when compared to that of a bare frame. They noticed that, in terms of the failure mechanisms, the corresponding bare frame experienced a soft-storey mechanism due to the formation of plastic hinges in the columns and they also observed the shear failure of columns in the bottom storey of the infilled frame.

In order to observe the seismic behaviour of RC frames strengthened by precast concrete panel infills, Süsoy (2004) tested eight 1:3 scale, single-storey single-bay RC frame specimens with different types of panel and connection designs. Specimens were subjected to cyclic lateral loading after being strengthened with precast concrete panels epoxy-bonded to the masonry infills. The effects of different panel shapes and connection techniques were investigated. Süsoy (2004) concluded that strengthened infills failed by excessive diagonal cracking of the panels, and the frame failed by crushing, failure at the column bases or at the beam-column joints. After failure of the infill, the behaviour of the system became similar to that of a bare frame. Stronger infills provided higher lateral load capacity but hampered frame action, thus limiting the ductility.

Using a shaking table, Hashemi*, et al.* (2006) tested a 3:4 scale one-bay masonry infilled RC frame as a model for a substructure of a five-storey prototype. They concluded that the existence of unreinforced masonry infills, in addition to their positive effect on stiffness and strength, also lead to an increase of the damping coefficient from 4 to 5-12%, depending on the excitation level, while also shortening the natural period of the tested structure by 50%.

In order to assess the seismic performance of existing frames with and without infill panels, Pinto*, et al.* (2006) conducted a series of pseudo-dynamic tests on two full-scale models of a four-storey RC frame representative of existing structures designed without specific seismic resisting characteristics. The specimens were also retested after being repaired. They confirmed the high vulnerability of the bare frame and they also reported that the infilled frame showed a completely different behaviour than the bare frame. While infills may protect the RC structure, they prompt the development of soft storey mechanisms and can cause shear failure of external columns in the joint regions. They also referred that retrofitting solutions based on k-bracing and dissipative devices, such as a shear-link, can substantially improve the storey behaviour and increase the energy dissipation capacity.

With the purpose of investigating the behaviour of ductile RC frames strengthened by introducing partial cast-in-place RC infills under cyclic lateral loading, Anil*, et al.* (2007) constructed nine specimens of one-bay one-storey 1:3 scale frames. They tested those specimens under reversed

cyclic loading. The aspect ratio of the infill wall (infill length to the height ratio) and its partial infill configuration were the main parameters of the study. This study indicated that partially infilled RC frames also exhibited significantly higher ultimate strength and higher initial stiffness than the bare frame. When the aspect ratio of the infill wall was increased, the lateral strength and the stiffness increased significantly. Furthermore, they observed a better performance, in terms of strength, for the frames with connections between the column, the beam and the infill. They reported that the fully infilled frame had seven times greater energy dissipation capacity than the bare frame.

Kakaletsis*, et al.* (2008), Kakaletsis (2009) conducted a series of tests on 1:3 scale single-storey single-bay frame specimens for cyclic horizontal loading up to a drift level of 4.0%. The specimens were different in terms of the masonry materials (they used weak and strong bricks), opening ratios with respect to the solid infill (from 0 to 100 %) and also in terms of the location of the openings. They concluded that infills with openings can significantly improve the performance of RC frames. Furthermore, specimens with strong infills exhibited better performance than those with weak infills.

Blackard*, et al.* (2009) carried out cyclic tests on six 2:3 scale masonry infilled non-ductile RC frames representing 1920's buildings of California. The main aspects of these specimens were the differences in terms of the existence, location and configuration of the openings. In addition to that, the infill panels in two of the specimens were retrofitted with an engineered cementitious composite material applied to the face of the walls. They observed that the stiffness and strength of the infilled frames were inversely proportional to the size of the opening.

More recently, Stylianidis (2012) tested about forty specimens with a 1:3 scale. The experimental tests were divided into three campaigns. The first two campaigns addressed several aspects of the RC frames with masonry infills, namely the quality of the mortar, the existence of a lintel beam, the contact condition between the RC frame and the infill panel, the material properties, the size of the masonry block and the frame aspect ratio. Ten damaged specimens from the first campaign were used in the third campaign which analysed different strengthening techniques. Among all the aspects addressed in this study, it was found that the aspect ratio of the frame has a minor effect on the behaviour of the bare frames but a major effect for infilled specimens. In addition, Stylianidis reported that when the shear-to-compressive strength ratio is high, exceeding the value of about 0.4, it can lead to brittle failure of the RC columns.

Stavridis*, et al.* (2012) also studied the dynamic behaviour, in a shaking table, of a 2:3 scaled two bays, three storeys masonry infilled non-ductile RC frame, representing a 1920's building of California, under scaled historical ground motion records. This specimen was fully infilled in one span and had

window openings in other spans. They concluded that for earthquake excitations less intense than a moderate design-level earthquake for the Los Angeles area, the structure behaved elastically. However, minor cracks developed in the infill during a design-level ground motion. As the intensity of the ground motion increased, the cracks in the masonry walls gradually propagated and caused the development of significant diagonal shear cracks in the RC columns when the level of shaking, in terms of the effective spectral intensity, exceeded the maximum considered earthquake by 43%. After this level of excitation, the damage in the structure was considerable but still repairable. As the intensity of the ground motion increased further, the structure was severely damaged and severe diagonal cracks developed in the columns in the first storey causing a soft-storey mechanism.

In order to investigate the behaviour of RC frames with different types of masonry, namely the standard masonry and locked masonry, Misir*, et al.* (2012) performed quasi-static tests for three specimens with half-scale specimens; two fully infilled RC frames with the referred type of masonry and one bare frame. They observed that locked brick infills maintain their integrity and stability up to very high in-plane drift levels with less damage when compared to that of stranded infills. Therefore, they reported that locked masonry infills have the potential to reduce injuries and fatalities related to falling hazards during severe ground shaking. However, they mentioned the out-of-plane behaviour of the locked masonry required further investigation.

To assess the effect of the existence of openings and of their configuration on the structural aspects of infilled frames, Sigmund*, et al.* (2013) tested six one-storey one-bay RC frame specimens. They tested one bare frame, one frame with a solid panel and the rest of the specimens had infill panels with openings of different sizes, positions and types. To establish the behaviour of the infill panels with openings, this study proposed correction factors for the behaviour of the bare frame that account for the type and position of the opening.

Mansouri*, et al.* (2014) also carried out a series of experimental tests to evaluate the influence of openings on the lateral behaviour of low-shear strength masonry infilled RC frames. They tested six half-scale single-storey single-bay frame specimens under in-plane lateral loading. They mainly investigated the influence of the shape, size and location of the openings. They concluded that the presence of openings modifies the failure mode, increases the damage level and reduces the ductility, strength and stiffness of the infilled frame. They also computed the reduction of the strength and the energy dissipation capacity due to the existence of openings in the infill panels. Based on these tests, they proposed empirical equations for estimating the overall reductions in stiffness and strength of

infilled frames due to the presence of openings, taking into account the size, shape and location of the openings.

Bergami, *et al.* (2015) tested three half-scale frames under cyclic lateral loads: one bare frame and two fully infilled specimens. They reported that the infill contribution to the overall structural performance is significant due to the high stiffness and strength that were observed. They correlated the behaviour and damage pattern of the tested specimens with the lateral drift in four ranges: up to a drift of 0.25%, there was no damage and the system behaved almost elastically; for drifts of 0.25%–0.35%, they observed minor damage to the infill; for drifts of 0.35%–0.6%, they observed a constant lateral capacity and damage to the infill that was still repairable; over a drift of 0.6%, the infill was heavily damaged and its contribution should no longer be considered.

In the same context, Basha, *et al.* (2016) tested eleven half-scale specimens with full and half scaled bricks. The tests were performed in two campaigns. The first campaign included eight specimens while the second campaign comprised three strengthened specimens. They reported that specimens from the first campaign exhibited a large increase in stiffness, strength, dissipated energy, which ranged from 7~10 times for the stiffness, 1.6~2.5 for the strength and 1~2.3 times in terms of dissipated energy, when compared with the behaviour of the corresponding bare frames. Based on their observations from the second campaign, they reported that provisions in current codes of practice do not seem to prevent the occurrence of shear failure in RC columns of infilled frames, even when using a weak infill with a strong frame. Therefore, they recommend improving the design methods for RC frames with masonry infills.

In order to simulate the failure of structural components due to abnormal loads or design flaws, Shan, *et al.* (2016) tested two 1/3 scaled, four-bay, two-storey RC frame specimens missing the central column of the first storey, one bare frame and the other with different configurations of the infill panel. Contrary to the previous tests, the frame specimens were quasi-statically pushed downward at the top of the centre column under controlled displacement. Even with this vertical loading, they reported that the infilled frames had a larger initial stiffness but lower ductility. They reported that for cases with large external loading or a fragile structure, the progressive collapse of the infill walls may lead to more damage to the structure. In addition, they observed the development of major cracks in the infill walls and cracks in beams formed at an early stage for a very small deformation. Finally, they recommended strengthening the beam regions near the corners of the opening to improve the progressive collapse performance.

Using four full-scale specimens, one bare frame, one fully infilled and two with partially infills, Zhai, *et al.* (2016) studied experimentally the effect of infills and of their different configurations on the global behaviour of RC structures. The specimens were tested under cyclic lateral loading. In addition to the high stiffness and strength recorded for the infilled specimens, this study reported that the existence of the masonry infill wall caused the development of cracks in the columns for a drift that was 60–70% smaller than the one of the bare frame. This implies that the infill accelerated the cracking of RC members.

Based on the presented studies, it can be concluded that all of the experimental studies confirmed that the existence of infills, whatever their material properties, leads to a higher strength and stiffness than that of the corresponding bare frame while reducing the available ductility which, depending on the earthquake intensity level, can have either positive or negative effects. Furthermore, most of these studies referred the formation of compression struts for low levels of force. However, for higher force levels, the contribution of the diagonal strut decreased and the stress distribution changed due to the occurrence of bed joint sliding at several locations in the wall (Buonopane*, et al.*, 1999). The studies also report that infilled frames have a much larger capacity for energy dissipation, when compared with that of bare frames, as well as more damping than bare frames, while the ductility of the infilled frame is lower than that of the bare frame (Fiorato*, et al.*, 1970, Oliveira*, et al.*, 2004). However, Lee*, et al.* (2002) reported that infilled frames have almost the same deformation capacity of the bare frame. Based on these facts, the behaviour of masonry infilled RC frames can clearly be seen to involve different aspects than those analysed for bare RC frames. Furthermore, these tests also show that the behaviour variability of masonry infilled frames, which depends, among other aspects, on the infill configuration and materials, is difficult to capture or generalize based on limited experimental data. Finally, it is noted that several specimens of the test campaigns reported herein were used in the modelling, analysis and calibration procedures developed throughout this thesis.

2.4 Analytical Research

In light of the experimental research that was conducted over the past decades, many researchers developed analytical models trying to capture the characteristics of the structural behaviour of infilled frame structures. A brief review of these analytical models is presented in chronological order in the following sections. This review divides analytical studies according to their modelling method for the

infill structure. Two main approaches are addressed: refined finite element models, also known as micro-models, and simplified strut-based models, also known as macro-models.

2.4.1 Refined finite element modelling.

Experimental tests of masonry infilled RC frames are considered to be the most realistic approach for researchers to investigate the complex seismic behaviour of these structures. However, the significant variation in the material properties, the construction techniques and geometry make the experimental approach unfeasible in many cases due to the cost of such procedures. With the enormous growth in the processing capacity of computers over the past years, researchers tried to develop alternative approaches to assess the seismic behaviour of infilled frame structures using refined finite element models. These refined finite-element models (also known as micro-models) require the modelling of the frame elements (either in steel or RC), the masonry bricks, as well as the interaction between bricks and with the adjacent frame. The highly nonlinear behaviour of the masonry or infill wall, due to the existence of brittle materials such as the mortar, makes the modelling of this part of the structure very complex. For this reason, this section will address pertinent issues related to the modelling of the masonry panel, followed by a review of previous studies that developed different types of micro models for infilled structures, focusing on their potentialities and their limitations.

2.4.2 Masonry infill modelling levels using refined finite element models.

All unreinforced masonry walls have common ingredients which are the bricks and the mortar. According to the modelling accuracy level, the representation of those materials and of their interaction can be classified according to three main categories: micro-continuum models, meso-continuum models and macro-continuum models. The configurations of these models are shown in Figure 2.3.

As shown in Figure 2.3 (a), in micro-continuum models, the brick and the mortar joints are modelled as continuum elements and the interaction between the two elements is represented by interface or contact elements. The behaviour of both the continuum elements and the interface elements is defined by nonlinear stress-strain relations, as described later in more detail. Autonomous constitutive models are used to define the bricks, the mortar joints and the interface between the

mortar and the bricks. Due to the refinement of all masonry wall components, this model has a high accuracy in terms of capturing all the expected failure mechanisms and, therefore, the structural response. However, it requires large input data and high computational efforts. Therefore, the use of this approach can only be feasible for small specimens such as one-bay one-storey specimens.

For the case of meso-continuum models, which involve a lower level of detail when compared with micro-continuum models, bricks are modelled by continuum elements, but the mortar joints and their interfaces with the bricks are modelled together as a single interface element, as shown in Figure 2.3 (b). This slight simplification makes the analysis of this type of model much faster than the previous one. It is possible to further improve the modelling of the bricks in both the micro- and meso-continuum modelling approaches since experimental results show that the diagonal cracking of the infill panel usually goes through the bed joints and head joints. However, cracking sometimes also occurs vertically between the bricks, possibly due to the dilatation effect of the mortar joints. Therefore, to capture this mechanism, a vertical interface can also be added between bricks. This model was used in several research studies found in the literature due to its balance between accuracy and simplicity.

When using a macro-continuum model (also known as a homogenized model), the behaviour of the brick, mortar and brick-mortar interfaces is modelled as one continuum element with equivalent material properties, as shown in Figure 2.3 (c). The interaction between the infill and the frame can be represented with interface contact elements, or it can also be considered to be continuous in all connecting points or in specific points. Although this modelling approach is less accurate, it can be used for preliminary studies due to its low computational cost. A brief review of research where these modelling approaches were considered is presented in the following section, alongside their main aspects and conclusions.

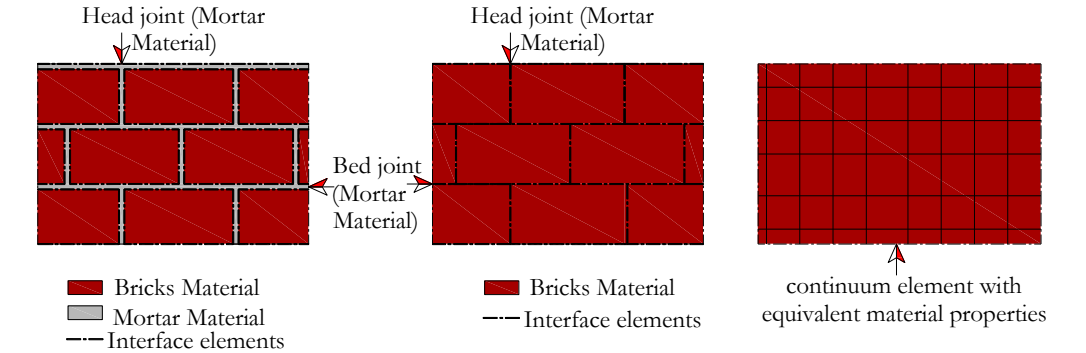

a) Micro-continuum models b) Meso-continuum models c) Macro-continuum models

Figure 2.3 Continuum models for masonry infills

2.4.3 Review of applications using continuum models for masonry infills

This section reviews previous studies where continuum finite element material models and/or structural models were developed and used to represent the behaviour of infilled frame structures. One of the earliest numerical studies which tried to develop continuum models for infilled structures was conducted by Mallick*, et al.* (1967). The interface between the frame and the infill was modelled by considering frictional shear forces in the contact region using a link element. They identified that the element was able to transfer compressive and bond forces, but unable to transfer tensile forces. Later, two alternative schemes, the exact and the constrained schemes, were suggested by Axley*, et al.* (1979) to determine the stiffness of the frame-infill system. Te-Chang*, et al.* (1984) proposed a plastic theory in which three different failure modes were identified, related to the relative strengths of the columns, the beams and the infill. These models captured the corner crushing with failure in columns and beams and the diagonal crushing of the infills.

Based on the assumption of homogenous behaviour of the infill panel, Dhanasekhar*, et al.* (1986) modelled infill walls using the macro-continuum model with nonlinear material properties calibrated from experimental results of one hundred and eighty six half-scale square panel specimens. The separation and the shear failure between the frame and the infill panel were modelled using one-dimension joint elements. The accuracy of the numerical models was verified by experimental racking tests of a masonry infilled steel frame and they concluded that the shear and the tensile strengths of the masonry infill have a significant influence in the load-deflection behaviour, the ultimate strength and the failure mechanism.

Lotfi*, et al.* (1991) investigated the accuracy of using a homogenous smeared-crack model to capture the response of a reinforced masonry wall. In the smeared-crack model, the uncracked material is considered as an isotropic material and the cracked material is modelled with a nonlinear orthotropic constitutive model. This modelling approach proved to be efficient and reliable to capture the flexural failure of a reinforced masonry wall. However, they reported that the brittle shear behaviour of the wall resulting from the diagonal cracking cannot be captured properly for lightly reinforced wall panels using this method. Later, Lotfi*, et al.* (1994) also developed a nonlinear interface constitutive model to capture the combined normal and shear stresses and also the dilatancy (the vertical displacement of the bricks due to the shear force, which occurs due to the wedging action of asperities) which had been observed in the experiments, in combination with their smeared crack model for masonry bricks. They evaluated the performance of their interface model by comparing their results with the available

experimental data and obtained an adequate prediction of the shear capacity and of the dilatancy. They reported that their model was capable of predicting structural features of infilled frames such as load capacity, failure modes, ductility and crack patterns.

In order to define a rational unit-joint model able to describe cracking, slip and crushing of the masonry material, Lourenço*, et al.* (1997) discretized the masonry components based on the softening plasticity for tension, shear and compression, with consistent treatment of the intersections defined by these modes. A zero thickness interface element was also used to model mortar joints while adding the mortar joints thickness to the masonry units. They showed the ability of their model to capture the peak load and post-peak behaviour of the masonry shear wall by comparing their results with experimental results on masonry walls.

In the same year, Mehrabi*, et al.* (1997) also presented a constitutive model for mortar joints in masonry infill panels. They used 4-node and 9-node smeared-crack finite element models to represent the behaviour of concrete in the RC frames and masonry units. This model considered the nonlinear hardening behaviour of the interface, the reversal shear dilatancy in cyclic loading, and the contraction of the interface under shear sliding due to the loss of particles. They concluded that the proposed finite element model provided a good matching with experimental results in terms of failure mechanism, lateral stiffness and sliding failure between masonry courses.

Based on the model developed by Lourenço*, et al.* (1997) and on plasticity theory, Oliveira*, et al.* (2004) proposed a constitutive model to simulate the cyclic behaviour of interface elements. They compared their numerical model with static cyclic experiments on three masonry walls (without frames) and reported that their model was able to describe the cyclic loading of interface elements. They also showed that the most relevant characteristics observed in experiments were captured by their model.

Stavridis (2009) and Stavridis*, et al.* (2010) developed a complex nonlinear finite element model for RC frames with masonry infills. This model combines the smeared (for masonry units) and the discrete crack (for mortar joints) approaches to overcome the weaknesses of the smeared-crack model to capture the brittle shear failure of the masonry mortar joints and of the RC frame, as shown in Figure 2.4. They used this new element to model the behaviour of concrete, brick and mortar and they used a 4-node smeared-crack element to model the brick. They showed that their model can capture different failure modes observed in experiments such as diagonal cracking, sliding, and crushing of the infill and flexural and shear failure of the concrete columns.

A year later, Koutromanos*, et al.* (2011) followed the Stavridis (2009) model, as shown in Figure 2.5, and used a cohesive cracked interface model with an improved smeared crack model to capture the cyclic behaviour of the masonry infilled frame. By comparing their results with quasi-static and shaking-table experimental results, they found a good agreement between the numerical simulation and the experimental data for both tests in terms of the hysteresis behaviour and failure mechanism. Bolis*, et al.* (2016) used the same modelling scheme in order to investigate the improvement in performance of RC frames with masonry infills constructed using sliding subpanel infills. Based on numerical analyses, it was found that the proposed solution allows the system to maintain its strength at high deformations exceeding drifts of 3%, without any substantial damage in the masonry.

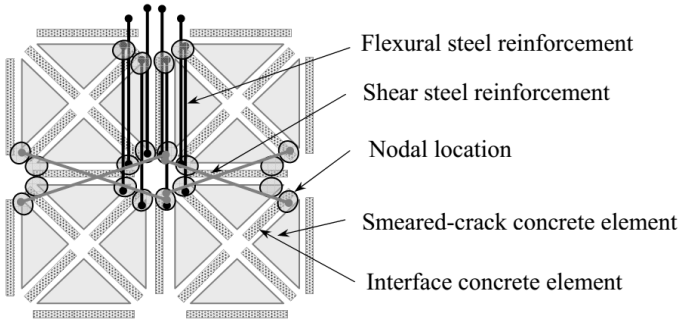

Figure 2.4. Finite element discretization of RC members proposed by Stavridis (2009).

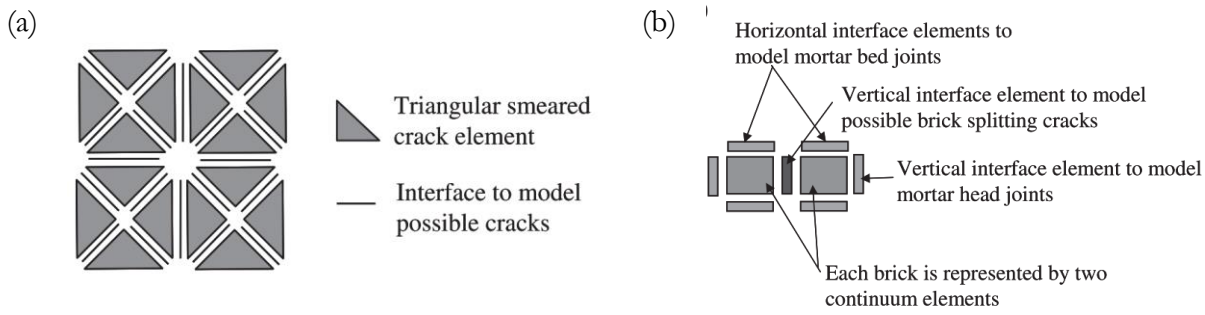

Figure 2.5 Discretization scheme used in finite element models by Koutromanos*, et al.* (2011): (a) RC columns and (b) unreinforced masonry panels.

Sattar (2013) reported that the model presented by Koutromanos*, et al.* (2011) and Stavridis (2009) is computational intensive and is not suitable for practical applications. Based on results presented by Al-Chaar*, et al.* (2008) and on the availability of multiple software packages, Sattar (2013) used the commercial software DIANA (2011) to develop a continuum finite element modelling approach that was more suitable in terms of computational effort. The potentialities of the DIANA software were used to implement a smeared-crack continuum model for the bricks employing two-

dimensional plane stress 4-node quadrilateral elements with 2*2 Gauss points. Line interface elements were also used to model the bed joints, head joints and the wall-to-frame joints, and a smeared crack model was adopted to model the concrete in the RC frame. The concrete elements as well as the brick elements were modelled with 4-node quadrilateral elements and reinforcement was modelled using a 1-D truss element with an elastic-hardening-plastic material model. Figure 2.6 shows the details of Sattar's model. Sattar concluded that the proposed model is capable of capturing the most important characteristics of the masonry infill behaviour such as cyclic shear sliding along the mortar joints, tensile cracking of the mortar joints, and tensile and compressive cracking of the bricks. However, this modelling approach could not capture the brittle shear failure that can occur in concrete columns or the discrete cracking that may occur through the bricks.

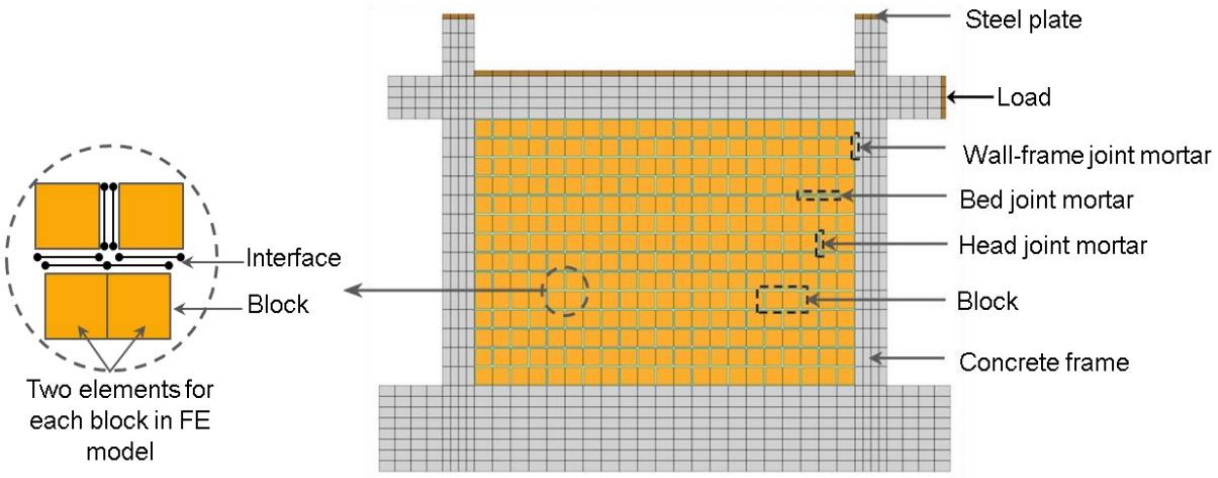

Figure 2.6. Nonlinear refined finite element (micro) model for masonry infilled RC frames implemented by Sattar (2013).

In the same context, Mohyeddin*, et al.* (2013a) used the potentialities of the ANSYS (ANSYS, 2012) software to develop a meso-model to represent the in-plane and out-of-plane behaviour of infilled RC frames. They used smeared-crack solid elements to represent RC and masonry parts and used surface contact elements to represent the interaction between the brick units and the RC frame. It is noted that they used an elastic material to represent mortar in the middle band, as shown in Figure 2.7, to prevent the occurrence of excessive damage in elements adjacent to the contact element. They concluded that the model can be used to predict the behaviour of the infilled frame over a wide range of lateral displacements and to interpret its response at various stages of in-plane or out-of-plane loading. However, they reported that the main drawbacks of their model were the need to use the referred middle elastic mortar band, the inability to represent the debonding between the reinforcing

bars and the concrete and the lack of stability of the contact elements when the underlying elements are fully cracked/crushed.

Also using ANSYS, Chen, *et al.* (2016) simulated the behaviour of steel frames with masonry infills. They used homogeneous continuum elements, where the masonry elements were modelled using a 4-node plane stress element and the mortar effect was simulated using a surface-based cohesive contact model to capture the cracking and sliding failure of the mortar joints. Although Chen, *et al.* (2016) used homogeneous continuum elements to model the infills, they had a reasonable agreement between the proposed model and the experimental data for monotonic loading analyses.

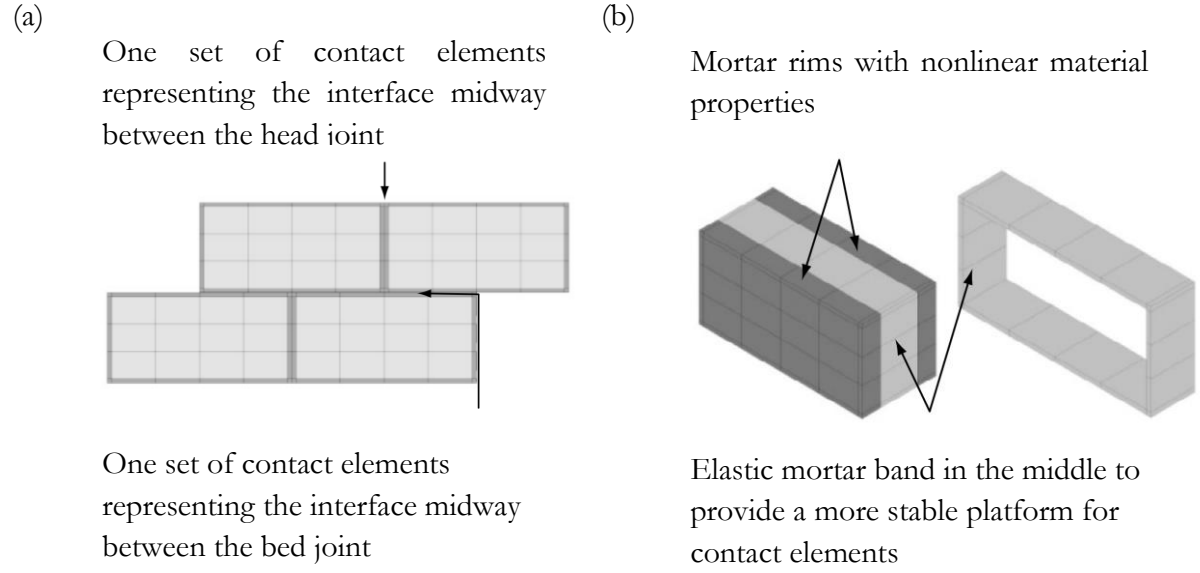

Figure 2.7 (a) The location of the interface (contact) elements in the masonry; (b) "masonry FE unit" used in the analyses comprising a nonlinear masonry block surrounded by nonlinear mortar rims and a central elastic mortar band (Mohyeddin, *et al.*, 2013a)

In the context of using commercial software as a tool to model the behaviour of infilled frames, Zhai, *et al.* (2016) used the potentialities of the software ABAQUS (2011) to model their experimental tests on RC frames with masonry infill. When comparing the results obtained from the monotonic analytical test with the experimental results, they reported that the adopted modelling technique can predict the seismic behaviours of the test specimens with acceptable accuracy. Using the same software, Yuen, *et al.* (2016) developed a detailed finite element for RC frames with masonry infills to study the interaction between the out-of-plane and the in-plane behaviours. Based on their analytical results, they concluded that the early-stage behaviour, including the initial stiffness and cracking load of the fully infilled frame, is less influenced by the out-of-plane load. However, the effect of out-of-plane loading increases after the development of cracks in the infill. For higher levels of out-of-plane

loading, the failure mechanism of the fully infilled frame was also seen to change from a brittle shear mode to a ductile flexural mode.

From the presented review, it can be seen that representing the structural behaviour of masonry infilled frames is complex due to the high number of parameters and phenomena involved, as well as due to the considerable uncertainty involved in many of those parameters. However, the previously presented models successfully capture several aspects of the behaviour of masonry infilled frames. Nonetheless, due to the high nonlinearity involved in this kind of model, these studies only analyse the behaviour of frames with infills in small scale systems, most of them involving a one-bay one-storey specimen. Based on this fact, the use of this kind of refined model is not feasible to analyse full scale structures. Therefore, the use of simplified modelling approaches is seen to be more practical for the analysis of large systems, as presented in next section.

2.4.4 Masonry infill modelling using strut models

As referred in the previous section, from a practical point of view, the use of continuum modelling approaches is not feasible for large systems due to the high computational cost. Due to their inherent simplicity, strut models (i.e. macro-models) are one of most practical approaches to represent the behaviour of infill panels, especially for design and performance assessment purposes. As shown in Figure 2.8, these modelling approaches are based on replacing the infill panel by an equivalent pinned diagonal strut system. A large amount of research has been dedicated to determine the main structural properties of the diagonal strut such as the width, stiffness, constitutive behaviour and the number of struts that should be considered. The characteristics of the diagonal strut model vary according to the type of analysis (i.e. linear elastic or nonlinear) and the loading procedure (monotonic, cyclic or transient loading). For example, the required properties for a diagonal strut in case of a linear elastic analysis are the geometric properties of the strut (length and cross-section size) and the modulus of elasticity. However, when the nonlinear behaviour of the material is considered, the complete force-displacement behaviour of the strut is needed instead. Furthermore, the required properties that are required for the diagonal strut become more complex in case of cyclic and dynamic loading.

Tucker (2007) classified available analytical methodologies defining the in-plane properties of strut models into two main approaches: stiffness methods and strength methods. Both methods

replace the infill panel by an equivalent strut but use different approaches to define the necessary properties of the strut. The stiffness method estimates the structural contribution of the infill wall based on the formation of the compression area along the infill. Therefore, this method focuses on estimating the geometric properties of the strut and associates these properties with equivalent material properties (usually the characteristic compressive strength of the masonry) in order to define the lateral capacity of the infill. The strength method defines the properties of the strut by quantifying the lateral forces carried by the infill wall. A more detailed discussion on these two methods is provided in the following, including the modifications that have been proposed over time to these modelling approaches.

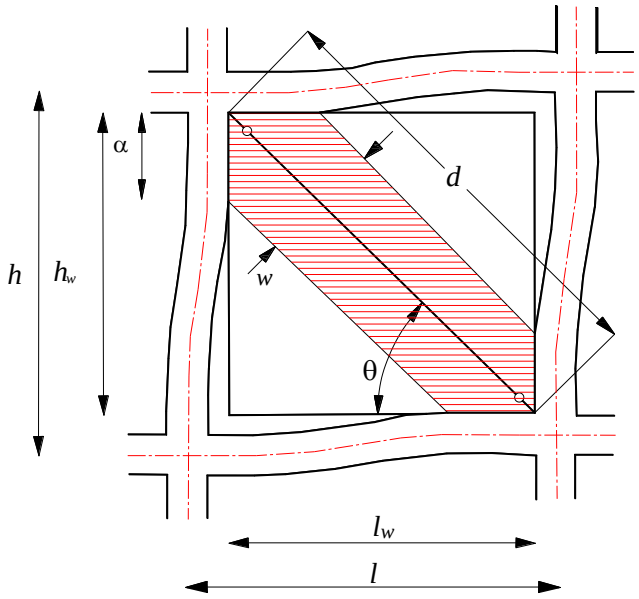

Figure 2.8 Formulation of the equivalent diagonal strut and its relevant parameters.

2.4.4.1 The stiffness method

Polyakov (1956) was the first to suggest the possibility of considering the effect of the infill panel as an equivalent diagonal bracing. Later Holmes (1961) adopted this suggestion and proposed a linear equivalent compressive strut model. Holmes replaced the infill panel by a diagonal strut with the same material and thickness of the infill panel, while the width w of the proposed strut was given by the following expression:

$$w = \frac{1}{3} d \tag{2.1}$$

where d, as shown in Figure 2.8, is the diagonal length of the infill panel. This rule is called the *one-third* rule and was suggested to be applicable irrespective of the relative stiffness of the frame and the infill. Based on that rule, Holmes proposed expressions to assess the horizontal displacement of the infilled frame at failure and to compute the horizontal load causing crushing failure in the corner regions. One year later, based on experimental data from a large series of tests in masonry infilled steel frames, Stafford-Smith (1962) reported that the ratio w/d varied from 0.10 to 0.25 for an infill having a side's ratio of 5 to 1.

Smith*, et al.* (1969) continued the development of the equivalent strut theory by assessing the interaction between the frame and the infill to compute the effective width of the struct. In their formulation, the effective width of the strut is a function of the relative stiffness of the column and the infill, the length-to-height proportion of the infill, the stress-strain relation of the infill material, and the value of the diagonal load acting on the infill. The length of contact α between the infill and the frame is defined by:

$$\frac{\alpha}{h} = \frac{\pi}{2\lambda h} \qquad (2.2)^{\ddagger}$$

where h is the height of the column between the centrelines of the beams and λ is a characteristic stiffness parameter given by:

$$\lambda = \sqrt[4]{\frac{E_I t \sin 2\theta}{4EIh_w}} \,. \qquad (2.3)$$

in which E_I is the modulus of elasticity of the masonry panel, EI is the flexural stiffness of the columns, t is the thickness of the infill panel and equivalent strut, h_w is the height of the infill panel and θ is the slope of the infill diagonal (in degrees). In addition, they also developed a set of empirical curves that relate the stiffness parameter to the effective width of an equivalent strut.

Based on experimental tests on model frames with two different materials (concrete and brick), Mainstone (Mainstone, 1971, Mainstone, 1974) investigated all variables likely to have a major influence on the contribution of the infill walls to the strength of a sidesway mechanism in multi-storey framed buildings. Based on this research, he proposed two empirical expressions to evaluate the width

---

‡ Hereon, λ_h is used to represent the dimensionless term λh in *Eq. (2.2)*

of the equivalent strut in case of brick and concrete infills: Eqs. (2.4) and (2.5) in case of λ_h in the range of 4~5 and Eqs. (2.6) and (2.7) in case of λ_h greater than 5.

$$w = 0.175 d \lambda_h^{-0.4} \qquad \textit{Brick} \tag{2.4}$$

$$w = 0.115 d \lambda_h^{-0.4} \qquad \textit{Concrete} \tag{2.5}$$

$$w = 0.16\, d \lambda_h^{-0.3} \qquad \textit{Brick} \tag{2.6}$$

$$w = 0.11 d \lambda_h^{-0.3} \qquad \textit{Concrete} \tag{2.7}$$

Tassios (1984) simplified the proposed diagram produced by Bazan, *et al.* (1980) to predict the width of the equivalent strut for the case of failure (cracking) across the diagonal of the infill panel by the following expression:

$$w \cong 0.20 d \sin\theta \sqrt{\frac{E_c A_C}{G_w A_w}} \quad \text{if } 1 < \frac{E_c A_C}{G_w A_w} < 5 \tag{2.8}$$

where G_w is the infill shear modulus. Based on previous experimental data, Te-Chang, *et al.* (1984) proposed a semi-empirical expression to calculate the width of the equivalent diagonal strut when θ is in the range 25°~50° given by:

$$w = \frac{0.95 h_w \cos\theta}{\sqrt{\lambda_h}} \tag{2.9}$$

where it is assumed that the ratio $\frac{h_w}{l_w}$ varies from 1.0 to 1.5, where l_w is the infill panel width.

Considering the state of the infill panel in terms of cracking, Decanini, *et al.* (1987) proposed the following two sets of expressions to quantify the equivalent diagonal strut width for cracked and uncracked panels:

$$\text{Uncracked panel: } w = \begin{cases} \left(\dfrac{0.748}{\lambda_h} + 0.085 \right) d & \textit{if } \lambda_h \le 7.85 \\ \left(\dfrac{0.393}{\lambda_h} + 0.130 \right) d & \textit{if } \lambda_h > 7.85 \end{cases} \tag{2.10}$$

Cracked panel: $$w = \begin{cases} \left(\dfrac{0.707}{\lambda_h} + 0.010 \right) d & \text{if } \lambda_h \le 7.85 \\ \left(\dfrac{0.470}{\lambda_h} + 0.040 \right) d & \text{if } \lambda_h > 7.85 \end{cases} \quad (2.11)$$

These expressions are plotted in Figure 2.9 as a function of parameter λ_h. The main advantage of the Decanini*, et al.* (1987) approach is that values of λ_h in Eqs. (2.10) and (2.11) have been evaluated based on Eq. (2.3) for different panel states (uncracked and cracked panel), thus providing a distinction between the uncracked and cracked stages that are known to have a major influence in the equivalent diagonal strut properties.

Based on experimental results of scaled brick infilled frames, Moghaddam*, et al.* (1988) proposed the following simple relation between the length of the diagonal equivalent strut and its width:

$$w = \frac{1}{6} d \quad (2.12)$$

For unreinforced masonry, compressive strut models have the potential to model the initial stiffness and the low-level behaviour of the infill before the occurrence of significant bed joint cracking. Hendry (1990) related the effective strut width w to the contact lengths by:

$$w = 0.5\sqrt{\alpha_l^2 + \alpha_h^2} \quad (2.13)$$

where α_h and α_l are vertical and horizontal contact lengths, respectively, given by the following expressions:

$$\alpha_h = \frac{\pi}{2} \sqrt[4]{\frac{4(EI)^* h_w}{E_I t \sin 2\theta}} \quad (2.14)$$

$$\alpha_l = \frac{\pi}{2} \sqrt[4]{\frac{4(EI)^* l_w}{E_I t \sin 2\theta}} \quad (2.15)$$

where the ***(EI)*** terms in Eqs. (2.14) and (2.15) are related to columns and beams, respectively. The remaining parameters involved are those also defined in Eq. (2.3).

Paulay, *et al.* (1992) pointed out that a high value of the strut width will result in a stiffer structure and, in turn, lead to a higher seismic demand. For seismic design purposes, they recommended using the following expression:

$$w = \frac{1}{4} d \tag{2.16}$$

To illustrate the performance of the previous expressions, Figure 2.9 shows the variation of the ratio *w/d* according to Eqs. (2.1), (2.4), (2.9) to (2.13) and (2.16) for masonry infill panels. In order to represent Eq. (2.9), it is assumed that the slope angle θ is equal to 25° and 50°, which represent the limit values of practical situations. Since the ratios *w/d* proposed by Holmes (1961) and Paulay, *et al.* (1992) are independent of parameter λ_h, they represent approximations which are, however, useful for simplified analyses. The ratios *w/d* proposed by Mainstone (1971) and Te-Chang, *et al.* (1984) are inversely proportional to λ_h because the contact length is smaller when the stiffness of the masonry panel is larger than the stiffness of the frame. It is worth mentioning that FEMA 306 (1998) and the Turkish Code for Buildings in Seismic Zones (TEC, 2007) recommend calculating the stiffness of masonry infilled frames by representing the masonry with an equivalent diagonal strut. The expression given for calculating the width of the strut matches Eq. (2.4) proposed by Mainstone (1971).

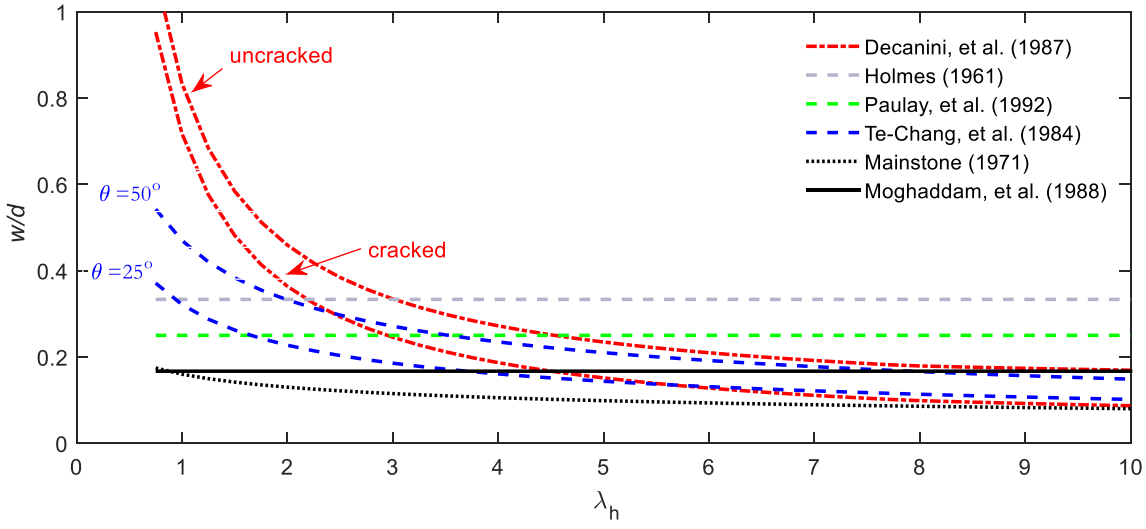

Figure 2.9. Variation of the ratio *w/d* for infilled frames as a function of λ_h.

In light of previous research and empirical fitting of finite element results, Durrani, *et al.* (1994) proposed the following semi-empirical expressions to assess the width of the equivalent diagonal strut:

$$w = \gamma\, d \sin(2\theta) \tag{2.17}$$

$$\gamma = 0.32\left[\frac{h^4 E_w t_w}{m E_c I_c h_w}\right]^{-0.1}\left[\sqrt{\sin 2\theta}\right] \tag{2.18}$$

$$m = 6\left(1 + \frac{6E_b I_b h}{\pi E_c I_c L}\right) \tag{2.19}$$

where E_b and E_c are the moduli of elasticity for the beam and column, respectively, while I_b and I_c are the moments of inertia of the beam and column, respectively.

Flanagan*, et al.* (1999) proposed a piecewise linear strut width calculated by:

$$w = \frac{\pi}{C\lambda \cos\theta} \tag{2.20}$$

where C is an *empirical* constant based on drift displacements and infill damage. The values of C vary with the type of frame and the infill material. Table 2.1, Table 2.2, Table 2.3 and Table 2.4 give the values of C for steel frames with a clay tile infill, steel frames with concrete masonry infill, concrete frames with concrete masonry, and concrete frames with brick masonry, respectively, according to Bennett*, et al.* (1996).

Table 2.1 Values of C according to Bennett*, et al.* (1996) for steel frames with clay tile infill

C	Displacement(cm)	Typical infill damage
5	0.00 – 0.127	None
7	0.127 – 0.508	Diagonal mortar joint cracking
11	0.508 – 1.016	Off diagonal mortar joint cracking
14	1.016 – 1.524	Banded diagonal mortar joint cracking
16	1.524 – 2.032	Corner mortar crushing and tile cracking
18	2.032 – 2.54	Tile face-shell splitting (primarily corner regions)

Table 2.2 Values of C according to Bennett*, et al.* (1996) for steel frames with concrete masonry infill

C	Displacement(cm)	Typical infill damage
4	0.00 – 0.254	None
5	0.254 – 0.762	Diagonal mortar joint cracking
8	0.762 – 1.651	Off diagonal mortar joint cracking
12	1.651 – 2.032	Extensive random cracking; possible corner crushing

Table 2.3 Values of C according to Bennett, *et al.* (1996) for RC frames with concrete masonry infill

C	Displacement(cm)	Typical infill damage
2	0.00 – 0.254	None
4	0.254 – 0.635	Diagonal sliding mortar joint cracking
8	0.635 – 1.143	Off diagonal mortar joint cracking, bed joint sliding; corner crushing

Table 2.4 Values of C according to Bennett, *et al.* (1996) for RC frames with brick masonry infill

C	Displacement(cm)	Typical infill damage
2	0.00 – 0.254	None
4	0.254 – 0.381	Diagonal mortar joint cracking
8	0.381 – 0.635	Off diagonal mortar joint cracking, bed joint sliding; corner crushing
10	0.635 – 0.889	Extensive random cracking; possible corner crushing

According to Al-Chaar (2002), the equivalent width of the infill strut in the elastic range can be estimated using Eqs. (2.21) to (2.23). It should be noted that linear interpolation is required for aspect ratios falling between 1.0 and 1.5.

$$w = 0.0835Cd\left(1+\frac{2.574}{\lambda_h}\right) \quad ; \quad {l_w}/{h_w} \geq 1.5 \tag{2.21}$$

$$w = 0.1106d\left(1+\frac{6.027}{\lambda_h}\right) \quad ; \quad {l_w}/{h_w} = 1.0 \tag{2.22}$$

$$\text{where} \quad C = -0.3905\left(\frac{l_w}{h_w}\right)+1.7829 \tag{2.23}$$

Chethan, *et al.* (2009) evaluated the width of the equivalent strut using the contact length between the infill wall, the beam and the column as follows:

$$w = \sqrt{\alpha_l^2 + \alpha_h^2} \tag{2.24}$$

where α_h and α_l are the vertical and horizontal contact lengths, respectively, given by Eqs. (2.14) and (2.15). In the same context, Khaja, *et al.* (2013) reported that α_l, the contact length between the infill wall and the beam, is approximately equal to half of the beam span length.

Recently, Turgay*, et al.* (2014) proposed alternative expressions to provide improved estimates for the stiffness and deformability of infilled RC frames. According to their proposal, the diagonal strut width is given by the following expression:

$$w = 0.18\frac{d}{\sqrt[4]{\lambda_h}} \tag{2.25}$$

The ratio h/l considered in this study varied from 1.2 ~2.

Based on this review, it is clear that there is a large variety between existing proposals to define the properties of the strut model. In the next chapter, several proposals are applied to define the properties of strut models and compared to available experimental data to assess their reliability.

2.4.4.2 The strength method

Contrary to the stiffness method, the strength method first defines the force-displacement relation for the infill and then associates this relation with the area of the strut to define the constitutive behaviour of the infill. A vast body of literature reports models that were proposed for the force-displacement relation of the equivalent diagonal strut. One of the early attempts to define the complete force-displacement behaviour of the infill panel was conducted by Klingner*, et al.* (1978). They proposed a nonlinear hysteretic response for the equivalent diagonal strut model based on experimental tests carried out in masonry infilled RC frames. They considered the strength and the reloading stiffness degradations in their cyclic model, as shown in Figure 2.10, while the unloading stiffness was assumed to be linear and equal to the initial stiffness. Even though their model assumed that the diagonal strut has a certain amount of tensile strength, they ignored this component in the implementation of the model in their numerical analyses. The experimental calibration of this model showed poor agreement. However, this model was the first attempt to consider the nonlinear cyclic feature of the diagonal strut response and represented the basic approach for further developments.

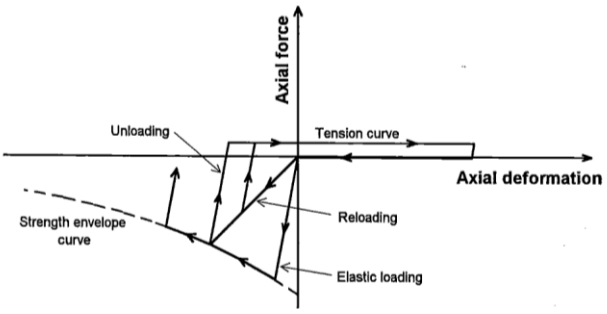

Figure 2.10. Force-displacement response of the strut proposed by Klingner, *et al.* (1978)

In order to define the nonlinear behaviour for their proposed model, Andreaus, *et al.* (1985) considered the hysteretic curve shown in Figure 2.11. According to this model, strength degradation starts immediately after the strut force reaches its maximum value and reloading occurs when the axial deformation is equal to the plastic deformation of the previous loop. Furthermore, their model does not consider any stiffness degradation effects.

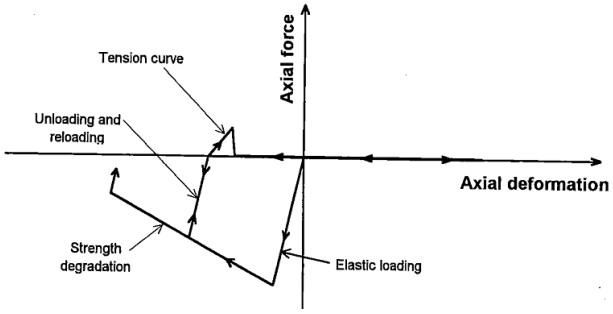

Figure 2.11. Hysteric model employed by Andreaus, *et al.* (1985)

Doudoumis, *et al.* (1986) also, proposed a hysteretic model which is illustrated in Figure 2.12. This model was developed for non-integral infilled frames in which a gap normally forms between the masonry panel and the surrounding frame. The envelope curve considered strength degradation but the hysteric cycles were described in a very simplistic way assuming that reloading occurs following the elastic branch.

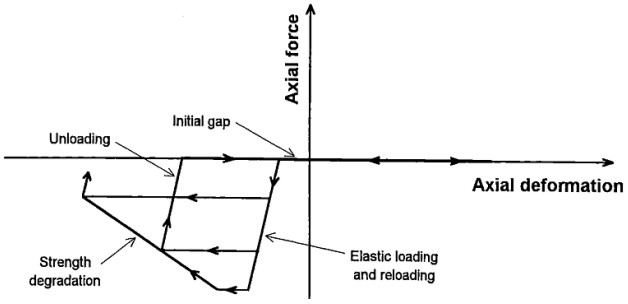

Figure 2.12. Hysteretic model for non- integral infilled frames proposed by Doudoumis, *et al.* (1986)

Based on results of tests carried out in thirty seven single-storey reinforced masonry shear walls, Soroushian*, et al.* (1988) derived a typical hysteretic model for masonry shear walls failing in shear and in flexure which is illustrated in Figure 2.13. The proposed model considers the severe stiffness and strength degradation, as well as the low energy dissipation capacity and brittle failure of reinforced masonry shear walls. Based on seismic analyses in which they implemented their proposed model, they concluded the following:

- The hysteretic behaviour and energy dissipation capacity of shear walls substantially reduce the seismic forces when compared with linear systems of similar initial periods of vibration;
- Viscous damping was less influential to the seismic response characteristics of the (nonlinear) shear walls, when compared with linear systems;
- Under seismic excitation, the walls with a shear failure mode have less ductility and energy dissipation capacity and larger degradation. Furthermore, they also required higher strength to survive similar earthquakes than the comparable shear wall failing in flexure;
- Systems with a more stable hysteretic behaviour than masonry shear walls did not necessarily perform better under earthquake ground motions. Large stiffness deterioration in shear walls produce elongations of the natural period of vibration that positively influence the response of certain shear walls for some earthquake ground motions.

It is worth mentioning that Chrysostomou*, et al.* (1992) used this proposed hysteresis behaviour model to simulate the nonlinear behaviour of their equivalent diagonal strut model but with some modifications.

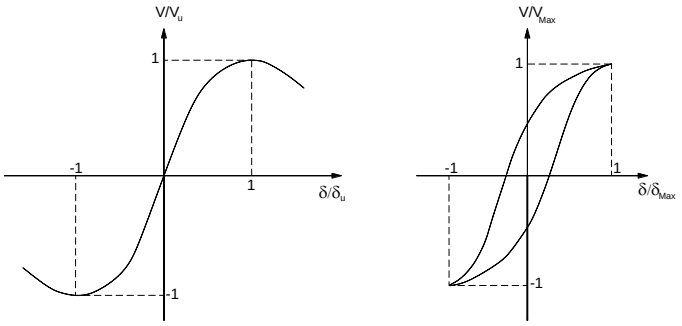

a) Strength envelope *b) Hysteretic loop*

Figure 2.13. Hysteretic model proposed by Soroushian*, et al.* (1988) for masonry walls and adopted by Chrysostomou*, et al.* (1992) for the diagonal strut model.

Madan*, et al.* (1997) combined a set of mathematical functions to develop the smooth force-displacement relation which is shown in Figure 2.14. By selecting adequate values of the nine parameters included in the model, their hysteretic force-deformation model accounts for strength and stiffness degradation, as well as for pinching resulting from the opening and closing of masonry gaps of the infill panel. It is noted that some of these parameters are empirical, while others depend on energy dissipation considerations. The implementation of this model is not straightforward and requires the numerical integration of a differential equation.

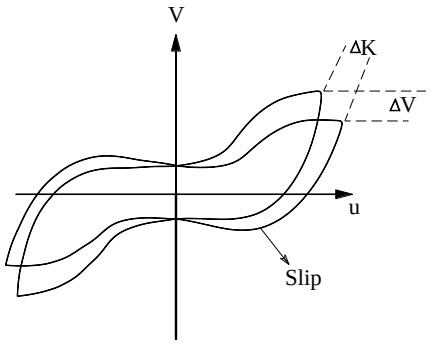

Figure 2.14 Integrated hysteretic model for degrading pinching elements according to (Madan*, et al.*, 1997).

Based on the simplified stress-strain relation of the masonry material, El-Dakhakhni*, et al.* (2003) employed a trilinear response model, which is shown in Figure 2.15, in their three diagonal strut model. Their scheme includes an elastic, plastic (ultimate strength) and post-capping branch for the envelope of the strut behaviour.

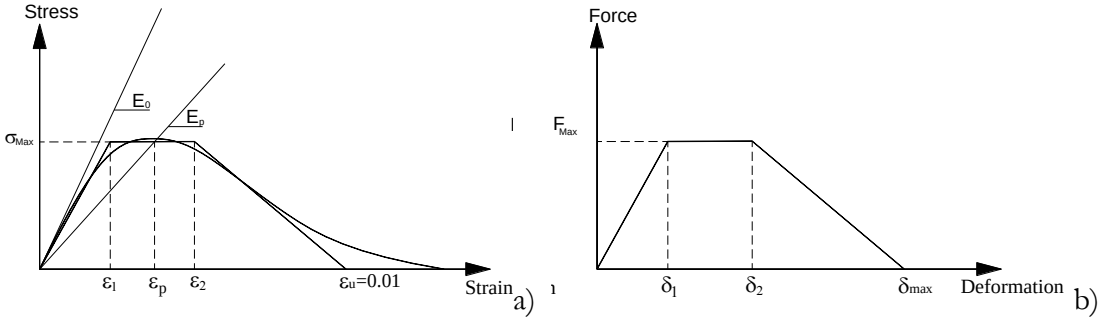

Figure 2.15 Simplified trilinear relation of the strut proposed by El-Dakhakhni*, et al.* (2003): a) stress-strain relation of masonry; b) typical force-deformation relation for the strut model

In the context of using a trilinear realation to represent the nonlinear behaviour of masonry infills, several expressions have been proposed, such as those by Panagiotakos*, et al.* (1994), Bertoldi*,*

et al. (1993), Uva*, et al.* (2012) or Dolšek*, et al.* (2008). As shown in Figure 2.16, this trilinear relation describes the evolution of the lateral force supported by the infill and the corresponding displacement. Therefore, to define the curve, the coordinates of the three main points in terms of the forces and corresponding displacements, are required. Available expressions to define these trilinear relations are either based on regression analysis using experimental data (e.g. see Panagiotakos*, et al.* (1994) and Bertoldi*, et al.* (1993)) or adopt and combine pre-existing expressions available from literature to get a more realistic curve (e.g. see Uva*, et al.* (2012) and Dolšek*, et al.* (2008)). The reliability of these expressions will be analysed in the next chapter using several experimental datasets.

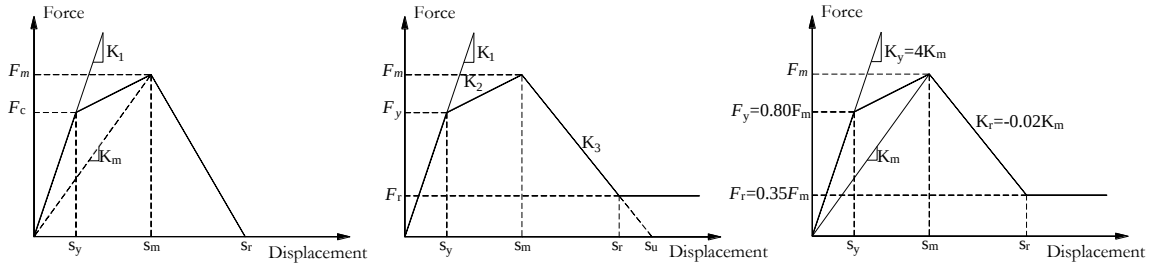

a) b) c)

Figure 2.16 Force-displacement trilinear curve proposed for a strut element based on three proposals: a) Dolšek*, et al.* (2008), b) Panagiotakos*, et al.* (1994) and c) Bertoldi*, et al.* (1993)

2.4.4.3 Strut models proposed by design standards

Based on the previous models, several codes and standards recommend using strut models to represent the behaviour of infilled RC frames. In this context, the New Zealand masonry code (NZS, 2004), recommends using an equivalent diagonal strut to represent the masonry infill for stiffness and force calculations. It further recommends that the width of the strut be equal to one-quarter of the length of the diagonal. Also, the Canadian standard (CCMPA, 2009) uses Eq. (2.24) to evaluate the width of the diagonal strut with modifications to the α_h and α_l expressions. The United States Masonry Standards Joint Committee (ACI, 2011) also recommends using an equivalent diagonal strut to represent the structural effect of infill walls. This standard defines an expression to evaluate the strut width based on the material and configuration of the infill panel. To summarize what is recommended by some of these standards to define the properties of the strut model, Table 2.5 shows the expressions they suggest to estimate the stiffness and strength of the equivalent diagonal strut.

Table 2.5. Summary of strut models for infill panels considered by various standards

Standard	Equivalent strut model	Strength model
Common expression	$E_I = Cf_m^{'}$, $\lambda_h = \sqrt[4]{\frac{E_I t \sin 2\theta}{4(EI)_{column} h_w}} h$	$A_{ni} = t_w l_w$
NZSEE (NZSEE, 2006)	$C = 500$, $w = 0.175\ d\ \lambda_h^{-0.4}$	$V_u = \begin{cases} 0.50 w t f_m^{'} \cos\theta \\ \frac{2.83 l_w^2 h_w t_w \sigma_{cr}}{h_w + l_w} \\ t_w l_w \tau_0 + 0.8P \end{cases}$ $\sigma_{cr} = \frac{f_m^{'}}{40}, \tau_0 = \frac{f_m^{'}}{20}$
ASCE 41-06 (ASCE, 2007)	$C = 550$, $w = 0.175\ d\ \lambda_h^{-0.4}$	$V_u = A_{ni}\tau_w$
TEC (TEC, 2007)	$C \approx 750$, $w = 0.175\ d\ \lambda_h^{-0.4}$	$V_u \le \begin{cases} A_{ni}\tau_w \\ 0.22 l_w t f_m^{'} \end{cases}$
CCMPA (CCMPA, 2009)	$C = 850$, $w \le \begin{cases} w_i / 2 \\ d/4 \end{cases}$, $w_i = \sqrt{\alpha_l^2 + \alpha_h^2}$ $\alpha_h = \frac{\pi}{2}\sqrt[4]{\frac{4(EI)_{column} h_w}{E_I t \sin 2\theta}}$ and $\alpha_l = \pi\sqrt[4]{\frac{4(EI)_{beam} l_w}{E_I t \sin 2\theta}}$	$V_u \le \begin{cases} 0.85\chi\phi_m w\,(f_m^{'} t) \\ 0.13\phi_m \sqrt{f_m^{'}} d \gamma_g \\ 0.16\phi_m \sqrt{f_m^{'}} t d_v \big/ 1 - 0.9\phi_m \tan\theta \end{cases}$ $d_v = 0.80\ l_w$,
ACI-530 (ACI, 2011)	$C = 700$, $w = \frac{0.30}{\lambda \cos\theta}$	$V_u \le \begin{cases} 3160 A_{ni}\sqrt{f_m^{'}} / 1.5 \\ 2070 A_{ni} / 1.5 \\ 0.152 t f_m^{'} \end{cases}$
ASCE 41-13 (ASCE, 2013)&&	$C = 550$, $k_1 = \frac{l_w t G_m}{h_w}$, $G_m = 0.40 E_I$	$V_u \le \begin{cases} 0.33 h_w t f_m^{'} \\ A_{ni}\tau_w \end{cases}$
NZSEE (NZSEE, 2016)	$C = 700$, $w = 0.18 d\ \lambda_h^{-0.4}$	$V_u \le \begin{cases} 0.33\ l t_m \sqrt{f_m^{'}} \\ 0.83 A_{ni} \\ 0.41 t l + 0.45 p \end{cases}$

Notations

$f_m^{'}$ is the masonry compressive strength in MPa, w is the strut width, A_{ni} is the shear area, d is the strut diagonal length, l_w is the infill length, h_w is the infill height, h is the height of the panel centre to centre, θ is the inclination angle of the strut on the horizontal plane, G_w is the shear modulus of the masonry, τ_w is the shear strength of masonry infill, E_I is the modulus of elasticity of masonry, t is the effective wall thickness, t_w is the wall thickness, I is the moment of inertia of the frame member, E is the modulus of elasticity of the frame, ϕ_m is a resistance factor for masonry considered to be 0.60, p is the vertical force acting on the masonry infill wall, χ and γ_g are factors whose values are found in the corresponding standard.

&& it provides an expression to directly compute the lateral stiffness k_1 of the infill wall

2.4.4.4 Modifications to the diagonal strut model.

As referred in previous sections, the interaction between the infill and the surrounding frame occurs along a certain contact area. However, the distribution of bending moments and shear forces in the frame members may not be adequately represented by a single diagonal strut connecting the two loaded corners of the frame (Reflak*, et al.*, 1991, Saneinejad*, et al.*, 1995, Buonopane*, et al.*, 1999). For these reasons, more complex macro-models were proposed to enhance the behaviour of single strut models by introducing modifications such as additional struts and modifying their arrangement, as shown in Figure 2.17.

In order to represent the response of infilled structures when horizontal shear sliding occurs between masonry courses, Leuchars*, et al.* (1976) suggested the model illustrated in Figure 2.17 (a). The double struts in this model can represent the large bending moments and shear forces induced in the central zone of the column. Furthermore, it is possible to consider the friction mechanism developing along the cracks which controls the strength of the system. However, this model was just a suggestion, since it has not been applied by any researcher, not even by the authors, to verify its accuracy.

During their experimental tests on infilled frames, Zarnic*, et al.* (1988) observed that the damage in the upper zone of the masonry panel occurred with an offset from the diagonal. Therefore, they modified the connection point of the diagonal strut to be lower, as shown in Figure 2.17 (b). This model could be applied in cases where a shear failure is expected to develop at the top of the column.

Figure 2.17 (c) and (d) show multiple struts models proposed by Schmid*, et al.* (1973) and Syrmakezis*, et al.* (1986), respectively. The main advantage of these models, in spite of their increase in complexity, is their ability to represent the internal forces in the frame more accurately. For example, the five struts model proposed by Syrmakezis*, et al.* (1986) is able to show the significant effect of the contact lengths on the bending moment distribution in frame members.

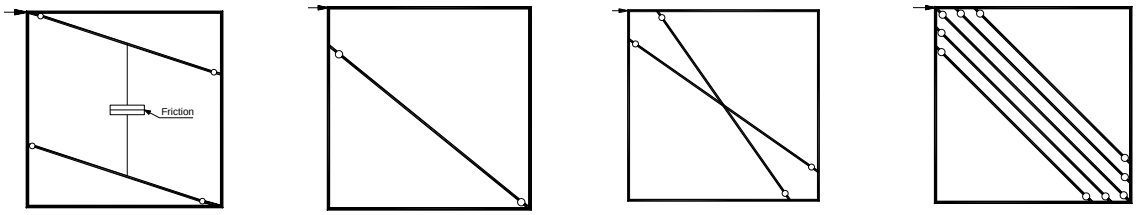

a) Leuchars*, et al.* (1976) b) Zarnic*, et al.* (1988) c) Schmid*, et al.* (1973) d) Syrmakezis*, et al.* (1986)

Figure 2.17. Modified systems for the diagonal strut model.

Andreaus, *et al.* (1985) generalized the equivalent diagonal strut theory and suggested that masonry can be replaced by a truss-like system, in order to generate a sort of finite element mesh formed by "cells", as shown in Figure 2.18. Every cell represents a 4-node element whose mechanical behaviour is defined by two truss members located along the diagonal direction of the element. Due to the refinement involved in this model, it can be considered as a micro-model although it is based on an equivalent diagonal strut system.

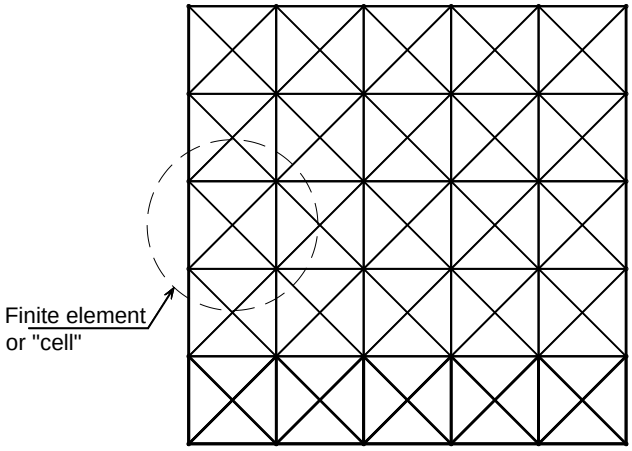

Figure 2.18. Finite element model proposed by Andreaus, *et al.* (1985) based on the diagonal strut concept

Chrysostomou (1991) and Chrysostomou, *et al.* (1992) replaced the infill panel by a six diagonal strut system, as shown in Figure 2.19. Three parallel struts were used in each diagonal direction and the off-diagonal ones were positioned at critical locations along the frame members. These locations are specified by parameters α_h and α_l associated with the position where a plastic hinge will develop in a beam or in a column. The evaluation of parameters α_h and α_l is theoretically based on the work of Te-Chang, *et al.* (1984). It is noted that, for a given instant of the analysis, only one group (three struts) of these struts is active, and the struts are replaced by those of the opposite direction whenever their compressive force is reduced to zero.

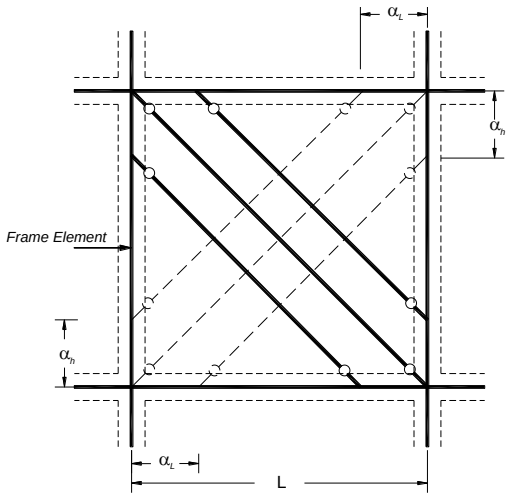

Figure 2.19. Six-strut model for masonry-infill panels in frame structures (Chrysostomou, 1991)

Based on experimental results and finite element analyses, Saneinejad*, et al.* (1995) proposed a method of analysis and design for steel frames with concrete or masonry infill walls subjected to in-plane forces by replacing the infill panel with a system of two diagonal struts. Their method accounts for the elastic and the plastic behaviour of the infilled frames, considering the limited ductility of the infill materials. This method is capable of predicting the strength and stiffness of infilled frames, as well as the infill diagonal cracking load. The infill aspect ratio, the shear stresses at the infill-frame interface, and the relative beam and column strengths are involved in this method. It is worth mentioning that they reported that, for steel frames infilled with concrete panels, the points of maximum bending moment of the frame members occur, approximately, at the end of the contact lengths, at distances from the beam-column connection given by:

$$\alpha_h = \alpha_c h = \sqrt{\frac{2\left(M_{pj} + \beta_c M_{pc}\right)}{\sigma_c t}} \quad \leq 0.40h \tag{2.26}$$

$$\alpha_l = \alpha_b l = \sqrt{\frac{2\left(M_{pj} + \beta_b M_{pb}\right)}{\sigma_b t}} \quad \leq 0.40l \tag{2.27}$$

where α_c is the ratio between the column contact length and its height, α_b is the ratio between the beam contact length and its length, M_{pj} is the minimum of the column's, the beam's or the connection's plastic moment capacity, referred to as the plastic moment capacity of the joint, M_{pc} and M_{pb} are the column and the beam plastic moment capacities, respectively, σ_c and σ_b are normal contact stresses at

the face of the column and the beam, respectively, β_c is the ratio between the maximum elastic bending moment developed within the height of the column and M_{pc}, β_b is the ratio between the maximum elastic bending moment developed within the span of the beam and M_{pb} and, finally, t is the thickness of the panel. Since β_c, β_b, σ_c and σ_b change during the loading history, the previous contact lengths are not constant. To overcome this problem, Saneinejad*, et al.* (1995) proposed the simplified Eqs. (2.26) and (2.27) that are valid throughout the loading history:

$$\alpha_h = \alpha_c h = \sqrt{\frac{2\left(M_{pj} + 0.20M_{pc}\right)}{tf'_{m-0}}} \leq 0.40h \tag{2.28}$$

$$\alpha_l = \alpha_b l = \sqrt{\frac{2\left(M_{pj} + 0.20M_{pb}\right)}{tf'_{m-90}}} \leq 0.40l \tag{2.29}$$

Where f'_{m-0} and f'_{m-90} are the compressive strength of the masonry panel parallel and perpendicular to the bed joint, respectively.

Crisafulli (1997) investigated the influence of using a different number of diagonal struts on the structural response in term of stiffness and forces in the perimeter of the frame by comparing results obtained from single, double and triple strut models with those obtained from a detailed finite element model, as shown in Figure 2.20. His remarks are summarized in the following:

- The lateral stiffness of the structure was similar in all the cases considered, with smaller values for two- and three-strut models. For the multi-strut models, the stiffness may change significantly depending on the distance between the struts;
- The single strut model underestimates the bending moment because the lateral forces are primarily transferred by a truss mechanism. On the other hand, the two-strut model leads to larger response values than those obtained with the finite element model;
- A better approximation is obtained from the three-strut model proposed by Chrysostomou (1991) and shown in Figure 2.19 , although some differences arise at the ends of both columns;
- Although the single strut model constitutes a sufficient tool for the prediction of the overall response, the triple strut model is superior in precision.

Eventually, Crisafulli (1997) recommended using the double strut model approach which is accurate enough and simpler when compared to the other models.

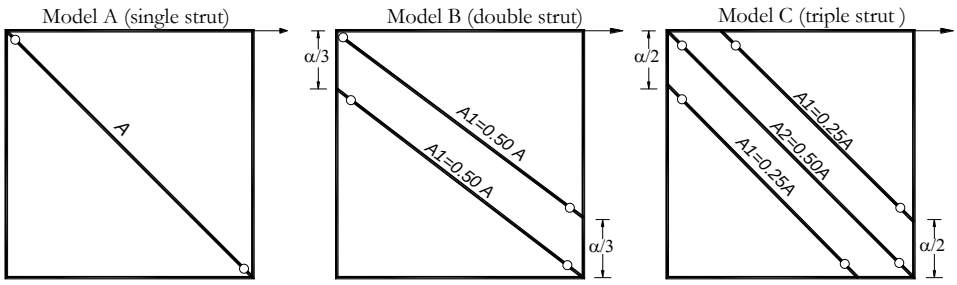

Figure 2.20. The strut models were considered by Crisafulli (1997), where α is the contact length proposed by Smith (1962)

In order to model steel frames infilled with concrete or masonry, El-Dakhakhni*, et al.* (2003) also suggested using two groups of struts where each group consists of diagonal struts with two offset struts, as illustrated in Figure 2.21. The total area of the proposed strut system, *A*, is given by the following expression:

$$A = \frac{\left(1-\alpha_c\right)\alpha_c h}{\cos\theta} t \tag{2.30}$$

where α_c is the ratio between the column contact length and its height and is given by Eq. (2.28).

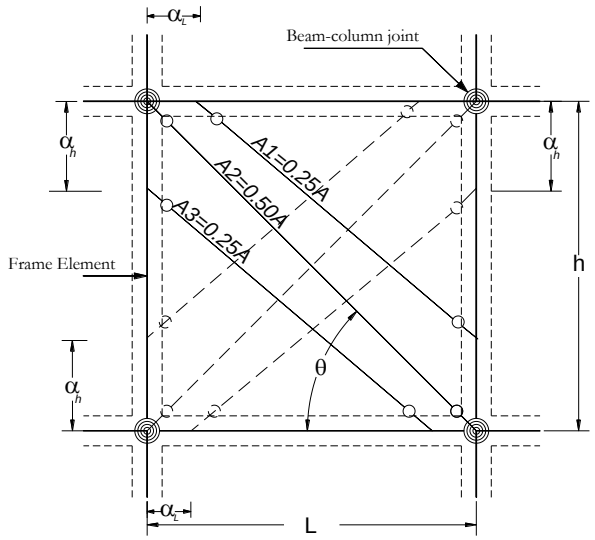

Figure 2.21. Six-strut model for masonry-infill panels in steel frame structures (El-Dakhakhni*, et al.*, 2003)

In order to represent the infill wall shear failure mechanism more adequately, Crisafulli*, et al.* (2007) suggested a different kind of multi-strut model which is implemented in a 4-node element that is connected to the frame at the beam-column joints. The offset of the struts from the diagonal, h_z, varies between $\alpha/3$ and $\alpha/2$, where α is the contact length between the panel and the frame which is given by Eq. (2.2). The model accounts for the compressive and shear behaviour of the infill panel using a nonlinear double strut and an elasto-plastic shear spring, as shown in Figure 2.22. The shear strength of the spring is evaluated based on the shear-friction mechanism that can represent the shear strength as a function of the maximum permissible shear stress, axial load, length and thickness of the infill. It is worth noting that the area of the struts in this model decreases as the axial strut displacement increases, due to the reduction of the contact length between the frame and the infill and also due to the cracking of the masonry infill. This configuration allows an adequate consideration of the lateral stiffness and of the strength of the masonry panel, particularly when shear failure along mortar joints or diagonal tensile failure is expected. Furthermore, the model is easy to apply in the analysis of large infilled frame structures. However, some aspects considered in this model require further investigation such as the reduction in the strut area (Crisafulli*, et al.*, 2007). In the same context of using multi-strut systems to model the infill, it is noted that when comparing the analytical macro model using single and double strut systems with the Pinto*, et al.* (2006) experimental results, Asteris*, et al.* (2011a) concluded that the two-strut model was able to capture the behaviour of the tested infilled frame with openings better than the single strut model.

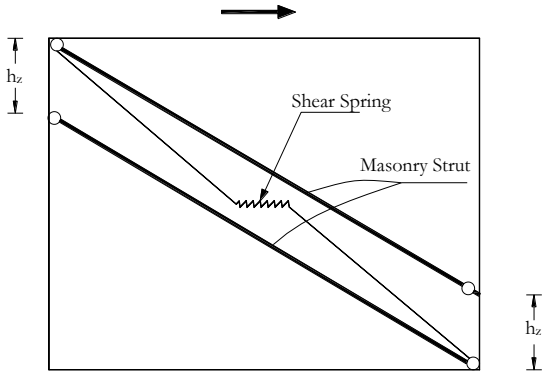

Figure 2.22. Proposed multi-strut model (Crisafulli*, et al.*, 2007) (only the struts and shear spring active in one direction are represented).

Further improving the behaviour of the equivalent diagonal strut system to represent the behaviour of infilled frame structures, Rodrigues*, et al.* (2010) proposed an equivalent bi-diagonal

compression strut model with a central strut element which is illustrated in Figure 2.23. The proposed model has been calibrated by different experimental results and Rodrigues*, et al.* (2010) concluded that their model is capable to represent the response of the structures in terms of displacement evolution, global shear-drift at each storey and cumulative dissipated energy.

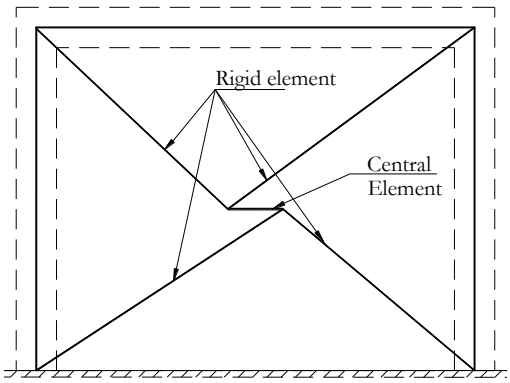

Figure 2.23 Macro- model proposed by Rodrigues*, et al.* (2010)

2.5 Final remarks

From the presented review, it can be seen that representing the structural behaviour of masonry infilled frames is complex due to the high number of parameters and phenomena involved, as well as due to the considerable uncertainty involved in many of those parameters. However, experimental tests of masonry infilled RC frames provide important results to understand and analyse the complex behaviour of these structures under seismic loading and, therefore, validate the structural parameters of the macro-models (strut models). Many experimental tests have been carried out to assess the behaviour of the infilled RC frames. These tests accounted for several structural aspects of infilled RC frames such as: material of the infills, configurations of the infill panels (i.e. with openings (window or/and door) with different sizes and locations), loading type (i.e. monotonic or cyclic loading) and status of the infilled panels (i.e. repaired or not). However, the significant variation in the material properties, the construction techniques and in the geometry, make the experimental approach unable to simulate all possibilities due to the cost of such procedures.

Numerical models introduce an alternative approach to the experimental tests in order to calibrate the structural parameters of strut models. According to the review of the studies which attempted to develop a realistic detailed numerical model representing the behaviour of RC infilled frames, it can be seen that existing numerical approaches are able to capture several aspects of the behaviour of these structures such as the maximum strength and their stiffness. In addition, numerical models can represent different failure mechanisms in the RC infilled frames such as bed joint sliding, tensile cracking and compressive crushing failure of the masonry panel, as well as the flexural failure of the concrete frame. However, most of these models were only used for monotonic loading and for small size specimens due to the high computational cost involved in this kind of modelling approach.

Macro-models can be seen to be the most practical approach to represent the behaviour of the infill panel, particularly for large structures or when multiple analyses need to be carried out. According to the review presented in this chapter, the single strut model is an efficient model to represent the structural contribution of the infill walls to the global structural behaviour due to its simplicity. This characteristic also facilitates the implementation of this model in general-purpose finite-element commercial software. However, the single strut model cannot fully capture the interaction between the bounding frame and the infill wall. On the other hand, multiple strut models can provide an acceptable representation of this interaction behaviour. However, their use in a general-purpose finite-element software is unfeasible because of the complexity involved in their implementation. Therefore, it can be concluded that the issue of modelling infill walls still needs more research.

Chapter 3.
Comparative review of procedures defining the properties of macro (single strut) models

3.1 Introduction

As referred before, the experimental observation made by Polyakov (1956) about the fact that an infill wall works as a lateral bracing for the surrounding frame was the first attempt to define an equivalent model to represent the behaviour of an infilled frame. Based on this observation, Stafford-Smith and Mainstone (Stafford-Smith, 1962, Mainstone, 1974) proposed that the compressive loading path in the masonry panel (due to horizontal loading) could be oriented mainly along its diagonal. Therefore, a way to represent the structural behaviour of the infill panel would be to replace the infill panel by an equivalent strut element. Since then, several studies were carried out to define the structural parameters of this equivalent strut. Generally, these studies can be categorized into two main groups: a) stiffness-based studies that define the geometric cross-section of the proposed strut, which is then combined with an equivalent material representing the masonry (Holmes, 1961, Mainstone, 1971, Hendry, 1990); b) strength-based studies that define a backbone curve for the force-displacement curve of the equivalent strut element (Bertoldi*, et al.*, 1993, Panagiotakos*, et al.*, 1996, Dolšek*, et al.*, 2008).

In this context, this chapter presents a comparative review of some of these empirical stiffness- and strength-based procedures and performs a detailed analysis of their reliability using experimental data available for different specimens. In addition, procedures proposed by several norms and standards are also analysed. The reliability of these procedures is analysed by comparing their strength and stiffness predictions with available experimental data. Additionally, a comparative review is also

carried out addressing the reliability of existing empirical procedures accounting for the strength reduction of the infill due to existence of openings.

3.2 Analysis of stiffness-based procedures

3.2.1 Selected procedures, experimental data and numerical modelling strategy

Stafford-Smith and Mainstone (Stafford-Smith, 1962, Mainstone, 1974) suggested the use of an equivalent diagonal strut with the same material of the masonry to account for the behaviour of the masonry infills and proposed a procedure to define the cross-section area of the strut element. Since then, several researchers have proposed alternative procedures to define the cross-section area of the diagonal strut based on experimental campaigns or numerical models.

The rationale behind stiffness-based procedures is to establish the geometrical properties of the strut element and combine them with an equivalent constitutive model representing the masonry material, as shown in Figure 3.1, to obtain an element able to simulate the structural behaviour of the infill panel. In this section, eight expressions and procedures proposed by different researchers (and reviewed in Chapter 2) were used to define the area of the strut element. The selected expressions are those found to be used more frequently due to their simplicity (Asteris*, et al.*, 2011a, Catherin*, et al.*, 2013, Buch*, et al.*, 2015). Furthermore, these expressions also cover a wide range of values of w/d (width of the strut over the length of the diagonal strut) which usually varies between 0.1 and 0.40, as reported in (Crisafulli*, et al.*, 2000, Smyrou*, et al.*, 2011). The performance of these expressions was analysed for sixteen different specimens from ten different experimental campaigns carried out on masonry infilled reinforced concrete (RC) frames. Table 3.1 specifies the notations and references for the experimental tests and specimens that were considered (for further details see Annex A). The details and auxiliary parameters needed to establish the cross-section area of the strut element according to the selected procedures are summarized in Table 3.2. The procedures provide expressions to define the strut width and the panel thickness was considered to be the effective thickness, i.e. the real thickness of the panel after subtracting the size of the perforations.

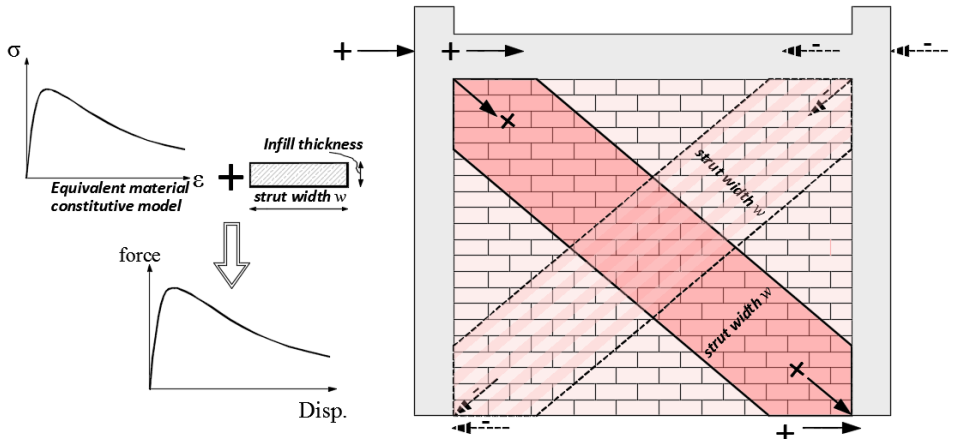

Figure 3.1 Illustration of the stiffness-based procedure

Table 3.1 Experimental tests and specimens that were considered in the comparative analysis

Specimen ID (Reference)	**Specimen ID (Reference)**
Specimen 2 (Zhai, *et al.*, 2016)	Specimen 6 (Mehrabi, *et al.*, 1996)
Specimen M2 (Pires, 1990)	Specimen 11 (Mehrabi, *et al.*, 1996)
Specimen III/2 (Sigmund, *et al.*, 2013)	Specimen 12 (Mehrabi, *et al.*, 1996)
Specimen S (Kakaletsis, 2009)	Specimen 7 (Mehrabi, *et al.*, 1996)
Specimen FT1 (Bergami, 2007, Bergami, *et al.*, 2015)	Specimen 4 (Mehrabi, *et al.*, 1996)
Specimen DFS (Basha, *et al.*, 2016)	Specimen 5 (Mehrabi, *et al.*, 1996)
Specimen F1 (Stylianidis, 2012)	Specimen IS (Kakaletsis, 2009)
Specimen SBF (Misir, 2015)	Specimen unit1 (Crisafulli, 1997)

With respect to the equivalent material constitutive model that is required, it is seen that defining such stress-strain relation is a complex task, given the heterogeneity of masonry. Most experimental campaigns do not report detailed information that can be used to establish the referred stress-strain relation. Typically, experimental campaigns only report the value of the masonry compressive strength (which is usually considered to be a characteristic value) obtained from compression tests performed on masonry samples. Therefore, the constitutive model proposed by Hendry (1990) for masonry was considered in the present analyses. For each case, the model considered the value of the masonry compressive strength obtained from the corresponding experimental data (when this information is available) and other parameters with values obtained from the literature (details are presented further ahead in this section). Furthermore, for cases where the masonry compressive strength was not available (e.g. for Specimen SBF (Misir, 2015)), the following expression proposed by Eurocode 6 (EC6) (EN6-1, 2005) was used to define the characteristic compressive strength of the masonry:

$$f_{k,m} = K f_{mo}^{\beta} f_{br}^{\alpha} \tag{3.1}$$

where f_{mo} and f_{br} are the mortar and brick compressive strength, respectively, and K, α and β are parameters defined by the national annexes of EC6. If no values are available in the annexes, EC6 refers that K ranges from 0.20 to 0.80, and that α and β can be set as 0.7 and 0.3, respectively.

Table 3.2 Summary of the expressions used in this study to define the strut width

Model	Expression	Notation and variables
Holmes (1961)	$w = \frac{1}{3} d$	d is the diagonal length of the infill panel
Mainstone (1971)	$w = 0.175 d \lambda_h^{-0.4}$	$\lambda_h = \lambda h_w$, h_w is the infill height and $\lambda = \sqrt[4]{\frac{E_I t \sin 2\theta}{4 E I h_w}}$, t is the wall thickness, E_I is the modulus of elasticity of the infill, E, modulus of elasticity of column material and I is the moment of inertia of the column
Te-Chang, *et al.* (1984)	$w = \frac{0.95 h_w \cos\theta}{\sqrt{\lambda_h}}$	θ is the diagonal strut inclination angle on the horizontal plane
Decanini, *et al.* (1987)	$w = \begin{cases} \left(\frac{0.748}{\lambda_h} + 0.085\right) d & if\ \lambda_h \le 7.85 \\ \left(\frac{0.393}{\lambda_h} + 0.130\right) d & if\ \lambda_h > 7.85 \end{cases}$	
Moghaddam, *et al.* (1988)	$w = \frac{1}{6} d$	
Hendry (1990)	$w = 0.5\sqrt{\alpha_l^2 + \alpha_h^2}$ where α_h and α_l are the horizontal and vertical contact length respectively	$\alpha_h = \frac{\pi}{2} \sqrt[4]{\frac{4(EI)_{beam} h_w}{E_I t \sin 2\theta}}$ $\alpha_l = \frac{\pi}{2} \sqrt[4]{\frac{4(EI)_{column} l_w}{E_I t \sin 2\theta}}$
Paulay, *et al.* (1992)	$w = \frac{1}{4} d$	
Durrani, *et al.* (1994)	$w = \gamma d \sin(2\theta)$ where γ is a variable	$m = 6\left(1 + \frac{6 E_b I_b h}{\pi E_c I_c L}\right)$ $\gamma = 0.32\left[\frac{h^4 E_w t_w}{m E_c I_c h_w}\right]^{-0.1} \left[\sqrt{\sin 2\theta}\right]$

In order to assess the reliability of the several stiffness-based procedures, the numerical simulation of the experimental tests corresponding to the selected sixteen specimens was performed using the software OpenSees (McKenna*, et al.*, 2000). The RC frame elements (i.e. beams and columns) were modelled using force-based elements considering fibre-sections (also known as the *Beam With*

Hinges element). The Modified Radau Hinge Integration method (Fenves*, et al.*, 2006, Scott*, et al.*, 2013) is the selected plastic hinge integration method to assign inelastic actions at the end regions of the element with a specified length. Still, additional fibre sections were also considered in the central part of the element to model its possible nonlinearity since recent modifications in this element (Scott*, et al.*, 2013) allow plasticity to be extended beyond the length of the plastic hinges. A total of six integration points are used in the element state determination (two for each hinge and two for the central part of the element). In order to establish a value for the plastic hinge length, several expressions found in the literature were examined. Typical estimates of the plastic hinge length provide values ranging from 0.45h to h (Alemdar, 2010, Zhao*, et al.*, 2011, Mortezaei*, et al.*, 2012), in which h is the depth of the element. In this study, the following expression proposed by Paulay*, et al.* (1992) was used to define the plastic hinge length l_p:

$$l_p = 0.08 l_e + 0.022 d_b f_y \tag{3.2}$$

where l_e is the element length, d_p is the diameter of the steel rebars and f_y is the steel yield stress in MPa.

As mentioned, the RC cross sections were modelled using a fibre discretization. The concrete cover was modelled using the concrete model termed Concrete01 in OpenSees representing the uniaxial concrete material with degraded linear unloading/reloading stiffness in compression and no tensile strength. Confined concrete was modelled using a confinement factor determined based on the expression proposed by Kent, *et al.* (1971) associated with the Concrete02 model. The Concrete02 concrete model is similar to the Concrete01 but considers the tensile strength of the concrete. This tensile strength was defined according to experimental data, when available, and based on the following expression (ACI 318-14, 2014) otherwise:

$$f_t = 0.623\sqrt{f_c} \tag{3.3}$$

where f_c is the compressive strength of the concrete. Steel reinforcing bars were modelled using the uniaxial Giuffre-Menegotto-Pinto model (Menegotto*, et al.*, 1973) with isotropic hardening, termed Steel02 in OpenSees, with the default parameters proposed by the software. For the beam-column joints, a rigid end-offset joint model was used (Mondal, *et al.*, 2008). The lengths of the rigid parts were considered to be half of the depth of the perpendicular element. The infills were modelled using a single compressive strut element with an area evaluated based on the previous expressions and the constitutive model for masonry was defined based on the model proposed by Hendry (1990) which

matches the shape of the Concrete01 constitutive model. The constitutive model proposed by Hendry (1990) is given by the following expression:

$$\sigma_m = f_m^{'}\left[2\frac{\varepsilon_m}{\varepsilon_{crm}} - \left(\frac{\varepsilon_m}{\varepsilon_{crm}}\right)^2\right] \tag{3.4}$$

where ε_m and σ_m are the compressive strain and the corresponding compressive stress of the masonry, respectively, $f_m^{'}$ is the maximum compressive strength of the masonry and ε_{crm} is the compressive strain at the onset of failure, which according to (Dolšek, *et al.*, 2008) ranges from 0.0015~0.002. In these analyses, the value of ε_{crm} was considered to be 0.002 in all models. Figure 3.2 shows the general description of the model implemented in OpenSees for the RC frame and the infill panel in addition to the detailed description of the RC element model. To be consistent with the experimental tests, all models were first analysed for a preliminary vertical loading and then followed by a cyclic lateral loading according to the loading protocol of each experimental campaign.

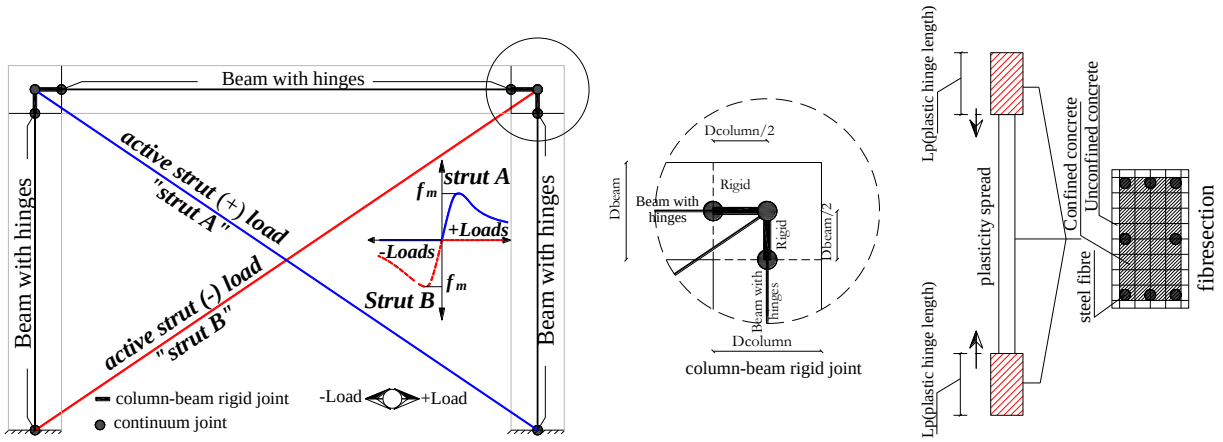

a) General description of the infilled frame model

b) Beam-column joints

c) Beam with hinges element used for the RC members

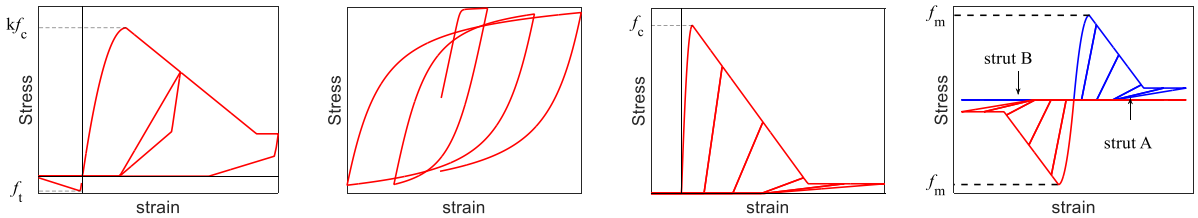

Confined concrete material (Concrete02)

Steel material (Steel02)

Unconfined concrete (Concrete01)

Strut material

d) Material models

Figure 3.2 Description of the implemented model for the infill panel using stiffness approach.

3.2.2 Preliminary results of the performance of the selected procedures

To obtain a first comparison of the differences between the selected stiffness-based procedures, Figure 3.3 shows the values of *w/d* (width of the strut over the length of the diagonal strut) that were obtained using the eight expressions of Table 3.2. The considered procedures are denoted as: (a) Holmes (1961), (b) Mainstone (1971) (c) Te-Chang, *et al.* (1984), (d) Decanini, *et al.* (1987), (e) Moghaddam, *et al.* (1988), (f) Hendry (1990), (g) Paulay, *et al.* (1992) and (h) Durrani, *et al.* (1994) in all the following figures. It is can be seen that, for most specimens, the *w/d* ratio ranges between 0.1 and 0.40. Exceptions are found for specimens S.S, S.F1, S.III/2 and S.SBF which present higher *w/d* ratios when using the expression proposed by Decanini, *et al.* (1987) which is notated as (d). As can be seen, the selected stiffness-based procedures lead to a wide range of diagonal strut width values.

Using the obtained strut widths and the infilled RC frame modelling strategy described in the previous section, the numerical cyclic responses of all the specimens were obtained. However, only the envelope curve of each analysis was considered for comparison with the corresponding experimental envelope for a clearer interpretation of the results. Figures 3.4 to 3.19 show the envelope curves of the hysteretic responses that were obtained from the referred numerical models along with the corresponding experimental envelopes. For all figures, the vertical axes represent the total shear force at the base in kN and the horizontal axes represent the lateral drift ratios in percentage.

The results show that some of the selected stiffness-based procedures are able to simulate the behaviour of part of the tested specimens with an adequate level of accuracy. However, when analysing the performance of a given expression for all the specimens, it can be seen that no expression is able to predict the behaviour of the entire set of specimens without exhibiting large errors for some of the tests. This difference in the results was somehow expected because of the wide range of materials and geometric configurations involved in the selected specimens. In this context, the differences between the experimental and numerical results obtained for specimen unit1 (Figure 3.19) should be highlighted due to their very large size, when compared to what was found for other specimens. However, no specific reasons were found to explain the large differences that were obtained and it is unclear if the fact that this specimen exhibits the highest masonry compressive strength while having the lowest lateral strength among all considered specimens plays any role in these differences.

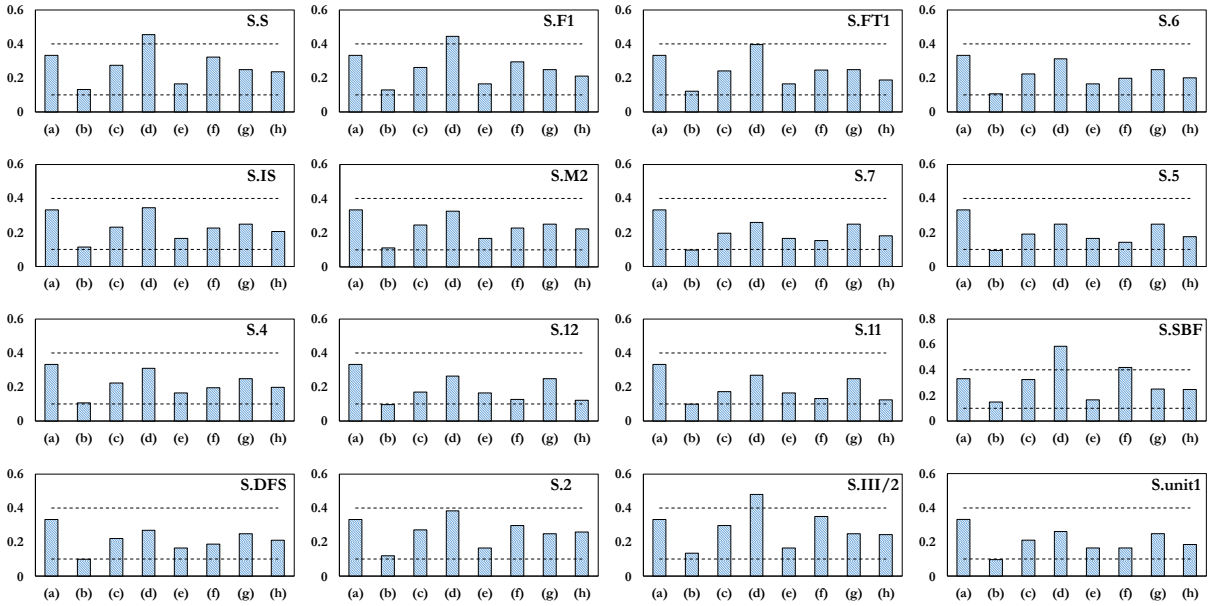

Figure 3.3 The *w/d* ratios obtained from the eight-different stiffness-based procedures for the sixteen specimens

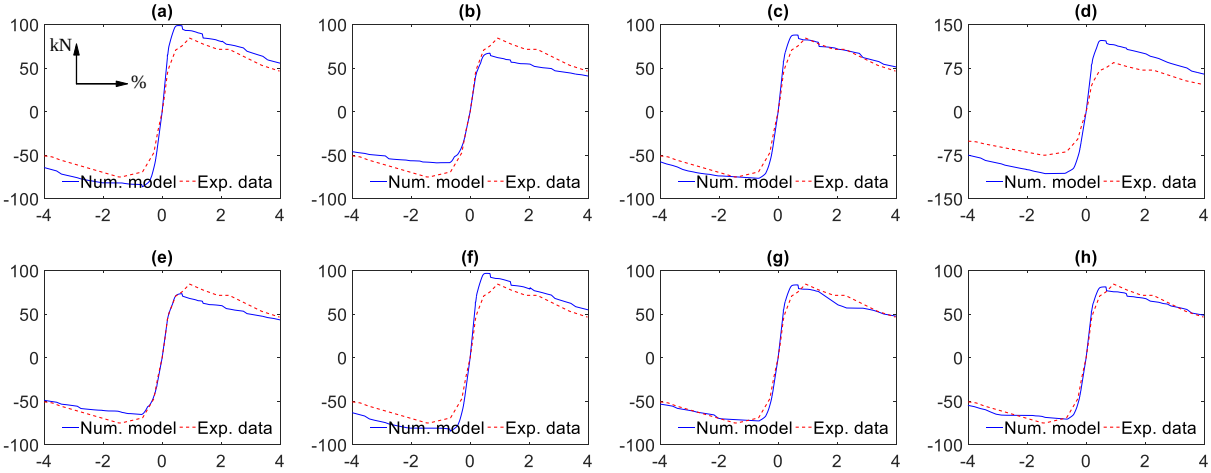

Figure 3.4 Envelope curves of the hysteretic response for Specimen S (Kakaletsis, 2009).

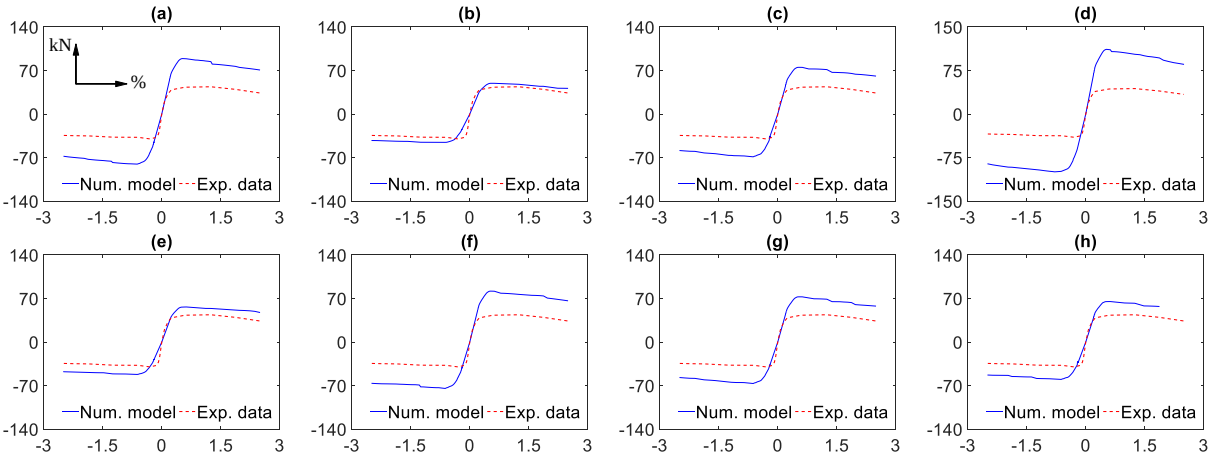

Figure 3.5 Envelope curves of the hysteretic response for specimen F1 (Stylianidis, 2012)

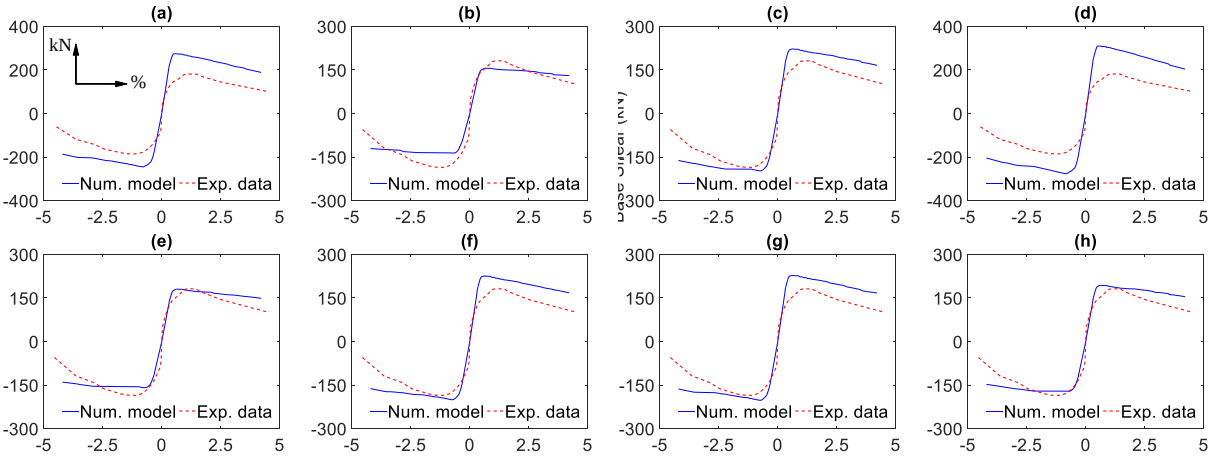

Figure 3.6 Envelope curves of the hysteretic response for Specimen FT1 (Bergami, 2007)

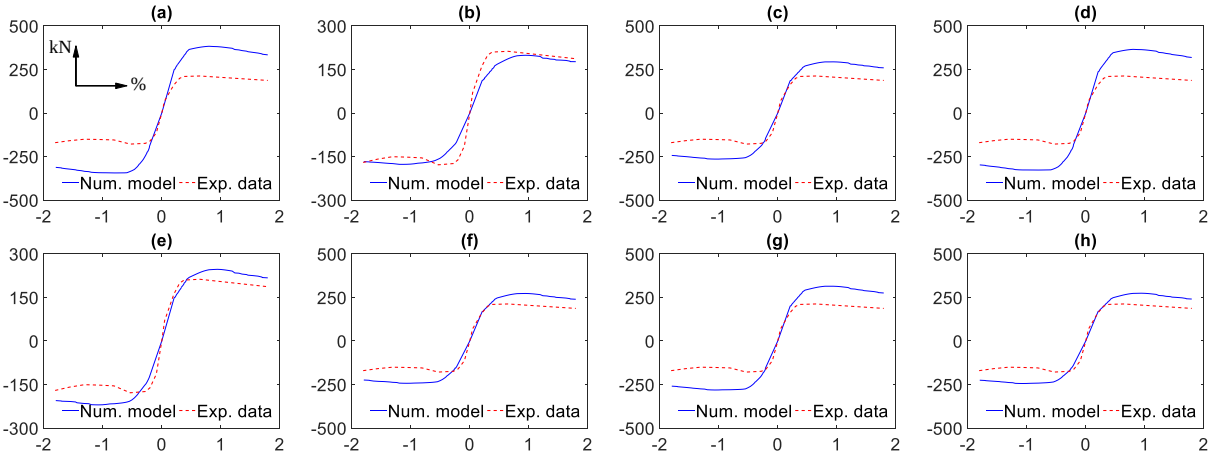

Figure 3.7 Envelope curves of the hysteretic response for Specimen 6 (Mehrabi, *et al.*, 1996).

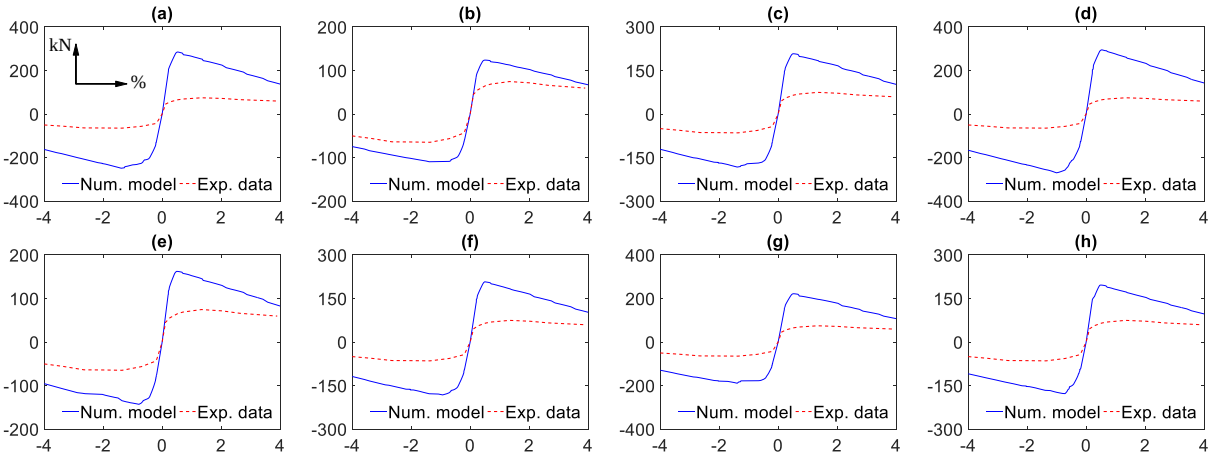

Figure 3.8 Envelope curves of the hysteretic response for Specimen IS (Kakaletsis, 2009).

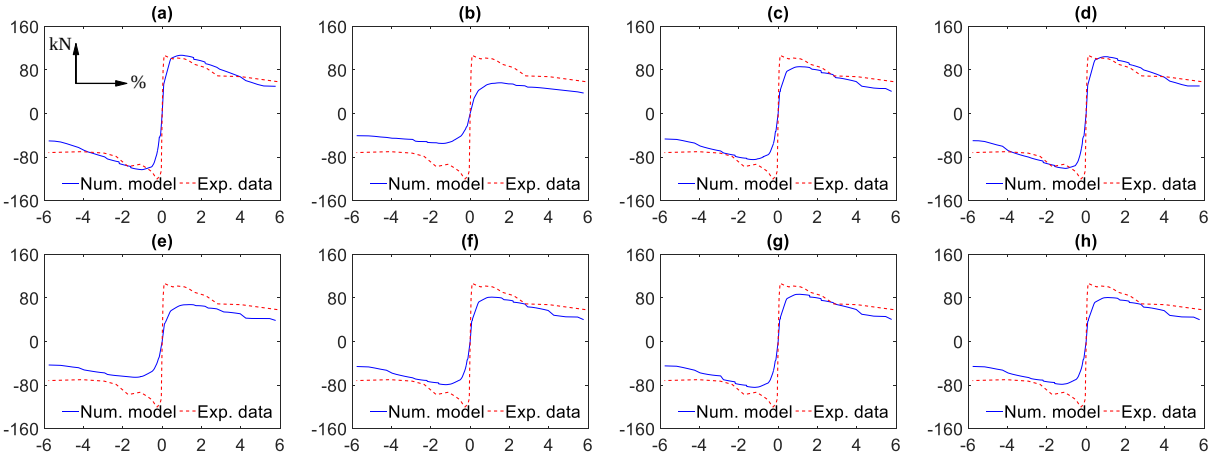

Figure 3.9 Envelope curves of the hysteretic response for Specimen M2 (Pires, 1990).

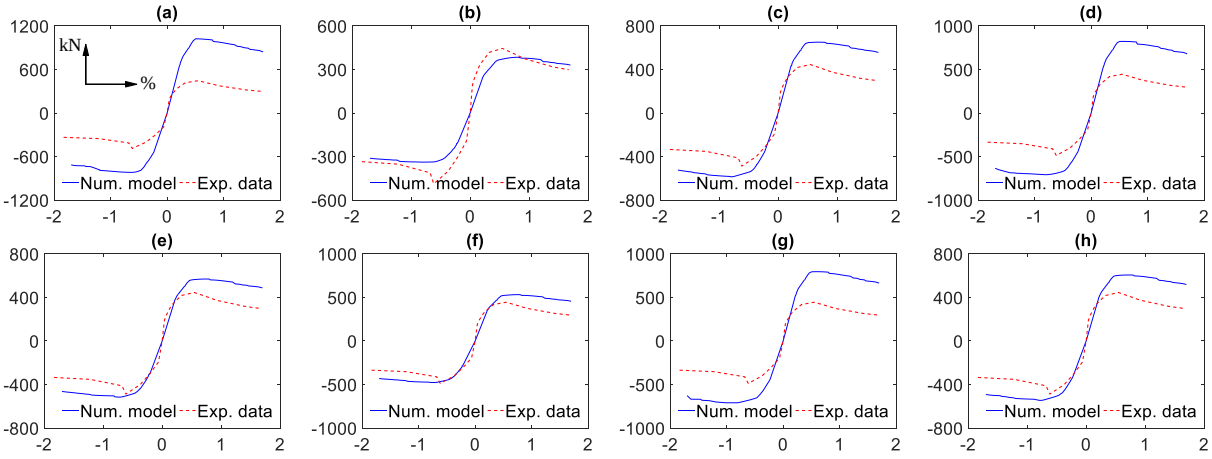

Figure 3.10 Envelope curves of the hysteretic response for Specimen 7 (Mehrabi, *et al.*, 1996).

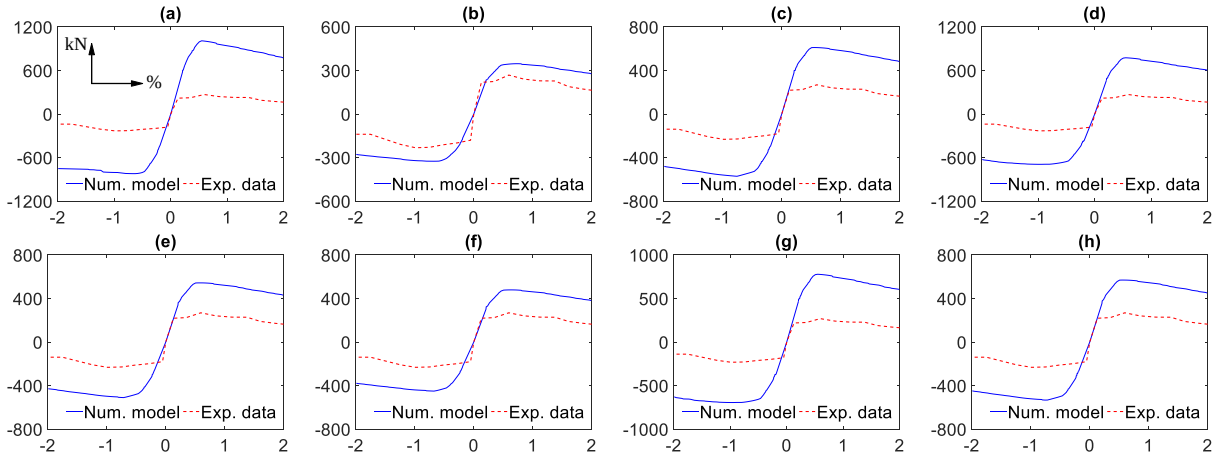

Figure 3.11 Envelope curves of the hysteretic response for Specimen 5 (Mehrabi, *et al.*, 1996).

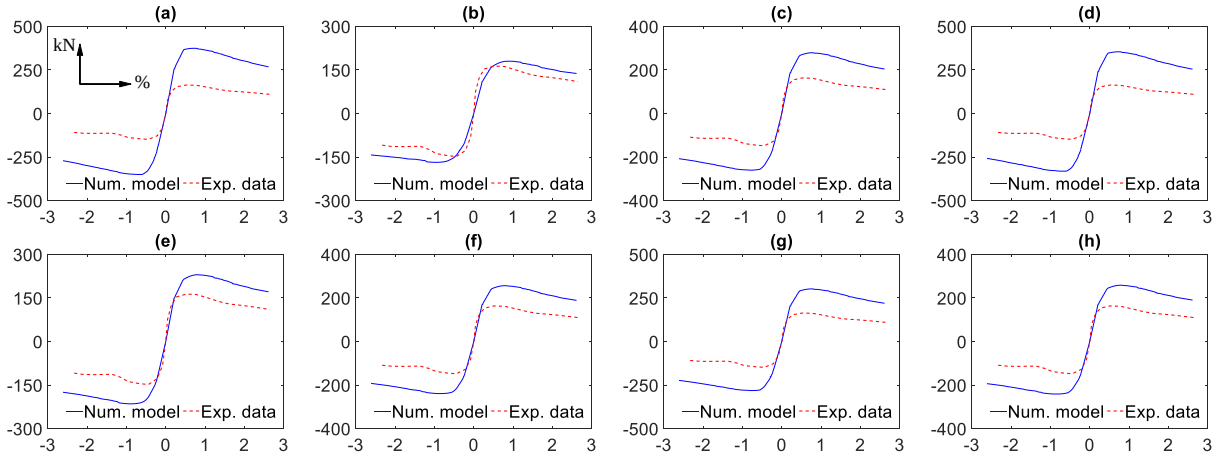

Figure 3.12 Envelope curves of the hysteretic response for Specimen 4 (Mehrabi, *et al.*, 1996).

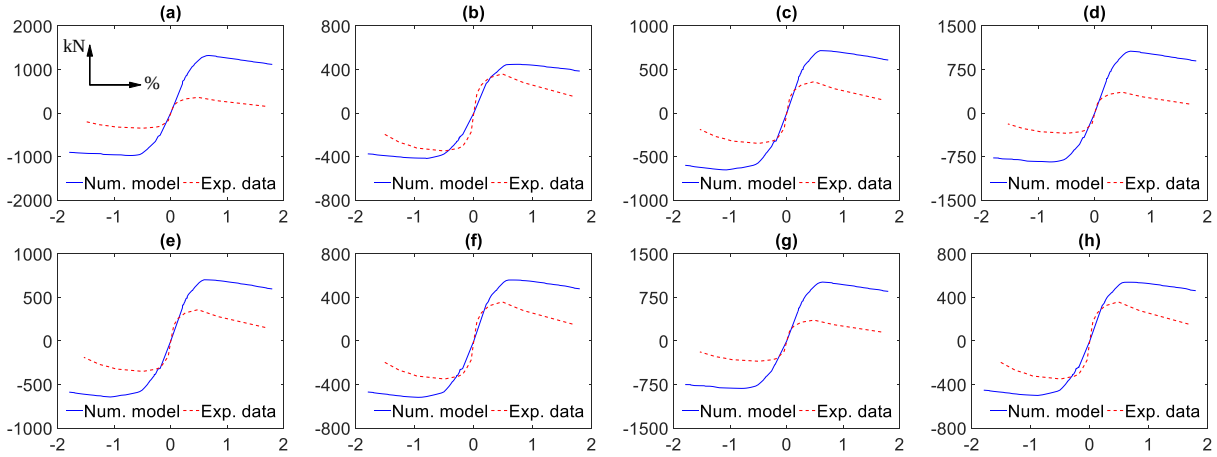

Figure 3.13 Envelope curves of the hysteretic response for Specimen 12 (Mehrabi, *et al.*, 1996).

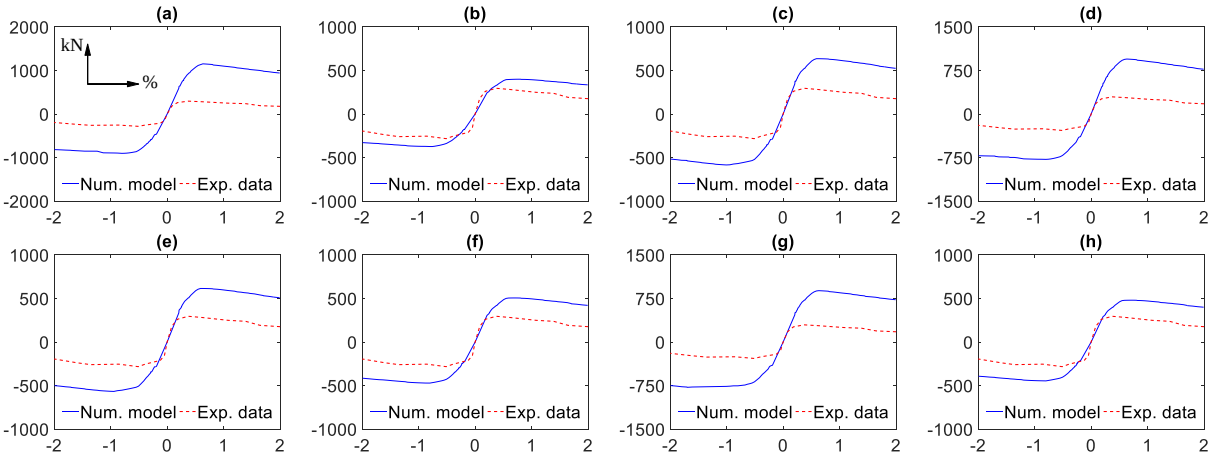

Figure 3.14 Envelope curves of the hysteretic response for Specimen 11 (Mehrabi, *et al.*, 1996).

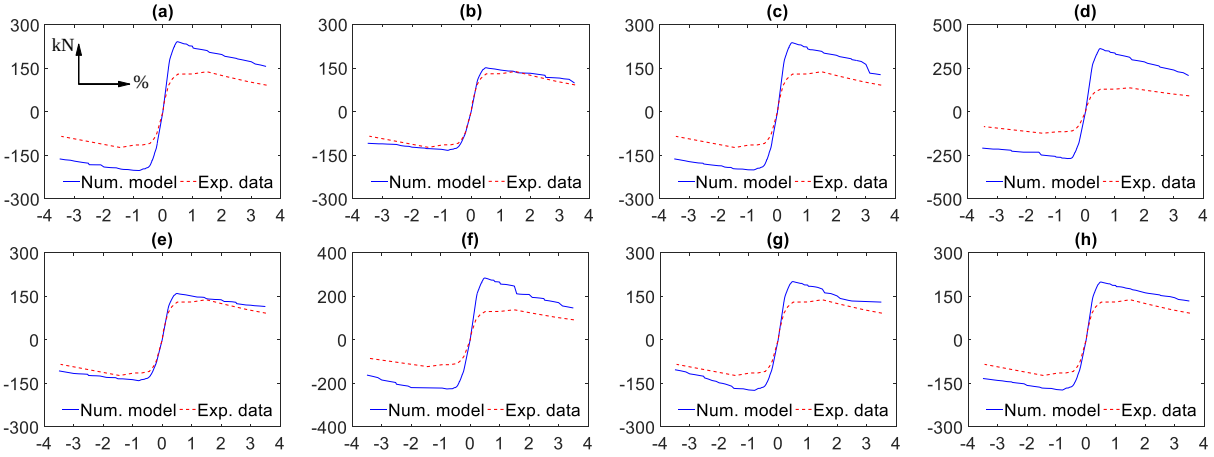

Figure 3.15 Envelope curves of the hysteretic response for Specimen SBF(Misir, 2015).

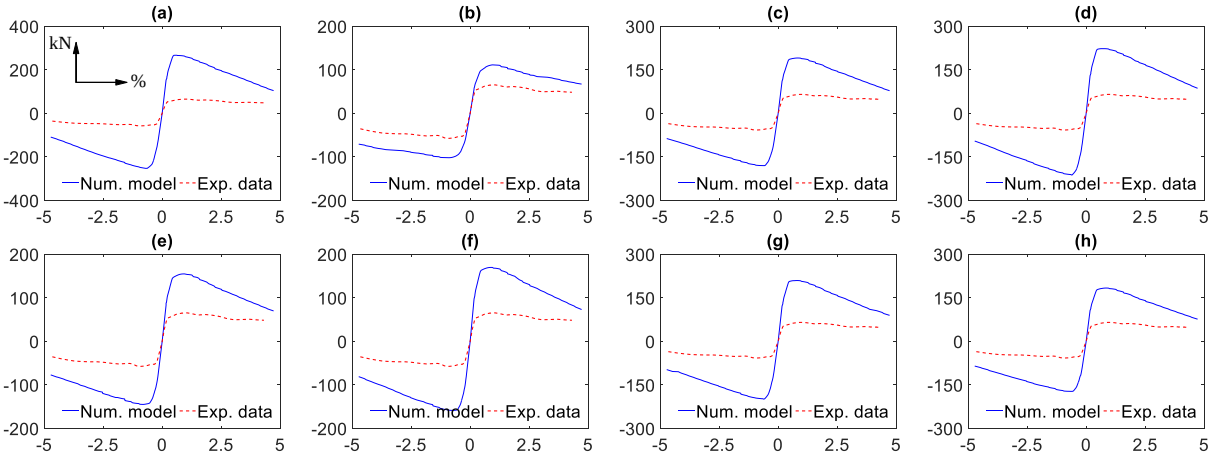

Figure 3.16 Envelope curves of the hysteretic response for Specimen DFS (Basha, *et al.*, 2016).

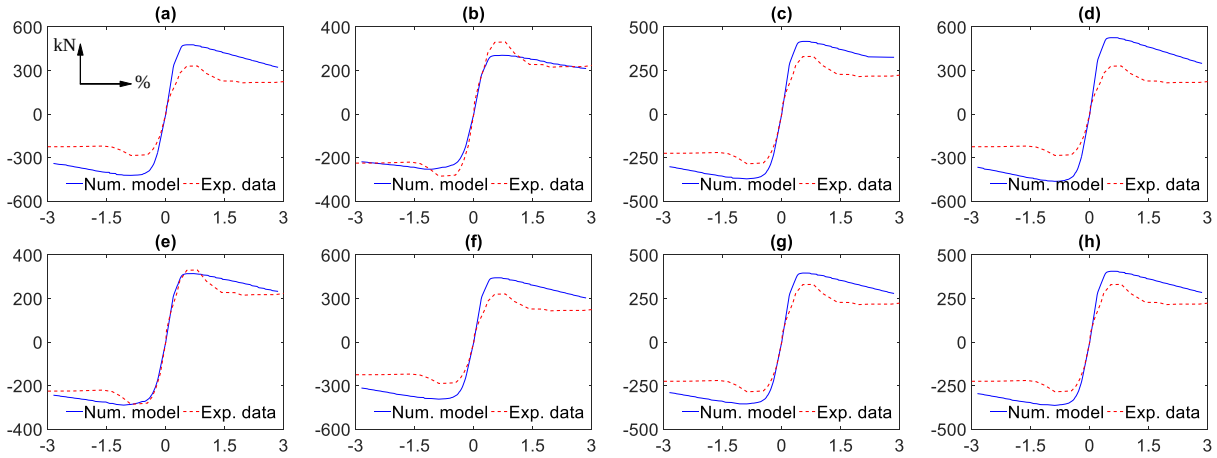

Figure 3.17 Envelope curves of the hysteretic response for Specimen 2 (Zhai, *et al.*, 2016).

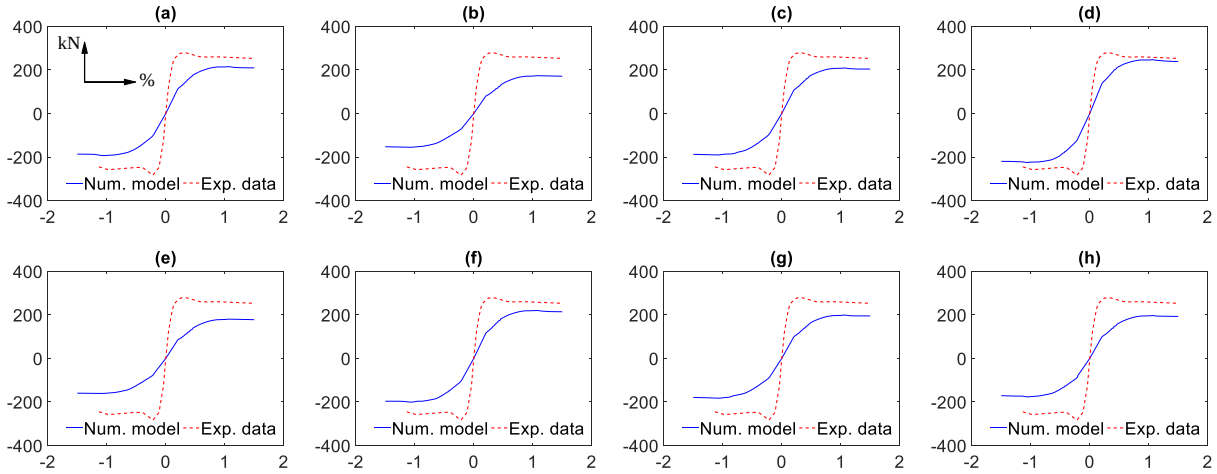

Figure 3.18 Envelope curves of the hysteretic response for Specimen III/2 (Sigmund, *et al.*, 2013).

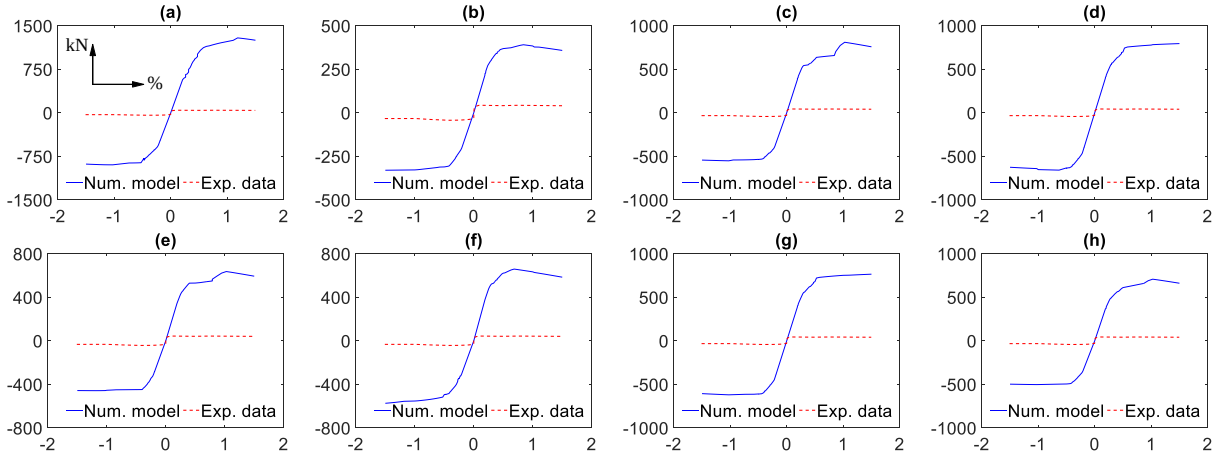

Figure 3.19 Envelope curves of the hysteretic response for Specimen unit1 (Crisafulli, 1997)

To further analyse the reasons behind the variability of the results obtained by each procedure, the experimental evolution of the strut width for increasing levels of strain in the infill panel was analysed. This analysis was carried out by extracting the contribution of the masonry infill from the global response curve. The masonry contribution is obtained by subtracting the RC frame response from the global response, considering that the global system is a parallel system made of a RC frame and a masonry infill panel (further details are provided on this subtraction process in Chapter 5). It is noted that for specimens from experimental campaigns without test results for the bare RC frame, a capacity curve of the RC frame obtained from the numerical model was considered instead to extract the experimental contribution of the masonry. For each strain level, the extracted response was then divided by the corresponding stress obtained from the considered constitutive material model to evaluate the area of the strut and, therefore, its width w (by considering that the thickness is constant).

Figure 3.20 shows the variation of the ratios w/d with the strain level of the diagonal strut for the sixteen specimens by ascending order of the corresponding masonry compressive strength. The evolutions of w/d shown in Figure 3.20 indicate that an increase in w/d is inversely proportional to an increase of the strain level (and also of the lateral displacement). These results confirm the hypothesis in (Smith*, et al.*, 1969, Crisafulli, 1997, Crisafulli*, et al.*, 2007) which refers that the area of strut decreases when the lateral displacement increases. This reduction in the area of the strut is a result of the reduction in the contact length between the panel and the frame as shown in Figure 3.21. In addition, the reduction in the area of the strut is also related to another factor. When cracking occurs in the masonry infill, the corresponding decrease in strength capacity is also due to a change in the geometry of the effective panel (i.e. the part of the panel that can be considered to be actively transferring the shear force). If the constitutive material model is unable to capture this change in the active geometry of the infill, this reduction in strength capacity implies the need to have also a reduction in the area of the strut.

From the analysis of Figure 3.20, it can also be seen that the larger contributions of the infill (captured by the higher values of w/d) occur for low strain levels, which means that the infill properties will control the initial stiffness of the structure. However, for strain levels around 0.2%~0.5%, all specimens exhibit a large decrease in the strut width that can be related to the significant loss of contact between the infill and the surrounding frame. However, Figure 3.20 shows that, for a certain range of the strain, the ratio w/d falls within the limit between 0.10 and 0.40 (defined by the two dotted lines). Therefore, some of the selected stiffness-based procedures leading to w/d values within that range are able to adequately simulate the behaviour of a particular specimen for that range of strain (i.e. the stress

level and, therefore, the force level in the strut will lead to the experimental strength value of the infill) Finally, Figure 3.20 also shows that specimens with a higher masonry compressive strength exhibit lower values of *w/d* in the constant part of the curve. This indicates the existence of a possible correlation between the evolution of the strut area and the maximum strength of the masonry. However, this correlation was not able to be evaluated due to insufficient data.

To complement this analysis, the following section presents a more focussed assessment of the variability of two important parameters needed for the simplified modelling of masonry infills: the initial stiffness and the maximum strength.

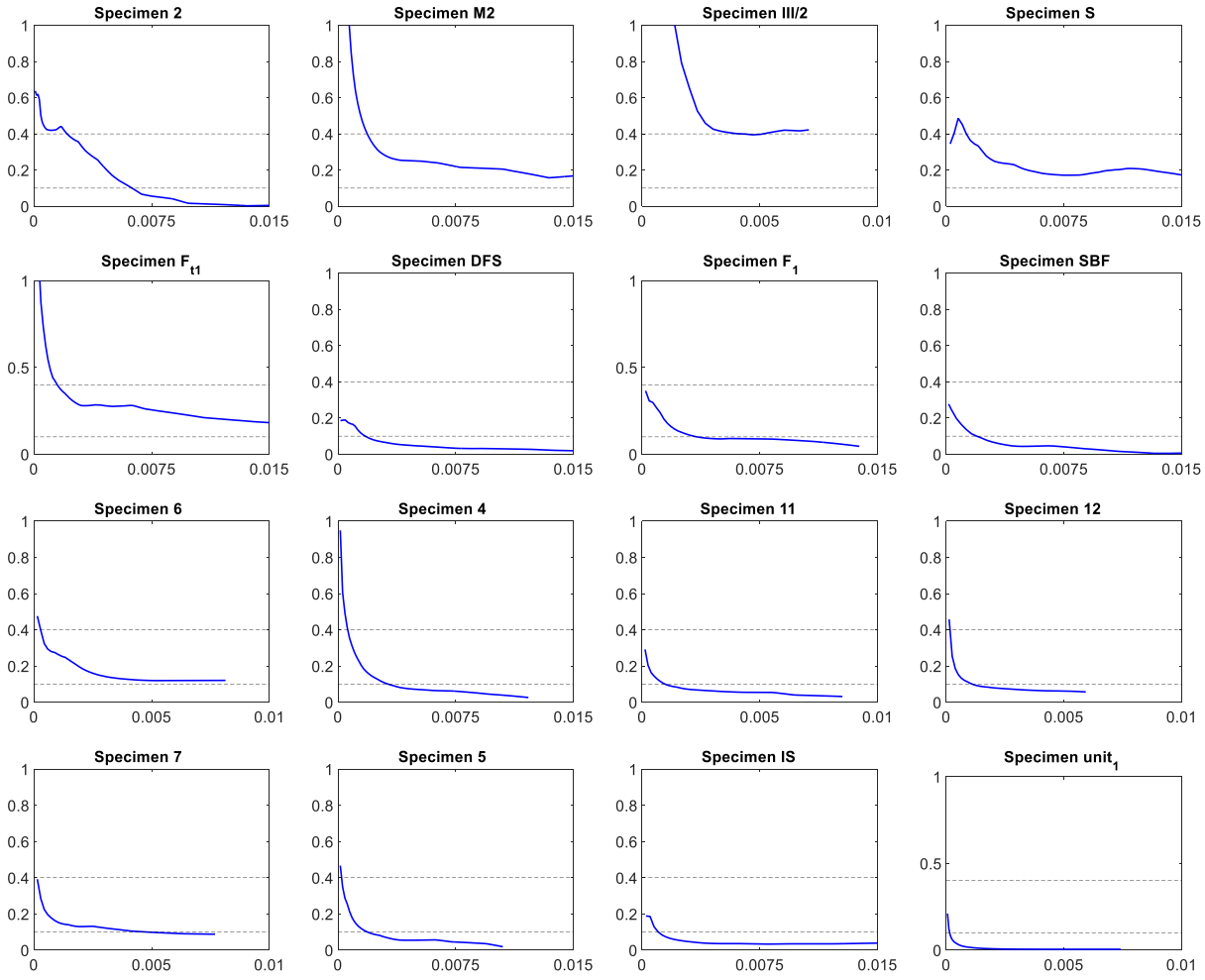

Figure 3.20 Variation of *w/d* with the strain level ε for different specimens (vertical axes are *w/d* and horizontal axes are strain *ε*)

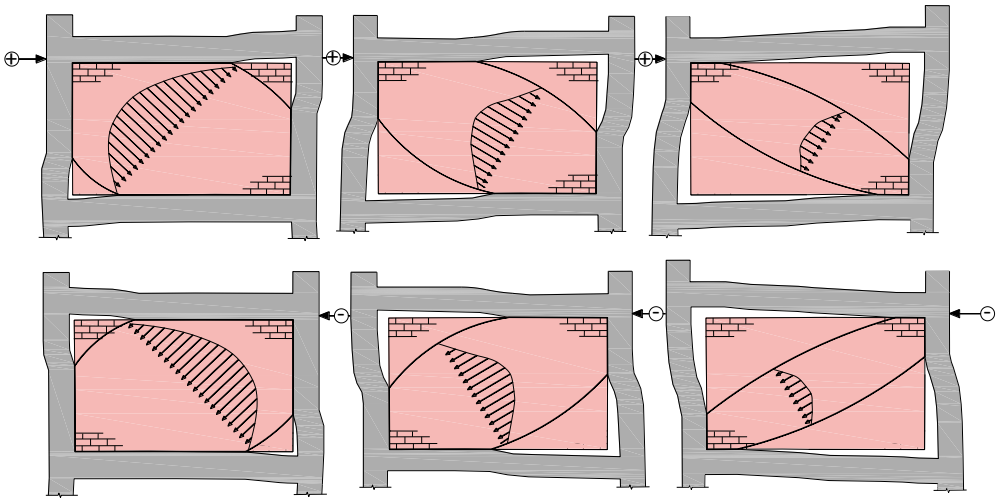

Figure 3.21 Variation of the effective loaded area of the infill panel with increasing lateral displacements.

3.2.3 Detailed results of the performance of the selected procedures: assessment of the initial stiffness and maximum strength

Although Figures 3.4 to 3.19 allow for the comparison of the global numerical and experimental responses of the sixteen specimens, thus providing an indicator about the reliability of using each stiffness-based procedure, these results involve the response of the RC frame. Therefore, part of the differences between the global experimental and numerical responses may result from differences that are solely related to the modelling of the RC frame. To remove this influence from the analysis, the performance of the selected stiffness-based procedures is analysed in this section using only the masonry component of the response, which is obtained by subtracting the RC frame response from the global response, as referred before. The analysis presented herein focusses on the differences found between the numerical and experimental data in terms of maximum strength and initial stiffness of the infill. Although the cyclic analyses resulted in response curves for the positive and negative directions, only the response of the positive direction was included in the comparisons. Strength degradation found in some cases in the negative direction due loading in the positive direction was not considered since it is expected that the stiffness-based procedures reflect undegraded conditions.

Figure 3.22 shows the force-displacement response component of the infills extracted from the experimental data of the sixteen specimens along with the best-fit trilinear curves and residual plateau that were found for each response curve. For each specimen, the maximum strength is obtained and the initial stiffness is defined from the initial segment of the trilinear fit. Numerical force-displacement

relations based on the selected stiffness-based procedures were then also extracted for the masonry infills using the same procedure and the maximum strength and initial stiffness were determined using a similar approach. It is noted that, when performing the extraction of the several infill response curves, it was found that the maximum strength of the infill does not occur for the level of lateral displacement where the RC bare frame reaches its maximum strength. Therefore, the maximum strength of the masonry infilled RC frame is not the sum of these components as referred by several authors (e.g. see (Burton*, et al.*, 2014, Decanini*, et al.*, 2014, Turgay*, et al.*, 2014)).

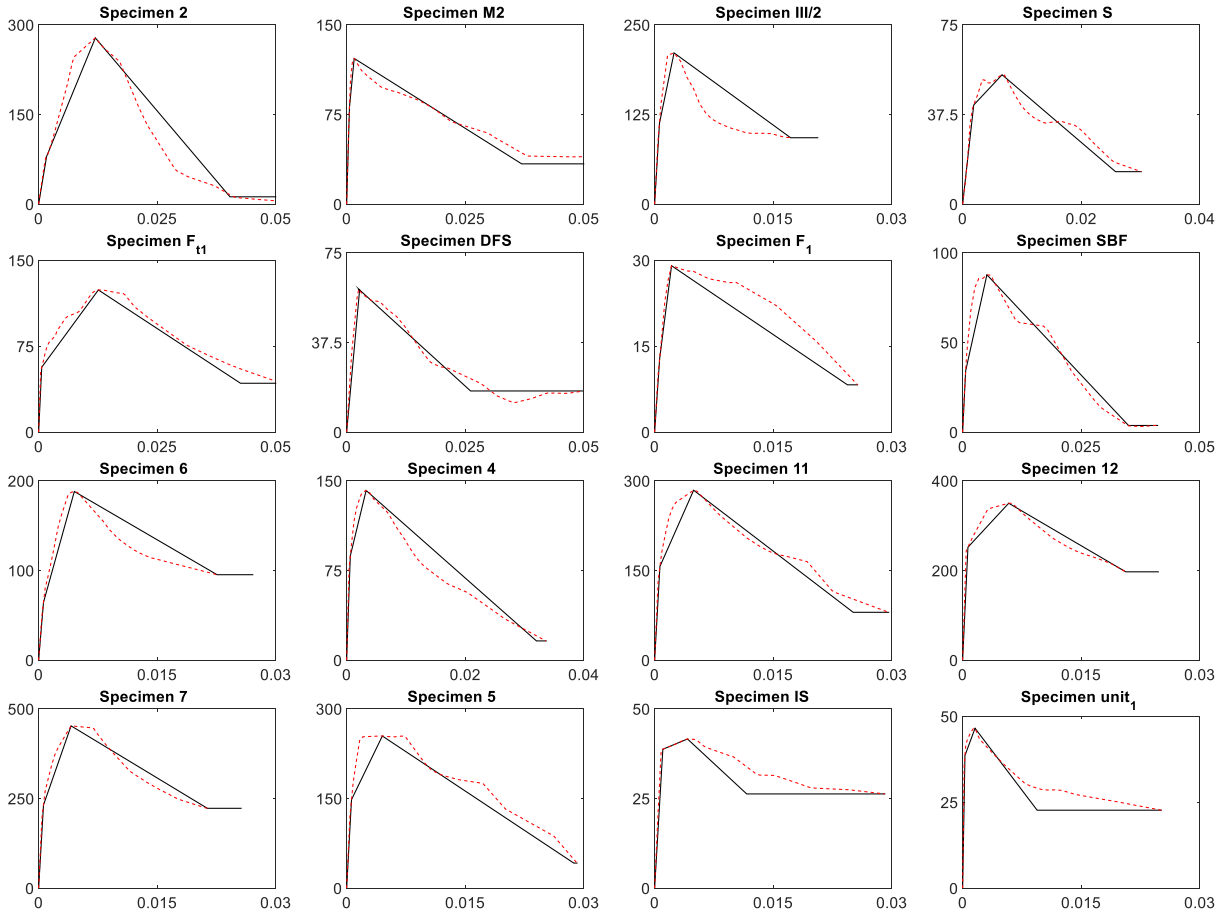

Figure 3.22 Extracted force-displacement response of the infill based on experimental data (red line) and the best-fit trilinear curves and residual plateau (continuous back line) for the sixteen specimens (vertical axes are lateral forces (kN) and horizontal axes are displacements (m)

Ratios of numerical over experimental initial stiffnesses and maximum strengths were then determined for all the specimens involving all the selected stiffness-based procedures. Table 3.3 and Table 3.4 show the ratios for the initial stiffness and maximum strength, respectively, obtained for the sixteen specimens. To facilitate the interpretation of the results shown in those tables, Figure 3.23 and

Figure 3.24 plot the ratios of Table 3.3 and Table 3.4, respectively, with a reference line corresponding to a unit value ratio. In terms of the initial stiffness, all of the selected stiffness-based procedures provide estimates of the initial stiffness that, on average, are within +/- 50% of the real value. However, when looking at the values of the coefficient of variation (CoV) obtained for each procedure, they can be seen to be very high for all the procedures (on average, the CoV is 0.88). This large variability of the ratios means that each procedure may significantly underestimate or overestimate the initial stiffness for any specimen. In terms of the maximum strength, all the selected stiffness-based procedures overestimated significantly the maximum experimental strength value. This result can be interpreted as corresponding to a significant overestimation of the strut area at the strain level leading to the maximum lateral force. From these results, it can also be seen that procedures with better performance when estimating the initial stiffness will have a worse performance when estimating the maximum strength, and vice-versa. For example, the procedure by Mainstone (1971) has the best performance when estimating maximum strength among all the procedures, but exhibits one of the worst performances when estimating initial stiffness.

Table 3.3 Comparison of the infill initial stiffness obtained from different stiffness-based procedures with those obtained from experimental tests

	Ratios of the initial stiffness							
Specimen ID	Holmes (1961)	Mainstone (1971)	Te-Chang, *et al.* (1984)	Decanini, *et al.* (1987)	Moghaddam, *et al.* (1988)	Hendry (1990)	Paulay, *et al.* (1992)	Durrani, *et al.* (1994)
S.2 (Zhai, *et al.*, 2016)	1.20	0.45	1.02	1.47	0.60	1.03	0.90	0.92
S. M2 (Pires, 1990)	0.24	0.08	0.17	0.22	0.12	0.12	0.18	0.15
S.III/2 (Sigmund, *et al.*, 2013)	0.15	0.06	0.14	0.22	0.08	0.13	0.12	0.10
S. S (Kakaletsis, 2009)	1.67	0.65	1.36	2.25	0.83	1.41	1.25	1.13
S. FT1 (Bergami, 2007)	0.45	0.17	0.34	0.58	0.22	0.31	0.34	0.25
S. DFS (Basha, *et al.*, 2016)	4.83	1.45	3.21	3.91	2.42	2.79	3.62	3.07
S.F1 (Stylianidis, 2012)	1.55	0.59	1.19	1.98	0.77	1.15	1.16	0.94
S.SBF(Misir, 2015)	2.41	0.86	1.72	2.59	1.21	1.46	1.81	1.32
S. 6 (Mehrabi, *et al.*, 1996)	0.90	0.30	0.61	0.83	0.45	0.43	0.67	0.50
S. 11(Mehrabi, *et al.*, 1996)	0.69	0.23	0.47	0.64	0.35	0.33	0.52	0.39
S.12(Mehrabi, *et al.*, 1996)	1.13	0.34	0.59	0.91	0.57	0.45	0.85	0.43
S. 7(Mehrabi, *et al.*, 1996)	0.82	0.24	0.42	0.64	0.41	0.32	0.61	0.30
S. 4 (Mehrabi, *et al.*, 1996)	0.81	0.24	0.48	0.63	0.40	0.37	0.60	0.45
S. 5 (Mehrabi, *et al.*, 1996)	1.29	0.37	0.74	0.96	0.64	0.56	0.97	0.69
S. IS (Kakaletsis, 2009)	4.40	1.52	2.98	4.43	2.20	2.69	3.30	2.61
S. unit1 (Crisafulli, 1997)	3.32	0.87	1.61	1.85	1.66	0.95	2.49	1.64
Mean	***1.62***	***0.53***	***1.06***	***1.51***	***0.81***	***0.91***	***1.21***	***0.93***
Coefficient of Variation	***0.88***	***0.85***	***0.87***	***0.84***	***0.88***	***0.92***	***0.88***	***0.93***

Table 3.4 Comparison of the infill maximum strength obtained from different stiffness-based procedures with those obtained from experimental tests

	Ratios of the maximum lateral strength							
Specimen ID	Holmes (1961)	Mainstone (1971)	Te-Chang, *et al.* (1984)	Decanini, *et al.* (1987)	Moghaddam, *et al.* (1988)	Hendry (1990)	Paulay, *et al.* (1992)	Durrani, *et al.* (1994)
S.2 (Zhai, *et al.*, 2016)	1.15	0.43	0.97	1.40	0.58	0.99	0.86	0.89
S. M2 (Pires, 1990)	1.00	0.34	0.72	0.95	0.50	0.51	0.75	0.62
S.III/2 (Sigmund, *et al.*, 2013)	0.44	0.17	0.39	0.63	0.22	0.35	0.33	0.29
S. S (Kakaletsis, 2009)	1.48	0.57	1.21	1.99	0.74	1.25	1.11	1.00
S. FT1 (Bergami, 2007)	1.20	0.46	0.91	1.55	0.60	0.83	0.90	0.67
S. DFS (Basha, *et al.*, 2016)	5.42	1.62	3.59	4.38	2.71	3.12	4.06	3.44
S.F1 (Stylianidis, 2012)	6.06	2.30	4.65	7.77	3.03	4.51	4.55	3.68
S.SBF(Misir, 2015)	5.15	1.83	3.69	5.54	2.58	3.11	3.86	2.81
S. 6 (Mehrabi, *et al.*, 1996)	1.84	0.62	1.25	1.72	0.92	0.89	1.38	1.04
S. 11(Mehrabi, *et al.*, 1996)	2.56	0.86	1.73	2.37	1.28	1.23	1.92	1.43
S.12(Mehrabi, *et al.*, 1996)	4.30	1.29	2.23	3.47	2.15	1.71	3.23	1.62
S. 7(Mehrabi, *et al.*, 1996)	4.06	1.20	2.07	3.20	2.03	1.57	3.04	1.51
S. 4 (Mehrabi, *et al.*, 1996)	2.48	0.73	1.47	1.92	1.24	1.15	1.86	1.37
S. 5 (Mehrabi, *et al.*, 1996)	4.50	1.28	2.59	3.34	2.25	1.95	3.37	2.42
S. IS (Kakaletsis, 2009)	8.53	2.95	5.77	8.59	4.27	5.21	6.40	5.06
S. unit1 (Crisafulli, 1997)	42.25	11.14	20.45	23.63	21.13	12.16	31.69	20.93
Mean	***5.78***	***1.74***	***3.36***	***4.53***	***2.89***	***2.53***	***4.33***	***3.05***
Coefficient of Variation	***1.73***	***1.51***	***1.43***	***1.24***	***1.73***	***1.16***	***1.73***	***1.62***

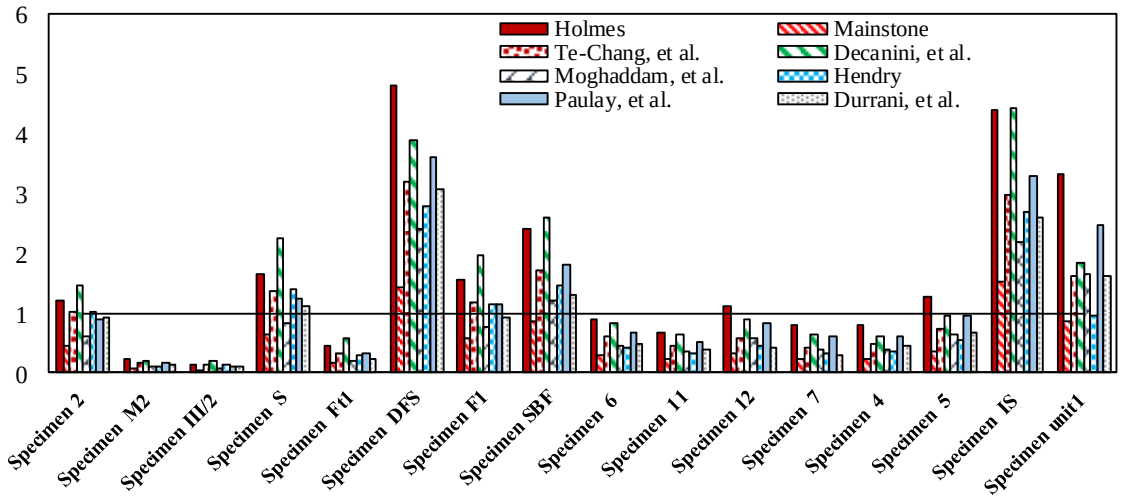

Figure 3.23 Ratios between the numerical initial stiffness and the initial stiffness obtained from the experimental data for sixteen specimens

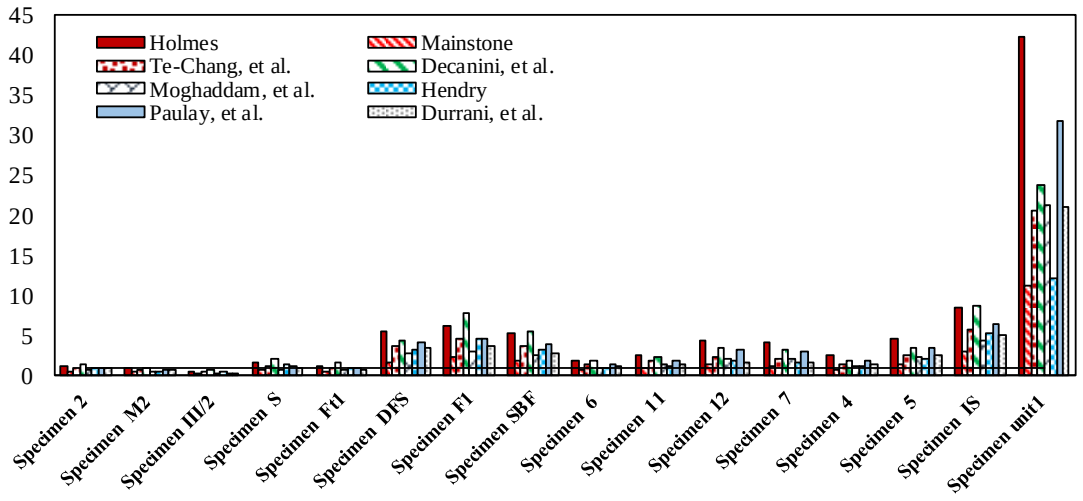

Figure 3.24 Ratios between the numerical maximum strength and the maximum strength obtained from the experimental data for sixteen specimens

Based on the results that were obtained from the performance analysis of the selected stiffness-based procedures, it can be seen that none of the procedures is able to globally represent the behaviour of the infills. In particular, all the procedures provide initial stiffness estimates that may significantly underestimate or overestimate the real initial stiffness while providing, in most cases, maximum strength estimates that significantly overestimate the real maximum strength. The fact that these procedures are unable to account for the reduction in the effective strut area as the lateral displacement increases was also seen to be an important factor in their lack of accuracy. In addition, these procedures also assume that the infill panel does not exhibit any failure mechanism other than crushing by excessive compression (e.g. such as shear failure in the mortar joints or diagonal tensile failure).

3.3 Analysis of strength-based procedures

Strength-based procedures are alternative methods that define a behaviour model for an infill wall. These procedures directly establish a force-displacement relation that represents the behaviour of the infill under lateral loading. As carried out for the stiffness-based procedures, the performance of several methods is analysed herein, including both empirical and standard-based approaches.

3.3.1 Selected empirical procedures

To define the force-displacement relation defining the behaviour of the strut element involves determining the evolution of forces transferred through the infill panel based on the (expected) governing failure mechanism. In this section, the three different procedures shown in Figure 3.25 were considered to define the force-displacement relation of the strut element. These procedures are those proposed by a) Dolšek*, et al.* (2008), b) Panagiotakos*, et al.* (1994) and c) Bertoldi*, et al.* (1993). These models were selected among the several proposals found in the literature to define the force-displacement relation (e.g. see section 2.4.4.2). In particular, these models were selected because they provide a complete description of the force-displacement relations using explicit expressions, a fact that led several researchers to use these models (e.g. see (Sattar*, et al.*, 2010, Celarec*, et al.*, 2012, Ricci*, et al.*, 2013, Furtado*, et al.*, 2016, Ricci*, et al.*, 2016) among others).

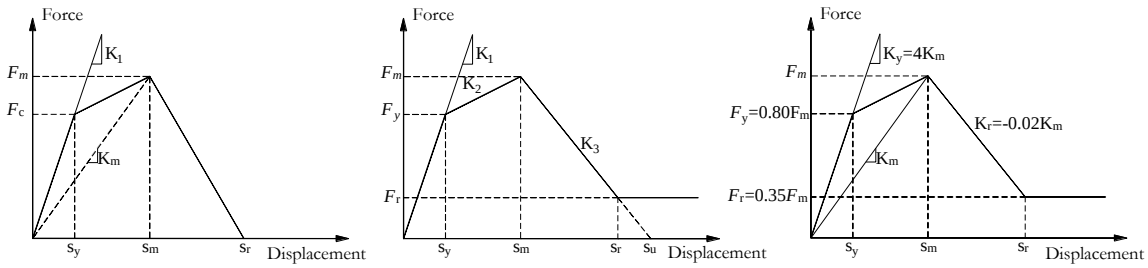

a) b) c)

Figure 3.25 Force-displacement trilinear curve for the strut element according to three proposals: a) Dolšek*, et al.* (2008), b) Panagiotakos*, et al.* (1994) and c) Bertoldi*, et al.* (1993)

To represent the forces that are transferred through the infill wall, Dolšek*, et al.* (2008) adopted the trilinear force-displacement relation shown Figure 3.25 a). The complete definition of the proposed relation uses Eqs. (3.5) and (3.6) reported in (Calvi*, et al.*, 1996, Žarnić*, et al.*, 1997) to define the maximum force (F_m) and the initial stiffness (K_1), respectively, where f_{tp} is the tensile strength of the panel evaluated by a diagonal compression test and G_w is the tangential elastic modulus of the masonry infill. If experimental data about the values of f_{tp} and G_w is unavailable, Eq. (3.7) (Crisafulli, 1997) and Eq. (3.8) (ACI, 2011), respectively, have been used to evaluated these parameters. To completely define the force-displacement relation, Dolšek*, et al.* (2008) assume that the ratio between the cracking force and the maximum force is 0.6, the drift s_m/L_D corresponding to the maximum force is 0.2% (L_D is the diagonal length of the infill panel), the residual force F_r is zero and the corresponding residual drift

s_r/L_D is 1%. It is also noted that Eq. (3.5) implies that the maximum force transferred through the infill is governed by a shear-based behaviour and will lead to a shear failure mechanism.

$$F_m = 0.818 \frac{L_w t_w f_{tp}}{C_I}\left(1+\sqrt{C_I^2+1}\right) \text{ where } C_I = 1.925\frac{L_w}{h_w} \tag{3.5}$$

$$K_1 = \frac{G_w L_w t_w}{h_w} \tag{3.6}$$

$$f_{tp} = 0.17 \sim 0.38\sqrt{f_m^{'}} \text{ where } f_m^{'} \text{ is the masonry compressive strength in MPa} \tag{3.7}$$

$$G_w = 0.40 E_m \tag{3.8}$$

The trilinear relation proposed by Panagiotakos*, et al.* (1994) to model the behaviour of the strut model is based on data from experimental cyclic tests on scaled frames with brick infill panels. The proposed force-displacement relation is shown in Figure 3.25 b) where the initial stiffness of the infill panel K_1 is also defined according to Eq. (3.6). The yield lateral force is defined according to Eq. (3.9) and the stiffness of the second branch K_2 is defined according to Eq. (3.10), where d is the diagonal length of the infill and b_w is the width of the strut. According to (Uva*, et al.*, 2012), the expression proposed by (Klingner*, et al.*, 1978), Eq. (3.11), was adopted to define b_w, F_m is assumed to be 1.3 F_y, the softening stiffness branch K_3 can be assumed to be around -0.005~-0.1 K_1 and F_r is assumed to range between 0~0.10 F_m.

$$F_y = f_{tp} t_w L_w \tag{3.9}$$

$$K_2 = \frac{E_m b_w t_w}{d} \tag{3.10}$$

$$b_w = 0.175 d\, \lambda_h^{-0.40} \tag{3.11}$$

The trilinear relation proposed by Bertoldi*, et al.* (1993), shown in Figure 3.25 c), is based on the seismic behaviour analysis of ten frames with two equal spans and different numbers of storeys ranging from (2~24). The initial stiffness (K_1) of this model is set as $4K_m$, where K_m is defined according to Eq. (3.12) in which θ is the angle of the strut element with respect to the horizontal plane. Evaluating the maximum lateral force F_m, according to this model involves computing the minimum force resulting from the following four possible collapse modes of the panel: crushing stress at the centre of the panel (σ_{centre}); crushing stress of the panel corner (σ_{corner}); sliding stress at the horizontal mortar joints ($\sigma_{silding}$)

and diagonal tensile stress ($\sigma_{diagonal}$). After defining the four failure stresses, the critical diagonal force is then obtained by Eq. (3.13), where b_w is the strut width evaluated according to (Uva*, et al.*, 2012) with the expression proposed by (Klingner*, et al.*, 1978). As reported in (Uva*, et al.*, 2012), the yield force (F_y) is defined as 0.8 F_m and the residual force F_r as 0.35 F_m.

$$K_m = \frac{E_m b_w t_w}{d} \cos^2 \theta \tag{3.12}$$

$$F_m = \min(\sigma_{centrer}, \sigma_{corner}, \sigma_{sliding}, \sigma_{diagonal}) t_w b_w \tag{3.13}$$

In order to compare the performance of these models against experimental data without involving the contribution of the RC bare frame, the trilinear responses of the idealized backbone curves are plotted in Figure 3.26 with the corresponding masonry components of the experimental data from the sixteen specimens previously obtained (see Figure 3.22). The results presented in Figure 3.26 show that, for some specimens, the selected empirical models provide a response close to the experimental one. However, for other specimens, there is a large difference between the predicted response and the real one. In order to assess the differences resulting from the use of the referred empirical models, ratios between the predicted initial stiffness and the experimental one, and between the predicted maximum lateral force and the experimental one are shown in Table 3.5. Moreover, to facilitate the interpretation of the results, the initial stiffness and maximum strength ratios presented in Table 3.5 are plotted in Figure 3.27 and Figure 3.28, respectively.

Generally, when compared to each other, the three empirical models are in close agreement in terms of their predictions for the initial stiffness and maximum infill strength. In terms of the initial stiffness, the three models overestimate the initial stiffness for most specimens. On the other hand, the selected models are better at predicting maximum strength of the infill panel and present adequate values for several specimens. The overestimation of the initial stiffness of the infill panel by the selected models maybe due to the use of the gross thickness of the infill instead of the effective one (i.e. the thickness of the panel after subtracting the size of the perforations). Therefore, the initial stiffness for all specimens was re-evaluated based on the effective thickness of the infill wall that was determined for each specimen based on the procedure defined by (CCMPA, 2009). The new ratios between the predicted initial stiffness and the experimental one are shown in Table 3.6 and plotted in Figure 3.29. As can be seen, using the effective wall thickness improved the performance of the empirical models

in predicting the initial stiffness. Nonetheless, the results still show a large overprediction of the initial stiffness.

Based on the presented results, strength-based procedures provide alternative approaches to establish the parameters of the strut model and simulate the behaviour of the infill with a performance that is generally better than that of the stiffness-based procedures previously analysed. However, strength-based procedures also establish the infill strength based on an (assumed) governing behaviour mechanism. Even though a large part of the global behaviour of the infill may be governed by one behaviour mechanism, infill panels experience several behaviour mechanisms that are globally interconnected and responsible for transferring forces in different ways. Therefore, assuming that only one mechanism controls the behaviour of the infill panel inevitably leads to differences between the numerical prediction and the real behaviour of the infill.

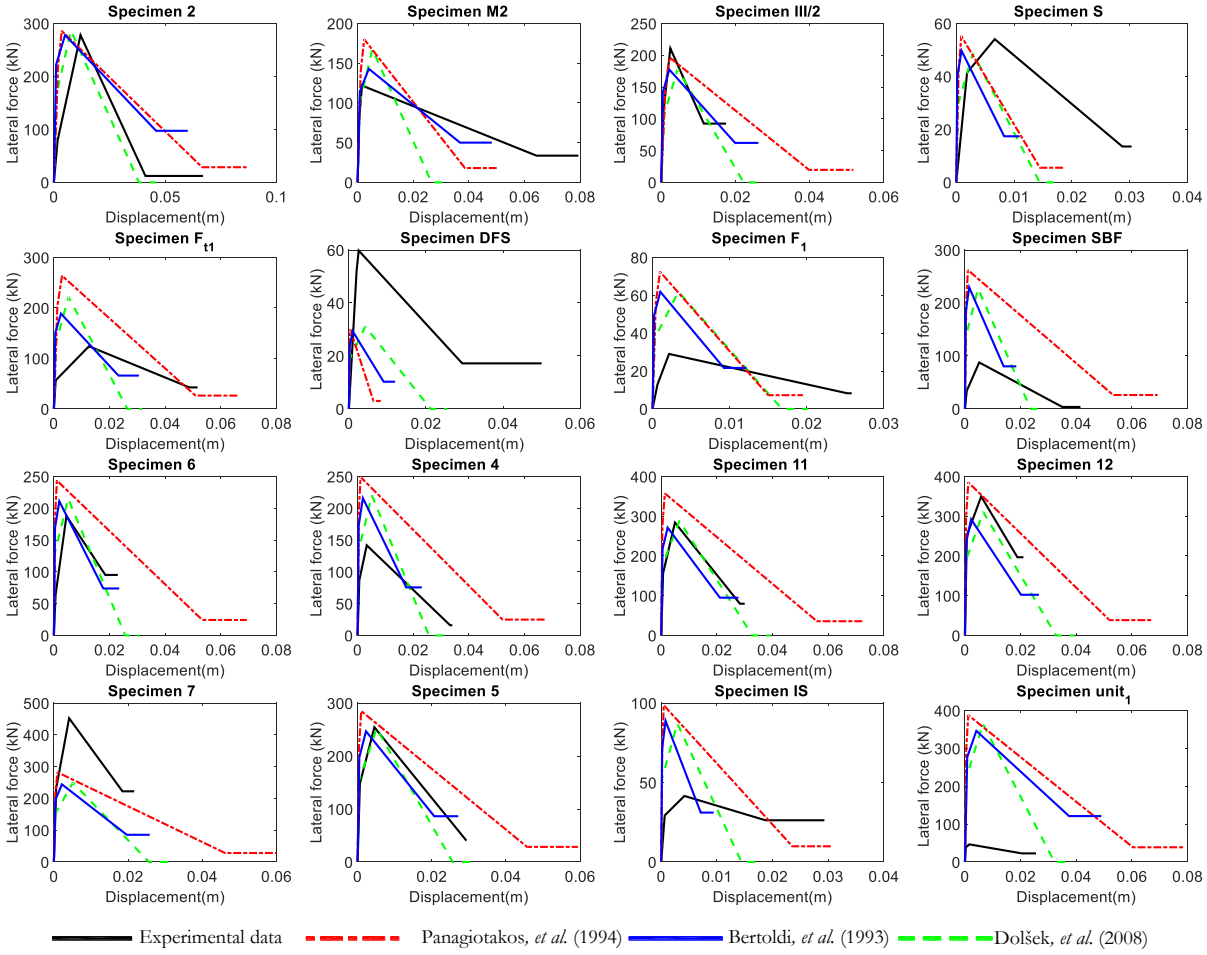

Figure 3.26 Trilinear curves obtained from three different strength-based procedures along with the idealized curves obtained from experimental data

Table 3.5 Comparison of the infill maximum strength and initial stiffness obtained from three different strength-based procedures with those obtained from experimental tests

Specimen ID	Ratios of the maximum lateral strength			Ratios of the initial stiffness		
	Dolšek, *et al.* (2008)	Panagiotakos, *et al.* (1994)	Bertoldi, *et al.* (1993)	Dolšek, *et al.* (2008)	Panagiotakos, *et al.* (1994)	Bertoldi, *et al.* (1993)
S.2 (Zhai, *et al.*, 2016)	1.03	1.03	1.00	2.46	2.46	4.67
S. M2 (Pires, 1990)	1.38	1.48	1.17	0.94	0.94	1.04
S.III/2 (Sigmund, *et al.*, 2013)	0.85	0.93	0.84	0.73	0.73	1.77
S. S (Kakaletsis, 2009)	0.90	1.02	0.92	4.72	4.72	9.89
S. FT1 (Bergami, 2007)	1.79	2.13	1.52	1.90	1.90	3.41
S. DFS (Basha, *et al.*, 2016)	0.52	0.50	0.49	5.91	5.91	5.45
S.F1 (Stylianidis, 2012)	3.80	4.45	3.80	5.16	5.16	9.46
S.SBF(Misir, 2015)	2.59	2.99	2.62	8.48	8.48	11.30
S. 6 (Mehrabi, *et al.*, 1996)	1.15	1.30	1.12	4.02	4.02	4.15
S. 11(Mehrabi, *et al.*, 1996)	1.55	1.76	1.52	3.11	3.11	3.19
S.12(Mehrabi, *et al.*, 1996)	1.02	1.26	0.96	2.81	2.81	2.02
S. 7(Mehrabi, *et al.*, 1996)	0.89	1.10	0.84	2.03	2.03	1.42
S. 4 (Mehrabi, *et al.*, 1996)	0.55	0.62	0.54	1.49	1.49	1.21
S. 5 (Mehrabi, *et al.*, 1996)	0.99	1.12	0.97	2.39	2.39	1.82
S. IS (Kakaletsis, 2009)	2.10	2.37	2.14	10.33	10.33	12.26
S. unit1 (Crisafulli, 1997)	7.85	8.34	7.45	5.01	5.01	2.58
Mean	1.81	2.03	1.74	3.84	3.84	4.73
Coefficient of Variation	**1.004**	**0.96**	**1.0**	**0.70**	**0.70**	**0.81**

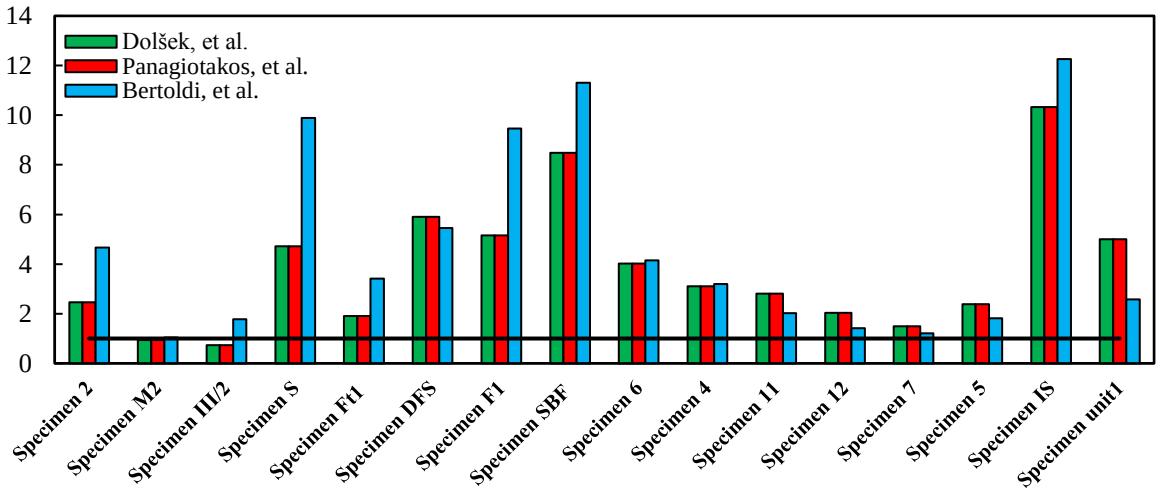

Figure 3.27 Ratios between the numerical initial stiffness and the initial stiffness obtained from the experimental data for sixteen specimens

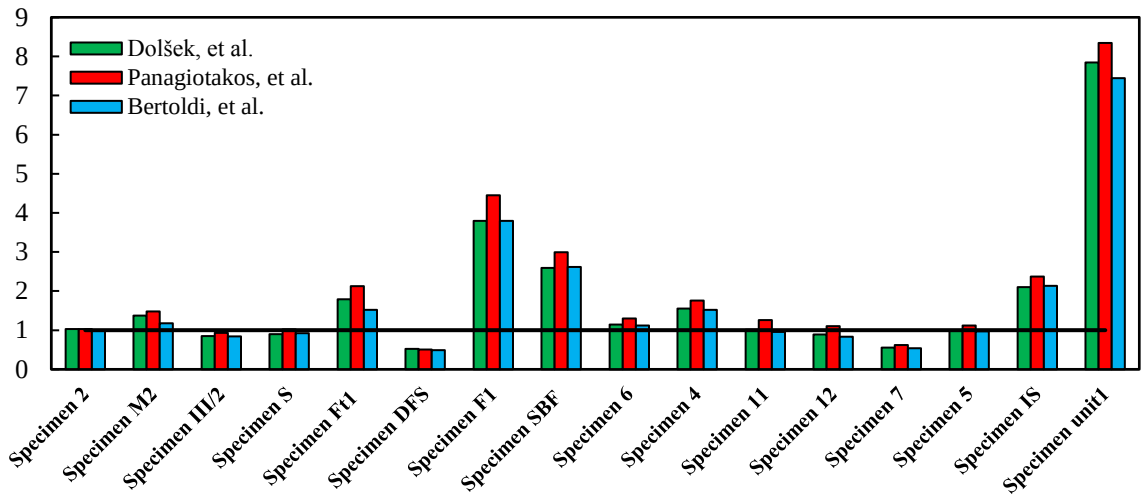

Figure 3.28 Ratios between the numerical maximum strength and the maximum strength obtained from the experimental data for sixteen specimens

Table 3.6 Ratios between the predicted initial stiffness using the effective wall thickness and the initial stiffness from the experimental data.

Specimen ID	**Ratios of the initial stiffness using effective thickness of the infill wall**		
	Dolšek, *et al.* (2008)	Panagiotakos, *et al.* (1994)	Bertoldi, *et al.* (1993)
S.2 (Zhai, *et al.*, 2016)	1.55	1.55	2.95
S. M2 (Pires, 1990)	0.37	0.37	0.41
S.III/2 (Sigmund, *et al.*, 2013)	0.26	0.26	0.62
S. S (Kakaletsis, 2009)	3.01	3.01	6.30
S. FT1 (Bergami, 2007)	0.95	0.95	1.71
S. DFS (Basha, *et al.*, 2016)	5.91	5.91	5.45
S.F1 (Stylianidis, 2012)	3.11	3.11	5.71
S.SBF(Misir, 2015)	4.78	4.78	6.38
S. 6 (Mehrabi, *et al.*, 1996)	1.66	1.66	1.72
S. 11(Mehrabi, *et al.*, 1996)	1.29	1.29	1.32
S.12(Mehrabi, *et al.*, 1996)	2.81	2.81	2.02
S. 7(Mehrabi, *et al.*, 1996)	2.03	2.03	1.42
S. 4 (Mehrabi, *et al.*, 1996)	1.49	1.49	1.21
S. 5 (Mehrabi, *et al.*, 1996)	2.39	2.39	1.82
S. IS (Kakaletsis, 2009)	7.93	7.93	9.41
S. unit1 (Crisafulli, 1997)	5.01	5.01	2.58
Mean	**2.78**	**2.78**	**3.19**
Coefficient of Variation	**0.77**	**0.77**	**0.82**

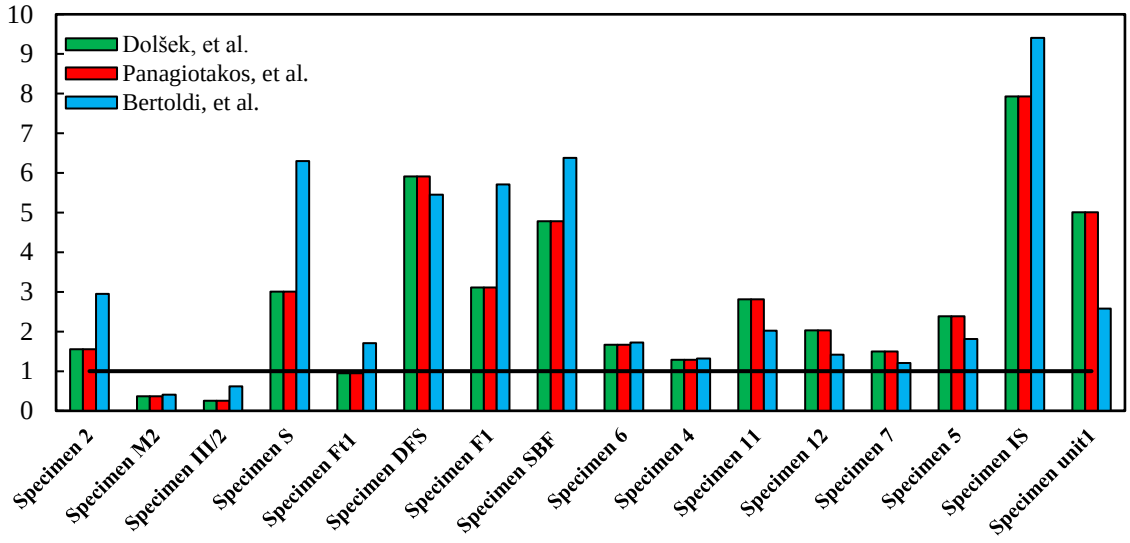

Figure 3.29 Ratios between the numerical initial stiffness and the initial stiffness obtained from the experimental data for sixteen specimens using the effective wall thickness

3.3.2 Selected procedures from standard and norms

The principles of strength-based procedures were adopted by several standard and norms to represent the infill behaviour under lateral loading. As such, this section analyses the performance of the strut modelling procedures adopted by the NZSEE (NZSEE, 2006), ASCE 41-6 (ASCE, 2007), CCMPA (CCMPA, 2009), ACI-530 (ACI, 2011), TEC (TEC, 2007), ASCE 41-13 (ASCE, 2013) and the draft revision of the NZSEE (NZSEE, 2016) to estimate the infill contribution to the lateral behaviour of RC frames. The base shear strength and the initial stiffness of the masonry infills adopted by these standards are defined by the expressions reported in Table 3.7. It worth mentioning that NZSEE (NZSEE, 2006) and its new draft (NZSEE, 2016) adopt the expression of ASCE/SEI 41-06 (ASCE, 2007) to define the strut width. The numerical values obtained for the initial stiffness and maximum strength of the masonry were then compared to those obtained from the experimental tests using an approach similar to the one in the previous section.

Table 3.7 Summary of strut models for infill panels considered by the considered standards

Standard	Equivalent strut model	Strength model
Common expression	$E_I = Cf_m^{'}$, $\lambda_h = \sqrt[4]{\frac{E_I t \sin 2\theta}{4(EI)_{column} h_w}} h$	$A_{ni} = t_w l_w$
NZSEE (NZSEE, 2006)	$C = 500$, $w = 0.175\ d\ \lambda_h^{-0.4}$	$V_u = \begin{cases} 0.50 wt f_m^{'} \cos\theta \\ \frac{2.83 l_w^2 h_w t_w \sigma_{cr}}{h_w + l_w} \\ t_w l_w \tau_0 + 0.8P \end{cases}$ $\sigma_{cr} = \frac{f_m^{'}}{40}, \tau_0 = \frac{f_m^{'}}{20}$
ASCE 41-06 (ASCE, 2007)	$C = 550$, $w = 0.175\ d\ \lambda_h^{-0.4}$	$V_u = A_{ni}\tau_w$
TEC (TEC, 2007)	$C \approx 750$, $w = 0.175\ d\ \lambda_h^{-0.4}$	$V_u \le \begin{cases} A_{ni}\tau_w \\ 0.22 l_w t f_m^{'} \end{cases}$
CCMPA (CCMPA, 2009)	$C = 850$, $w \le \begin{cases} w_i / 2 \\ d/4 \end{cases}$, $w_i = \sqrt{\alpha_l^2 + \alpha_h^2}$ $\alpha_h = \frac{\pi}{2}\sqrt[4]{\frac{4(EI)_{column} h_w}{E_I t \sin 2\theta}}$ and $\alpha_l = \pi\sqrt[4]{\frac{4(EI)_{beam} l_w}{E_I t \sin 2\theta}}$	$V_u \le \begin{cases} 0.85\chi\phi_m w\ (f_m^{'} t) \\ 0.13\phi_m \sqrt{f_m^{'}} d \gamma_g \\ 0.16\phi_m \sqrt{f_m^{'}} t d_v \big/ 1 - 0.9\phi_m \tan\theta \end{cases}$ $d_v = 0.80\ l_w$,
ACI-530 (ACI, 2011)	$C = 700$, $w = \frac{0.30}{\lambda \cos\theta}$	$V_u \le \begin{cases} 3160 A_{ni}\sqrt{f_m^{'}} / 1.5 \\ 2070 A_{ni} / 1.5 \\ 0.152 t f_m^{'} \end{cases}$
ASCE 41-13 (ASCE, 2013)&&	$C = 550$, $k_1 = \frac{l_w t G_m}{h_w}$, $G_m = 0.40 E_I$	$V_u \le \begin{cases} 0.33 h_w t f_m^{'} \\ A_{ni}\tau_w \end{cases}$
NZSEE (NZSEE, 2016)	$C = 700$, $w = 0.18 d\ \lambda_h^{-0.4}$	$V_u \le \begin{cases} 0.33\ l t_m \sqrt{f_m^{'}} \\ 0.83 A_{ni} \\ 0.41 tl + 0.45 p \end{cases}$

Notations

$f_m^{'}$ is the masonry compressive strength in MPa, w is the strut width, A_{ni} is the shear area, d is the strut diagonal length, l_w is the infill length, h_w is the infill height, h is the height of the panel centre to centre, θ is the inclination angle of the strut on the horizontal plane, G_w is the shear modulus of the masonry, τ_w is the shear strength of masonry infill, E_I is the modulus of elasticity of masonry, t is the effective wall thickness, t_w is the wall thickness, I is the moment of inertia of the frame member, E is the modulus of elasticity of the frame, ϕ_m is a resistance factor for masonry considered to be 0.60, p is the vertical force acting on the masonry infill wall, χ and γ_g are factors whose values are found in the corresponding standard.

&& it provides an expression to directly compute the lateral stiffness k_1 of the infill wall

In order to assess the errors resulting from the use of the reffered models, ratios between the predicted initial stiffness and the experimental one, and between the predicted maximum lateral force and the experimental one are shown in Table 3.9 and Table 3.8, respectively. Moreover, to facilitate the interpretation of the results, maximum strength ratios and the initial stiffness presented in Table 3.9 and Table 3.8 are plotted in Figure 3.30 and Figure 3.31, respectively. In terms of the maximum force, as shown in Table 3.9 and Figure 3.30, the TEC (2007) and ACI-530 approaches are those exhibiting a mean strength ratio closest to 1. However, the values of the CoV are very large which means that each procedure may significantly underestimate or overestimate the maximum strength for any specimen. With respect to estimating the initial stiffness, the NZSEE (NZSEE, 2016) approach provides a better prediction than the other methods (on average) as shown Figure 3.31. Still, the values of the CoV are very large for all the procedures which means that each prediction is associated with a significant amount of uncertainty. Interestingly, the CCMPA approach provides the worst predictions for both the strength and the stiffness: on average, it exhibits the largest overestimation for the initial stiffness and underestimation for the maximum strength. The ASCE41-6 and ACI-530 methods were found to yield reasonable results for some specimens but, for the majority of the specimens, their strength and initial stiffness predictions deviate severely from the experimental values. Even though, ASCE41-13 provides reasonable results for the maximum strength, its predictions for the initial stiffness, which adopt an expression similar to the one used by Dolšek, *et al.* (2008), deviate significantly from the experimental values.

In sum, all the methods considered in this study generally exhibited large uncertainty in predicting the initial stiffness and the maximum strength. These large deviations could partly be the result of adopting the concept that only one behaviour mechanism controls the overall behaviour of the infill, when, in reality, the fact that one behaviour mechanism reaches failure does not mean that the infill is unable to bear additional loads by alternative mechanisms. Developing one failure mechanism can delay/accelerate the occurrence of other failure mechanisms. For example, after failure by a shear slip mechanism occurring at the mid-layer of the infill, the loads can be transferred diagonally through the infill by developing a behaviour mechanisms in the two sub-panels, as shown in Figure 3.32 (based on the experimental observation of (Pires, 1990)), a mechanism which has been used recently as a new construction technique (Bolis*, et al.*, 2016).

Table 3.8 Comparison of the infill maximum strength obtained from seven different standard-based methods with those obtained from experimental tests

Specimen ID	Ratios of the maximum lateral strength						
	NZSEE-2006	ASCE 41-6	TEC	CCMPA	ACI-530	ASCE 41-13	NZSEE-2016
S.2 (Zhai, *et al.*, 2016)	0.20	0.79	0.61	0.14	0.17	0.39	0.75
S. M2 (Pires, 1990)	0.16	1.07	0.82	0.18	0.20	0.32	0.62
S.III/2 (Sigmund, *et al.*, 2013)	0.06	0.46	0.35	0.08	0.10	0.12	0.24
S. S (Kakaletsis, 2009)	0.13	0.69	0.54	0.12	0.49	0.34	0.66
S. FT1 (Bergami, 2007)	0.19	0.74	0.57	0.13	0.22	0.29	0.55
S. DFS (Basha, *et al.*, 2016)	0.78	1.70	1.31	0.30	1.52	1.31	2.54
S.F1 (Stylianidis, 2012)	0.35	1.64	1.27	0.29	0.96	0.76	1.48
S.SBF(Misir, 2015)	0.78	1.99	1.54	0.35	1.07	0.87	1.51
S. 6 (Mehrabi, *et al.*, 1996)	0.29	0.88	0.68	0.15	0.37	0.28	0.43
S. 11(Mehrabi, *et al.*, 1996)	0.41	1.19	0.92	0.21	0.51	0.38	0.57
S.12(Mehrabi, *et al.*, 1996)	0.62	0.79	0.61	0.14	0.62	0.61	0.88
S. 7(Mehrabi, *et al.*, 1996)	0.58	0.69	0.53	0.12	0.58	0.53	0.71
S. 4 (Mehrabi, *et al.*, 1996)	0.36	0.42	0.33	0.07	0.41	0.33	0.43
S. 5 (Mehrabi, *et al.*, 1996)	0.63	0.76	0.59	0.13	0.73	0.59	0.77
S. IS (Kakaletsis, 2009)	0.77	1.61	1.24	0.28	1.54	0.95	1.15
S. unit1 (Crisafulli, 1997)	4.87	6.01	4.65	1.05	5.76	4.65	5.02
Mean	0.70	1.34	1.03	0.23	0.95	0.79	1.15
Coefficient of Variation	1.63	0.99	0.99	1.00	1.42	1.35	1.03

Table 3.9 Comparison of the infill maximum initial stiffness obtained from seven different standard-based methods with those obtained from experimental tests

Specimen ID	**Ratios of the initial stiffness**						
	NZSEE-2006	ASCE 41-6	TEC	CCMPA	ACI-530	ASCE 41-13	NZSEE-2016
S.2 (Zhai, *et al.*, 2016)	0.49	0.53	0.53	1.44	0.68	1.14	0.68
S. M2 (Pires, 1990)	0.14	0.15	0.15	0.25	0.13	0.27	0.19
S.III/2 (Sigmund, *et al.*, 2013)	0.12	0.13	0.13	0.18	0.15	0.19	0.17
S. S (Kakaletsis, 2009)	0.71	0.77	0.77	2.03	0.80	2.20	0.99
S. FT1 (Bergami, 2007)	0.24	0.26	0.26	0.52	0.21	0.70	0.33
S. DFS (Basha, *et al.*, 2016)	1.02	1.11	1.11	4.95	1.07	4.33	1.41
S.F1 (Stylianidis, 2012)	0.87	0.95	0.95	2.38	0.84	2.93	1.21
S.SBF(Misir, 2015)	1.07	1.16	1.16	2.63	0.93	3.51	1.48
S. 6 (Mehrabi, *et al.*, 1996)	0.50	0.54	0.54	0.97	0.41	1.22	0.70
S. 11(Mehrabi, *et al.*, 1996)	0.39	0.42	0.42	0.75	0.31	0.94	0.54
S.12(Mehrabi, *et al.*, 1996)	0.23	0.25	0.25	1.10	0.12	2.06	0.32
S. 7(Mehrabi, *et al.*, 1996)	0.17	0.18	0.18	0.78	0.08	1.49	0.23
S. 4 (Mehrabi, *et al.*, 1996)	0.17	0.18	0.18	0.82	0.12	1.10	0.23
S. 5 (Mehrabi, *et al.*, 1996)	0.26	0.28	0.28	1.30	0.17	1.75	0.36
S. IS (Kakaletsis, 2009)	1.34	1.46	1.46	4.72	1.20	5.81	1.86
S. unit1 (Crisafulli, 1997)	0.54	0.59	0.59	2.30	0.31	3.67	0.75
Mean	0.51	0.56	0.56	1.70	0.47	2.08	0.72
Coefficient of Variation	0.74	0.74	0.74	0.85	0.82	0.76	0.74

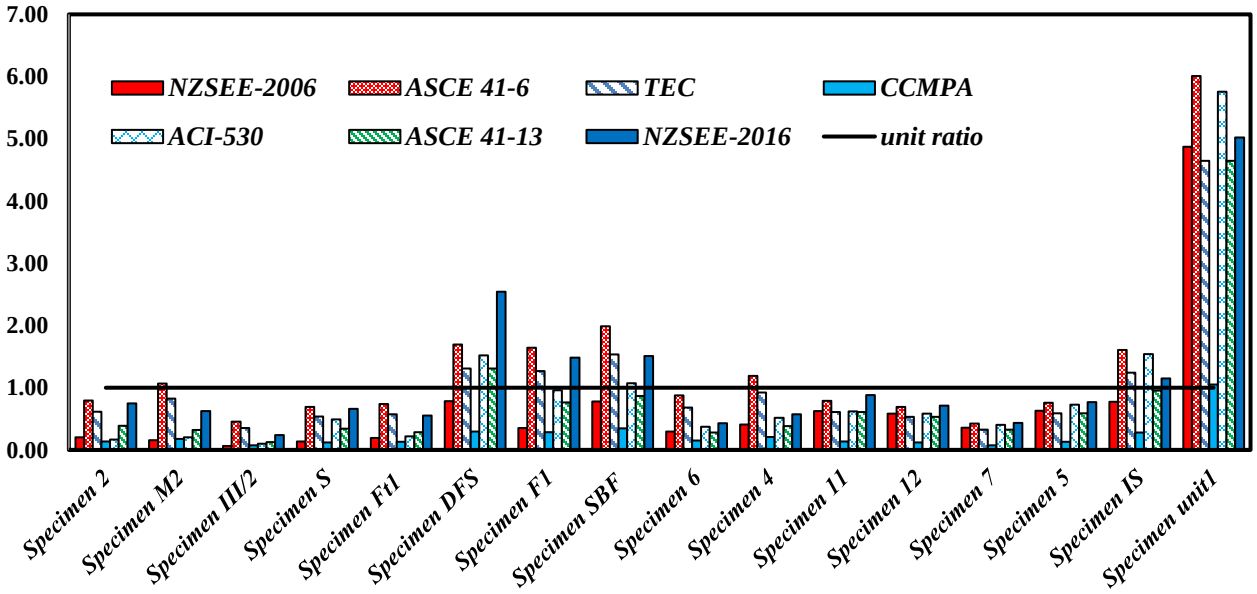

Figure 3.30 Ratios between the numerical maximum strength and the maximum strength obtained from the experimental data for sixteen specimens

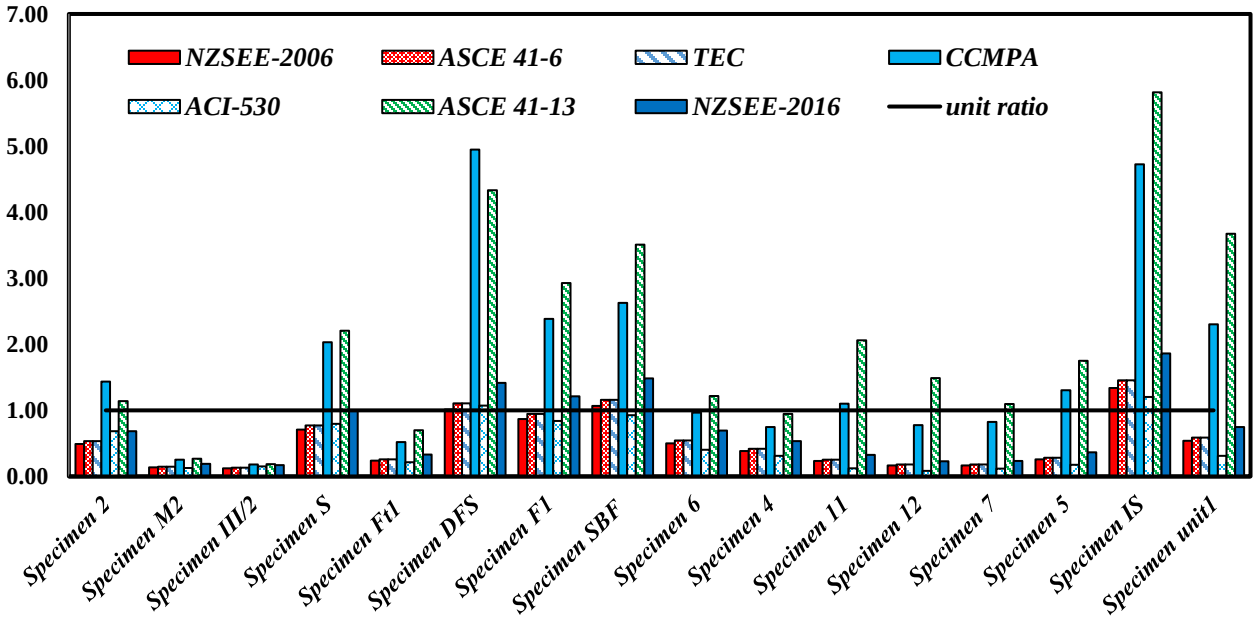

Figure 3.31 Ratios between the numerical initial stiffness and the initial stiffness obtained from the experimental data for sixteen specimens

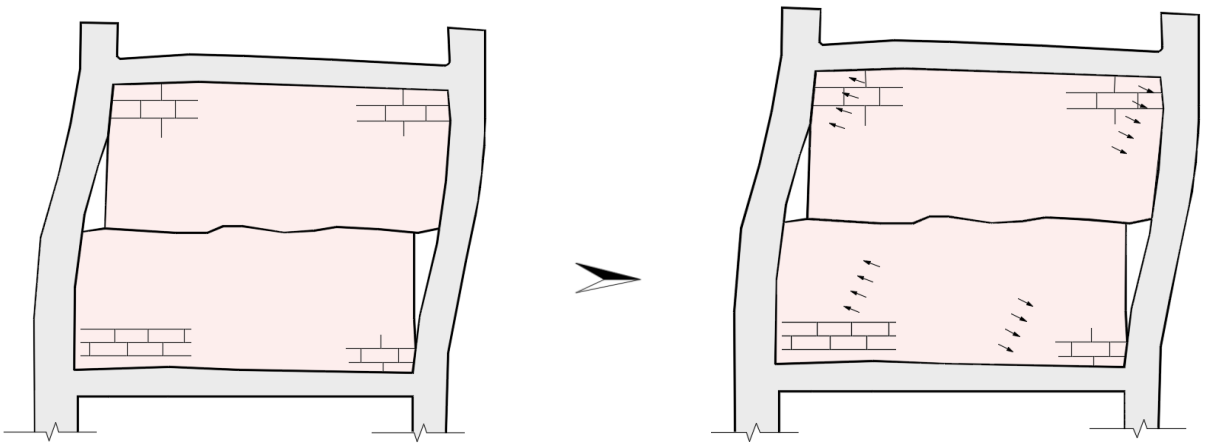

a) b)

Figure 3.32 a) Shear slip at the mid-layer of the infill; b) load paths through the infill panel after the shear slip failure

3.4 Empirical procedures to account for partially infilled panels

Although an infill panel can be simulated using a diagonal strut model representing the stiffening and strengthening effects of the infill, the presence of an opening in the masonry panel causes a deviation in the development of the referred diagonal strut. Therefore, the models that were previously considered to simulate the behaviour of a fully infilled panel must now be modified to account for the existence of an opening (i.e. a window or a door). Several studies can be found in the literature that attempted to model the behaviour of partially infilled panels. Some of these attempts tried to simplify the existence of the opening by applying a reduction factor to the strength and stiffness of the corresponding fully infilled panel. Other attempts developed new configurations of the strut system e.g. see the configurations shown in Figure 3.33 and Figure 3.34. By using such alternative strut configurations, a new configuration of the RC frame modelling is also required, i.e. the elements representing the RC frame need to be subdivided to introduce additional nodes to connect with the strut system. As such, these approaches might lead to unbalanced computational models (due to the existence of a large number of low-strength masonry elements with the potential to have a null or very small stiffness after failure) or to high-cost computational models which are not seen as the best approaches particularly for probabilistic performance studies that require a high number of analyses.

Therefore, the performance assessment carried out herein only focuses on approaches that use a reduction factor applied to the fully infilled panel properties to account for openings instead of methods relying on a reconfiguration of the strut system. The next section reviews the approaches proposing reduction factors to establish the strength and stiffness of the partially infilled panel that were selected for the performance assessment that was carried out.

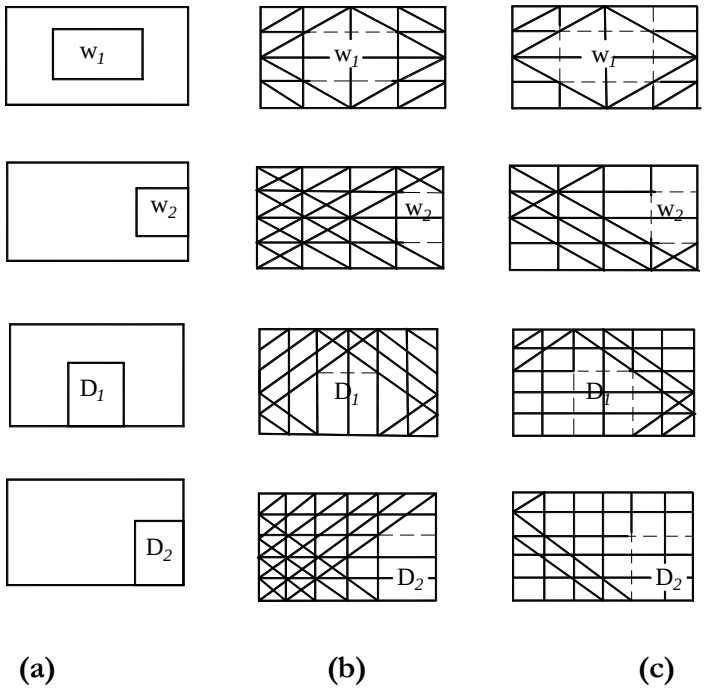

Figure 3.33 Formulation of struts around openings: a) position of openings; b) struts for infills with a monolithic connection with the surrounding frame; c) struts for infills with a non-monolithic connection with the surrounding frame (Thiruvengadam, 1985)

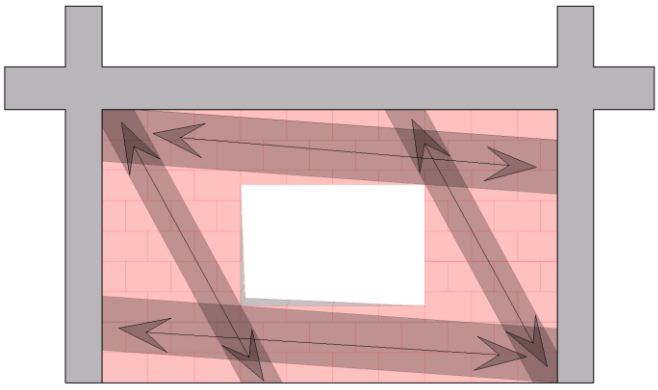

Figure 3.34 Equivalent struts system for partially infilled panel proposed in (Hamburger, *et al.*, 1993)

3.4.1 Selected procedures establishing reduction factors for partial infills and experimental data

In general, the presence of openings implies a reduction of the stiffness and ultimate strength of the panel, as well as of the energy dissipation capacity. Several experimental campaigns were carried out in the past to assess these reductions in strength and stiffness. In addition to his observation regarding the use of a bracing strut to model the behaviour of the infill panel, Polyakov (1956) reported that the ultimate strength of partially infilled models have a reduction between 23% and 76%, when compared to the corresponding fully infilled steel frame. Benjamin*, et al.* (1958) also conducted one of earliest studies in this context which involved an infilled steel frame with a central opening with a size ratio of 1:3 of the infill panel size. Benjamin*, et al.* (1958) observed a reduction of the ultimate strength due to the opening of about 45%. In the same context, based on experimental and numerical investigations, Sachanski (1960), Dawe*, et al.* (1988), Imai*, et al.* (1989), Bertoldi*, et al.* (1993), Durrani*, et al.* (1994), Al-Chaar (2002) and Mondal*, et al.* (2008), among others, have performed studies to analyse the reduction factor accounting for openings. More recently, based on their experimental tests, Kakaletsis*, et al.* (2009) observed a strength reduction between 18.7% to 25.17 % for window openings with a width in the range of 25 to 50% of the infill panel length and a strength reduction between 32% to 47.2% for door openings. In the same context, Sigmund*, et al.* (2013) tested four specimens with centric and eccentric door and window openings. Sigmund*, et al.* (2013) proposed expressions to quantify the diagonal strut width based on the opening type and the damage state of the structure. It is worth noting that, in their studies, the reduction in area of the strut was only detected for cases involving moderate damage of the infill (which corresponded to drift ratios ranging between 0.2~0.3%). In order to quantify the reduction in strength and stiffness, several empirical expressions have also been proposed, some of which are briefly reported in Table.3.10. These expressions were gathered from the recent reviews on this topic presented in (Mohammadi*, et al.*, 2012, Surendran*, et al.*, 2012, Decanini*, et al.*, 2014, Buch*, et al.*, 2015) and also include the recent proposal by Asteris, *et al.* (2016). The resulting reduction factor (δ) is used to modify the backbone response of fully infilled panels to account for the openings as illustrated in Figure 3.35. The notations used in this analysis are defined in Figure 3.36.

In order to illustrate the values obtained by the selected expressions, Figure 3.37 shows the variation of the reduction factor with the configuration of the opening. As can be seen, the expressions proposed by Al-Chaar (2002), Mondal, *et al.* (2008), Asteris*, et al.* (2011b) and Tasnimi, *et al.* (2011) only

considered the effect of the relative area of the opening without accounting for the actual size of the opening. On the other hand, the remaining expressions considered both these effects by introducing either the opening height ratio ξ_h or the opening width ratio ξ_l in their proposed expressions.

Table.3.10 Reduction factors proposed by previous researchers

Model	**Reduction factor**	**Remarks and notations**
Polyakov (1956)	$\delta = 1-(1.15\xi_h + 0.385\xi_{area})$	Valid for $\xi_h \le 0.65$ and $\xi_{area} \le 0.60$ where $\xi_h = (h_o / h_w)$ and $\xi_{area} = (h_0 l_0 / \mathrm{h_w L_w})$
Sachanski (1960)	$\delta = 1-(0.4\xi_l + 0.6\xi_h)$	$\xi_l = (l_o / L_w)$
Dawe, *et al.* (1988)	$\delta = 1-1.5\xi_l$ *if* $\delta < 0$, $\delta = 0$; adopted by (NZSEE, 2006);	Infill panels with an opening with a width larger than two-thirds of the infill panel width are neglected
Imai, *et al.* (1989)	$\delta = \min\begin{cases} 1-\xi_l \\ 1-\sqrt{\xi_{area}} \end{cases}$	Based on both theoretical and experimental research
Durrani, *et al.* (1994)	$\delta = 1-\left(\frac{A_d}{L_w h_w}\right)^2$	Based on finite element analyses. $A_d = L_w h_w - \frac{(d\sin(2\theta) - d_0\sin(\theta+\varphi))^2}{2\sin(2\theta)}$
Bertoldi, *et al.* (1993)	$\delta = .78e^{-0.322\ln 100\xi_{area}} + .93e^{-0.762\ln 100\xi_l}$	$\delta \le 1$
Al-Chaar (2002)	$\delta = 0.6\xi_{area}^2 - 1.6\xi_{area} + 1$	Valid for $\xi_{area} < 0.60$; otherwise the effect of the infill panel is neglected.
Mondal, *et al.* (2008)	$\delta = 1 - 2.47\xi_{area}$	Valid for $\xi_{area} < 0.385$; otherwise the effect of the infill panel is neglected.
Asteris, *et al.* (2011b)	$\delta = 1 - 2\xi_{area}^{0.54} + \xi_{area}^{1.14}$	Based on a finite element model
Tasnimi, *et al.* (2011)	$\delta = 1.49\xi_{area}^2 - 2.238\xi_{area} + 1$	Does not account for the surrounding conditions of the opening Valid for $\xi_{area} < 0.40$
Decanini, *et al.* (2014)	$\delta = \nu e^{\beta\xi_{area}} + \varsigma e^{\kappa\xi_l} \pm \sigma\varepsilon$	B, ν, ζ ans κ are obtained from regression analyses and depend on the surrounding conditions of the infill (values given in Table 3.11), σ is the standard deviation of the error of the regression and ε is 0 when defining the mean value of δ and 1 when defining the mean value plus or minus one standard deviation of δ)
Asteris, *et al.* (2016)	$\delta = 1 + 0.24\xi_h - 4.23\xi_h^2 - 2.6\xi_h^3 + 12.73\xi_h^4 - 7.15\xi_h^5$	For the square opening only

Table 3.11 Parameters for the reduction factor proposed by Decanini, *et al.* (2014)

Reinforcement around opening	ν	β	ς	κ
Not reinforced (NR)	0.55	-0.035	0.44	-0.025
Partially reinforced (PR)	0.58	-0.030	0.42	-0.020
Reinforced (R)	0.63	-0.020	0.40	-0.010

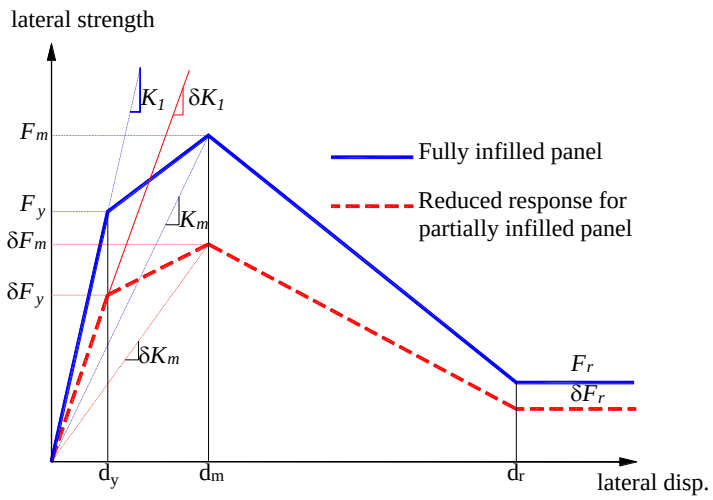

Figure 3.35 Schematic representation on how to apply the reduction factor (δ) to the fully infill lateral load-displacement envelope to obtain the force-displacement envelope for the partially infilled panel.

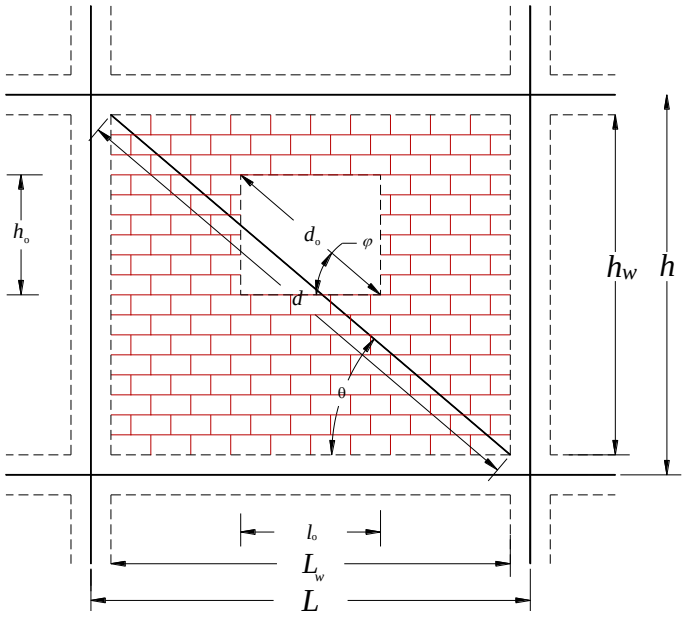

Figure 3.36 Notations used in the expressions of Table.3.10

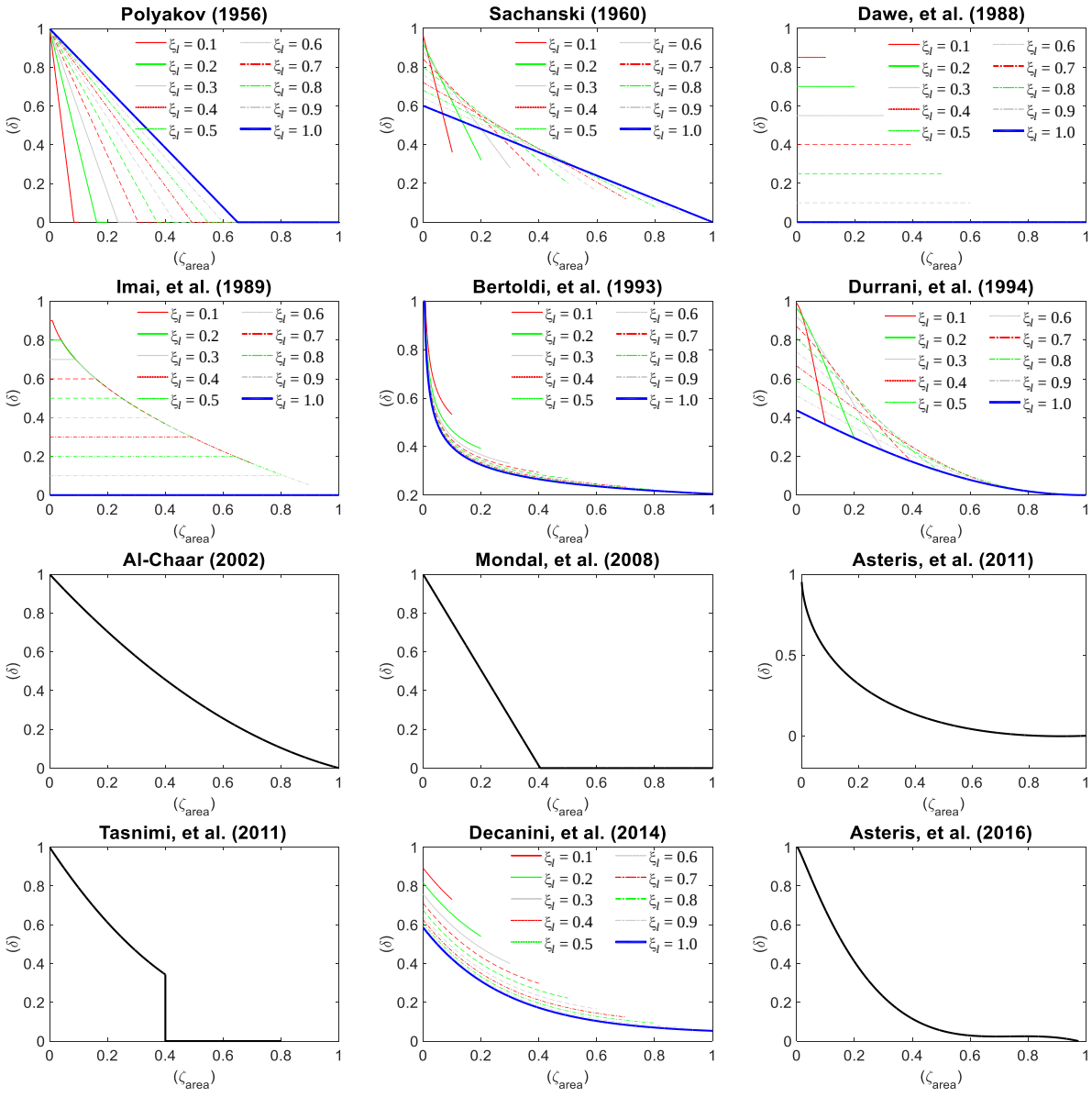

Figure 3.37 Variation of the reduction factor with configurations of the opening according to the formulas stated in Table.3.10.

In order to assess the reliability of these expressions which account for the existence of an opening in the infill panel, sixteen partially infilled specimens gathered from three different test campaings were used to analyse the reduction factor. These specimens have different opening configurations in terms of the size, location and type of opening. Table 3.12 presents the references and the notations of these specimens, along with their main characteristics.

Table 3.12 Notation and main characteristics of the considered partially infilled specimens.

ID	Opening type	Eccentricity	L_w (m)	h_w(m)	l_o(m)	h_o(m)
do2[1]	door	Centric	1.2	0.8	0.3	0.666
do3[1]	door	Centric	1.2	0.8	0.46	0.666
do4[1]	door	Centric	1.2	0.8	0.6	0.666
dx1[1]	door	Eccentric	1.2	0.8	0.3	0.666
dx2[1]	door	Eccentric	1.2	0.8	0.3	0.666
wo2[1]	window	Centric	1.2	0.8	0.3	0.333
wo3[1]	window	Centric	1.2	0.8	0.46	0.333
wo4[1]	window	Centric	1.2	0.8	0.6	0.333
wx1[1]	window	Eccentric	1.2	0.8	0.3	0.333
wx2[1]	window	Eccentric	1.2	0.8	0.3	0.333
I/1[2]	door	Centric	1.8	1.3	0.35	0.9
I/2[2]	window	Centric	1.8	1.3	0.5	0.6
PW1[3]	window	Centric	2.26	1.8	0.5	0.5
PW 2[3]	window	Centric	2.26	1.8	0.7	0.8
PW 3[3]	window	Centric	2.26	1.8	1.2	0.6
PW 4[3]	door	Centric	2.26	1.8	0.7	1.45

[1] **(Kakaletsis*, et al.*, 2009, Kakaletsis, 2009)**
[2] **(Sigmund*, et al.*, 2013)**
[3] **(Tasnimi*, et al.*, 2011)**

3.4.2 Results of the performance of the selected procedures

Table 3.13 reports the reduction factors obtained by the selected methods for the sixteen experimental specimens referred in the previous section along with those obtained directly from the experimental data. The reduction factors based on experimental data were obtained by extracting the response of the masonry component from the system response for both the fully infilled and partially infilled panels of a given specimen. As shown in Figure 3.38, the difference between the response of the partially infilled and fully infilled panels is not regular. Therefore, the reduction factor obtained from experimental data was computed by two methods. In the first method, the reduction factor was computed with respect to the maximum force F_m, regardless of the corresponding strain. In the second method, an average value of the reduction factors computed for all the recorded levels of strain was defined, as illustrated in Figure 3.38. It is noted that the latter method accounts for the reduction in both the stiffness and the strength. These procedures were implemented for both the positive and the negative directions. As can be seen from Table 3.13, for each direction, the experimental reduction factors obtained by both methods are similar, which agrees with the findings by Decanini, *et al.* (2014) that suggest the use of a unique reduction factor for both the stiffness and the strength of partially infilled frames. The results presented in Table 3.13 indicate that most empirical expressions provide reasonable values for the reduction factor with an average absolute error (AAE) that does not exceed

25%. The expressions proposed by Polyakov (1956), Bertoldi, *et al.* (1993) and Asteris, *et al.* (2011b) are those exhibiting the largest AAE but it does not exceed 41%. On the other hand, the expressions proposed by Sachanski (1960), Imai, *et al.* (1989), Durrani, *et al.* (1994), Mondal, *et al.* (2008), and Tasnimi, *et al.* (2011) exhibit the lowest values of the AAE. It is worth to noting that, even though, the expression proposed by Asteris, *et al.* (2016) is based on analysis of a square openings, it gives a reasonable AAE for other types of openings.

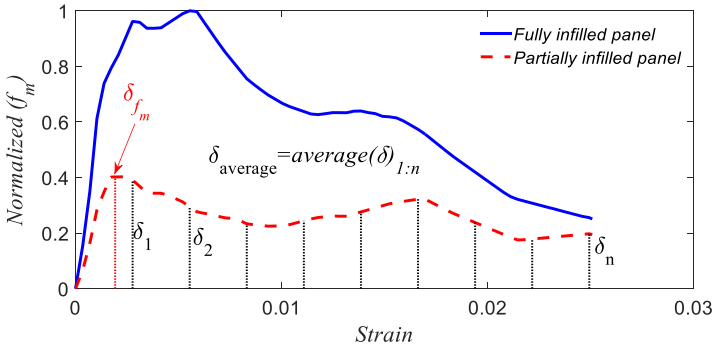

Figure 3.38 Illustrative example of computing the reduction factor based on the experimental data

Table 3.13 Comparison of reduction factors obtained from empirical expressions with those obtained for the experimental data

	Computed reduction factors												Experimental factors			
ID	**(a)**	**(b)**	**(c)**	**(d)**	**(e)**	**(f)**	**(g)**	**(h)**	**(i)**	**(j)**	**(k)**	**(l)**	**(m)**	**(n)**	**(o)**	**(p)**
do2	n/a	0.40	0.63	0.54	0.38	0.37	0.69	0.49	0.31	0.60	0.50	0.39	0.41	0.41	0.41	0.34
do3	n/a	0.35	0.43	0.44	0.28	0.31	0.55	0.212	0.19	0.44	0.35	0.20	0.52	0.48	0.52	0.36
do4	n/a	0.30	0.25	0.36	0.21	0.28	0.44	n/a	0.12	0.33	0.25	0.10	0.40	0.33	0.24	0.16
dx1	n/a	0.40	0.63	0.54	0.38	0.37	0.69	0.49*	0.31	0.60	0.50	0.39	0.57	0.54	0.35	0.33
dx2	n/a	0.40	0.63	0.54	0.38	0.37	0.69	0.49*	0.31	0.60	0.50	0.39	0.46	0.44	0.62	0.64
wo2	0.48	0.65	0.63	0.68	0.69	0.45	0.84	0.74	0.49	0.78	0.62	0.66	0.71	0.68	0.71	0.71
wo3	0.46	0.60	0.43	0.60	0.59	0.38	0.76	0.61	0.38	0.68	0.48	0.50	0.66	0.63	0.91	0.90
wo4	0.44	0.55	0.25	0.50	0.50	0.34	0.69	0.49	0.31	0.60	0.39	0.39	0.66	0.64	0.64	0.67
wx1	0.48	0.65	0.63	0.68	0.69	0.45	0.84	0.74*	0.49	0.78	0.62	0.66	0.74	0.69	0.82	0.87
wx2	0.48	0.65	0.63	0.68	0.69	0.45	0.84	0.74*	0.49	0.78	0.62	0.63	0.68	0.67	0.66	0.76
I/1	0.15	0.51	0.71	0.63	0.52	0.44	0.80	0.67	0.42	0.73	0.61	0.57	0.95	0.94	n/a	n/a
I/2	0.42	0.61	0.58	0.64	0.64	0.42	0.81	0.68	0.44	0.74	0.57	0.59	1.11	1.11	n/a	n/a
PW1	0.66	0.75	0.67	0.75	0.81	0.52	0.90	0.85	0.60	0.87	0.70	0.80	0.92	0.84	0.86	0.70
PW2	0.43	0.61	0.54	0.63	0.63	0.40	0.79	0.66	0.42	0.72	0.54	0.56	0.81	0.62	0.69	0.56
PW3	0.55	0.59	0.20	0.47	0.54	0.35	0.74	0.56	0.35	0.65	0.41	0.46	0.69	0.52	0.58	0.48
PW4	n/a	0.39	0.54	0.50	0.35	0.35	0.64	0.38	0.26	0.53	0.43	0.31	0.54	0.42	0.58	0.48
AAE (%)	35.0	14.3	28.7	13.6	17.1	33.4	29.4	16.08# 18.46$	40.2	18.0	20.0	24.0				

(a) (Polyakov, 1956) (b) (Sachanski, 1960) (c) (Dawe, *et al.*, 1988) (d) (Imai, *et al.*, 1989) (e) (Durrani, *et al.*, 1994) (f) (Bertoldi, *et al.*, 1993) (g) (Al-Chaar, 2002) (h) (Mondal, *et al.*, 2008) (i) (Asteris, *et al.*, 2011b) (j) (Tasnimi, *et al.*, 2011) (k) (Decanini, *et al.*, 2014) (l) Asteris, *et al.* (2016) (m) Experimental reduction factor for maximum strength F_m for the positive direction (n) Experimental average reduction factor for the positive direction. (o) Experimental reduction factor for maximum strength F_m for the negative direction (p) Experimental average reduction factor for the negative direction.

* the (Mondal, *et al.*, 2008) expression is not applicable (it is only valid for centric openings), but it applied nevertheless

$ AAE value obtained for all specimens; # AAE value obtained only for cases where the expression is applicable

3.5 Conclusion

The current chapter reviewed the performance of existing stiffness-based procedures in establishing adequate values for the parameters needed to simulate the behaviour of masonry infills using the single strut modelling approach. The principle that an infill panel works as a constant area member under compression loads throughout the entire loading history (which is the main assumption of stiffness-based procedures) leads to large errors in predicting both the maximum lateral strength and the initial stiffness of the infill. One of the main reasons for this lack of accuracy was seen to be related to the fact that such procedures do not account for the change in geometry of the actively loaded area of the masonry panel throughout the loading history. Due to the large variability of the performance of the tested stiffness-based procedures, none of them is actually recommended to establish the parameters needed to simulate the behaviour of masonry infills using the single strut modelling approach.

As an alternative to stiffness-based procedures, the performance of strength-based procedures was also analysed. Three empirical strength-based models and another seven models suggested by standards were analysed. The results obtained from the empirical strength-based procedures were seen to provide better predictions of the maximum lateral strength and the initial stiffness of the infill. However, to obtain more realistic predictions, it is recommended to compute the infill stiffness using the infill's effective thickness instead of using the wall's gross (real) thickness. With respect to the models proposed by several standards, the TEC (2007) and ACI-530 approaches were found to be those providing better average predictions of both the maximum lateral strength and the initial stiffness. However, the large variability of the predictions obtained for the several experimental specimens that were considered renders the applicability of these models highly uncertain. In the overall, all the strength-based procedures that were analysed exhibit a large variability of their performance. Even if some procedures provided reasonable predictions for part of the specimens, their significant underestimation or overestimation of the parameters analysed for other specimens is a clear reflection of their empirical nature and uncertain performance.

Based on these results, the use of either stiffness-based or strength-based procedures is not recommended to define the parameters needed to use the referred single strut modelling approach. To establish a more reliable framework to obtain data based on which the strut parameters can be determined, the next chapter will analyse the possibility of using refined finite element models to simulate experimental data as an alternative for the actual experimental tests.

Finally, in order to assess the effect openings in the infill panel, two different approach are proposed in the literature: either use new configurations for the strut system or use the same single strut model as for the solid panel but with a reduced strength and stiffness. The use of a reduction factor for the strength and stiffness of the solid infill is seen to be more efficient when compared to the use of a new configuration of struts which involves several additional elements. Therefore, several existing empirical expressions proposing reductions factors were analysed. By comparing the predicted strengths based on these expressions with those measured experimentally, most expressions exhibited a reasonable absolute error that does not exceed 25%. The expressions proposed by Polyakov (1956), Bertoldi*, et al.* (1993) and Asteris*, et al.* (2011b) exhibited the largest absolute average error but it did not exceed 41%. On the other hand, the expressions proposed by Sachanski (1960), Imai*, et al.* (1989), Durrani*, et al.* (1994), Mondal*, et al.* (2008) and Tasnimi*, et al.* (2011) exhibited the lowest absolute error.

Chapter 4.
Proposed continuum finite element modelling approach for masonry infilled RC frames

4.1 Introduction

According to the analyses presented in the previous chapter, adequate procedures are needed to define the parameters of strut elements with sufficient reliability. In this context, experimental tests on masonry infilled reinforced concrete (RC) frames provide important results to understand and analyse the complex behaviour of these structures under seismic loading and, therefore, can be used to define the parameters of strut models. However, the economic and time resources needed to carry out these tests, as well as the level of variability in the material properties of the different components of the infilled frames, stand as the main barriers to the widespread use of the experimental approach. As such, the use of an approach based on refined finite element modelling, as presented in Chapter 2, is seen as a viable alternative to reproduce the physical behaviour of the RC frames with masonry infills.

In light of this, the use of adequate refined numerical models that are able to represent the complex behaviour of RC masonry-infilled structures is proposed herein as an alternative for cases where experimental data are not available or experimental tests are unable to be carried out. In this context, the current chapter addresses the development of a refined finite element modelling approach (sometimes also termed *micro-modelling* approach in the literature), that is able to reproduce the more important features of the in-plane behaviour of RC masonry-infilled frames under monotonic and cyclic loading. By using this modelling approach, a realistic simulation of the masonry infill behaviour

is obtained, as well as reliable data to define the properties of simplified macro-models such as those based on strut elements. The proposed modelling approach was developed using the commercial software ANSYS (ANSYS, 2012) in order to be more easily replicated by other researchers. After presenting the characteristics and features of the proposed approach, the results of several experimental tests are simulated to validate this numerical strategy.

4.2 Proposed finite element modelling approach

4.2.1 Detailed structural modelling strategy

The main objective of the proposed modelling approach is to develop numerical models of masonry infilled RC frames that balance the level of detail with the computational cost that, while providing reliable data to define the parameters of simplified macro-models. Therefore, the characteristics of the finite element model were developed in order to capture the various failure mechanisms that masonry infill panels may exhibit under both monotonic and cyclic loading conditions.

To illustrate the proposed nonlinear finite element modelling approach, Figure 4.1 shows the schematics of the finite element mesh components for a one-bay and one storey masonry-infilled RC frame. This frame, termed specimen M2 (Pires, 1990), will be used in a subsequent section to analyse the performance of the proposed modelling approach. The RC and masonry components are modelled using the 8-node hexahedral solid finite element named SOLID65 in ANSYS (Release 14.0) (ANSYS, 2012). With respect to the longitudinal reinforcement of the RC elements, the performance of two different modelling approaches was analysed: a smeared modelling approach and a discrete modelling approach. For the smeared approach, the cross-section of the beams and columns, and their connections, are meshed using the SOLID65 finite element and the longitudinal reinforcement rebars are merged with a limited number of elements according to the actual rebar locations (using the ANSYS programme option known as "real constants" see Annex B). For the discrete modelling approach, each steel rebar is represented by a separate bar element (i.e. a truss element), termed

LINK180 in ANSYS. With respect to the transversal reinforcement, the corresponding rebars were not modelled but its confinement effect was included in the behaviour of concrete in compression, as referred in a subsequent section.

The masonry brick units (i.e. the brick blocks) are modelled according to their real geometry, i.e. including the voids of the hollow brick units, to represent the contact between surfaces and the fragility of the brick units more realistically. In order to represent the interaction between different brick units and their interaction with the surrounding RC frame, contact elements (CONTA174 and TARGE170 available in ANSYS) were combined with a cohesive zone material (CZM) model using different parameters to accommodate different joint situations. To reduce the number of interface elements needed and the computational costs, the thickness of the mortar joints was divided in two parts that were connected to the adjacent masonry units, using an approach similar to that of (Lourenço*, et al.*, 1997). The interaction between the two parts of the mortar joint (and their adjacent masonry units) is then defined by the properties of the contact elements.

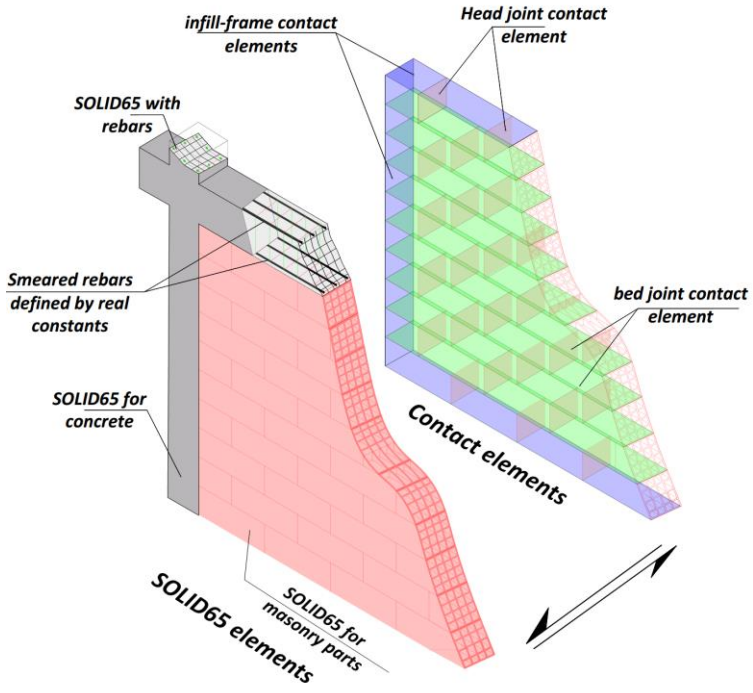

Figure 4.1 General schematics of the proposed refined modelling approach for masonry-infilled RC frames.

The ability of element SOLID65 to represent both materials of RC members (i.e. concrete and steel, for the smeared approach) reduced the number of element typologies involved in the modelling which, in turn, reduced the level of computational effort required. Furthermore, by using contact elements with the CZM model, several aspects of the complex interaction between the masonry infill and the RC frame are able to be captured by the numerical model. Given its characteristics, the proposed modelling approach is able to capture the more common failure mechanisms of masonry infills (e.g. crushing and tensile fracture of the masonry, cracking and shear slipping at the masonry interfaces (Shing*, et al.*, 2002)). Furthermore, when cracking or shear slipping occurs at a masonry interface, the model is also able to account for the discrete behaviour of the post-failure interface system. On the other hand, when the crushing or tensile fracture of a masonry unit occurs, the post-failure separation/splitting of the brick into discrete blocks is not accounted in order to reduce the computational effort.

The proposed modelling approach is also able to represent flexural failure modes of the RC elements but does not account for the possible shear failure of these elements. In this context, it is noted that the main purpose of the numerical model is not to represent the behaviour of the masonry-infilled RC frame system, but to characterize the behaviour of the masonry infill while accounting for the influence of the surrounding RC frame. Therefore, the inability to capture the shear failure of RC elements is not seen to be particularly important. Finally, it is noted that ANSYS has limited modelling capabilities to represent the cyclic degradation of materials. Therefore, cyclic degradation effects resulting in unloading/reloading stiffness degradation, strength degradation or pinching effects are only able to be represented in a simplified way.

4.2.2 Material modelling of the concrete

The concrete material model, termed CONCR in ANSYS, was combined with the SOLID65 element to represent the behaviour of concrete due to its ability to represent cracking in tension and crushing in compression. The CONCR material model requires the definition of four parameters: the

β_t and β_c shear coefficients, the concrete tensile strength f_t and the concrete compressive strength f_c. Parameters β_t and β_c control the amount of shear that is transferred across an opened and closed crack, respectively, and their values range from 0 to 1 (Kwan*, et al.*, 1999), where 0 represents a smooth crack (i.e. with total loss of shear transfer) and 1 represents an irregular crack (i.e. with no loss of shear transfer). The occurrence of numerical convergence problems was reported in (Vijaya*, et al.*, 2014) when parameter β_t is lower than 0.20 and no significant changes in the response were found as a result of using different values of this parameter. Therefore, in the present study, parameter β_t was set to 0.40 and parameter β_c was set to 0.80 (Xiaohan*, et al.*, 1996). The CONCR material model follows the failure surface proposed in (William*, et al.*, 1975) where the material behaves linearly until crushing or cracking. The tensile behaviour of concrete follows the stress-stain relation shown in Figure 4.2 where E is the modulus of elasticity of the concrete defined according to the behaviour model in compression.

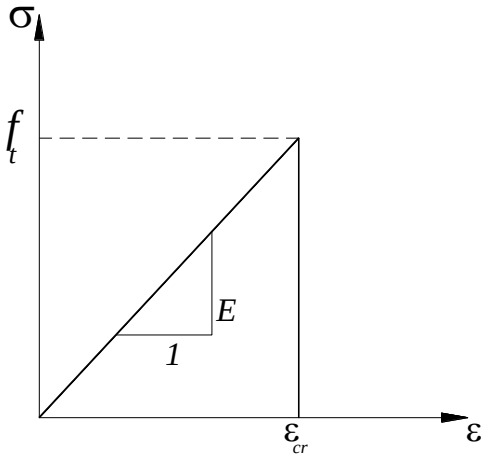

Figure 4.2 Stress-strain curve of the CONCR material model in tension (ANSYS, 2012).

Since the CONCR material model behaves as a linear elastic material in compression, it was combined with a nonlinear model in order to produce a realistic nonlinear stress–strain relation. The constitutive model proposed in (Kent*, et al.*, 1971) known as the "Kent-Park model" and its modified version (Scott*, et al.*, 1982) are used to define the envelope curves for the unconfined and confined concrete hysteretic behaviour in compression, respectively. These models are known to exhibit a good agreement with experimental results (Scott*, et al.*, 1982, Mohyeddin*, et al.*, 2013b) and provide a good balance between simplicity and accuracy (Taucer*, et al.*, 1991). The Kent-Park model was used to define a multi-kinematic material model MKIN for the concrete behaviour in compression with the crushing capability of the SOLID65 element deactivated to avoid the premature failure of the concrete (Chansawat*, et al.*, 2001) and to guarantee that the concrete element follows the selected constitutive

model. The Poisson ratio is considered to be 0.20 and the modulus of elasticity E is defined according to the Kent-Park constitutive model.

In order to validate the behaviour of this combined material model, the structural model shown in Figure 4.3 a) was tested. The structure is a unit cube made of concrete SOLID65 elements with characteristics from (Kakaletsis*, et al.*, 2009) connected to interface elements supported by two fixed plates. This structure was subjected to incremental uniform pressures in both the X and Y directions until failure in order to trace the failure surface of the combined material. The failure surface produced from that numerical test is shown in Figure 4.3 b) along with the Willam Warnke and the Von Mises failure surfaces (Mises, 1913). Figure 4.3 b) shows that the failure surface of the combined material matches the Willam Warnke failure surface in all the stress domains except in the compression-compression domain where it matches the Von Mises failure surface. This is caused by the deactivation of a parameter of the CONCR material model which switches the behaviour of the concrete in that domain to the multi-kinematic hardening material that follows the Von Mises failure surface.

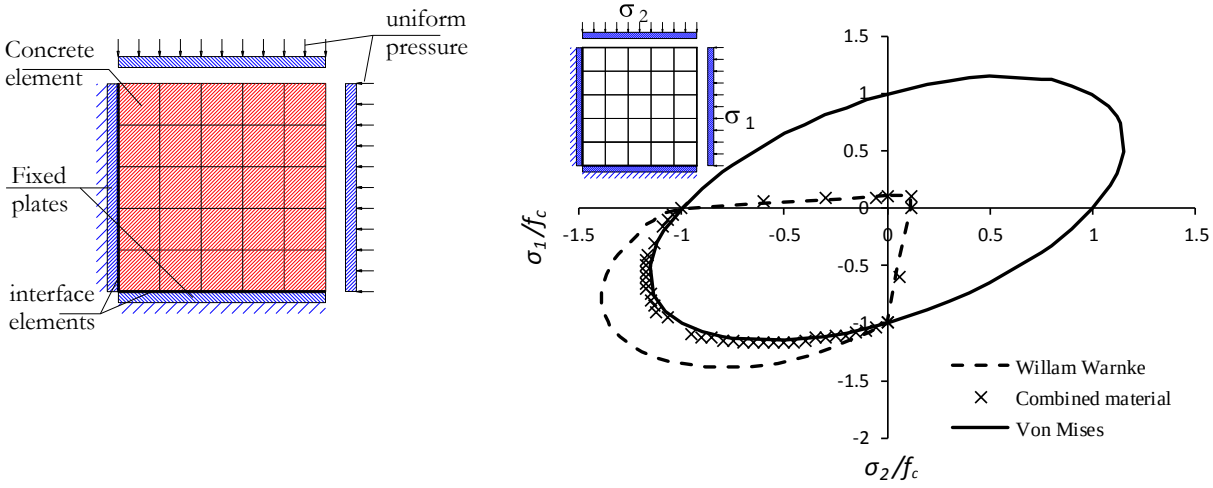

a) b)

Figure 4.3 a) Biaxial loading test structure, b) A comparison between the Von Mises and Willam Warnke failure surfaces with the combined material failure surface which is used to represent concrete material.

4.2.3 Material modelling of the steel reinforcement

In this study, the steel behaviour was represented by a bilinear stress-strain relation. As shown in Figure 4.4, the bilinear material is defined by the value of the yield stress σ_{yield} and of the post-yield tangent modulus E_T. This material exhibits kinematic hardening accounting for the Bauschinger effect (Hu*, et al.*, 2016) for cyclic loading, as shown in Figure 4.4. If experimental data about the post-yield behaviour of steel is unavailable, E_T is assumed to be equal to 2.5% of the initial modulus of elasticity (Mohyeddin*, et al.*, 2013a). The Poisson ratio of the steel material is considered to be 0.30.

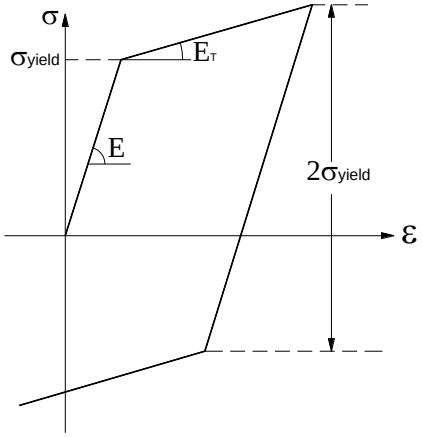

Figure 4.4 Bilinear steel stress-strain curve with Bauschinger effect

4.2.4 Material modelling of the masonry brick units

The modelling approach selected for the concrete is also used to model the masonry units. Therefore, all the details provided for the concrete material modelling in terms of tensile behaviour and failure surface are also applicable to the modelling strategy that was selected for the masonry units. The following nonlinear stress–strain curve from (Angel, 1994) is adopted for the compression stress state of the masonry material:

$$\sigma_m = \frac{27 f_{cm}^{'}\left(250\varepsilon_{crm}-1\right)}{4\varepsilon_{crm}^3}\varepsilon_m^3 + \frac{27 f_{cm}^{'}\left(1-333.33\varepsilon_{crm}\right)}{4\varepsilon_{crm}^2}\varepsilon_m^2 + E_m\varepsilon_m \qquad (4.1)$$

where ε_m and σ_m are the compressive strain and the corresponding compressive stress of the masonry, respectively, $f_{cm}^{'}$ is the maximum compressive strength of the masonry, ε_{crm} is the compressive strain at the onset of failure and E_m is the modulus of elasticity given by:

$$E_m = 750 f_{cm}^{'} \tag{4.2}$$

It is noted that the second derivative of Eq. (4.1) is only negative as long as ε_{crm} is within 0.003~0.0048; otherwise a positive value is obtained which leads to a situation where it is not possible to match the behaviour of the expression with experimental data. For larger values of ε_{crm}, the following expression proposed in (Hendry, 1990) is suggested as an alternative model for the compression stress state of the masonry material:

$$\sigma_m = f_{cm}^{'}\left[2\frac{\varepsilon_m}{\varepsilon_{crm}} - \left(\frac{\varepsilon_m}{\varepsilon_{crm}}\right)^2\right] \tag{4.3}$$

With respect to the tensile behaviour, if experimental data for the tensile strength of the masonry units are unavailable, its value is set as 10% of the compressive strength, as suggested in (Crisafulli, 1997). Based on (Anthoine, 1992), the Poisson ratio for masonry is considered to be 0.19.

4.2.5 Modelling of the interface elements

The surface contact pair elements, termed CONTA174 and TARGE170 in ANSYS, are used to represent the interaction between the masonry units and between the masonry infill and the RC frame. To model the separation and the slip of the contact surfaces, the CZM model is assigned to these contact elements along with a friction material model. Generally, the CZM model involves a constitutive relation between traction stresses acting at the interface, either in shear or in tension, and the corresponding interface slip or separation δ. According to this model, the contact pair is connected until the contact displacement exceeds the maximum separation/slip value δ_{max}, as shown in Figure 4.5 a). Before δ_{max} occurs, the contact elements behave according to one of the considered bilinear CZM models that are used to account for debonding in tension (mode I) and in shear (mode II), Figure 4.5 b) and c), respectively (Alfano*, et al.*, 2001). The bilinear relation between the traction stress and its

corresponding traction distance δ can be defined by the maximum stress and the maximum traction distance or, alternatively, by the maximum traction stress and the corresponding fracture energy (Alfano, *et al.*, 2001). In the current modelling approach, the input parameters that were selected to define the CZM are the maximum normal contact stress σ_{max} and the contact separation at full debonding δ_n^c for mode I, and the maximum equivalent tangential contact stress τ_{max} and the tangential slip at full debonding δ_s^c for mode II. For completeness, Annex C illustrates the different real constants which were defined to control the contact element behaviour.

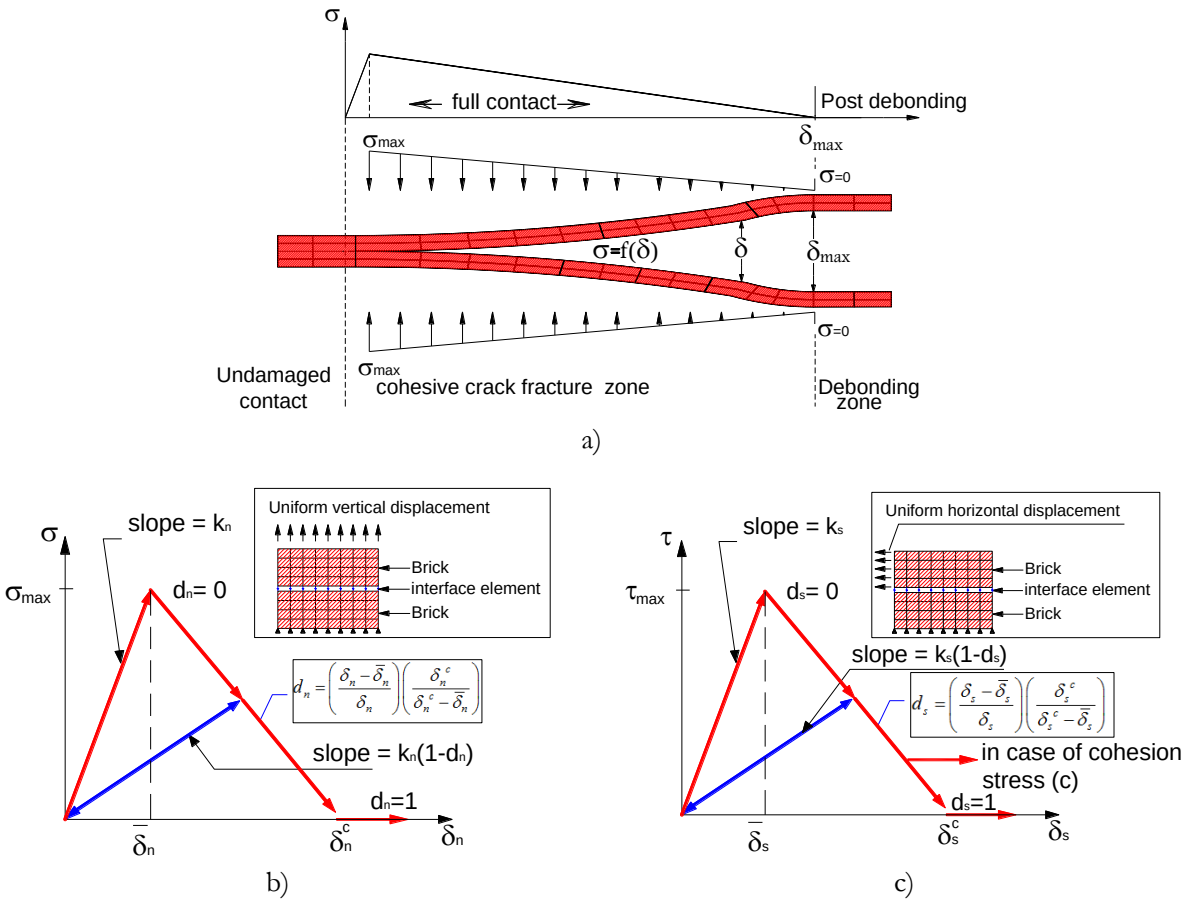

Figure 4.5 a) Definition of the CZM model; b) bilinear definition of the CZM for tensile debonding (mode I) c) bilinear definition of the CZM for shear debonding (mode II)

The tensile debonding parameters were defined in order to represent the tensile behaviour of mortar. As such, the maximum normal contact stress σ_{max} is considered to be equal to the tensile strength of the mortar and the maximum normal contact gap δ_n^c is assumed to be six times the value of $\bar{\delta}_n$, the displacement corresponding to σ_{max} (Induprabha, *et al.*, 2011). For the shear debonding

behaviour, the maximum equivalent tangential contact stress τ_{max} was defined according to available experimental results, while the tangential slip at full debonding δ_s^c was assumed to be within 2~7mm (Lotfi*, et al.*, 1994, Lourenço*, et al.*, 2004). In order to accommodate cases of partial joint filling or inferior quality conditions of the head joints and horizontal joints between the infill panel and the RC beam of the frame, the cohesion stress between the contact pair was ignored for the contact between the masonry and the surrounding RC frame. In addition, the debonding stresses in these joints were also reduced to seventy percent of the value for the bed joints (Mohyeddin*, et al.*, 2013a).

After full debonding, the surface interaction is governed by standard contact constraints for the normal and tangential directions. For normal stresses, these constraints establish that only compression stress is transferred through the contact pair. For the case of tangential stresses, these are transferred according to the classical Coulomb friction law, as shown Figure 4.6 where μ is the friction coefficient. For bed joints, the value of μ is based on available experimental results or considered to be 0.77 otherwise. The value of μ for head joints and between the masonry infills and the surrounding RC frame was defined as sixty percent of the value considered for bed joints to accommodate partial joint filling and the inferior quality conditions of these joints (Mohyeddin*, et al.*, 2013a).

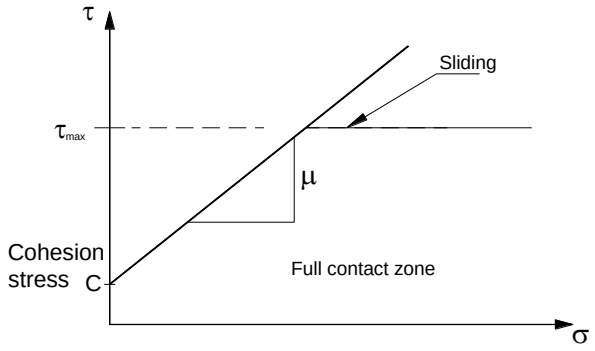

Figure 4.6 Behaviour of the contact element after full debonding according to Coulomb's friction law.

4.3 Experimental data selected for the validation of the proposed modelling approach

A set of specimens from three different experimental campaigns (Pires, 1990, Mehrabi*, et al.*, 1996, Kakaletsis*, et al.*, 2008, Kakaletsis*, et al.*, 2009, Kakaletsis, 2009) were selected to validate the

refined finite element modelling approach. The selected data are those from specimens M1 and M2 from (Pires, 1990) and specimens B, S, DO2, DX1, DX2, WO4, WO3, WO2, WX2 and WX1 from (Kakaletsis*, et al.*, 2008, Kakaletsis*, et al.*, 2009, Kakaletsis, 2009) and Specimen1 and Specimen9 for (Mehrabi*, et al.*, 1996). The latter two specimens were tested under monotonic loading while the rest of the specimens were tested under increasing cyclic lateral loading. The common aspect between these tests is that all specimens were scaled models and are one-bay one-storey frames.

Specimens Specimen1, M1 and B are bare RC frames, specimens Specimen9, M2 and S are fully infilled RC frames, and the remaining specimens (DO2, DX1, DX2, WO4, WO3, WO2, WX2, and WX1) are partially infilled RC frames with various configurations as shown in Figure 4.7 and Table 4.1. The geometric description of the RC frames of specimens Specimen1, M1 and B along with their reinforcement detailing are shown in Figure 4.8. It is noted that the RC frame of the masonry infilled specimens of a given test campaign has a configuration identical to that of the corresponding bare frame. The cyclic lateral displacement loading histories considered in the experimental tests and represented in Figure 4.9. The average mechanical properties of the materials involved in these specimens are summarized in Table 4.2. With respect to these properties, the significant difference between the relative strengths of the brick units and mortar of specimens Specimen9, M2 and S should be noted. Furthermore, it is also noted that the brick units used in the test of specimen M2 were real size (unscaled) brick units.

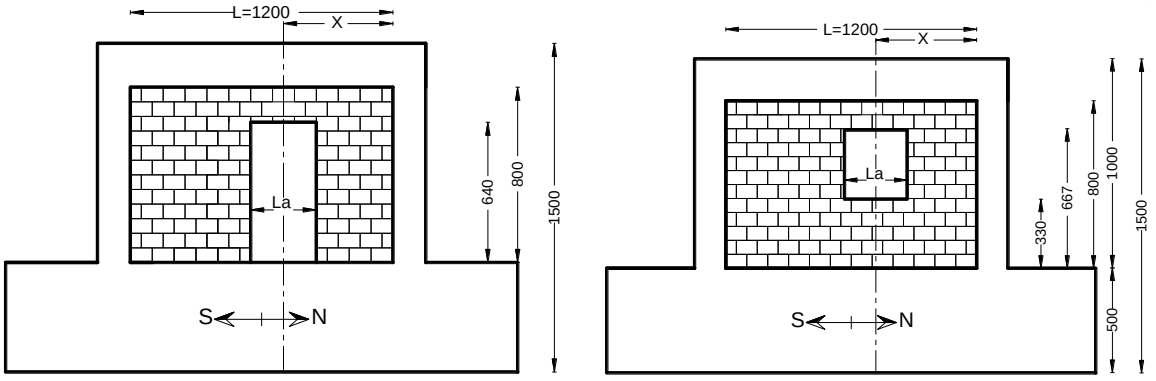

a) b)

Figure 4.7 Description of the partially infilled specimens: a) specimens with door openings; b) specimens with window openings (Kakaletsis*, et al.*, 2008, Kakaletsis*, et al.*, 2009, Kakaletsis, 2009). (All dimensions are in millimetre).

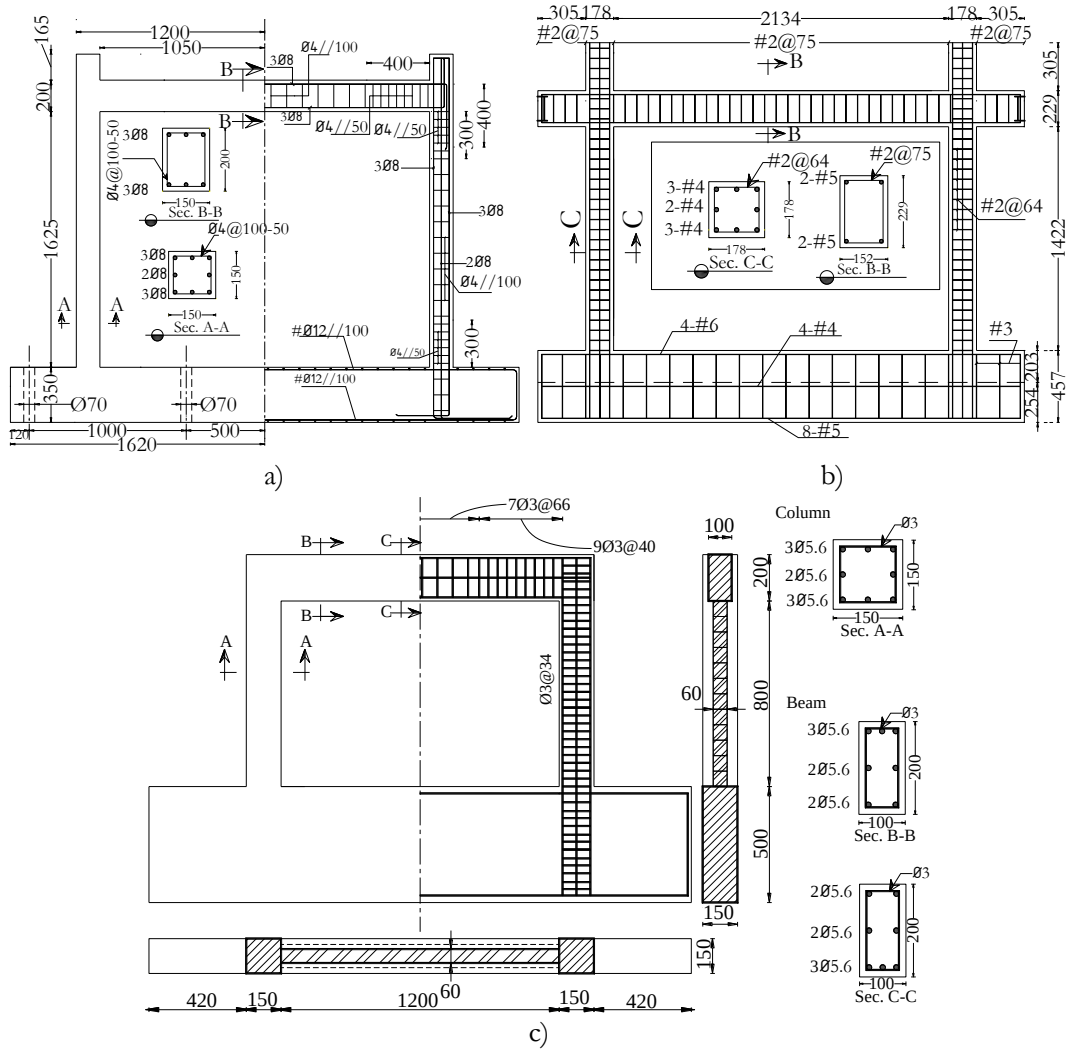

Figure 4.8 Geometry and reinforcement details of the bare frames for three test campaigns: a) M1 (Pires, 1990), b) Specimen1 (Mehrabi*, et al.*, 1996) and c) specimen B (Kakaletsis*, et al.*, 2008, Kakaletsis*, et al.*, 2009, Kakaletsis, 2009) (All dimensions are in millimetre).

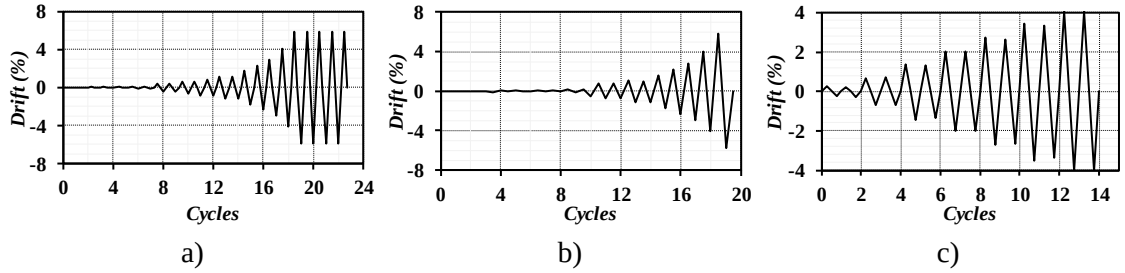

Figure 4.9 Cyclic displacement evolutions defining the loading considered for specimen M1 (a), for specimen M2 (b) and for specimens B, S and all the partially infilled frames (c).

Table 4.1 Characteristics of the test specimens with partially infilled RC frames (Kakaletsis*, et al.*, 2008, Kakaletsis*, et al.*, 2009, Kakaletsis, 2009)

Specimen ID	Specimen description	Opening type		Opening size La/L	Opening location X/L
		Window	Door		
WO2	Centred window	√		0.25	0.50
WO3	Centred window	√		0.375	0.50
WO4	Centred window	√		0.50	0.50
WX1	Non-centred window	√		0.25	0.1667
WX2	Non-centred window	√		0.25	0.3333
DO2	Centred door		√	0.25	0.50
Dx1	Non-centred door		√	0.25	0.1667
Dx2	Non-centred door		√	0.25	0.3333

Table 4.2 Mechanical properties of the materials involved in the experimental specimens

Specimen ID	Concrete		Steel reinforcement			Infill panel		Vertical loading (kN)
	f_c (MPa)	f_t (MPa)	Size (mm)	σ_{yield} (MPa)	$\sigma_{ultimate}$ (MPa)	Brick unit f_m (MPa)	Mortar f_{mo} (MPa)	
M1	(24.6*, 33.1**)[1]	n/a	ϕ8	434.3	519.3	--	--	200
M2	(23.5*, 28.3**)[1]	n/a	ϕ4	522.7	552.3	4.80	6.2*,6.4**	220
Specimen1	30.90	3.29	#4	420.7	622.1	--	--	294
Specimen9	26.80	2.77	#5 #2	413.8 367.6	622.1 449.6	15.59	12.48	294
B[2]	28.5	n/a	ϕ5.6	390.5	516.3	--	--	100
S[2]	28.5	n/a	ϕ3	212.2	321.1	3.10	1.53	100

- f_c is the compressive strength of concrete, f_t is the tensile strength of concrete, σ_{yield} is the steel yield stress and $\sigma_{ultimate}$ is the ultimate strength of steel

[1] cubic strength which was converted to cylinder strength.

[2] the rest of the specimens from this test campaign have the same mechanical properties

* at 28 days, ** when the specimen was tested

- the brick unit used in specimen M2 has dimensions of 200*150*300 mm^3, the dimensions of the brick unit used in specimens from (Kakaletsis*, et al.*, 2008, Kakaletsis*, et al.*, 2009, Kakaletsis, 2009) are 60*60*93 mm^3, and the brick for Specimen 9 are 92*92*164 mm^3

4.4 Validation of the proposed micro-modelling approach.

In this section, the results obtained from the numerical simulations are presented along with the corresponding experimental data. These results are categorized according to the infill conditions of the frame: bare frame specimens, fully infilled frame specimens and partially infilled frames. The results of each category are also presented according to the loading type (i.e. monotonic loading and cyclic loading).

4.4.1 Analysis of the RC bare frames under monotonic loading

To validate the modelling approach selected for the RC members under monotonic loading, the experimental monotonic lateral loading tests carried out for Specimen1 was simulated numerically. As referred, two different modelling approaches were implemented to represent the steel reinforcement: the smeared and the discrete modelling approaches. Both models were developed according to the available experimental data and following the modelling details presented in previous sections. In order to be consistent with the experimental procedures, the analysis of the numerical models started with the analysis for gravity loading, which is equal to a 294 kN load applied on each column of this specimen (the gravity load was applied to the columns only). After completing this analysis, a new analysis procedure starts to submit the structure to imposed lateral displacements (the structure is laterally loaded using displacements rather than forces which is consistent with the experimental procedure).

Figure 4.10 shows a comparison of the load-deflection curves obtained from the numerical analyses along with the experimental data. Lateral displacements are represented in terms of the drift ratio (i.e. lateral displacement normalized by the height of the frame) for a better interpretation of the results. As shown, the initial stiffness is generally overestimated by both numerical models and there are several factors that may contribute to these differences. Mohyeddin*, et al.* (2013a) refers the effect of the failure surface considered in the material model which tends to overestimate the strength in tension–compression stress states (Figure 4.3), i.e. when cracking initiates. Since the initiation of nonlinearity occurs mainly because of cracking instead of crushing, the model shows a stiffer behaviour at the beginning of the analysis. Additionally, the initial cracks due to shrinkage are not considered in the numerical model. Figure 4.10 shows a slightly better match between the model with the discrete steel model and the experimental results. However, since this modelling approach requires more computational effort, the marginally higher accuracy of the discrete steel modelling may not be justifiable to model the specimens subjected to transient or cyclic loading. As such, only the smeared steel modelling approach will be considered in the non-monotonic analyses presented in the following sections.

To complement these results, Figure 4.11 shows the crack patterns obtained from the experimental tests and from the numerical model using both the discrete and smeared steel modelling approaches. As can be seen, the numerical results are generally in good agreement with the experimental data.

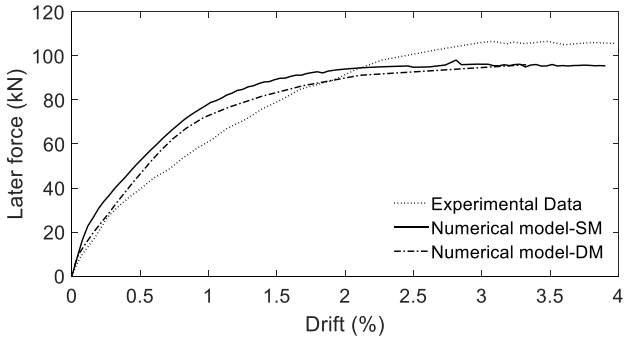

Figure 4.10 Load–deflection curves obtained from the experimental test of Specimen1 and from two numerical models involving different modelling approaches for the steel reinforcement: the smeared model (SM) and the discrete model (DM)

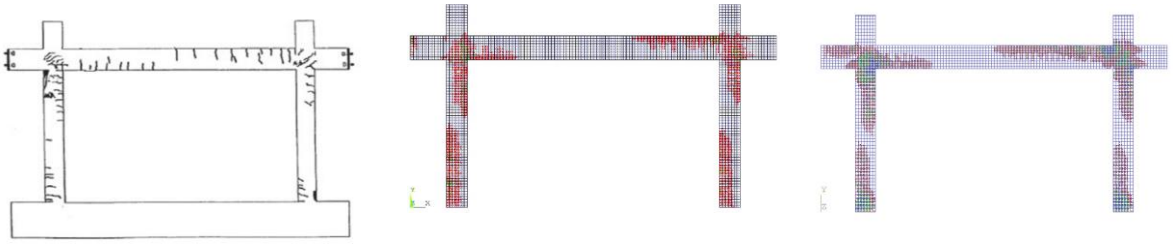

a) b) c)

Figure 4.11 Crack patterns of Specimen1: a) Experimental data b) Numerical data (discrete steel modelling) c) Numerical data (smeared steel modelling)

4.4.2 Analysis of the RC bare frames under cyclic loading

To validate the modelling approach selected for the RC members under cyclic loading, the experimental cyclic lateral loading tests carried out in two bare frame specimens (specimens M1 and B) were simulated numerically. It is noted that the lateral displacement loading histories considered in these simulations (as well as in those presented in the next sections) are not exactly the ones applied in the experimental tests. Due to numerical simplicity issues, regularized versions of the displacement histories were used instead. Before applying the lateral displacement loading history, the experimental vertical loads were applied. To illustrate the performance of the numerical model, Figure 4.12a) and b) compare the experimental lateral load-deflection curves for specimens M1 and B, respectively, with those that were obtained from the numerical analyses. To provide a better analysis of the level of lateral

deflection involved in the tests, this parameter is represented in terms of lateral drifts. Furthermore, to increase the readability of the results, both the full cyclic lateral load-deflection curves and the overall envelope curves are shown for both frames. The results indicate that the numerical models are able to adequately match the experimental cyclic response. However, when the lateral drift exceeds 2.5%, the numerical unloading/reloading branches deviate slightly from the experimental results. These differences are due to the unloading and reloading stiffnesses associated to the model representing the concrete compressive behaviour which is unable to represent cyclic degradation effects, i.e. the unloading and reloading stiffnesses are always equal to the initial stiffness. To complement these results, Figure 4.13 compares the crack patterns of specimen M1 and specimen B obtained from the numerical analyses with those obtained experimentally. It can be seen that the numerical models are able to capture the crack propagation in the columns and the beam for both specimens.

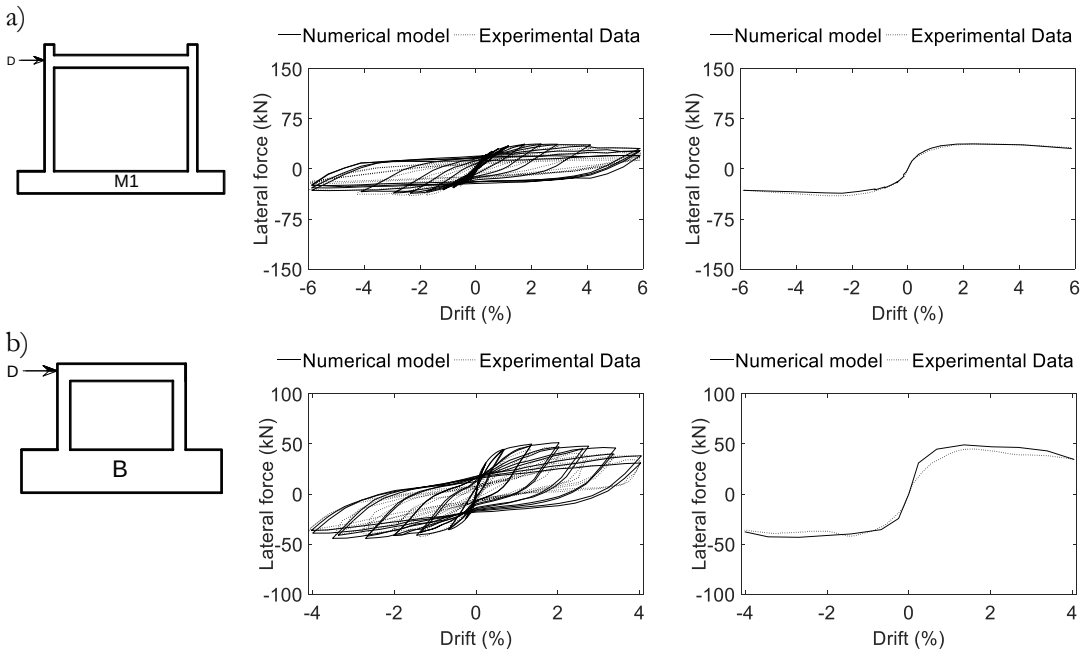

Figure 4.12 Load–deflection curves obtained from the experimental tests and from the numerical models: a) specimen M1; b) specimen B.

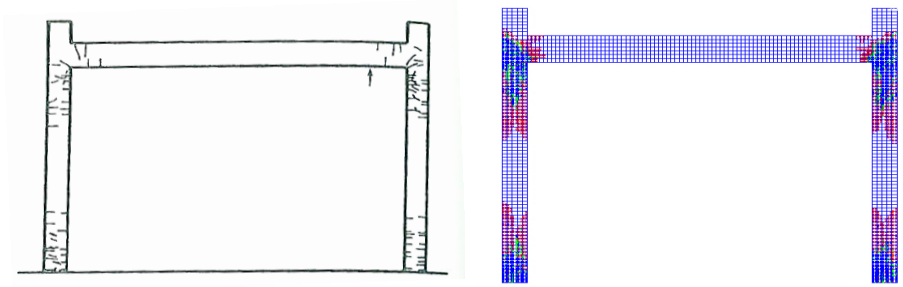

Experimental data *Numerical model*

a) Specimen M1

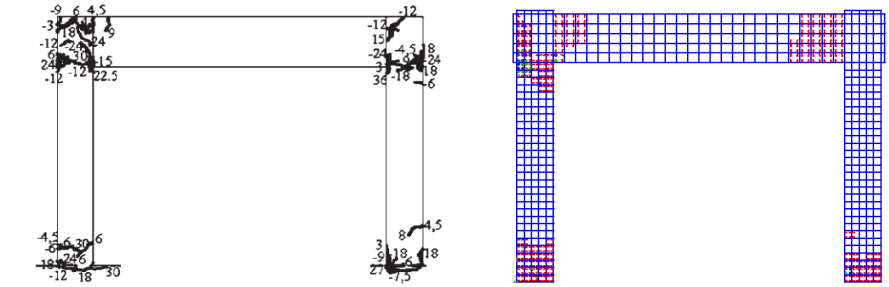

Experimental data *Numerical model*

b) Specimen B

Figure 4.13 Experimental and numerical crack patterns: a) specimen M1; b) specimen B.

4.4.3 Analysis of the RC fully infilled frames under monotonic loading

The RC frame of Specimen 9 was also analysed using both the smeared and the discrete modelling approaches for the steel reinforcement. In order to accommodate partial filling and the inferior quality conditions of the head joints and of the horizontal joints between the infill panel and the RC frame, the coefficient of friction at these joints was assumed to be approximately sixty percent of that of the bed joints. In addition, the debonding stresses in these joints were also reduced to seventy percent of the value for the bed joints. The gravity loading was applied according to the experimental data and the lateral loading was applied as an incremental imposed displacement in agreement with the experimental test.

In order to analyse the adequacy of the finite element models, force-displacement curves obtained from the numerical analyses are plotted against the experimental results as shown in Figure 4.14. It is worth mentioning that this frame was first used in two other experimental tests (one involving cyclic loading), repaired and was then used in the test modelled herein as Specimen 9. As

such, the numerical models are not expected to be able to simulate the true conditions of the Specimen 9 test. Nonetheless, it can be seen that, in general, there is a good agreement between the numerical and the experimental results. Furthermore, the finite element models successfully capture the maximum strength of the physical specimen (the numerical value of the strength is 291 kN while it is 294 kN for the physical specimen). Based on these results, it can be seen that both numerical models are able to adequately reproduce the experimental behaviour. However, the smeared modelling approach proved to be more efficient in term of the computational effort and accuracy.

In order to analyse the contact length between the infill panel and the RC frame, the status of the boundary contact elements is plotted in Figure 4.15 for different drift ratios. Based on these plots, it can be seen that the interaction between the infill panel and the RC frame is inversely proportional to the drift ratio (i.e. smaller contact lengths are found for larger drift ratios). In addition, the RC frame can be seen to lose most of the contact length with the infill panel at a low level of drift, which confirms some of the findings of Chapter 3.

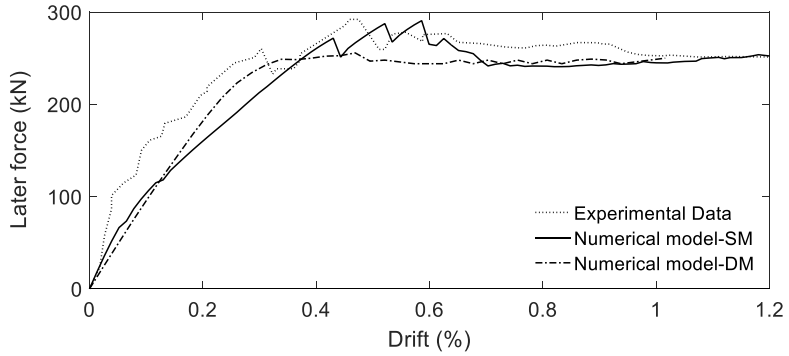

Figure 4.14 Load–deflection curves obtained from the experimental test of Specimen 9 and from two numerical models involving different modelling approaches for the steel reinforcement: the smeared model (SM) and the discrete model (DM)

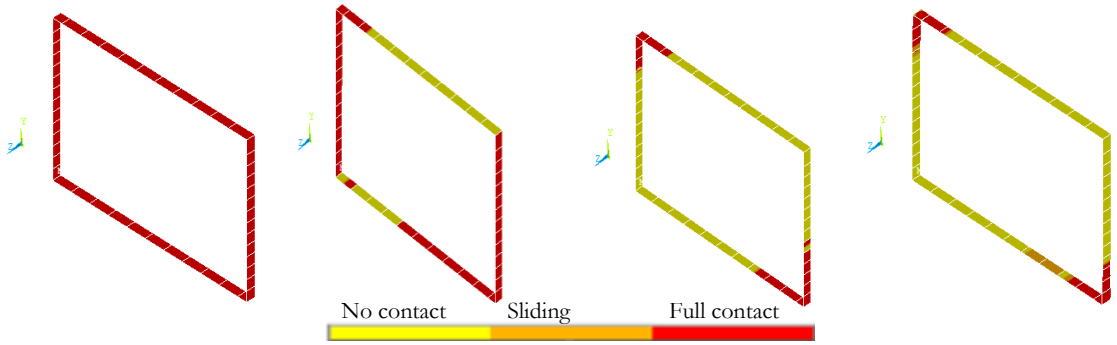

Figure 4.15. The boundary contact status for different drift ratios: a) 0.15%, b) 0.20%, c) 0.30% and, d) 1.40%

4.4.4 Analysis of the RC fully infilled frames under cyclic loading

Two different specimens with fully infilled RC frames were analysed using the referred numerical models for the RC frame and the infill panel. As for the previous analyses, the experimental vertical loads were applied before applying the lateral displacement loading history. To demonstrate the performance of the numerical model, Figure 4.16a) and b) compare the experimental lateral load-deflection curves for specimens S and M2, respectively, with those that were obtained from the numerical analyses. As for the previous analyses, the lateral deflection is represented in terms of drift ratios and both the full cyclic lateral load-deflection curves and the overall envelope curves are shown for both frames. The figures show a reasonable agreement between experimental results and those obtained from the developed refined modelling approach, particularly in terms of the global behaviour (stiffness and strength). However, as for the bare frames, the unloading/reloading stiffness of the numerical results deviates from the experimental one for larger drifts (i.e. when it exceeds a drift around 2.5%) which is due to the factors referred in the previous section. The larger differences found between the numerical and experimental behaviour of specimen M2 are assigned to an experimental factor that was not able to be accounted for in the numerical model. During the experimental test, a horizontal crack was developed between the 5^{th} and 6^{th} masonry courses for a lateral drift of 0.14% (a low level of drift) (Pires, 1990). The development of this crack and the subsequent debonding of the interface changed the load transfer mechanism of the infill panel and delayed the post-peak strength degradation of the infill due to crack propagation effects. It is assumed that this occurred in the physical specimen due to a lower quality of the mortar between the referred masonry courses. This weaker mortar layer and its post-failure frictional behaviour were not accounted for in the numerical modelling since no data was available (e.g. the strength of that weaker mortar) to represent that experimental behaviour. Furthermore, simulating this experimental test under these conditions emphasizes the performance of the numerical model when unforeseen material conditions are found.

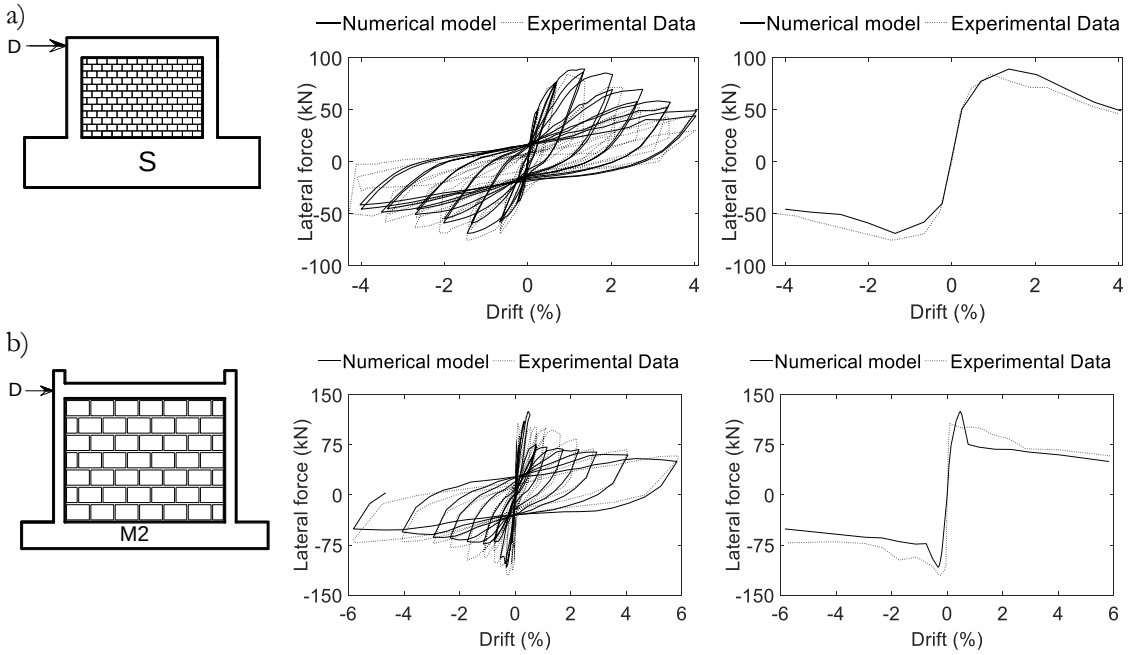

Figure 4.16 Load–deflection curves obtained from the experimental tests and from the numerical models: a) specimen S b) specimen M2.

In order to summarize these results, Table 4.3 presents the absolute errors recorded between the numerical models and the experimental data in terms of the maximum lateral force and the maximum vertical difference between the two curves (i.e. maximum difference in terms of lateral force between the numerical and experimental results).

Given these results, the proposed modelling approach is seen to provide a useful alternative to experimental tests since it is able to capture adequately the global behaviour envelope in terms of strength and stiffness. Additionally, this type of analysis also provides important information regarding the contact length between the infill panel and the RC frame (Figure 4.17), which can be used to calibrate the parameters of an equivalent diagonal strut model. As can be seen from Figure 4.17, the evolution of the interaction between the infill panel and the RC frame confirms what was found for the monotonic test analyses (i.e. the contact length is inversely proportional to the drift ratio). Furthermore, as referred for the monotonically tested specimen, the RC frame loses most of the contact length with the infill panel for low levels of drift.

Table 4.3 Lateral force differences between experimental and numerical results for the fully infilled specimens

Specimen	Difference in the numerical maximum lateral force with respect to the corresponding experimental lateral force (%)	Maximum difference in the numerical lateral force with respect to the corresponding experimental lateral force (%)
S	5.6	15.8
M2	14.4	38.6

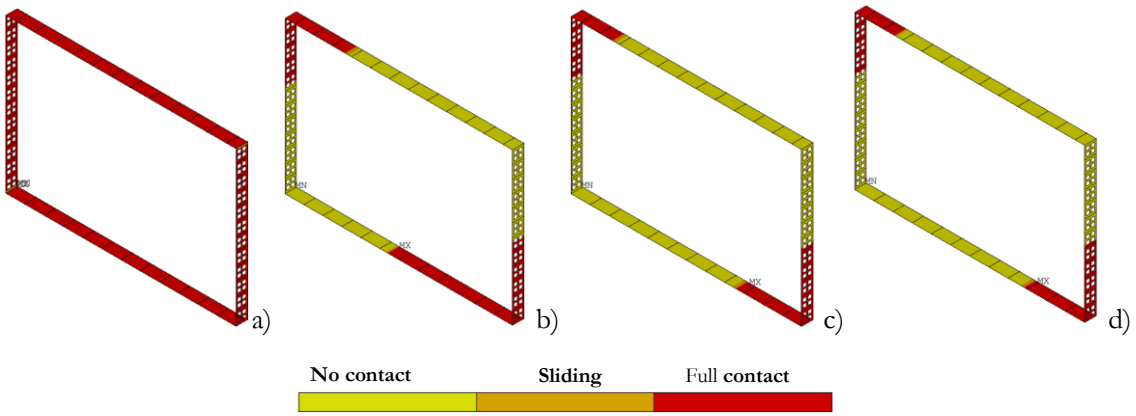

Figure 4.17 The boundary contact status for specimen S for different levels of the drift ratio: a) 0.01%, b) 0.10%, c) 0.20% and d) 0.40%.

4.4.5 Analysis of the RC infilled frames with openings

Eight experimental tests on specimens with partially infilled RC frames were simulated using the proposed numerical modelling strategy: three models with a door opening (the door is always the same size but at different locations), and five models with a window opening (the window changes in size and location). To analyse the performance of the numerical model, Figure 4.18 and Figure 4.19 compare the experimental and numerical lateral load-deflection curves of the specimens. As for the previous cases, the lateral deflection is represented in terms of drifts and both the full cyclic lateral load-deflection curves and the overall envelope curves are shown. As for the previous cases, the results indicate there is a good agreement between the experimental and the numerical behaviour curves, namely in terms of the global envelope representing the strength and stiffness evolution. Furthermore, the differences between the fully infilled frames (Figure 4.16) and the partially infilled frames in terms of lateral stiffness and maximum strength is also clearly captured by the proposed numerical modelling

approach. Still, differences between the unloading and reloading stiffnesses of the numerical and experimental results are also noticeable as a result of factors previously referred. As for the previous case, Table 4.4 summarizes the results by presenting the absolute errors recorded between the numerical models and the experimental data in terms of the maximum lateral force and the maximum vertical difference between the two curves (i.e. maximum difference in terms of lateral force between the numerical and experimental results).

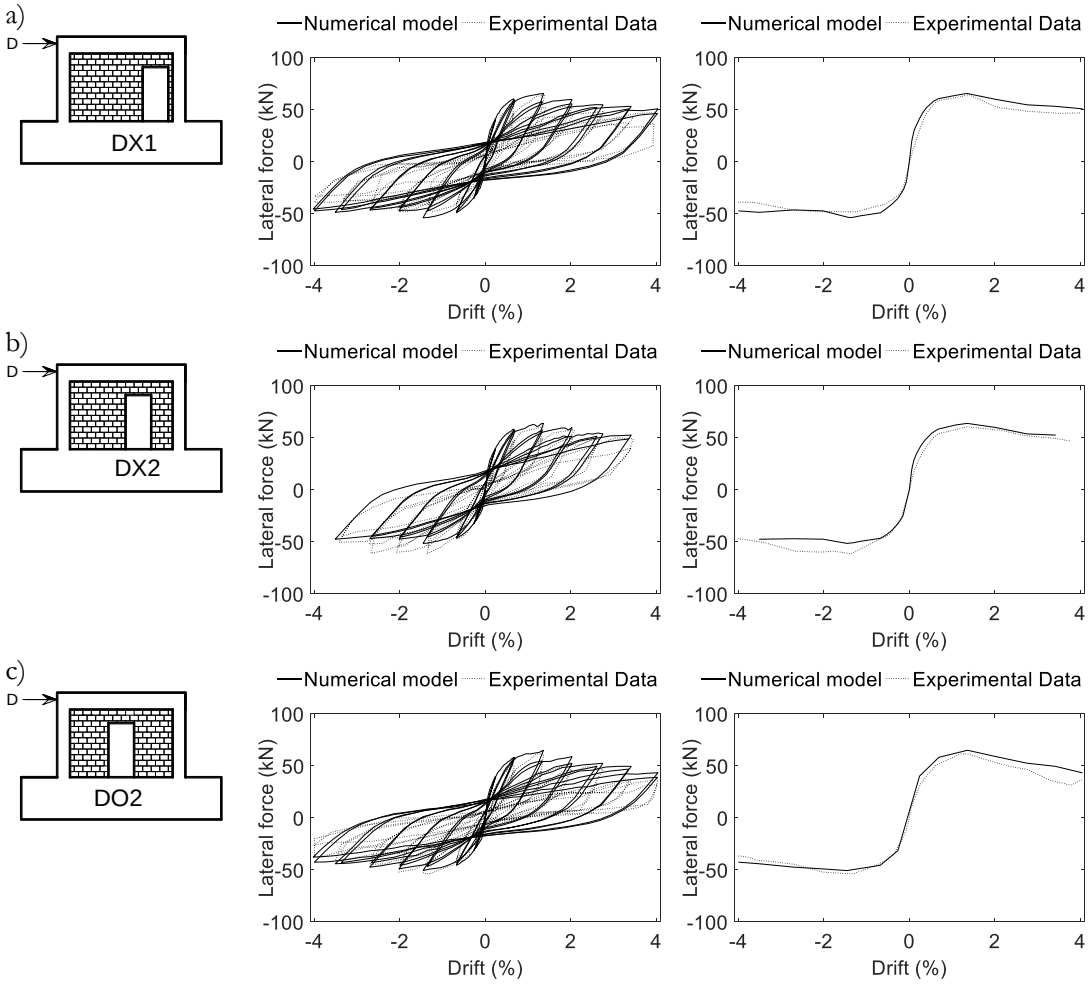

Figure 4.18 Load–deflection curves obtained from the numerical models along with the experimental data: a) specimen DX1, b) specimen DX2, c) specimen DO2.

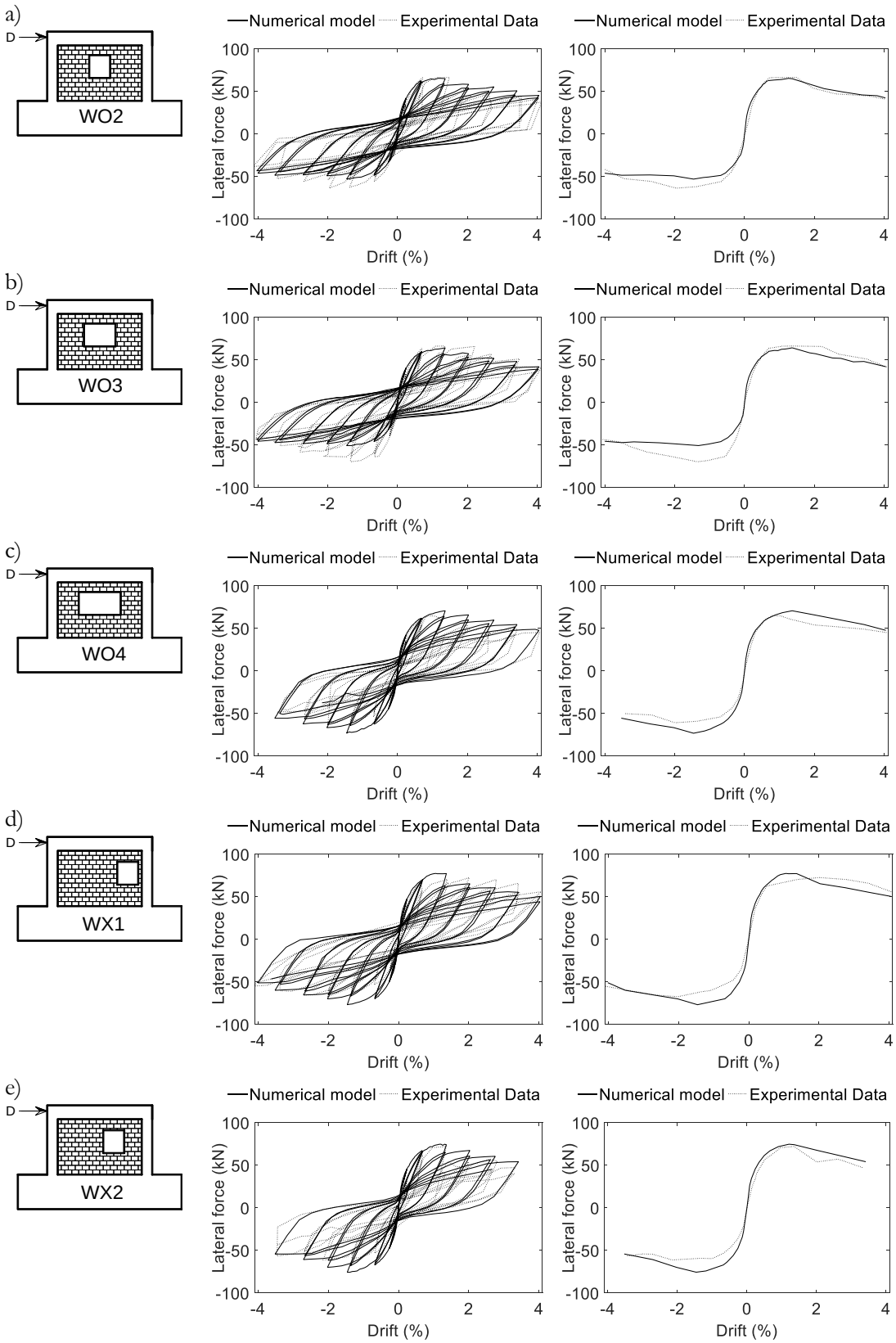

Figure 4.19 Load–deflection curves obtained from the numerical models along with the experimental data: a) specimen WO2, b) specimen WO3, c) specimen WO4, d) specimen WX1 and e) specimen WX2.

Table 4.4 Lateral force differences between experimental and numerical results for the partially infilled specimens

Specimen	Difference in the numerical maximum lateral force with respect to the corresponding experimental lateral force (%)	Maximum difference in the numerical lateral force with respect to the corresponding experimental lateral force (%)
DO2	5.2	23.7
DX1	2.1	21.8
DX2	5.3	18.9
WO2	1.7	21.2
WO3	3.5	15.2
WO4	8.0	18.0
WX1	6.2	15.7
WX2	3.5	18.8

4.5 Conclusion

In cases where experimental data are not available and experimental tests are unable to be carried out, numerical simulations using refined finite element modelling (also known as micro-models) capable of representing the behaviour of RC masonry-infilled structures can be used as a proxy for the experimental testing. In this context, a refined modelling approach was developed in the software ANSYS to simulate the behaviour of RC masonry-infilled frames under in-plane monotonic or cyclic loading with adequate accuracy and an affordable computational effort. To test the reliability of the proposed modelling strategy, several examples of RC infilled frames with different infill configurations subjected to cyclic loading were analysed.

The results show that the refined modelling approach is able to represent the behaviour of masonry infilled RC frames adequately and can be used to simulate this type of structural system using only the essential mechanical properties of the materials involved (i.e. without the need to test an entire specimen). This conclusion is supported by the ability of the model to adequately account for the more common masonry failure mechanisms, as well as to represent the strength and stiffness envelopes with a reasonable accuracy when compared to experimental results. The numerical results that were obtained also indicate there is no clear increase in their accuracy when modelling the longitudinal reinforcement of RC members using a discrete steel modelling approach. Given the significant computational effort required by this approach, the use of a smeared steel modelling approach is recommended instead.

Based on these facts, the refined model can be used as a powerful alternative for the experimental data needed to estimate the parameters of simplified models such as those based on strut elements, therefore overcoming the limitations identified in the approaches analysed in the previous chapter. The following chapter will then present a procedure to estimate the parameters of simplified models which will be tested and it performance will be analysed using both experimental and numerical data.

Chapter 5.
Calibration procedures to establish the parameters of infill macro models

5.1 Introduction

Macro-models, namely the single strut element, have been found to be reliable tools to represent the structural contribution of an infill panel. However, as discussed in Chapter 3, using existing and uncalibrated empirical proposals (such as the stiffness-based and strength-based procedures that were analysed) can lead to large errors in predicting the behaviour of infilled reinforced concrete (RC) frames. Therefore, the characteristics and parameters of these models need to be defined using robust data to ensure the reliable simulation of the real behaviour of the infill. Still, assuming that such data is available (e.g. from experimental data or results obtained by refined finite element simulations), specific procedures need to be developed to establish the parameters of macro-models. In this context, the present chapter proposes calibration procedures for the parameters of macro models. The procedures are first presented for single strut models, followed then by their application for multi-strut systems and for another macro-model with a special configuration.

The overarching objective behind the calibration procedures proposed for the single strut element is to obtain a reliable representation of the in-plane infill panel behaviour. This behaviour can then be further enhanced to introduce other structural aspects (e.g. the action of infills on the surrounding RC columns which can be modelled by dividing the single strut into multiple struts or by using a macro model with a different configuration) as presented later in this chapter. Furthermore,

establishing a reliable strut model can then be also associated with other elements or modelling features to account for more complex phenomena such as the out-of-plane response of the infill.

The proposed calibration procedures were defined based on experimental data representing the behaviour of the bare and of the fully infilled RC frames. The calibration procedures involve extracting the behaviour of the infill panel from the global behaviour by subtracting the contribution of the bare frame from the response of the fully infilled frame. The extracted response was then used to develop calibration procedures associated to both stiffness- and strength-based approaches. To simulate a scenario where experimental data is unavailable, the calibration procedures were also applied for the data obtained from the refined finite element models presented in the previous chapter. In order to validate the calibration procedures for different macro model configurations, the calibrated responses of the single strut model were implemented with multi-strut models (with two and three struts) and with the model proposed by Rodrigues*, et al.* (2010). Finally, the reliability of the global and local demand results obtained by different macro models was also compared with the results obtained from the refined finite element model.

5.2 Basis of the calibration procedure: extracting the force-displacement response of the infill

The behaviour of the infill panel, as part of a system that involves the surrounding frame, is different from the behaviour that would be obtained by testing the infill panel only. Since the surrounding RC frame confines the infill, it enhances its ability to transfer loads. Therefore, the infill response data that is used to establish the macro-model behaviour must account for this effect. In light of this, the main concept of the proposed calibration procedures is to consider that the infilled RC frame structure can be represented as a two-component parallel system, as shown in Figure 5.1. The fundamental features of the behaviour of this parallel system can be represented by:

$$K = k_1 + k_2 \tag{5.1}$$

$$F = f_1 + f_2 \tag{5.2}$$

where F and K are the global force and stiffness of the entire system, respectively, f_1 and k_1 are the force and stiffness of the RC frame, respectively, and f_2 and k_2 are the force and stiffness of the infill panel.

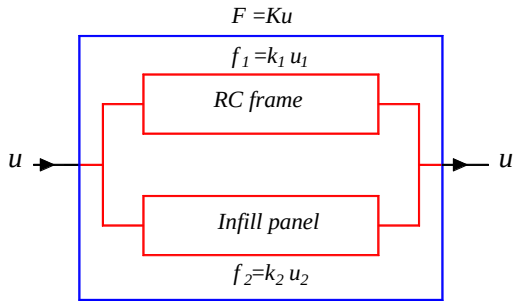

Figure 5.1 Representation of the infilled RC frame as a two-component parallel system

Based on this system behaviour, the infill force component can be computed by subtracting the bare frame response from the response of the fully infilled specimen, as illustrated in Figure 5.2. To then get the force-displacement response for the equivalent diagonal strut element, the force and displacement components need to be projected onto the diagonal direction of the strut as represented in Figure 5.3 using the following expressions:

$$u_{diagonal} = u\cos\theta \tag{5.3}$$

$$f_{diagonal} = f_2/\cos\theta \tag{5.4}$$

where θ is the inclination angle of the diagonal strut with respect to the horizontal plane (Figure 5.3). Given that the maximum strength of the infill always occurs for a low level of loading, for which the RC components are mostly expected to exhibit linear behaviour (e.g. see Figure 3.22), the process of extracting the masonry component of the response is applicable for this range of the response. Furthermore, this process also provides the most important parameters for characterizing the behaviour of the diagonal strut (i.e. the maximum strength and the initial stiffness). However, the process assumes that the influence of the (nonlinear) interaction between the infill and the RC frame in the post-peak behaviour of the masonry will not be crucial. It is also worth noting that this process assumes the RC frame components of both the bare and fully infilled specimens exhibit mostly flexural behaviour.

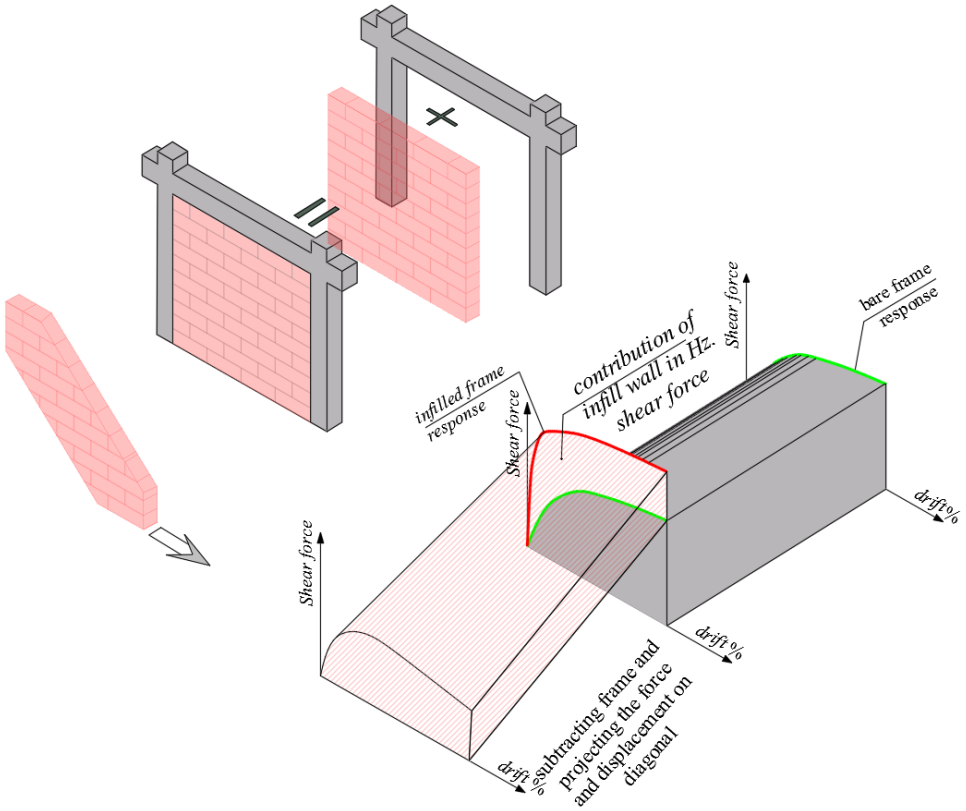

Figure 5.2 Procedure to extract the force displacement response of the infill wall

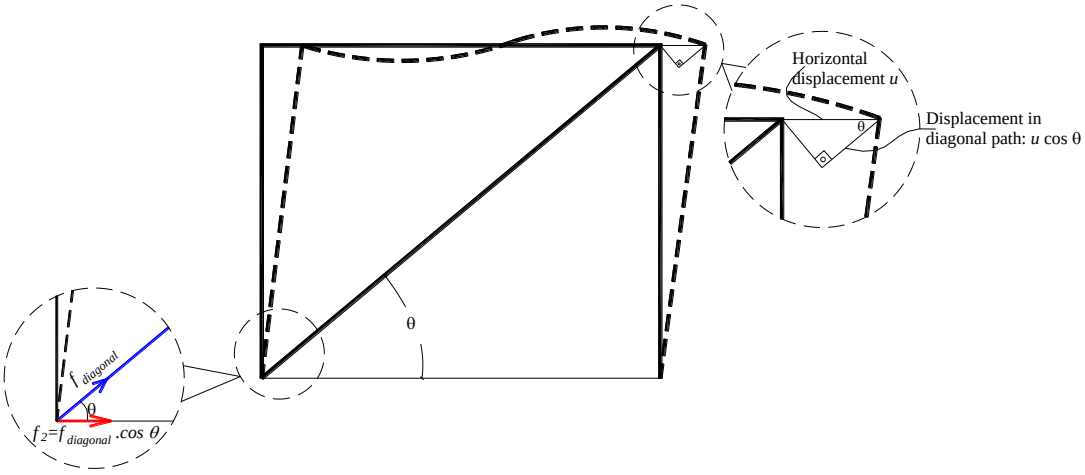

Figure 5.3 Derivation of the diagonal component of the horizontal displacement.

As presented in Chapter 3, several expressions from stiffness-based procedures (e.g. see (Holmes, 1961, Moghaddam, *et al.*, 1988, Paulay, *et al.*, 1992)) assume that infill panels have a unique behaviour, regardless of the characteristics of the surrounding frame. In order to analyse this

hypothesis, the proposed extraction procedure was applied to obtain the response of an infill panel with different surrounding frames. Nine RC frames with different configurations but with the same aspect ratio were analysed using ANSYS considering the modelling strategy presented in Chapter 4. Each model was analysed with two different types of masonry infill: a Type 1 masonry (with a compressive strength equal to 2.1 MPa) and a Type 2 masonry (with a compressive strength equal to 3.1 MPa). Figure 5.4 presents the model archetype for these nine frames while the detail of the sections and reinforcements are provided in Table 5.1. Each analysis started first with the vertical loading which was imposed as a displacement to maintain the same level of confinement of the infill for all specimens. A lateral monotonic loading was then imposed until a 1.2% lateral drift was reached.

The results obtained from the numerical models of the bare frames specimens are plotted in Figure 5.5, normalized to the lateral strength of frame 1 (F1). As shown in Figure 5.5, the normalized lateral strength of the bare frame varies from 0.75 to 1.75. After analysing the fully infilled specimens with the two types of masonry, the referred procedure to obtain the diagonal forces of the infill was implemented. The obtained masonry infill responses are plotted in Figure 5.6, normalized to the response of the fully infilled frame with the bare frame 1 (F1). As shown in Figure 5.6, the response curves of both masonry types exhibit some deviations before reaching the maximum strength of the infill, mostly because nonlinear behaviour is triggered at different steps in each model. After the peak strength is reached, the response curves of both types of masonry exhibit larger deviations which are believed to be the result of the differences in the relative stiffness of all the considered RC frames. Based on these results, it can be concluded that the response of the infill panel is correlated with the characteristics of the surrounding frame. Therefore, the proposed calibration procedures should be implemented using the RC frame that reflects the true boundary conditions of the infill panel in order to get realistic results.

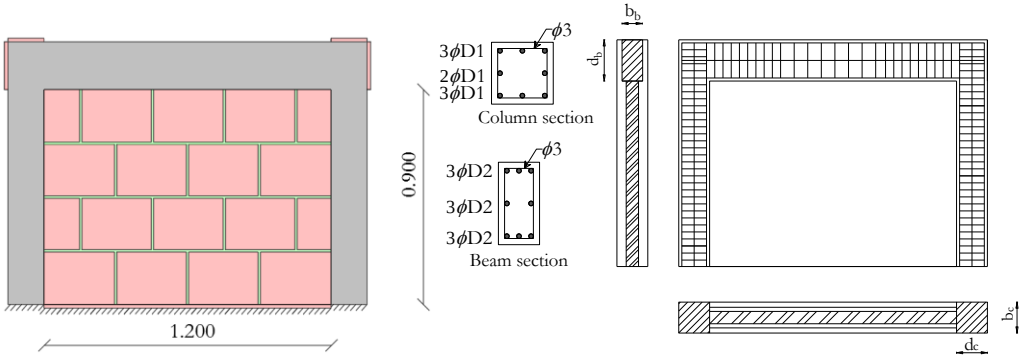

a) Geometry of the model b) Reinforcement details

Figure 5.4 The model frame used to study the confinement effect of the infill response

Table 5.1 Bare frame configurations

Frame no.	Column properties				Beam properties			
	Width d_b(m)	Depth d_c (m)	Main reinforcing steel		Width (m)	Depth (m)	Main reinforcing steel	
			No of rebar	D_1 (mm)			No of rebar	D_2 (mm)
F_1	0.15	0.15	8	5.6	0.10	0.20	8	5.6
F_2	0.15	0.15	8	4	0.10	0.20	8	4
F_3	0.15	0.15	8	3	0.10	0.20	8	3
F_4	0.15	0.17	8	5.6	0.10	0.20	8	5.6
F_5	0.15	0.20	8	5.6	0.10	0.20	8	5.6
F_6	0.15	0.20	8	5.6	0.15	0.20	8	5.6
F_7	0.15	0.15	8	5.6	0.15	0.20	8	5.6
F_8	0.15	0.17	8	5.6	0.15	0.20	8	5.6
F_9	0.15	0.22	8	5.6	0.10	0.20	8	5.6

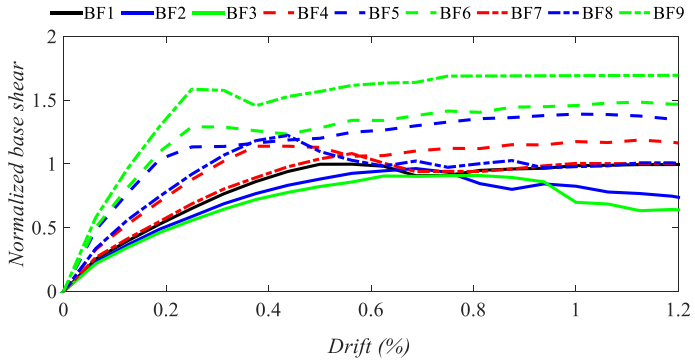

Figure 5.5 Normalized shear force-lateral drift curves obtained from the different bare frames

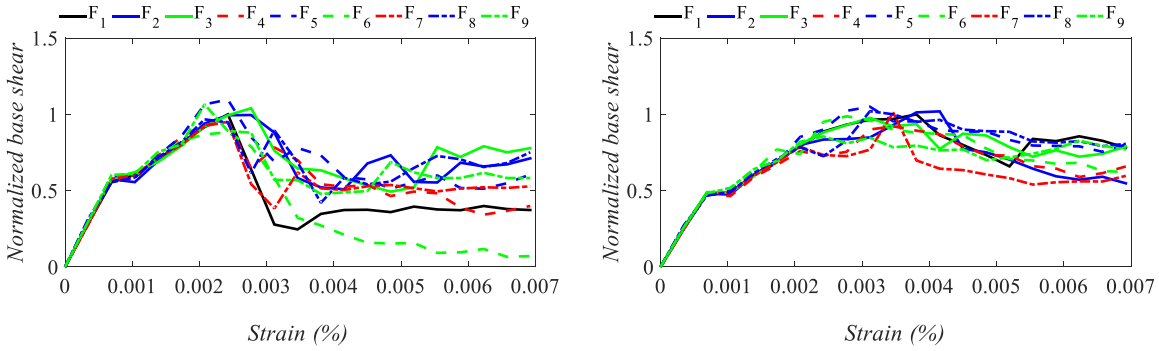

a) Type 1 b) Type 2

Figure 5.6 Normalized force-strain curves of the fully infilled specimens considering different bare frames: a) masonry Type 1 b) masonry Type 2

5.3 Calibration procedures for single strut models based on experimental data

Calibration procedures defining the characteristics of single strut models representing the infill are presented herein using two approaches: a stiffness-based approach and a strength-based approach. The performance of the strut models defined from the calibration procedures is then tested for sixteen fully infilled RC frame specimens from ten different experimental campaigns and for eight partially infilled RC frame specimens from the test campaign performed by (Kakaletsis*, et al.*, 2008).

5.3.1 Calibration procedure for the stiffness-based approach

After obtaining the diagonal force-displacement curve representing the masonry component of the infilled frame behaviour, the calibration procedure for the stiffness-based approach is carried out according to the diagram of Figure 5.7. As can be seen, the force-displacement relation is transformed into a stress-strain relation using the area corresponding to the cross-section of the strut and the length of the strut. In order to maintain the stress levels in the infill panel within a realistic range, the area of the cross-section of the strut is defined by dividing the maximum force by the masonry compressive strength. After reaching the peak stress, the stress-strain relation degrades until the stress level reaches a residual stress defined by the minimum value between the last force value of the extracted masonry response and 60% of the maximum force. It is noted that the proposed procedure does not simulate a reduction in the cross-section area of the strut element to overcome the limitations highlighted in Chapter 3 regarding the usual way this approach is used. Instead, the proposed approach uses a constitutive model that accounts for stress degradation to simulate a similar overall effect. It is noted that by using this calibration procedure, no specific expression or process needs to be considered to determine the panel thickness or the strut width. Furthermore, since the procedure starts by defining the response contribution of the infill from the global response of the structure, the same procedure can be applied for fully and partially infilled frames. Therefore, the use of reduction factors to account for the existence of openings is not necessary.

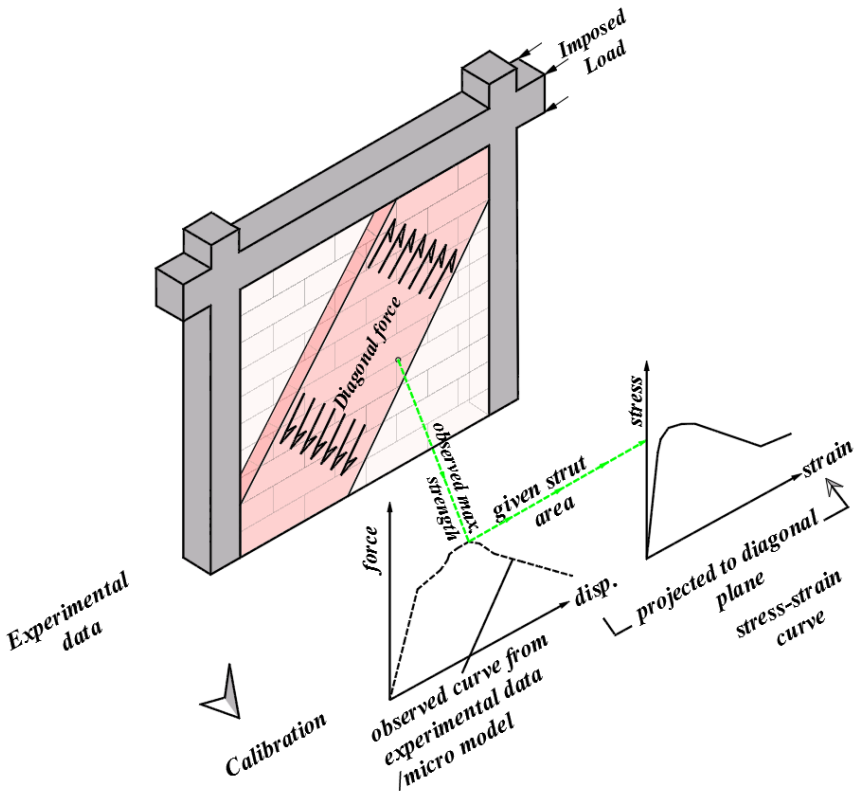

Figure 5.7 Calibration procedures for strut element using stiffness approach.

5.3.1.1 Performance of the calibration procedure for the stiffness-based approach: experimental data on fully infilled specimens

The performance of the proposed calibration procedure was analysed using the experimental data from the sixteen fully infilled specimens also considered in previous chapters (see Table 3.1 and Annex A). The force-displacement response components of the sixteen infills that were extracted according to the previously referred procedure from the corresponding experimental data are presented in Figure 5.8. As referred in Chapter 3, these response curves were obtained from the positive response of the experimental data. As also referred in Chapter 3, for experimental campaigns that did not perform a test on the corresponding bare frame, the capacity curve of the bare frame was obtained numerically. Table 5.2 presents the essential data of these response curves needed to define the stress-strain relation representing the constitutive material model that will be assigned to the strut element. This table presents the values of the maximum diagonal force F_{max}, the residual force F_{res} and

their corresponding computed strains (i.e. the displacement projected over the diagonal length of the infill panel divided by the length of the diagonal) ε_m and ε_{res}, respectively. It is noted that the strain corresponding to the maximum strength ranges from 0.05% to 0.48%, that the residual force of the infills ranges from 5% to 60% of the maximum strength and that the ultimate strain of the infill ranges from 0.90% to 2.50%. Furthermore, as an illustrative value, Table 5.2 presents the estimated *w/d* ratios. As can be seen, these ratios have a wide spread and vary from 0.01 to 0.76, which implies that there is no single ratio defining the relation between the strut width and its diagonal length.

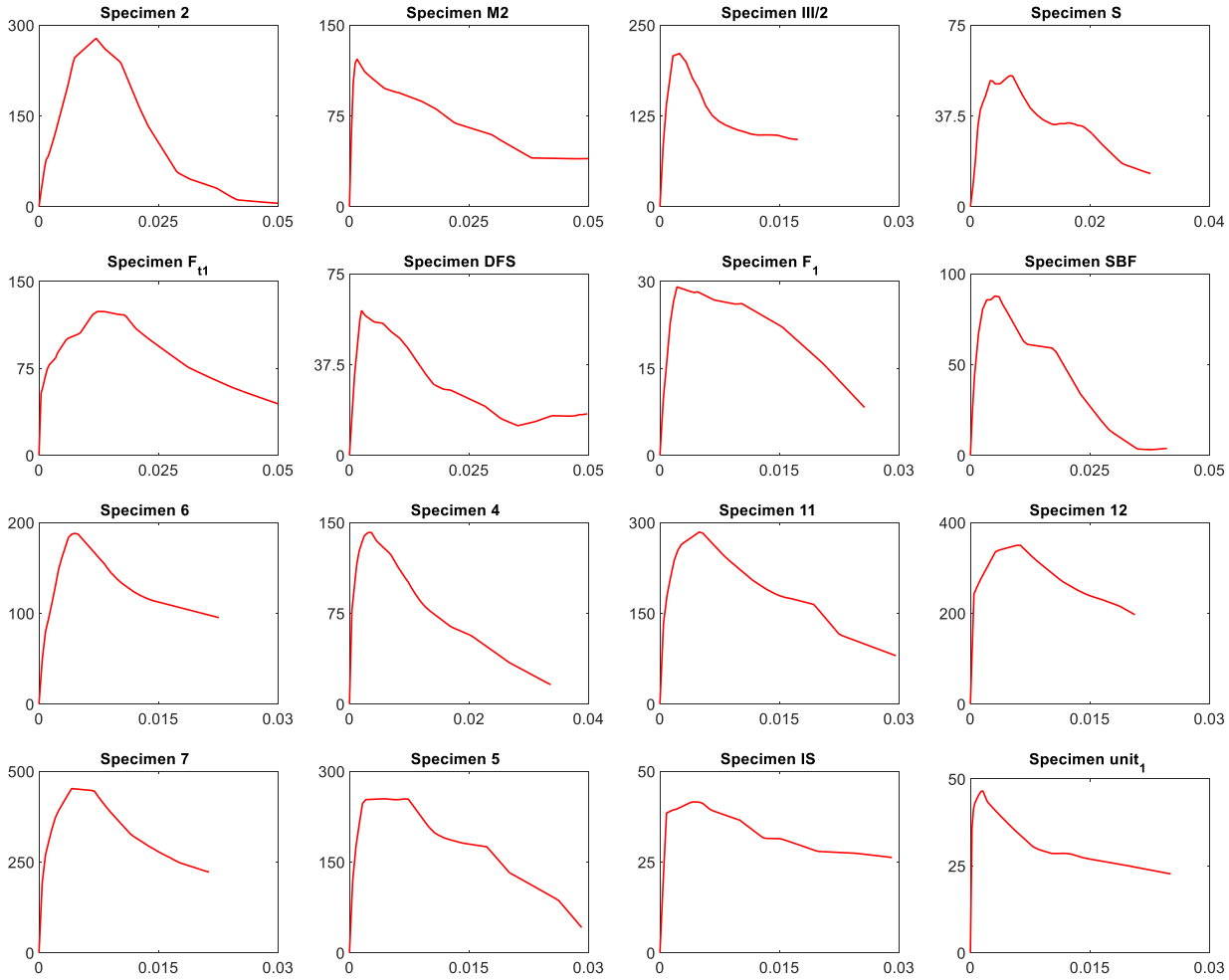

Figure 5.8 Extracted force-displacement response of the infill based on experimental data for the sixteen specimens (vertical axes are lateral forces (kN) and horizontal axes are displacements (m))

Table 5.2 Essential parameters extracted from the experimental data needed for the strut material model

Specimen ID	F_{max}*	F_{res}**	F_{res}/F_{max}	w/d	ε_m^	ε_{res}^^
S.2 (Zhai, *et al.*, 2016)	278.00	13.90	5.00	0.29	0.0028	0.012
S. M2 (Pires, 1990)	121.836	33.63	27.60	0.33	0.0006	0.018
S.III/2 (Sigmund, *et al.*, 2013)	210.77	92.45	43.86	0.76	0.0010	0.012
S. S (Kakaletsis, *et al.*, 2009)	54.08	13.54	25.04	0.23	0.0034	0.025
S. FT1 (Bergami, 2007)	124.08	42.61	34.34	0.28	0.0044	0.018
S. DFS (Basha, *et al.*, 2016)	59.80	17.20	28.76	0.06	0.0011	0.022
S.F1 (Stylianidis, 2012)	16.30	8.34	51.16	0.05	0.0048	0.016
S.SBF(Misir, 2015)	87.71	3.70	4.22	0.06	0.0019	0.020
S. 6 (Mehrabi, *et al.*, 1996)	188.03	95.20	50.63	0.18	0.0016	0.011
S. 11(Mehrabi, *et al.*, 1996)	141.85	16.00	11.28	0.13	0.0012	0.014
S.12(Mehrabi, *et al.*, 1996)	284.17	79.90	28.12	0.08	0.0014	0.009
S. 7(Mehrabi, *et al.*, 1996)	349.82	196.80	56.26	0.08	0.0017	0.009
S. 4 (Mehrabi, *et al.*, 1996)	452.24	222.40	49.18	0.13	0.0015	0.011
S. 5 (Mehrabi, *et al.*, 1996)	254.38	41.80	16.43	0.07	0.0016	0.011
S. IS (Kakaletsis, *et al.*, 2009)	41.56	24.50	58.95	0.04	0.0026	0.019
S. unit1 (Crisafulli, 1997)	46.51	22.70	48.81	0.01	0.0005	0.009
Minimum			**5.0%**	**1.0 %**	**0.05%**	**0.90%**
Maximum			**58.95%**	**76.0%**	**0.48%**	**2.50%**

* Maximum lateral force
** Considered residual lateral force
^ Strain at maximum strength
^^ Strain at residual force

In order to assess the reliability of the calibration procedures, the numerical simulation of the experimental tests corresponding to the selected sixteen specimens was performed using the software OpenSees (McKenna, *et al.*, 2000). The RC frame elements (i.e. beams and columns) were modelled using force-based elements considering fibre-sections. The Modified Radau Hinge Integration method (Fenves, *et al.*, 2006, Scott, *et al.*, 2013) is the selected plastic hinge integration method to assign inelastic actions at the end regions of the element with a specified length. Still, additional fibre sections were also considered in the central part of the element to model its possible nonlinearity since recent modifications in this element (Scott, *et al.*, 2013) allow plasticity to be extended beyond the length of the plastic hinges. A total of six integration points are used in the element state determination (two for each hinge and two for the central part of the element). In order to establish the value of the plastic hinge length, the following expression proposed by Paulay, *et al.* (1992) was used to define the plastic hinge length l_p:

$$l_p = 0.08 l_e + 0.022 d_b f_y \tag{5.5}$$

where l_e is the element length, d_p is the diameter of the steel rebars and f_y is the steel yield stress in MPa.

As referred, the RC cross sections were modelled using a fibre discretization. The concrete cover was modelled using the concrete model termed Concrete01 in OpenSees representing the uniaxial concrete material with degraded linear unloading/reloading stiffness in compression and no tensile strength. Confined concrete was modelled using a confinement factor determined based on the expression proposed by Kent, *et al.* (1971) associated with the Concrete02 model. The Concrete02 concrete model is similar to the Concrete01 but considers the tensile strength of the concrete. This tensile strength was defined according to experimental data, when available, and based on the following expression (ACI 318-14, 2014) otherwise:

$$f_t = 0.623\sqrt{f_c} \tag{5.6}$$

where f_c is the compressive strength of the concrete. Steel reinforcing bars were modelled using the uniaxial Giuffre-Menegotto-Pinto model (Menegotto*, et al.*, 1973) with isotropic hardening, termed Steel02 in OpenSees, with the default parameters proposed by the software. For the beam-column joints, a rigid end-offset joint model was used (Mondal, *et al.*, 2008). The lengths of the rigid parts were considered to be half of the depth of the perpendicular element.

The infills were modelled using a single compressive strut element with an area established based on the extracted maximum lateral force and on the masonry compressive strength in order to keep the infill stress levels lower than the masonry compressive strength. In order to define the constitutive material model of the strut, the computed area was associated with the maximum diagonal strength. The parameters obtained from this procedure (i.e. the maximum stress, the residual stress and their corresponding strains) were used to define the masonry material with zero tensile strength simulated by the Concrete01 constitutive model. Figure 5.9 shows the general description of the model implemented in OpenSees for the RC frame and the infill panel in addition to the detailed description of the RC element model. To be consistent with the experimental tests, all models were first analysed for a preliminary vertical loading followed then by a cyclic lateral loading according to the loading protocol of each experimental campaign.

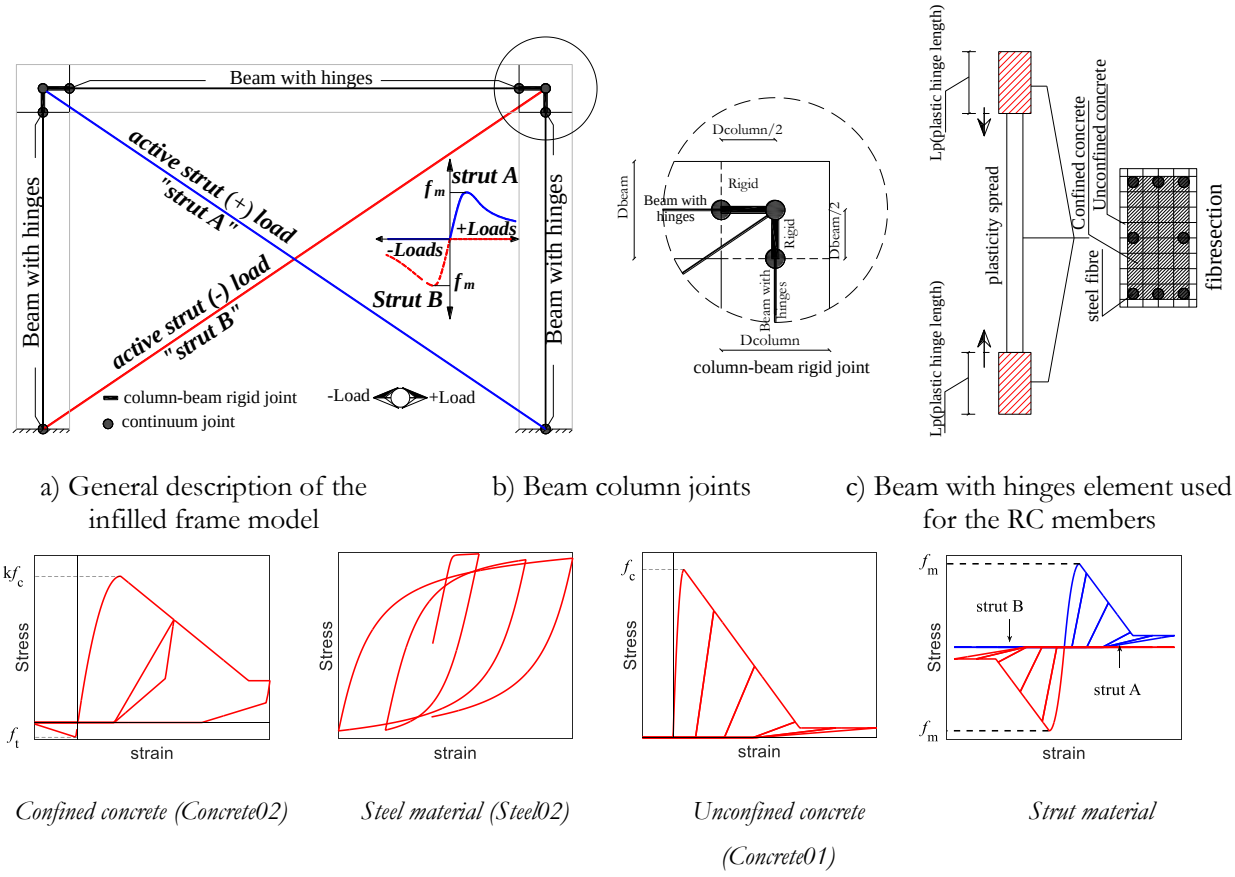

Figure 5.9 Description of the implemented model for the infill panel using the stiffness-based approach.

After modelling the sixteen cyclic experimental tests, the corresponding force-displacement envelopes were obtained. To analyse the reliability of the results obtained, Figure 5.10 shows the numerical and experimental envelope curves of the hysteretic response for the sixteen fully infilled specimens. As can be seen, the numerical model properties calibrated using the proposed procedure are able to reproduce the structural response of the physical specimens adequately in terms of the strength and monotonic stiffness. As can be seen, some numerical curves exhibit larger deviations in their negative part mainly due to the fact that the experimental response is not symmetric and that all the data that was used to calibrate the strut models was obtained from the positive part of the experimental response. The asymmetry of the experimental response can be partially connected to the fact that the loading in a given direction can cause degradation that will affect the loading in the opposite direction. However, this effect is not captured numerically by the considered model. Moreover, differences between the numerical and experimental bare frame behaviour can also be a factor that affects the differences in the envelope. Nevertheless, in the overall, the results obtained by

using the proposed stiffness-based calibration procedure are seen to exhibit a significant agreement with the experimental ones.

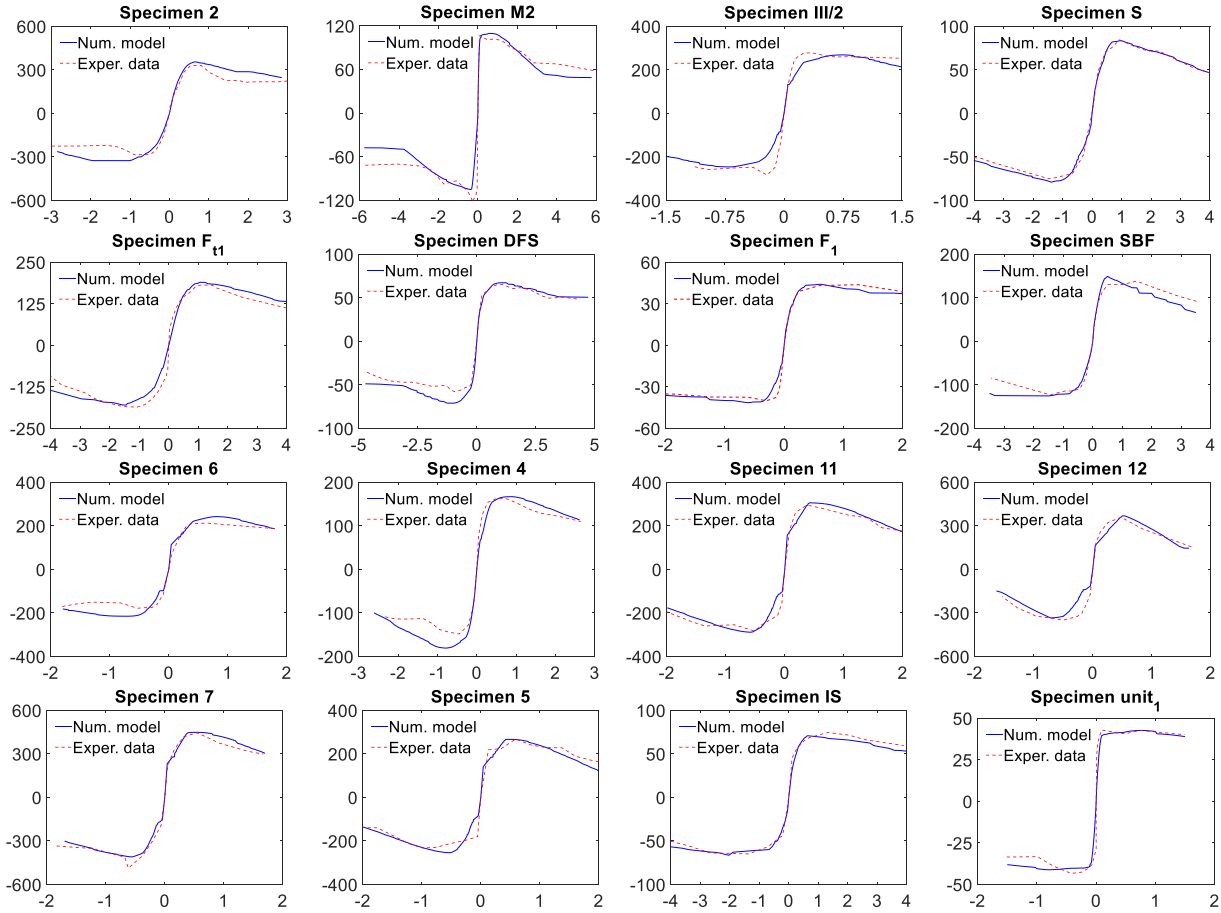

Figure 5.10 Numerical and experimental envelope curves of the hysteretic response for the sixteen fully infilled specimens - single strut calibrated from experimental data using the stiffness-based approach (vertical axes are the total shear force at the base in kN and the horizontal axes represent the lateral drift ratios in %)

5.3.1.2 Performance of the calibration procedure for the stiffness-based approach: experimental data on partially infilled specimens

The performance of the proposed calibration procedure was analysed for partially infilled RC frames using the experimental data from the eight partially infilled specimens that were also considered in Chapter 3 (see Table 3.12). The force-displacement response envelopes for the masonry component of the eight partially infilled specimens from (Kakaletsis, *et al.*, 2008, Kakaletsis, 2009) were extracted according to the previously referred procedure from the corresponding experimental data and are

presented in Figure 5.11. Table 5.3 presents the essential data of these response curves that are needed to define the stress-strain relation representing the constitutive material model that will be assigned to the strut element. This table presents the values of the maximum diagonal force F_{max}, the residual force f_{res} and their corresponding computed strains ε_m and ε_{res}, respectively. As for the fully infilled RC frames, the reliability of the calibration procedure was analysed for these frames. The numerical simulation of these experimental tests was performed using the software OpenSees considering the modelling approach that was presented in the previous section. The Concrete01 material model representing the constitutive material of the compressive strut was now defined using the data presented in Table 5.3.

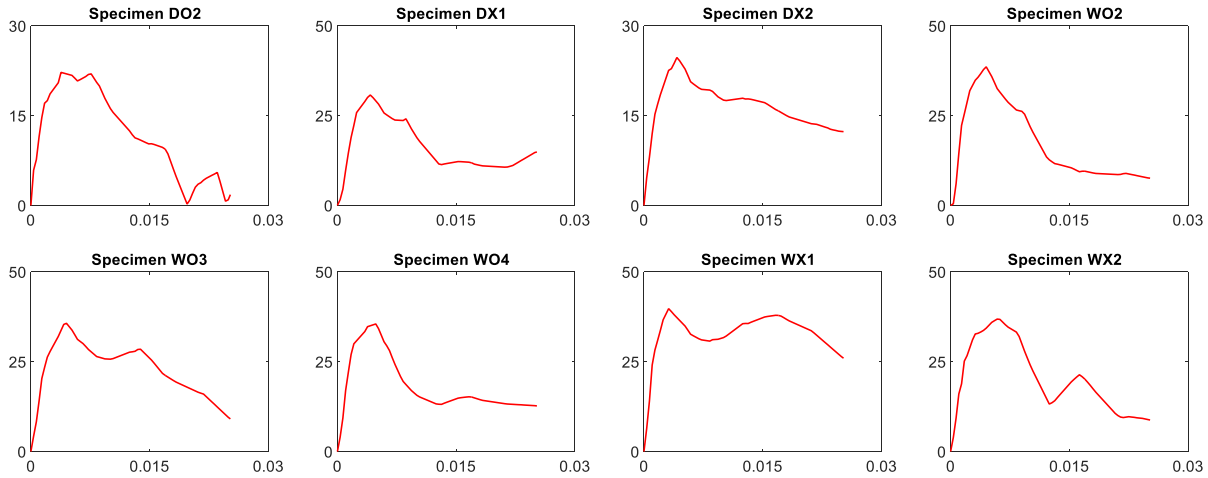

Figure 5.11 Extracted force-displacement response of the partially infilled panels based on experimental data from eight specimens (vertical axes are lateral forces (kN) and horizontal axes are displacements (m))

Table 5.3 Essential parameters extracted from the experimental data needed for the strut material model

Specimen ID	F_{max}	F_{res}	ε_m	ε_{res}
Specimen DO2	22.222	1.80	0.0023	0.013
Specimen DX1	30.739	14.88	0.0026	0.010
Specimen DX2	24.702	12.33	0.0026	0.0103
Specimen WO2	38.581	7.59	0.0028	0.010
Specimen WO3	35.678	9.09	0.0028	0.015
Specimen WO4	35.498	12.69	0.003	0.010
Specimen WX1	39.756	25.97	0.0019	0.0103
Specimen WX2	36.854	8.77	0.0036	0.0128

To analyse the reliability of the results, Figure 5.12 shows the numerical and experimental force-displacement envelope curves of the hysteretic response of the eight partially infilled specimens. As can be seen, the numerical models are able to adequately simulate the global response of the physical specimens. However, as for the fully infilled model, the deviations between the numerical and the experimental curves in the negative side of the response are mainly due to the fact that the implemented model does not capture the unsymmetrical behaviour shown by the experimental data. As mentioned before, the reason for this asymmetry may be due to the fact that the loading in a given direction can cause degradation that will affect the loading in the opposite direction. Moreover, differences between the numerical and experimental bare frame behaviour can also be a factor that affects the differences in the envelope, as well as the fact that the data that was used to calibrate the strut models was obtained from the positive part of the experimental response. Still, as for the fully infilled frames, the numerical results obtained by using the proposed stiffness-based calibration procedure are seen to exhibit an overall good agreement with the experimental ones.

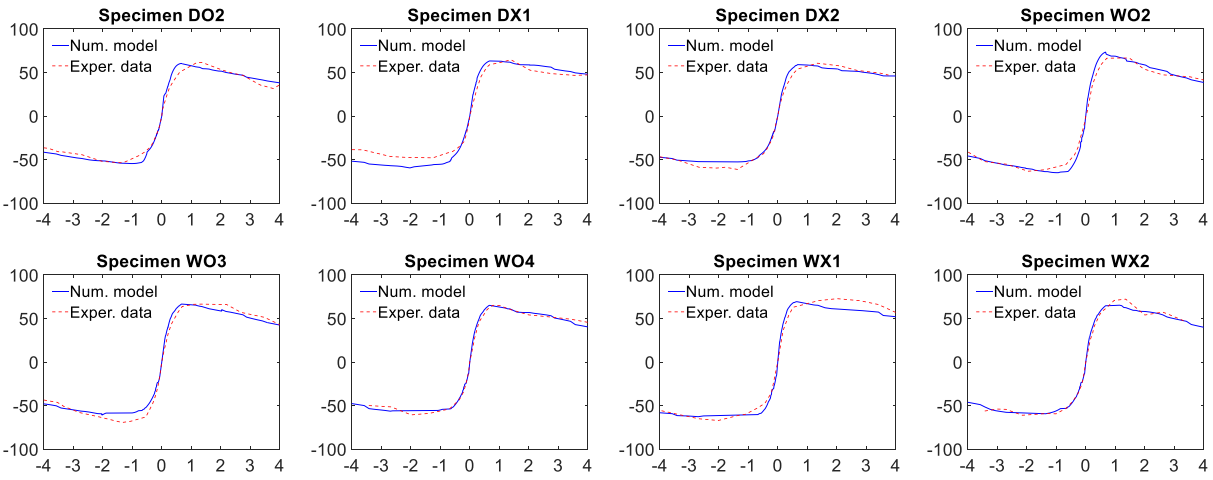

Figure 5.12 Numerical and experimental envelope curves of the hysteretic response for the eight partially infilled specimens - single strut calibrated from experimental data using the stiffness-based approach (vertical axes are the total shear force at the base in kN and the horizontal axes represent the lateral drift ratios in %)

5.3.2 Calibration procedure for the strength-based approach

After obtaining the diagonal force-displacement curve representing the masonry component of the infilled frame behaviour, the calibration procedure for the strength-based approach requires fitting a trilinear idealized curve to the data to establish an equivalent force-displacement model. The proposed procedure is therefore similar to what was done in Chapter 3 but without defining a fixed relation between the parameters of the trilinear curve. As for the stiffness-based approach, since the procedure starts by defining the response contribution of the infill from the global response of the structure, the same procedure can be applied for fully and partially infilled frames and there is no need for reduction factors to account for the existence of openings.

5.3.2.1 Performance of the calibration procedure for the strength-based approach: experimental data on fully infilled specimens

The performance of the proposed calibration procedure was analysed using the experimental data from the sixteen fully infilled specimens previously considered. For this procedure, the force-displacement response components of the sixteen infills that were previously extracted were now used to fit trilinear force-displacement envelope curves. The trilinear fits defined the yield, maximum and residual forces along with their corresponding displacements (see Figure 5.13) according to the following conditions:

- The maximum force F_{max} and its corresponding displacement d_m are defined based on the maximum strength and corresponding displacement of the extracted masonry response curve;
- The yield force F_y is based on the evolution of the step-by-step reduction of the secant stiffness of the masonry response and on the evolution of the force. When the reduction of the secant stiffness from one step to the next is equal to 10% or if 90% of the maximum force is reached, the yield force and its corresponding displacement d_y are defined as the average value between the force/displacement achieving one of these two conditions and the force/displacement of the previous step;

- For the softening part of the behaviour curve, the last value of the force that was recorded is assumed to define the last point of the plateau, (F_r, d_u) in Figure 5.13. The first point of the plateau corresponds to the point (F_r, d_r) in Figure 5.13 where the true force in the masonry behaviour curve is about 10% to 30% higher than the residual force F_r. This condition needs to be assessed case by case, depending on the post-peak behaviour of the masonry response.

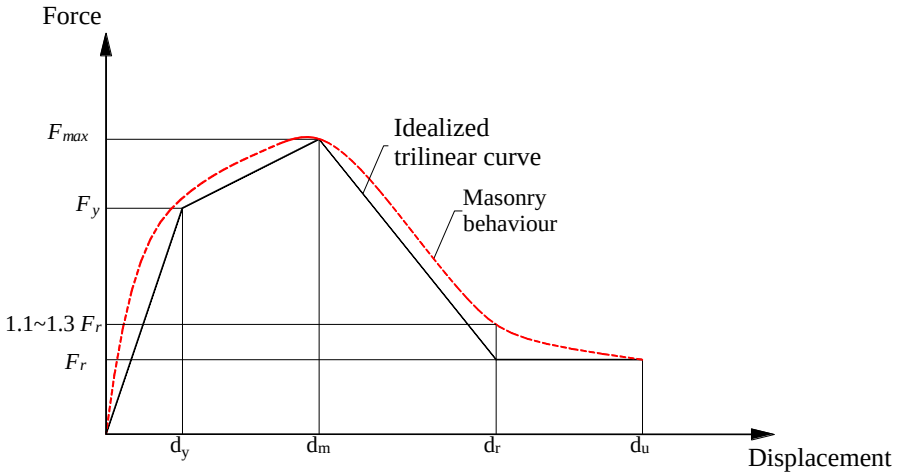

Figure 5.13 Definition of the fitted trilinear model

The trilinear fits that were obtained for the sixteen infills are presented in Figure 5.14. As can be seen, the fundamental advantage of the strength-based approach over the stiffness-based approach is that it has the potential to capture more adequately the whole behaviour envelope of the masonry force-displacement response. While the stiffness-based approach only enforces the maximum strength and corresponding deformation (the remaining aspects of the behaviour being defined by the equivalent constitutive material), the strength-based approach is able to potentially enforce the whole behaviour envelope. According to the trilinear fits that are presented in Figure 5.14, it can be seen that the selected fitting conditions are able to provide adequate fits for the majority of the cases. However, in some cases, the idealized trilinear fit is not able to fully capture the true masonry response due to the complex evolution of such response (e.g. for specimens III/2, F1 or 5). For such cases, a quadrilinear curve could have led to a better fit to the experimental data.

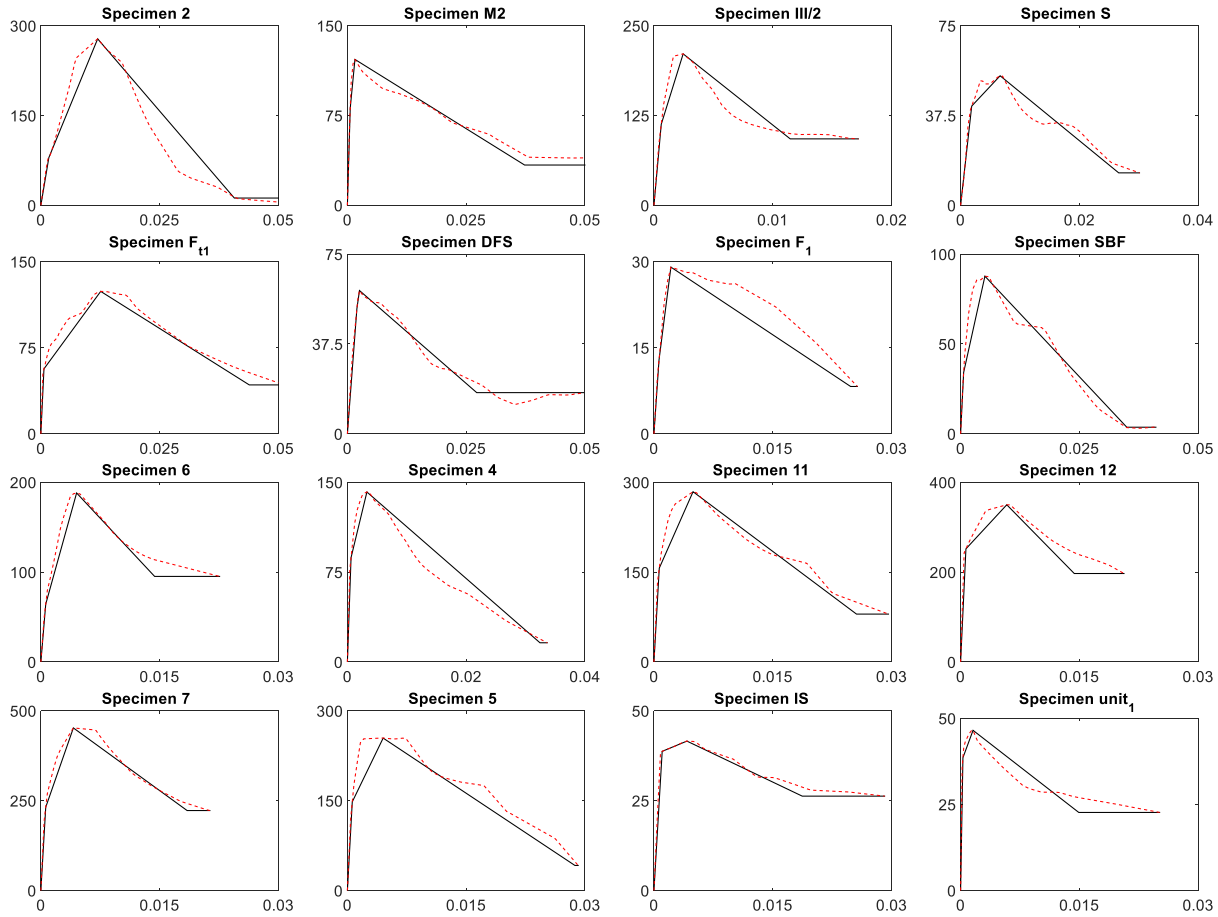

Figure 5.14 Extracted force-displacement response of the infill based on experimental data (red line) and the best-fit trilinear curves and residual plateau (continuous back line) for the sixteen specimens (vertical axes are lateral forces (kN) and horizontal axes are displacements (m)

After defining the trilinear force-displacement curves for the masonry, these needed to be assigned to a strut element in OpenSees to simulate the experimental tests. However, OpenSees does not possess an element with a formulation that allows a compression-only force-displacement piecewise linear curve to be assigned. Since defining the tensile part of the behaviour curve of an element with zero stiffness will lead to numerical convergence problems, the masonry was modelled using strut elements that are active in both compression and tension. Therefore, each of the struts has a symmetric behaviour where the force values in each direction correspond to half of the force values of the trilinear behaviour curve. Figure 5.15 illustrates the model that was implemented model in OpenSees for the RC frame and the infill panel. In addition, an illustration of the masonry response is also presented by showing the partial response of both tension-compression struts for a given loading

and the corresponding total response. The trilinear curves of the infill panels were modelled using truss elements associated with the Pinching4 material of OpenSees while the RC frame elements were modelled using the same approach that was used for the stiffness-based approach. The Pinching4 parameters reflecting strength degradation, stiffness degradation and pinching that were considered are those calibrated experimentally by (Furtado, *et al.*, 2016).

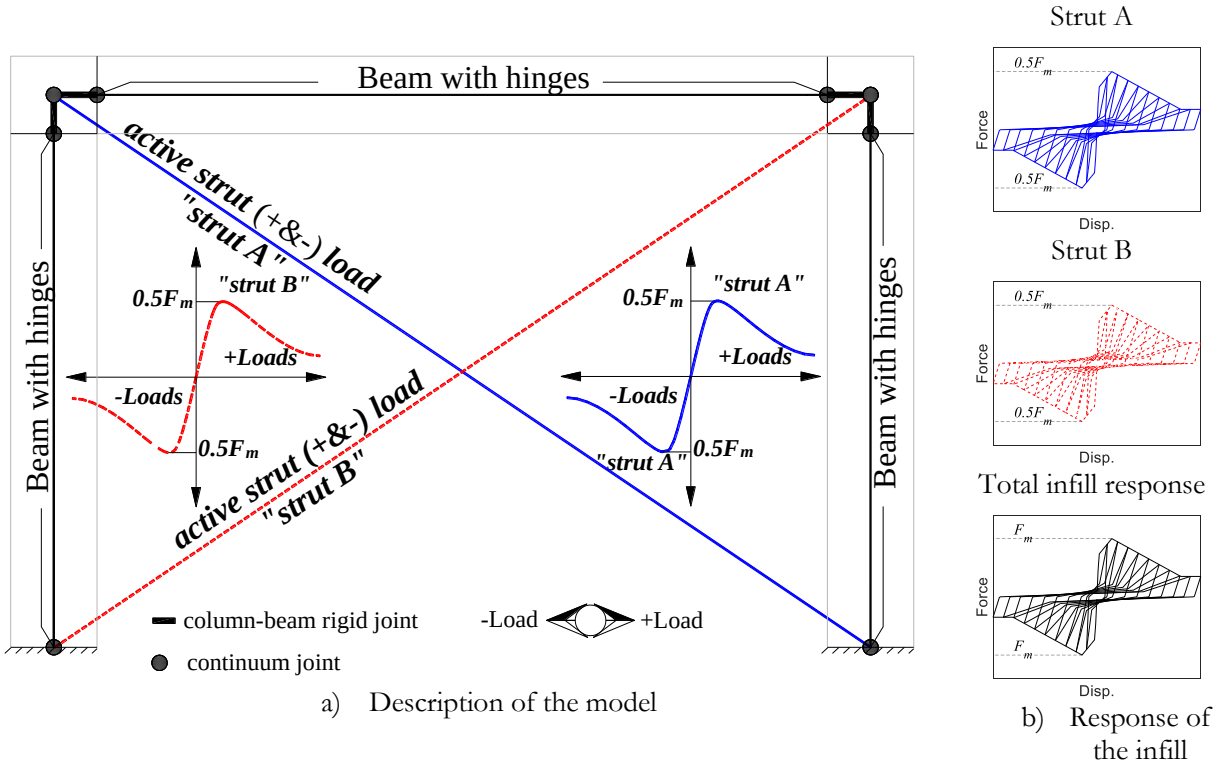

Figure 5.15 Description of the implemented model for the infill panel using the strength-based approach

After simulating the sixteen specimens using the referred modelling approach, the corresponding force-displacement envelopes were obtained. The comparison between the numerical and experimental results can be carried out based on Figure 5.16 that shows the numerical and experimental envelope curves of the hysteretic response for the sixteen fully infilled specimens. As can be seen, the numerical models are able to reproduce the global structural response of the physical specimens adequately. In some cases, a slight deviation between the numerical and experimental results can be seen in the negative part of the response. Since all the data that was used to calibrate the strut models was obtained from the positive part of the experimental response, these deviations only occur for specimens that exhibited a more asymmetrical experimental response. As mentioned before, the

asymmetry of the experimental response might be partially connected to the fact that the loading in a given direction can cause degradation that will affect the loading in the opposite direction. Having strut elements with cyclic behaviour both in tension and in compression such as in the considered models implies that reloading stages start with a degraded stiffness and some asymmetric behaviour might be captured by this effect. Nevertheless, in the overall, the results obtained by using the proposed stiffness-based calibration procedure are seen to exhibit a significant agreement with the experimental ones.

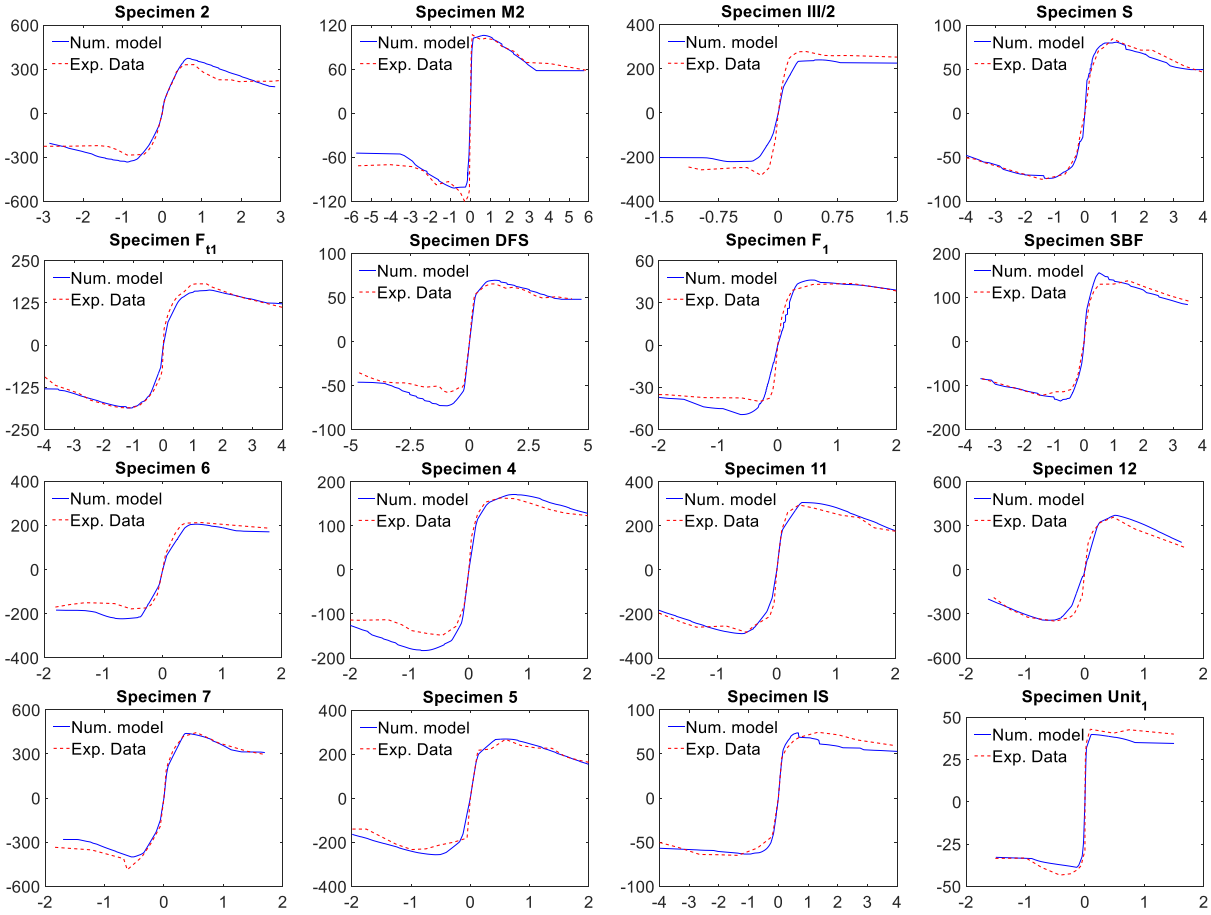

Figure 5.16 Numerical and experimental envelope curves of the hysteretic response for the sixteen fully infilled specimens - single strut calibrated from experimental data using the strength-based approach (vertical axes are the total shear force at the base in kN and the horizontal axes represent the lateral drift ratios in %)

5.3.2.2 Performance of the calibration procedure for the strength-based approach: experimental data on partially infilled specimens

The performance of the proposed calibration procedure was also analysed for the eight partially infilled RC frames previously considered. The force-displacement response components of the eight infills that were previously extracted were now used to fit trilinear force-displacement envelope curves, as shown in Figure 5.17. The trilinear fits were defined according to the same conditions that were considered for the fully infilled frames. As can be seen, for some specimens, the idealized trilinear fit is not able to fully capture the true masonry response due to the complex evolution of such response (e.g. for specimens WX1 or WX2).

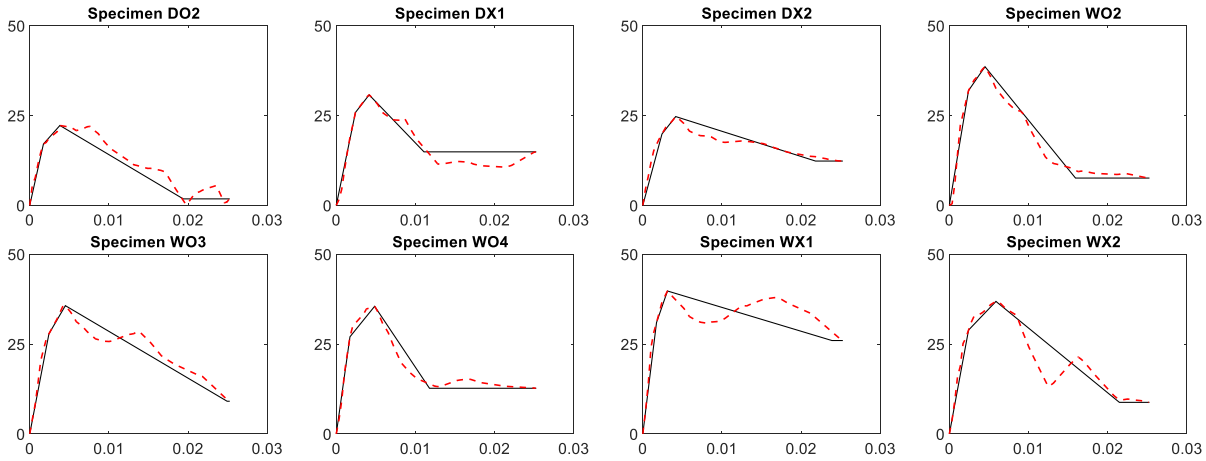

Figure 5.17 Extracted force-displacement response of the infill based on experimental data (red line) and the best-fit trilinear curves and residual plateau (continuous back line) for the eight specimens with partially infilled panel (vertical axes are lateral forces (kN) and horizontal axes are displacements (m)

As for the fully infilled RC frames, the reliability of the calibration procedure was also analysed for these frames. The numerical simulation of these experimental tests was performed using the modelling approach that was presented in the previous section for the fully infilled frames. Figure 5.18 shows the envelope curves for the hysteretic response of the eight partially infilled specimens obtained from the numerical and experimental data. As can be seen, the numerical models adequately simulate the global response of the physical specimens. However, as for the fully infilled models, larger deviations can be found in the negative part of the response due to the factors previously mentioned. Nevertheless, as for the fully infilled frames, the numerical results obtained by using the proposed

strength-based calibration procedure are seen to exhibit an overall good agreement with the experimental ones.

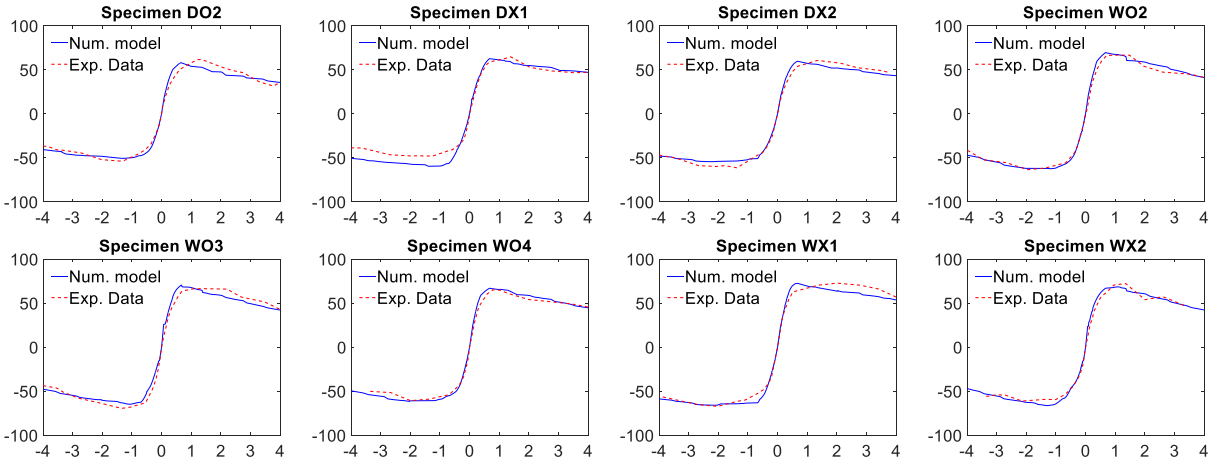

Figure 5.18 Numerical and experimental envelope curves of the hysteretic response for the eight partially infilled specimens - single strut calibrated from experimental data using the strength-based approach (vertical axes are the total shear force at the base in kN and the horizontal axes represent the lateral drift ratios in %)

5.4 Validation of the proposed calibration procedures based on numerical data

The performance of the proposed calibration procedure when using numerical results from detailed finite element models instead of experimental data is now analysed and illustrated. The response of the specimens that were modelled in Chapter 4 is now used to replicate the macro-models and compare their responses with those obtained in the previous sections. The procedures that were implemented herein are exactly those that were considered in the previous section, replacing the experimental data with the numerical data obtained from the models presented in Chapter 4.

Recently, an alternative approach has been also proposed to calibrate the parameters of strut elements based on results from detailed finite element models, e.g. see (Sattar*, et al.*, 2016a). This approach determines the evolution of the force transferred through the infill (and its maximum value) based on the integration of the stresses in the middle zone of the infill panel combined with the monitoring of the contact length between the infill and the RC frame to evaluate the strut width.

However, a limitation of this approach is that it does not account for the potential contribution of other parts of the infill that are not included in this strut region to the load capacity of the infill. An alternative procedure was presented in (Ahmed*, et al.*, 2017) which also monitors the evolution of the force transferred through the infill now based on the integration of the compressive stresses in the whole infill panel. This new procedure overcomes a limitation of the procedure by (Sattar*, et al.*, 2016a). and provided good results to establish the parameters of the macro-model. Still, it is noted that both these procedures are not applicable when the available behaviour data is experimental (i.e. where the distribution of stresses in the structure is usually not available) and they involve complex computational steps to get the forces in the infill panel. Therefore, the calibration procedure that was considered in the previous sections is preferred and was also considered herein.

5.4.1 Performance of the calibration procedure for the stiffness-based approach

5.4.1.1 Results obtained for the numerical data on fully infilled specimens

The performance of the proposed calibration procedure was analysed using the numerical data from the two fully infilled specimens that were analysed in Chapter 4: specimen M2 and specimen S. The force-displacement response components of the infills were extracted according to the previously referred procedure considering the positive response of the data, as carried out for the cases based on experimental data. The responses of the corresponding bare frames were also modelled considering the modelling options presented in Chapter 4. The force-displacement response that was obtained for the masonry components of specimens M2 and S are presented in Figure 5.19. Table 5.4 presents the essential data of these response curves that are needed to define the stress-strain relation representing the constitutive material model that will be assigned to the strut element. This table presents the values of the maximum diagonal force F_{max}, the residual force F_{res} and their corresponding computed strains ε_m and ε_{res}, respectively.

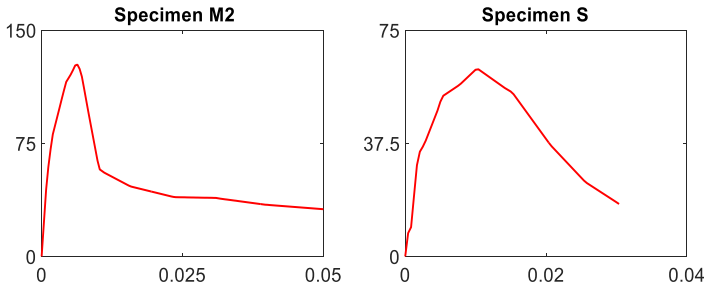

Figure 5.19 Extracted force-displacement response of the infill based on the results obtained from the refined finite element models for specimen M2 and specimen S (vertical axes are lateral forces (kN) and horizontal axes are displacements (m))

Table 5.4 Essential parameters extracted from the numerical model needed for the strut material model

Specimen ID	F_{max}	F_{res}	ε_m	ε_{res}
Specimen M2	127.13	24.16	0.0018	0.022
Specimen S	61.11	17.40	0.0053	0.017

The numerical simulation of these tests was performed in OpenSees considering the modelling approach that was presented in the previous section for the cases involving the stiffness-based procedure. To analyse the reliability of the results obtained, Figure 5.20 shows the numerical and experimental envelope curves of the hysteretic response for specimens M2 and S. The results that were obtained indicate there is a reasonable agreement between the experimental results and those obtained from the numerical macro-model, particularly in terms of global behaviour (stiffness and maximum strength). Aside from the previously referred issues related to the asymmetry of the experimental response, the differences between the experimental and numerical responses can be seen to be larger than those found when the strut parameters are calibrated using experimental data. These differences can be seen to be the direct result of the compound effect of two errors: one error resulting from the differences between the experimental data and the results obtained from the refined finite element model and another error resulting from the differences between the detailed numerical masonry component response and its approximate representation by the strut element. These aspects are particularly relevant for specimen M2.

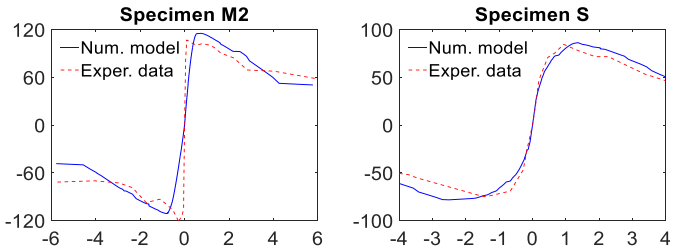

Figure 5.20 Numerical and experimental envelope curves of the hysteretic response for the two fully infilled specimens - single strut calibrated based on the refined finite element model data using the stiffness-based approach (vertical axes are the total shear force at the base in kN and the horizontal axes represent the lateral drift ratios in %)

5.4.1.2 Results obtained for the numerical data on partially infilled specimens

The performance of the proposed calibration procedure was also analysed using the numerical data from the eight partially infilled specimens that were analysed in Chapter 4. The force-displacement response components of the infills were extracted according to the previously referred procedure and the response of the corresponding bare frames were also modelled considering the modelling options presented in Chapter 4. The force-displacement response that was obtained for the masonry components of the eight specimens are presented in Figure 5.22. Table 5.5 presents the essential data of these response curves that are needed to define the stress-strain relation representing the constitutive material model that will be assigned to the strut element, namely the values of F_{max}, F_{res}, ε_m and ε_{res}.

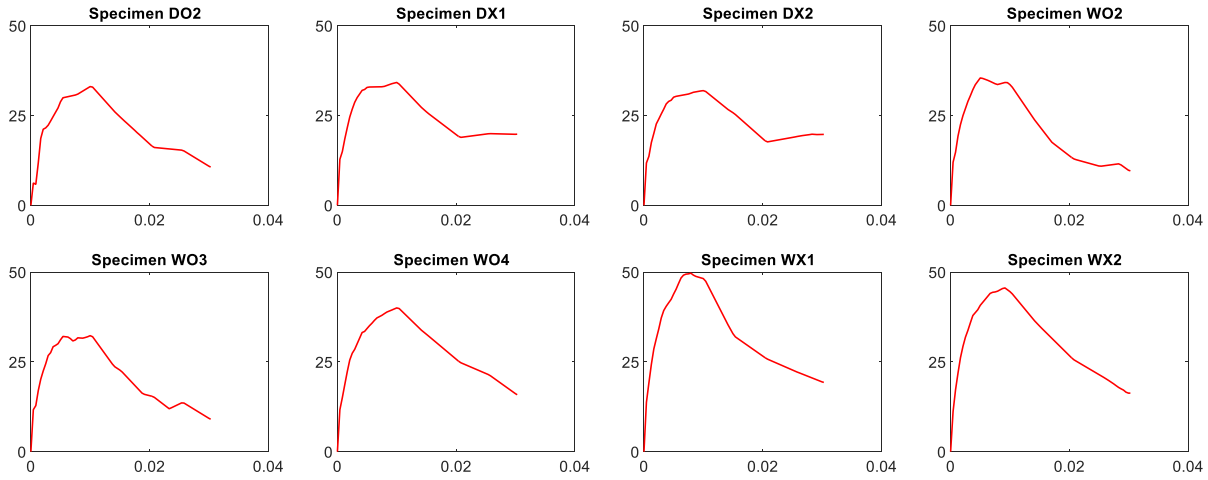

Figure 5.21 Extracted force-displacement response of the partially infilled panel based on refined finite element model for eight specimens (vertical axes are lateral forces (kN) and horizontal axes are displacements (m))

Table 5.5 Essential parameters extracted from the finite element model needed for the strut material model

Specimen ID	F_{max}	F_{res}	ε_m	ε_{res}
Specimen DO2	33.05	10.6	0.0051	0.018
Specimen DX1	34.2	19.8	0.0051	0.013
Specimen DX2	31.92	19.74	0.0051	0.01
Specimen WO2	35.45	9.59	0.0026	0.010
Specimen WO3	32.301	9.04	0.0028	0.011
Specimen WO4	40.0	15.8	0.0051	0.010
Specimen WX1	49.69	19.2	0.0041	0.010
Specimen WX2	45.58	16.30	0.0047	0.011

The numerical simulation of these tests was performed in OpenSees considering the modelling approach of the previous cases involving the stiffness-based procedure. To analyse the reliability of the results obtained, Figure 5.22 shows the numerical and experimental envelope curves of the hysteretic response of the eight specimens. As for the fully infilled frames of the previous section, the results that were obtained indicate there is a reasonable agreement between the experimental results and those obtained from the numerical macro-model, particularly in terms of global behaviour (stiffness and maximum strength). Also, like for the fully infilled frames of the previous section, the differences related to the asymmetry of the experimental response are seen to be larger in these cases than for those where the strut parameters are calibrated using experimental data. As previously referred also, these differences can be seen to be the direct result of the compound effect of two errors. However, for these specimens, the overall differences are smaller than those found for the fully infilled

frames since the detailed finite element model was able to capture the experimental response more adequately.

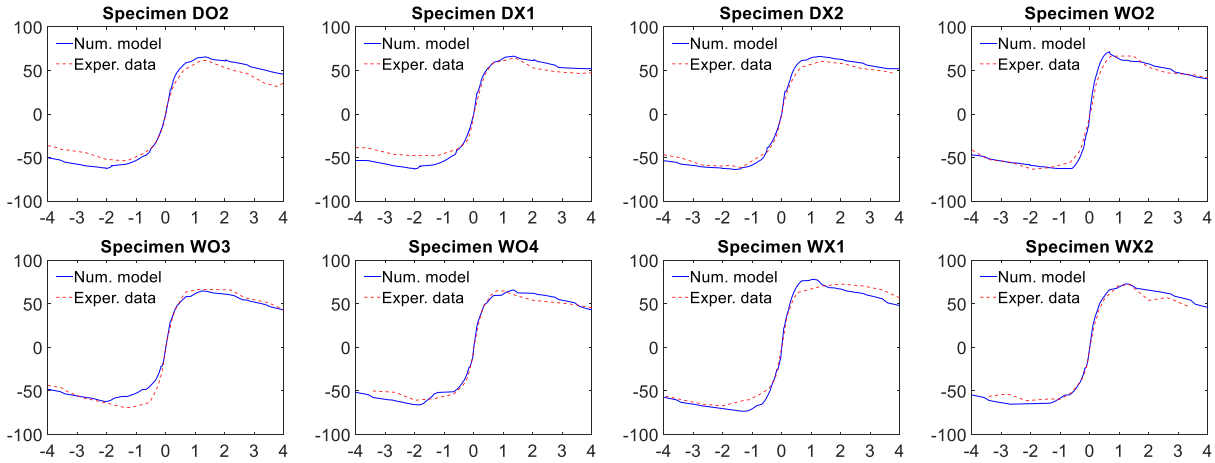

Figure 5.22 Numerical and experimental envelope curves of the hysteretic response for the eight partially infilled specimens - single strut calibrated based on the refined finite element model data using the stiffness-based approach (vertical axes are the total shear force at the base in kN and the horizontal axes represent the lateral drift ratios in %)

5.4.2 Performance of the calibration procedure for the strength-based approach

5.4.2.1 Results obtained for the numerical data on fully infilled specimens

The performance of the proposed strength-based calibration procedure was also analysed using the numerical data from the two fully infilled specimens that were analysed with the refined finite element models. The procedure and assumptions that were considered herein as those also considered for the cases that were analysed based on experimental data in the previous section.

The trilinear force-displacement envelope curves that were fitted to the numerical data of specimens M2 and S are shown in Figure 5.26. It can be seen that the selected fitting conditions are able to provide an adequate fit for specimen S but not entirely for specimen M2 (unlike what was seen for the fit based on experimental data shown in Figure 5.14). For this case, a quadrilinear curve could have led to a better fit to the numerical data.

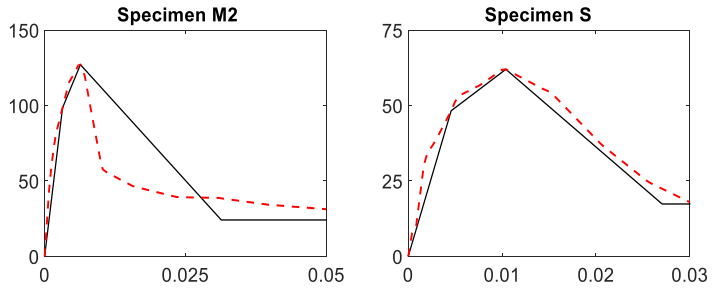

Figure 5.23 Extracted force-displacement response of the infill based on refined finite element model (red line) and the best-fit trilinear curves and residual plateau (continuous back line) for the specimen M2 and specimen M2 (vertical axes are lateral forces (kN) and horizontal axes are displacements (m)

The numerical simulation of these tests was performed in OpenSees considering the modelling approach that was presented in the previous section for the cases involving the strength-based procedure. The results obtained from these models are plotted in Figure 5.24 as envelope curves of the hysteretic response along with the corresponding experimental data. The results that were obtained indicate there is a reasonable agreement between the experimental results and those obtained from the numerical macro-model. However, as for the results obtained for these two cases using the stiffness-based approach, the differences between numerical and experimental results are larger for specimen M2. As discussed before, these differences are the direct result of the compound effect of two errors where, in this case, the lack of fit of the trilinear curve in the post-peak behaviour of the masonry may have a larger influence than for previous cases.

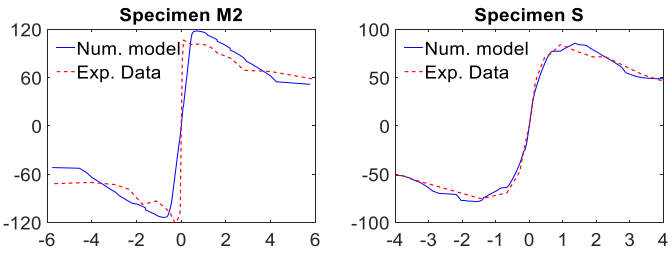

Figure 5.24 Numerical and experimental envelope curves of the hysteretic response for the two fully infilled specimens - single strut calibrated based on the refined finite element model data using the strength-based approach (vertical axes are the total shear force at the base in kN and the horizontal axes represent the lateral drift ratios in %)

5.4.2.2 Results obtained for the numerical data on partially infilled specimens

The performance of the proposed calibration procedure was also analysed using the numerical data from the eight partially infilled specimens that were considered in Chapter 4. The force-displacement response components of the infills were extracted according to the previously referred procedure and the corresponding trilinear force-displacement envelope curves that were fitted to the numerical data of the specimens are shown in Figure 5.25. It can be seen that the selected fitting conditions are able to provide adequate fits for these specimens.

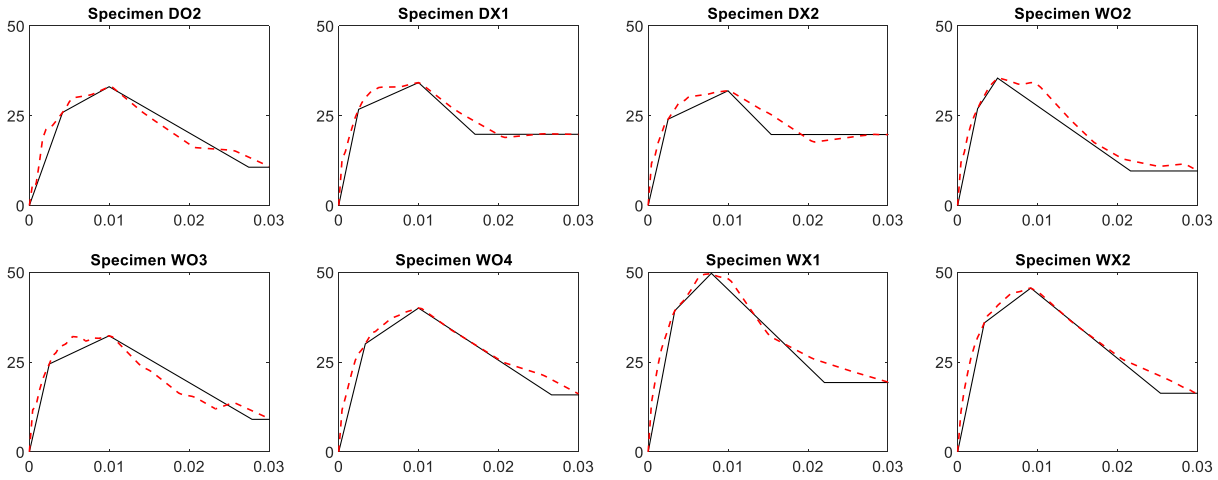

Figure 5.25 Extracted force-displacement response of the infill based on refined finite element model (red line) and the best-fit trilinear curves and residual plateau (continuous back line) for the eight specimens with partially infilled panel (vertical axes are lateral forces (kN) and horizontal axes are displacements (m)

The numerical simulation of these tests was performed in OpenSees considering the modelling approach that was presented in the previous section for the cases involving the strength-based procedure. The results obtained from these models are plotted in Figure 5.26 as envelope curves of the hysteretic response along with the corresponding experimental data. The results that were obtained indicate there is a good agreement between the experimental results and those obtained from the numerical macro-model. Still, as for the fully infilled models, larger deviations can be found in the negative part of the response due to the factors previously mentioned. Nevertheless, as for the fully

infilled frames, the numerical results obtained by using the proposed strength-based calibration procedure are seen to exhibit an overall good agreement with the experimental ones.

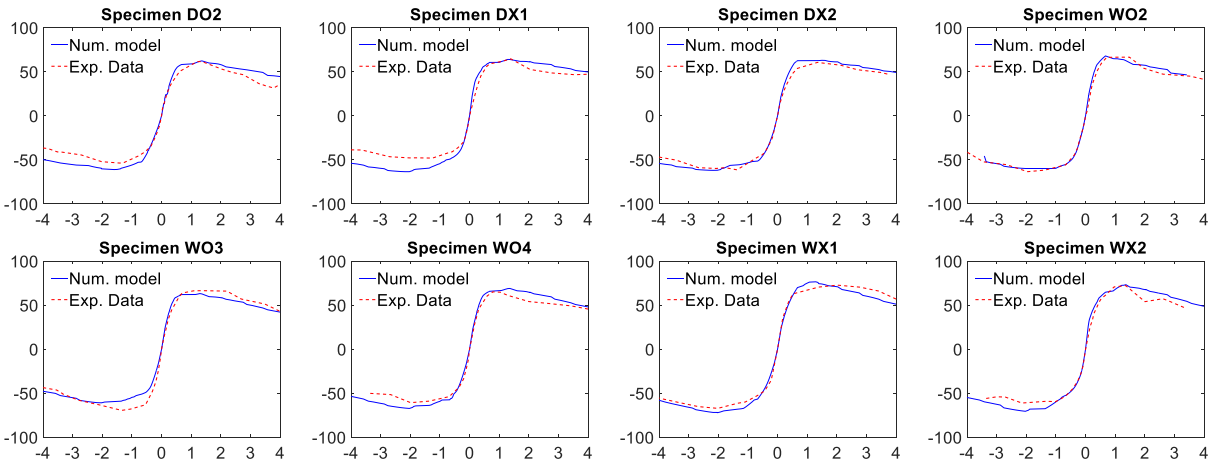

Figure 5.26 Numerical and experimental envelope curves of the hysteretic response for the eight partially infilled specimens - single strut calibrated based on the refined finite element model data using the strength-based approach (vertical axes are the total shear force at the base in kN and the horizontal axes represent the lateral drift ratios in %)

5.4.3 Generalized procedure to calibrate the parameters of strut models

The analyses presented in the previous sections demonstrate the potential of the proposed procedures to define the parameters of strut-based models representing the behaviour of masonry infills. When the calibration procedure is based on experimental data, the macro-models were seen to be able to simulate the behaviour of the physical specimens with a good agreement. In case experimental data is unavailable or inaccessible, simulating the necessary experimental data using detailed finite element models was seen as an affordable and efficient alternative. When the calibration procedure is based on this numerical data, the macro-models were also seen to be able to simulate the behaviour of the physical specimens adequately, although their performance is now also dependent on the accuracy of the detailed finite element model results.

To summarize the overall procedure based on the use of detailed finite element models, a generalized calibration procedure, illustrated by the flowchart of Figure 5.27, is presented herein to

facilitate the implementation of the different steps. As shown, the calibration procedures involve two stages. The first stage includes determining the capacity curves of the bare frame and of the infilled frame. The second stage corresponds to the definition of the parameters of the strut model based on the data obtained in the first stage. The first stage involves running two different finite element analyses, a first one for the model of the bare RC frame to obtain the corresponding capacity curve, followed by a second analysis of the infilled RC frame to obtain the corresponding capacity curve. Having both these capacity curves, the process then enters into the second stage where the capacity curve of the masonry infill is obtained by subtracting the RC bare frame capacity curve from that of the infilled RC frame. The masonry capacity curve is then projected onto the required direction (i.e. the diagonal direction) and transformed into the strut model behaviour curve either using a stiffness- or strength-based approach, as presented previously in section 5.2.

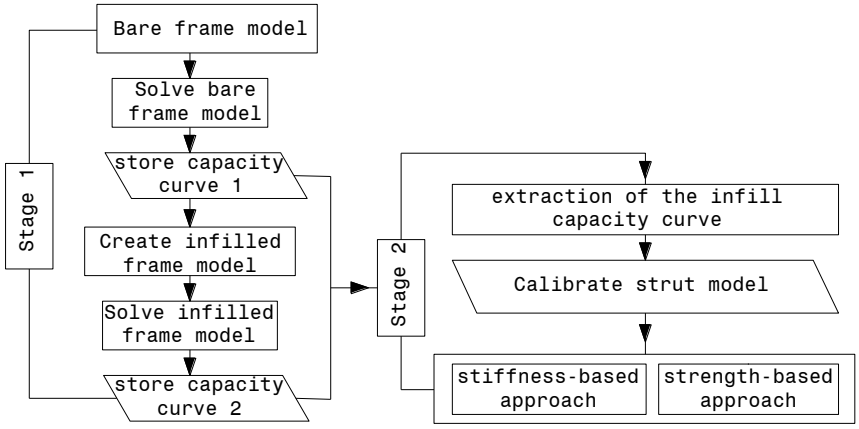

Figure 5.27 Flowchart of the proposed calibration procedure based on the use of refined finite element models to replace experimental testing.

5.5 Extending the proposed calibration procedure for macro-models with special configurations

In order to extend the range of applications of the proposed calibration approach, its performance was analysed when used to calibrate the parameters of macro-models with special configurations such as multi-strut models (i.e. with two struts and three struts) and the model proposed

by Rodrigues*, et al.* (2010). The following sections analyse the calibration of these special configuration macro-models and simulate several specimens that were considered in the previous sections.

5.5.1 Multi-strut models

As discussed in the previous chapter, the load transfer between frame members and the infill occurs through the contact length between these elements. Therefore, the beam and column ends are constrained due to the direct action of the infill on those RC members. In light of this, the frame members, particularly the columns, may exhibit shear failure due to this infill action (Varum, 2003). In order to capture this interaction between the infill and the frame more adequately, single strut models can be replaced by multi-strut models. In this section, the two-strut and the three-strut models proposed by (Sattar*, et al.*, 2016b) and (Crisafulli, 1997) shown in Figure 5.28 are considered and their implementation and calibration is discussed.

Unlike for the previous models that involved single-strut approaches, when using multi-strut models, the nonlinear behaviour of the RC members is now modelled using a lumped plasticity approach. This modification is necessary due to the additional nodes that are needed to connect the RC members to the new strut configurations. Since the previously considered RC member modelling approach (i.e. the beam with hinges model) assumes that one element represents an entire member, and since using other options such as other force-based elements or elements with a displacement-based formulation would require using very small-size elements, lumped plasticity was considered to be the best alternative. Therefore, the nonlinearity of the RC members is lumped in zero-length springs at the member ends as shown in Figure 5.28, while the remaining part of the member is assumed to have elastic behaviour. Assuming this elastic behaviour solves the numerical issues that might occur due to the need to subdivide a given element into multiple small-size elements to create the nodes needed to connect the multiple struts. One additional and important aspect for the definition of these multi-strut macro-models involves establishing the length of the off-distance β (see Figure 5.28). The approach that was considered is described in the following.

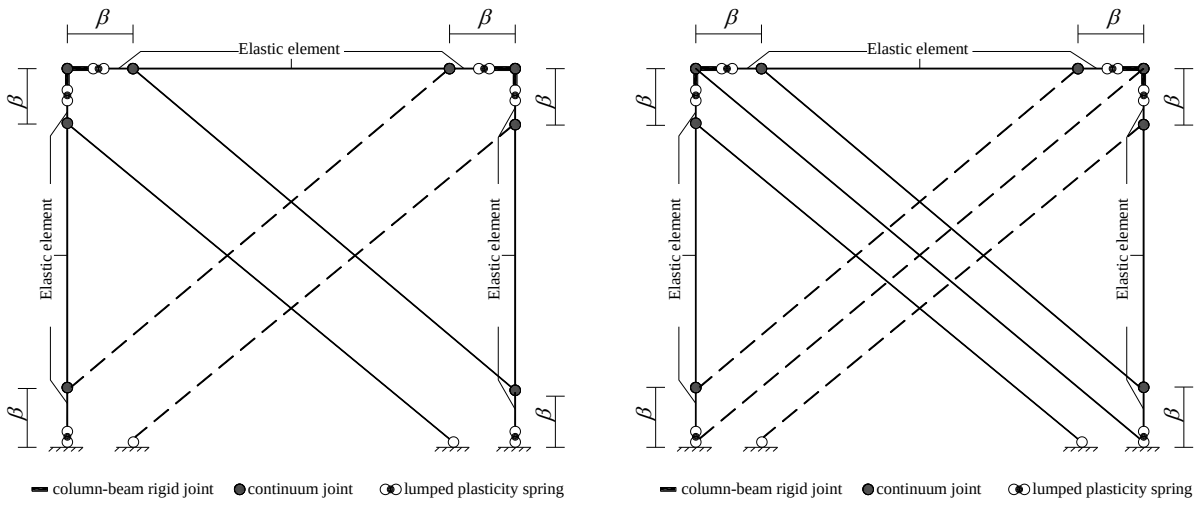

a) Two-strut model b) Three-strut model

Figure 5.28 Model configuration for multi-struts models: a) two struts (Sattar*, et al.*, 2016b); b) three struts (Crisafulli, 1997)

The standard CCMPA (2009) refers that the loading zone of the infill panel can be idealized by a triangular shape which is then reflected along the RC members by the contact lengths. Based on the results obtained from the numerical model developed in Chapter 4 and those presented in (Sattar, 2013), this idealization is considered to be realistic enough. To illustrate this phenomenon, Figure 5.29 a) shows the considered idealized interaction between the infill panel and the surrounding RC frame, where the contact stresses are distributed along part of the beam and of the column defining the contact lengths. Based on these lengths, the forces of the multi-strut model and their location can be defined. Several expressions can be found in the literature to evaluate the size of the contact lengths. In order to be consistent with the considered models, the relation proposed by (Smith, *et al.*, 1969) is considered to define the contact lengths α which provides equal contact lengths between the infill and both frame components (i.e. the beam and column):

$$\alpha = \frac{\pi}{2\lambda} \tag{5.7}$$

where λ is a characteristic stiffness parameter (in m^{-1}) given by:

$$\lambda = \sqrt[4]{\frac{E_I t \sin 2\theta}{4EIh_w}} \,. \tag{5.8}$$

in which E_I is the modulus of elasticity of the masonry panel, EI is the flexural stiffness of the columns, t is the thickness of the infill panel and of the equivalent strut, and h_w is the height of the infill panel. According to this proposal, the vertical and horizontal contact lengths are assumed to be equal. Assuming this contact length and by determining the force-displacement behaviour of a single strut by the previously presented stiffness- or strength-based procedures, the distribution of forces by the two and three struts that leads to the definition of the off-distance β is as follows.

For the double strut model, the force in the single strut was divided equally by the two struts (Crisafulli*, et al.*, 2007), as shown in Figure 5.29 b). For the three strut model, the sum of the forces in the external struts is equal to the force of the central strut (Crisafulli*, et al.*, 2007), as shown in Figure 5.29 c). To have deformations compatible with the single strut model, the area of the single strut was distributed across the two or three struts according to the corresponding force distribution. The location of the connections between the struts and the RC members was determined based on the location of the resultant force obtained from the integration of the idealized contact stress distributions for the two and three strut models, as shown in Figure 5.29 b) and Figure 5.29 c). For the two-strut model, the stresses acting on the beam (i.e. area a_1) are aggregated in a force associated to strut 1 and the stresses acting on the column (i.e. area a_2) are aggregated in a force associated to strut 2. As can be seen from Figure 5.29 b), the location of these resultant forces defines the value of β as α /3. For the three-strut model, half of the idealized triangular stress area (i.e. area a_5) is assumed to be supported by the central strut while the remaining stresses (i.e. areas a_3 and a_4) are assumed to be supported by the external struts as shown in Figure 5.29 c). Based on this idealization, the location of the connection between the struts and the RC members defined by the location of the resultant force of each area establishes the value of β as 0.5286α. In order to maintain the ratio between the forces in each strut as proposed, the off-distance β is computed based on the ratio χ (see Figure 5.29 c)) which enforces that adding areas a_3 and a_4 yields area a_5. To summarize these considerations, Table 5.6 presents the properties considered for the used multi-strut models and their relations with those considered in the single strut approach.

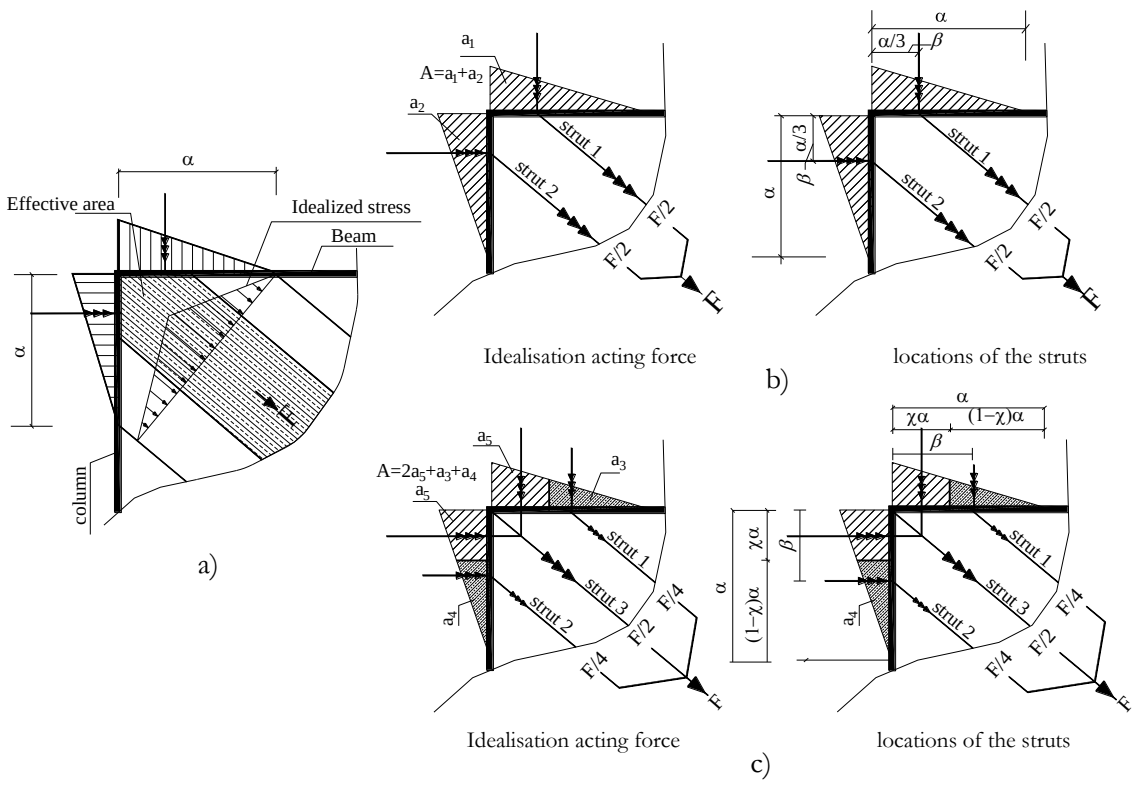

Figure 5.29 Idealized contact stresses and distribution of forces by the struts: a) idealized contact stress between the infill panel and the RC members (CCMPA, 2009); b) forces and their location for the two-strut model; c) forces and their location for the three-strut model

Table 5.6 Properties of the multi-strut models and relations with the single strut properties

	Single strut	**Two struts**		**Three struts**		
		Strut 1	Strut 2	Strut 1	Strut 3 (central strut)	Strut 2
Area of strut	A	A/2	A/2	A/4	A/2	A/4
Off-distance (*β*)	0	$\alpha/3$	$\alpha/3$	$\alpha\left(\frac{3-\sqrt{2}}{3}\right)$	0	$\alpha\left(\frac{3-\sqrt{2}}{3}\right)$
Force	F	F/2	F/2	F/4	F/2	F/4

To illustrate the performance of the multi-strut models, four fully infilled specimens were modelled using the two and three strut models where the strut properties were defined using the stiffness-based approach and the OpenSees modelling approach considered in the previous sections.

The selected specimens are specimens S, F_1, M2 and IS that were previously analysed. The nonlinear behaviour of the RC frame members of these specimens were modelled using a lumped plasticity approach compatible with the previously considered frames that involved single strut models. In this context, as previously referred, zero-length rotational springs associated with the Hysteretic material model in OpenSees were used to simulate the nonlinear behaviour of the RC members. The parameters defining the backbone behaviour of the rotational spring were computed based on the empirical equations proposed by (Haselton, 2008). To illustrate the results that were obtained using these modelling approaches, Figure 5.30 shows the envelope curves for the hysteretic response of the four fully infilled specimens obtained by using two- and three-strut models along with the corresponding experimental data. As can be seen, the two models (i.e. the two- and three-strut models) exhibit very close responses in most cases. Also, both models are also able to capture the behaviour of the physical specimens with a good agreement, thus validating the proposed approach to calibrate the properties of multi-strut models. Aside from the previously addressed asymmetry issues and other differences found for the single strut model results, two aspects should be further noted. For the particular specimens that were analysed herein, there is no particular advantage in using multi-strut models since these are usually more relevant for cases where the interaction between the infill and the RC members is considered to be important and might lead to the occurrence of shear failure mechanisms in the RC members. Multi-strut models were only considered in the present study to analyse the global validity of the procedure defining their parameters. Additionally, it is also referred that the influence of the modelling approach considered for the RC members in these cases is not accounted for. Therefore, the apparent better performance of the single strut approach for specimens F_1 and IS for example (see Figure 5.10) may be influenced by the modelling approach selected for the RC members.

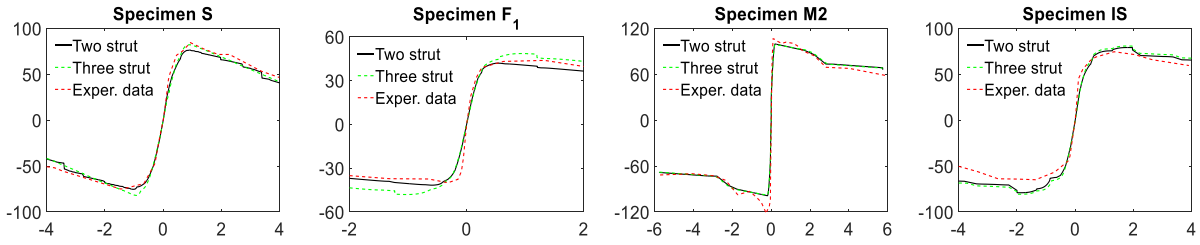

Figure 5.30 Numerical and experimental envelope curves of the hysteretic response for the four fully infilled specimens - multi struts model calibrated from experimental data using the stiffness-based approach (vertical axes are the total shear force at the base in kN and the horizontal axes represent the lateral drift ratios in %)

In order to analyse the performance of the multi-strut models for partially infilled specimens, eight partially infilled specimens were modelled using two- and three- strut models. The RC frame of these specimens was modelled using the same approach as for the fully infilled frames and the stiffness-based approach was considered to define the parameters of the struts which were modelled in OpenSees according to the approach considered in the previous sections. Figure 5.31 shows the envelope curves for the hysteretic response of the eight partially infilled specimens obtained by using two- and three-strut models along with the corresponding experimental data. Unlike for the fully infilled frames, it can be seen that the two models exhibit larger differences for these specimens, particularly in their post-peak behaviour. Nevertheless, both models are still able to capture the behaviour of the physical specimens with a good agreement, thus validating the proposed approach to calibrate the properties of multi-strut models. As referred for the fully infilled specimens, the influence of the modelling approach considered for the RC members in these cases is not accounted for and the comparison of the performance of the single strut models for these specimens should not disregard this effect.

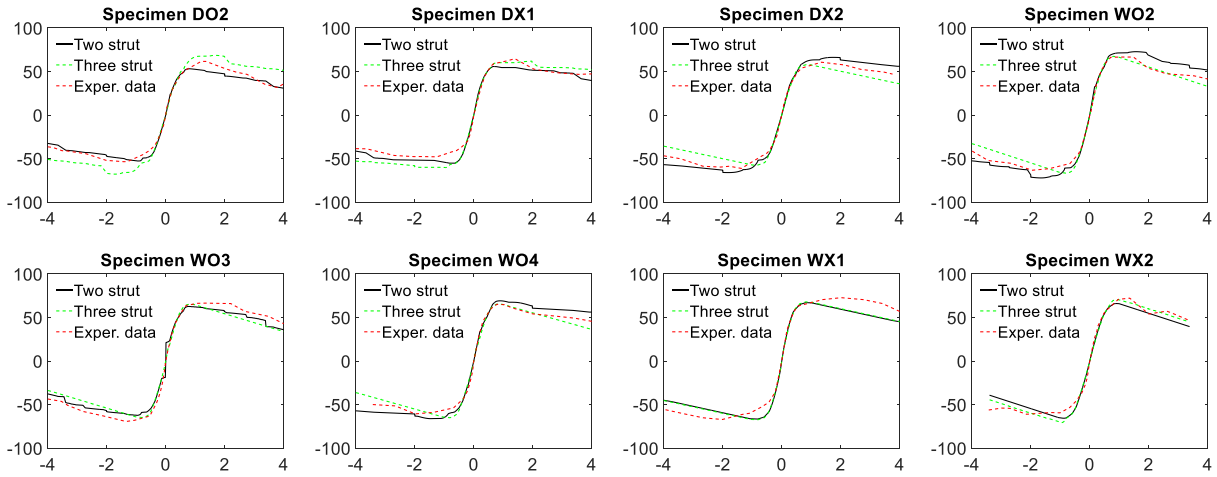

Figure 5.31 Numerical and experimental envelope curves of the hysteretic response for the eight partially infilled specimens - multi strut model calibrated from experimental data using the stiffness-based approach (vertical axes are the total shear force at the base in kN and the horizontal axes represent the lateral drift ratios in %)

5.5.2 Model by Rodrigues, *et al.* (2010)

In order to also validate the proposed calibration procedures for a different type of infill model, the model proposed by Rodrigues*, et al.* (2010) was considered as a case study. This model simulates the behaviour of masonry infills by considering four rigid elements and a central element where the nonlinear behaviour is concentrated, as shown in Figure 5.32. By concentrating the nonlinear behaviour of the panel in a single element that will exhibit both positive and negative behaviour, the model has the capability of representing the interaction between both directions of loading (i.e. damage of the panel in one direction can affect its behaviour in the other direction). Furthermore, since this central element introduces two additional nodes, it allows the model to be potentially extended to include the out-of-plane behaviour of the infill. To test the reliability of the model, its behaviour was first analysed by simulating the test of one of the previously considered fully infilled specimens. Specimen S was selected and its corresponding infill behaviour was defined by the previously obtained force-displacement trilinear envelope. The RC frame members were simulated using the force-based modelling approach presented in previous sections and the Pinching4 material of OpenSees was used to model the behaviour of the central element using the same hysteric rules that were also considered in the previous sections. To illustrate the results obtained, Figure 5.33 shows the envelope curves of the hysteretic response and of the experimental data. As can be seen, there are significant differences between the numerical and experimental responses. However, these differences are mostly in the stiffness and indicate that the numerical model is stiffer than the physical specimen.

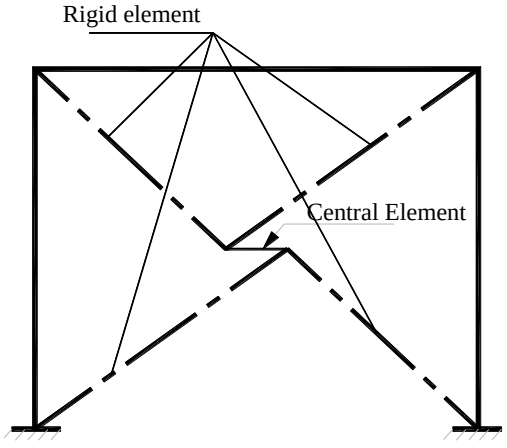

Figure 5.32 The configuration of the model proposed by Rodrigues*, et al.* (2010)

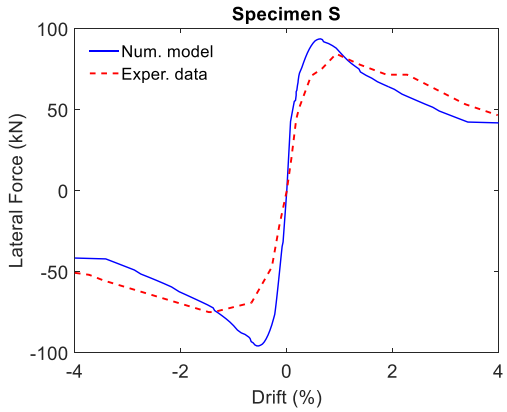

Figure 5.33 Envelope of the hysteretic curve of specimen S obtained from using the model by Rodrigues, *et al.* (2010) with direct parameter input along with the experimental data.

To overcome the problems found in the previous example, an adequate procedure needs to be defined to establish the parameters of this model. At first, the equivalent lateral stiffness of the elements involved in the model was analysed, as shown in Figure 5.34. The equivalent stiffness K_j of this system can be seen to be given by:

$$K_j = \left(\frac{1}{k_1 + k_2} + \frac{1}{k_c} + \frac{1}{k_3 + k_4} \right)^{-1} \tag{5.9}$$

where the terms k_1, k_2, k_3 and k_4 reflect the stiffness of the rigid struts. Therefore, the reverse of those terms is negligible. As such, the behaviour of this model is controlled by the central element and the equivalent stiffness K_j is equal to k_c. The stiffness of the central element is given by equation (5.10) where l^* is the length of the central element. In order to have realistic results from this model, k_c should be equal to the stiffness of the diagonal stiffness given by equation (5.11). By comparing the lateral stiffness of the diagonal strut given by equation (5.11) with that of equation (5.10), it can be seen that k_c should be divided by the factor defined by equation (5.12).

$$k_c = \frac{(EA)}{l^*} \tag{5.10}$$

$$k_d = \frac{(EA)}{l_{diagonal}} \cos^2 \theta \tag{5.11}$$

$$C = \frac{l_{diagonal}}{l^* \cos^2 \theta} \tag{5.12}$$

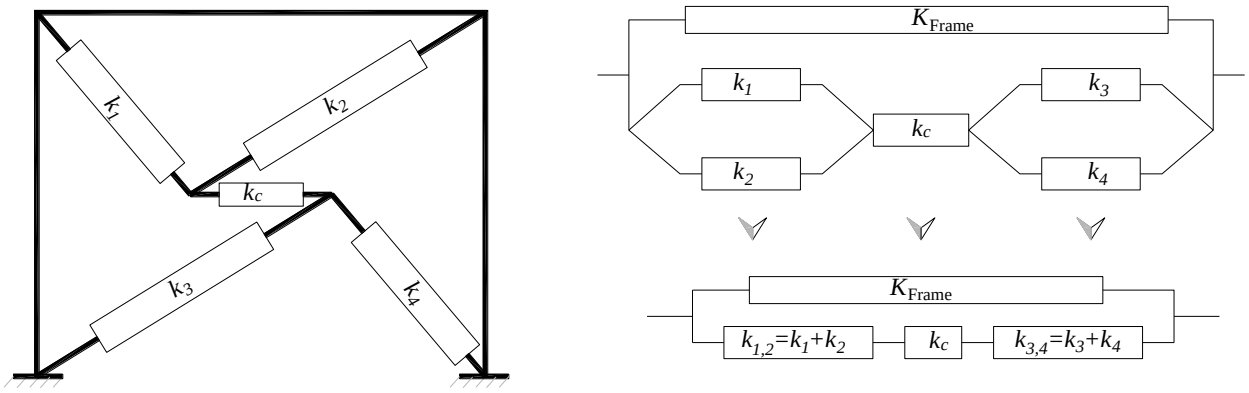

Figure 5.34 Lateral stiffness analysis for the model proposed by Rodrigues*, et al.* (2010)

Using the correction factor defined by equation (5.12) to establish the behaviour of the infill, eight different fully infilled specimens and eight partially infilled specimens were modelled using the Rodrigues*, et al.* (2010) model. To illustrate the results that were obtained using this modelling approach, Figure 5.35 shows the envelope curves for the hysteretic response of the fully infilled specimens obtained by the numerical models along with the corresponding experimental data. As can be seen, the behaviour of the Rodrigues*, et al.* (2010) model with the corrected stiffness is able to capture the behaviour of the physical specimens. Issues related with the inability to fully capture the asymmetry of the real behaviour are related to the factors discussed in the previous sections. To illustrate the results that were obtained for the partially infilled frames, Figure 5.36 shows the envelope curves for the hysteretic response and the corresponding experimental data. As for the fully infilled frames, the Rodrigues*, et al.* (2010) model with the corrected stiffness is able to adequately represent the behaviour of the specimens.

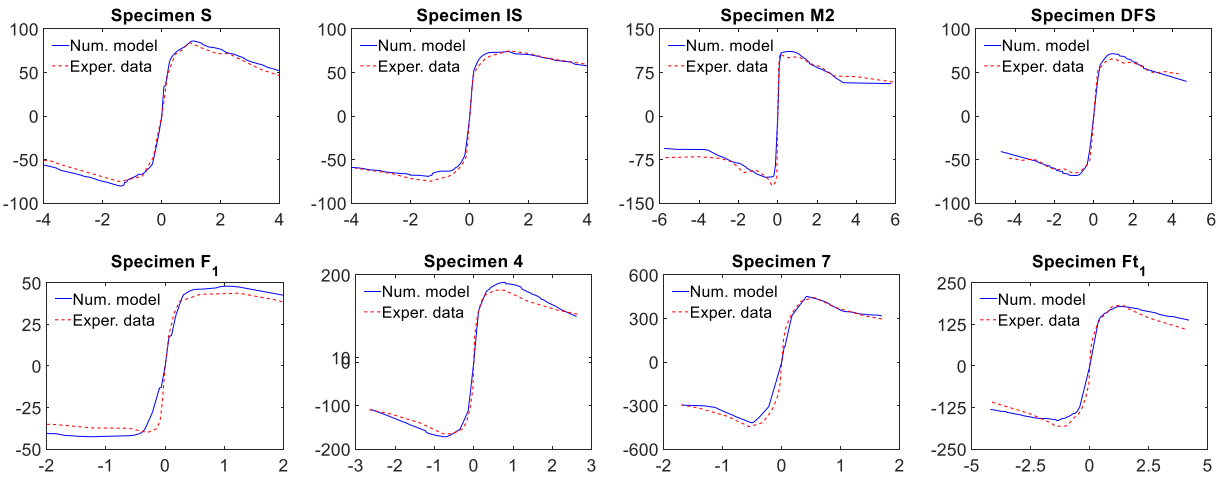

Figure 5.35 Numerical and experimental envelope curves of the hysteretic response for the eight fully infilled specimens using the model by Rodrigues, *et al.* (2010) with a corrected stiffness (vertical axes are shear at base (kN) and horizontal axes are the lateral drifts (%))

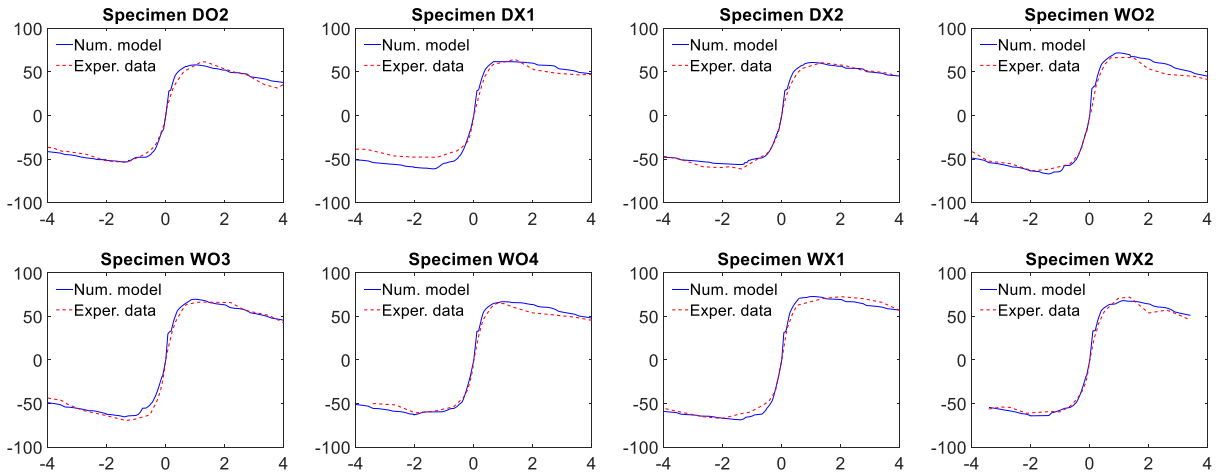

Figure 5.36 Numerical and experimental envelope curves of the hysteretic response for the eight partially infilled specimens using the model by Rodrigues, *et al.* (2010) with a corrected stiffness (vertical axes are shear at base (kN) and horizontal axes are the lateral drifts (%))

5.6 Influence of the infill model on local structural demand

In this section, the reliability of the different models was evaluated by analysing their effects on the local structural demand of the RC members, namely on the value of the shear force in the columns. To analyse this effect, the frame F1 presented at the beginning of this chapter with a Type 1 masonry

(with a compressive strength equal to 2.1 MPa) was considered as a case study. Since the load transferred through the infill depends on the type of contact between the infill and the RC frame, two types of contact were tested: a) a strong contact interaction and b) a weak contact interaction. The detailed finite element model of frame F1 provided the reference results of the demand that were then compared to those obtained by modelling the frame using different macro-models for the infill. In these analyses using macro-models (hereon termed simplified models), the bare frame was modelled using force-based elements for the RC members following the modelling assumptions presented in the previous sections. However, in order to minimize the uncertainties in the bare frame response, the parameters of the steel material of the detailed finite element model were fine-tuned to match the response obtained from the simplified model. In order to analyse the comparability of the two bare frame models, these were first analysed under a vertical loading imposed as a displacement followed by a lateral monotonic loading imposed until a 0.60% lateral drift was reached. The results obtained are presented in Figure 5.37 which shows the evolution of the total base shear and of the shear force in each column. As can be seen, there is a good match between the models and the global shear force can be seen to be divided equally among both columns.

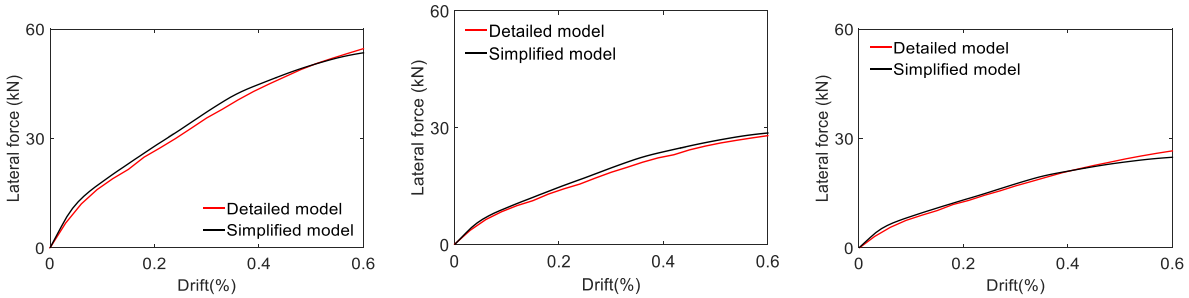

a) total base shear b) shear at column 1 c) shear at column 2

Figure 5.37 Capacity curves obtained from the detailed finite element model and from the simplified model for the bare frame F1

As referred, the effect of the simplified models in the local structural demand was analysed for two different types of contact between the infill and the RC frame. For the case of strong contact interaction, it is assumed there is full contact between the infill and the surrounding frame. For this kind of connection, the contact elements between the infill and the surrounding RC frame of the detailed finite element model were simulated using conditions similar to those of the normal bed joints (see Chapter 4 for additional details). For the case of a weak contact interaction, the contact elements

between the infill and the surrounding RC frame of the detailed finite element model were simulated using frictional and compressive contact only.

In order to simulate the behaviour of the detailed finite element model (DM) for these conditions, four different simplified models were used: one involving a compression-only strut termed CS (involving a model similar to those considered in section 5.3.1), one involving the Rodrigues*, et al.* (2010) model termed RM, one involving a strut active both in tension and in compression termed CTS (involving a model similar to those considered in section 5.3.2) and one involving a compression strut that has a tensile strength of 10% of the compressive strength termed C-10%T (involving a model similar to those considered in section 5.3.1 but with the material Concrete02 of OpenSees assigned to the strut instead of Concrete01). The parameters required to model the infill were defined based on the calibration procedure presented in the previous section where the masonry response was extracted from the DM model. Furthermore, all the models were analysed for the same loading as the bare frame.

The results obtained for the case where there is a strong contact between the infill and the frame are presented in Figure 5.38 which shows the capacity curves that were obtained for the DM model and for the four simplified models. The results include the global shear response obtained for each specimen and also the shear force at each column to evaluate the local response of each model. Globally all models are able to capture the evolution of the total shear force with the increase of the lateral displacement. On the contrary, when analysing the shear force evolution in each column, there are clear differences from the simplified models to the DM model. The response of the DM model shows that a large portion of the lateral force is supported by column 2 and a lower part is supported by column 1. This trend is captured by models CS and C-10%T, although the distribution between columns is not exactly the same as in model DM. Including some tensile strength in the strut appears to provide better results at early stages of the loading and for the later stages of the loading in column 2. On the contrary, models RM and CTS assume that the shear forces are equally divided between both columns which does not simulate the real situation. In order to analyse the load pattern through the infill, the principal stress vectors of model DM were plotted in Figure 5.39 where it can be seen that the loads are transferred diagonally through the infill but distributed along the panel. This means that using a single strut model might not be the best option to represent this type of infill; a carefully selected multi-strut system might yield a more realistic distribution of forces.

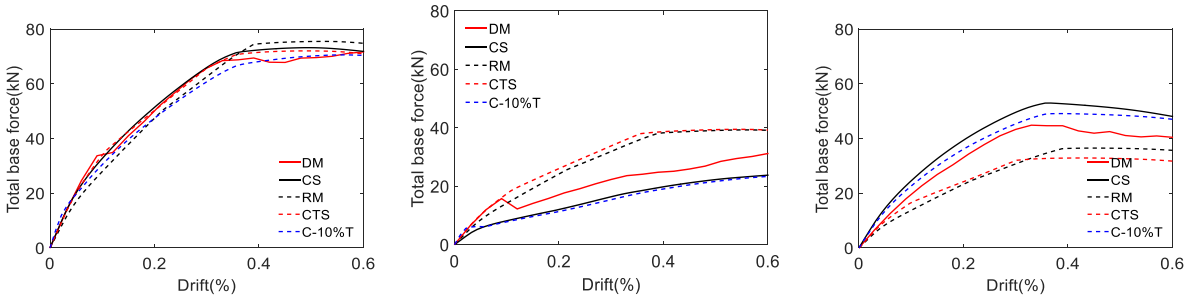

a) total base shear b) shear at column 1 (left side) c) shear at column 2 (right side)

Figure 5.38 Capacity curves obtained from the detailed finite element model and from the four different simplified modelling procedures for frame F1 with a strong contact with the frame

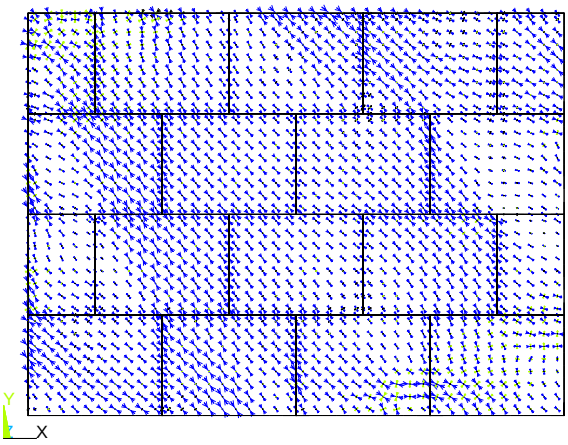

Figure 5.39 Principal stresses in the specimen with strong contact obtained from the detailed finite element model

The results obtained for the case where there is a weak contact between the infill and the frame are presented in Figure 5.40. The figure shows the capacity curves that were obtained for the DM model and for the four simplified models. The results include the global shear response obtained for each specimen and also the shear force at each column to evaluate the local response of each model. Again, all models are able to globally capture the evolution of the total shear force with the increase of lateral displacement. On the contrary, when analysing the shear force evolution in each column, there are again clear differences from the simplified models to the DM model. The DM model shows that there is a 30%-70% distribution of shear forces between the left and right columns. Models CS and C-10%T are able to capture this distribution very closely because the single compression-only strut

simulates very closely the force transfer mechanism when there is a weak contact between the infill and the frame. On the other hand, models RM and CTS assume that the shear forces are equally divided between both columns which does not simulate the real situation. In order to analyse the load pattern through the infill, the principal stress vectors of model DM were plotted in Figure 5.41 where it can be seen that the loads are transferred diagonally through the infill mainly in the mid-diagonal zone of the infill. This means that this area of the panel can be idealized as one active strut for this loading direction.

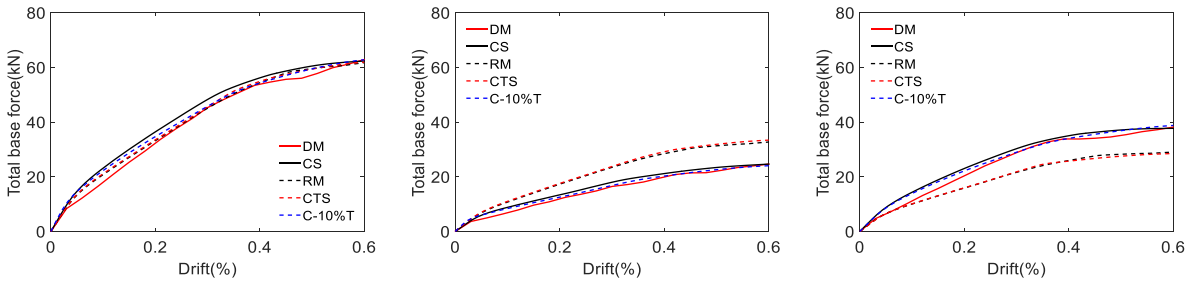

a) total base shear b) shear at column 1 (left side) c) shear at column 2 (right side)

Figure 5.40 Capacity curves obtained from the detailed finite element model and from the four different simplified modelling procedures for frame F1 with a weak contact with the frame

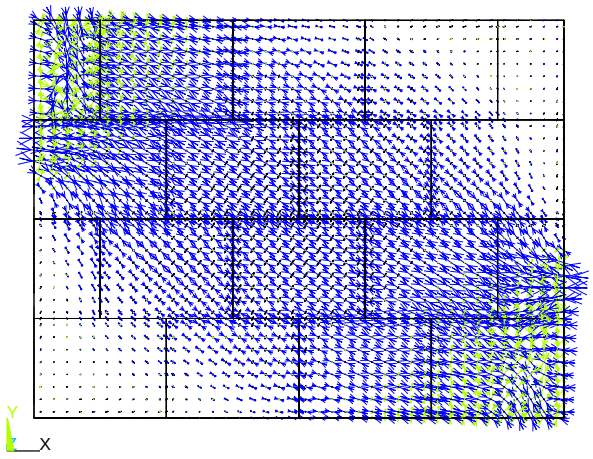

Figure 5.41 Principal stresses in the specimen with weak contact obtained from the detailed finite element model

5.7 Conclusions

Procedures to calibrate and define the parameters of strut models were presented throughout this chapter. The main idea behind the calibration procedures involves extracting the contribution of the infill panel from the global structural behaviour of the frame. The procedures were tested using fully and partially infilled specimens with different configurations and using both experimental and numerical data from detailed finite element models. Procedures were developed to define the parameters of strut models for both stiffness- and strength-based approaches. Parameters obtained from a stiffness-based approach were implemented in stress-strain compression-only strut models using predefined and adapted constitutive models. On the other hand, the strength-based approach enables the definition of a force-displacement envelope that has the potential to capture more closely the post-peak behaviour of the masonry infill. However, due to limitations of the software OpenSees, the force-displacement envelopes representing the behaviour of the masonry were not able to be associated with a compression-only element. This limitation has, however, the potential to allow the inclusion of degradation effects where loading in one direction might affect the behaviour when loading is reversed. Still, this possibility was not analysed in the present study. When comparing the experimental results of the specimens analysed with the global behaviour obtained from the simplified models involving single-strut elements with parameters defined by either a stiffness- or a strength-based approach, it can be seen that both cases provide a good agreement with the experimental data.

In order to generalize the use of the proposed calibration procedures, these were extended to be applicable to macro-models with special configurations. Procedures were defined for two multi-strut models and for the model proposed by (Rodrigues*, et al.*, 2010). By simulating the behaviour of several masonry infilled specimens using these special macro-models, their global behaviour was seen to exhibit a good agreement with the corresponding experimental data, thus validating the proposed calibration procedures.

Even though the presented macro-models were seen to be able to capture the global behaviour of the physical specimens, analysing the local structural demand they yield led to different conclusions. When analysing the shear force distribution in columns of masonry infilled frames simulated using different macro-models, it was seen that compression-only macro-models were able to provide more realistic shear force distributions in columns, when compared to models involving elements active in both loading directions.

Chapter 6.
Seismic vulnerability assessment of RC frames with masonry infills

6.1 Introduction

As mentioned in previous chapters, reinforced concrete (RC) frames with masonry infill walls are common building systems worldwide. Such systems often experience significant damage during earthquakes (e.g. see (Romão*, et al.*, 2013, Ohsumi*, et al.*, 2016, Shakya*, et al.*, 2016)), a fact implying the need to assess their seismic vulnerability in order to identify their strengthening needs. In this context, the current chapter presents a study addressing the seismic vulnerability assessment of several 2D frames with different infill panel configurations and number of storeys. Since fragility functions are increasingly used in the modern performance-based evaluation of structures to relate the seismic hazard of the site to the probability of exceedance of a given limit state of the structure, a detailed analysis addressing the development of fragility functions for different limit states was carried out for the considered cases-studies.

Even though the chapter addresses the fundamental differences in terms of performance between structures with and without masonry infills, the focus is not on establishing definitive fragility curves for specific building typologies. Instead, the proposed study analyses the influence of several parameters related to the structural modelling and of assumptions regarding the probabilistic modelling on the final fragility curves. To determine the fragility data, numerical models of the structures were developed simulating the infills using single strut models. The models were analysed under nonlinear dynamic analysis using incremental dynamic analysis (IDA) (Vamvatsikos*, et al.*, 2002). Experimental

data was considered as the reference scenario to define the parameters of the strut models and develop the seismic fragility analysis. However, numerical data obtained from refined finite element models (see Chapter 4) was also used to define the parameters of the strut models and to replicate the seismic fragility analysis for comparison. Additionally, a statistical analysis examining the probabilistic model that best fits the fragility data was also carried out. Finally, fragility analyses were also carried out considering both deterministic and probabilistic limit states to establish the influence of the limit state definition.

6.2 Characteristics of the considered buildings

An overall description of the building configurations and general characteristics that were considered to define the RC frames structures that were analysed is presented in the following. The selected RC frames are considered to be part of office buildings. The architectural plan view of the typical floor of the buildings is presented in Figure 6.1 a) while the structural system of the typical floor is presented in Figure 6.1 b). The frame of the vertical axis 5 between the horizontal axes A-D, termed herein as frame F5A-D, is the considered frame for the vulnerability analysis. This frame was analysed with different configurations (bare, fully infilled, soft-storey and partially infilled frames) and with two different numbers of storeys (four and eight storeys) as shown in Figure 6.2 and Figure 6.3.

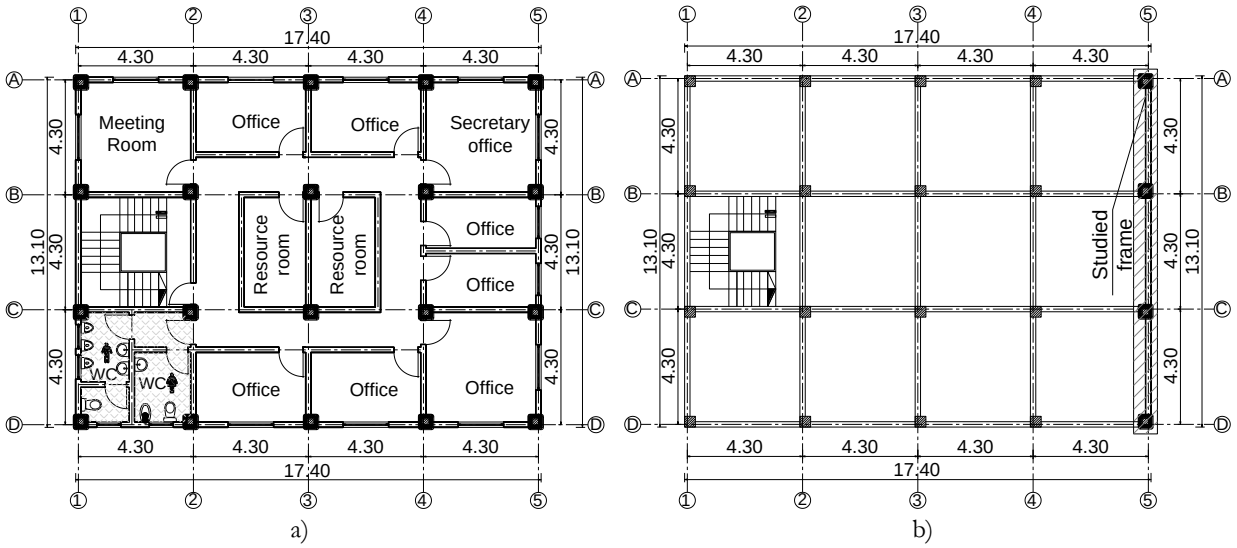

Figure 6.1 Typical plan view for the considered office building: a) architectural plan b) structural system showing the considered frame (all dimensions in m)

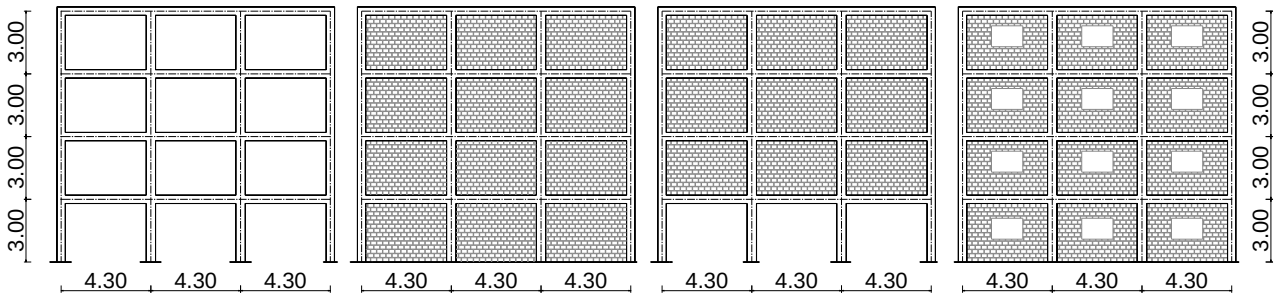

a) Bare frame BF-4 b) Fully infilled FF-4 c) Soft storey frame SF-4 d) Partially infilled PF-4

Figure 6.2 Different frame configurations for the four-storey building (all dimensions in m)

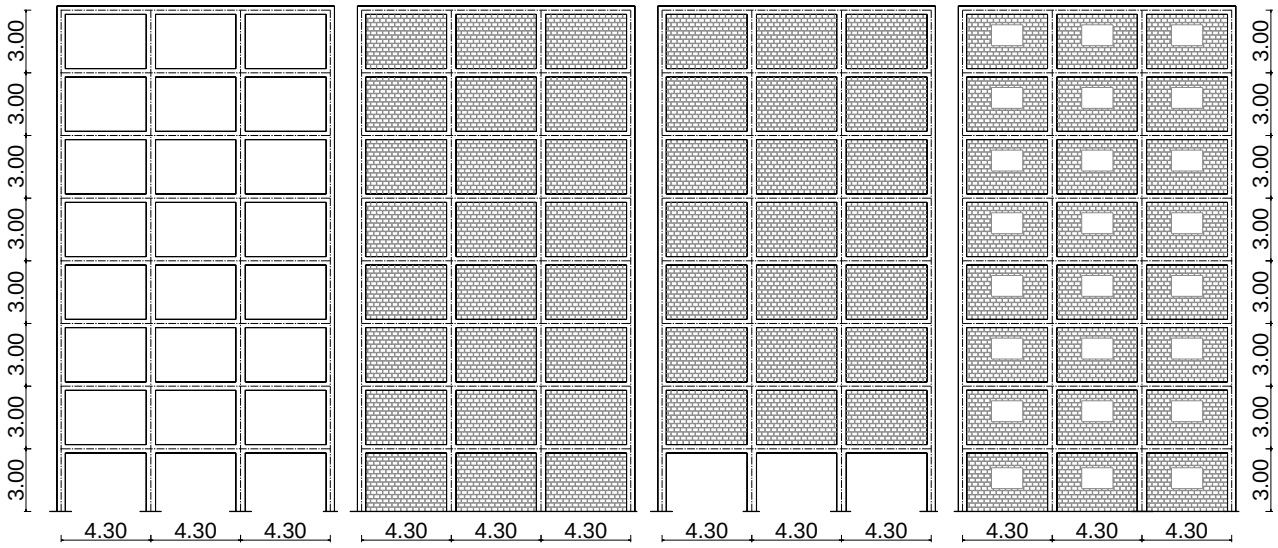

a) Bare frame BF-8 b) Fully infilled FF-8 c) Soft storey frame SF-8 d) Partially infilled PF-8

Figure 6.3 Different frame configurations for the eight-storey building (all dimensions in m)

The structures were designed for gravity loading only to represent a scenario of non-seismically designed structures. The mechanical properties of the selected materials are presented in Table 6.1 and the cross-section details for frame F5A-D are shown in Table 6.2. It is noted that the reinforcement details were homogenised in order to have a small number of different cross sections. The infills were defined according to the data from the experimental campaign of (Kakaletsis*, et al.*, 2009). The size and configurations of the infill panels were scaled to match the real size of the building while maintaining the aspect ratio of the panels equal to that of the test panels.

Table 6.1 Mechanical properties of the materials

Concrete compressive strength f_c (MPa)	Steel		Infill panel material	
	Yield stress σ_y (MPa)	Elastic modulus (GPa)	Brick unit compressive strength f_m (MPa)	Mortar compressive strength f_{mo} (MPa)
25.0	522.0	190.0	3.1	1.53

Table 6.2 Cross-section details for frame F5A-D

No of storeys	Axis	Columns		Beams						
		Section (cm^2)	Reinforcement	Section (cm^2)	Reinforcement					
					Start		Middle		End	
					upper	lower	upper	lower	upper	lower
Four storeys	A	30x30	8 Ø 15	25x40	4 Ø 12	4 Ø 12	4 Ø 12	4 Ø 12	4 Ø 12	4 Ø 12
	B	30x30	8 Ø 15	25x40	4 Ø 12	4 Ø 12	4 Ø 12	4 Ø 12	4 Ø 12	4 Ø 12
	C	30x30	8 Ø 15	25x40	4 Ø 12	4 Ø 12	4 Ø 12	4 Ø 12	4 Ø 12	4 Ø 12
	D	30x30	8 Ø 15	25x40	4 Ø 12	4 Ø 12	4 Ø 12	4 Ø 12	4 Ø 12	4 Ø 12
Eight storeys	A	30x30	8 Ø 15	25x40	4 Ø 12	4 Ø 12	4 Ø 12	4 Ø 12	4 Ø 12	4 Ø 12
	B	45x45	10 Ø 15	25x40	4 Ø 12	4 Ø 12	4 Ø 12	4 Ø 12	4 Ø 12	4 Ø 12
	C	45*45	10 Ø 15	25x40	4 Ø 12	4 Ø 12	4 Ø 12	4 Ø 12	4 Ø 12	4 Ø 12
	D	30x30	8 Ø 15	25x40	4 Ø 12	4 Ø 12	4 Ø 12	4 Ø 12	4 Ø 12	4 Ø 12

6.3 Description of the numerical model

6.3.1 Modelling of the RC frame

The software OpenSees (McKenna*, et al.*, 2000) was used to perform the nonlinear dynamic analyses for all the considered numerical models. The RC frame elements (i.e. beams and columns) were modelled using force-based elements considering fibre-sections. The Modified Radau Hinge Integration method (Fenves*, et al.*, 2006, Scott*, et al.*, 2013) was the selected plastic hinge integration method to assign inelastic actions at the end regions of the element with a specified length. Additional fibre sections were also considered in the central part of the element to model its possible nonlinearity (Scott*, et al.*, 2013). A total of six integration points are used in the element state determination (two for each hinge and two for the central part of the element). The value of the plastic hinge length l_p was defined by the following expression proposed by Paulay*, et al.* (1992):

$$l_p = 0.08 l_e + 0.022 d_b f_y \tag{6.1}$$

where l_e is the element length, d_p is the diameter of the steel rebars and f_y is the steel yield stress in MPa.

For the fibre discretization of the RC cross sections, the concrete cover was modelled using the concrete model termed Concrete01 representing the uniaxial concrete material with degraded linear unloading/reloading stiffness in compression and no tensile strength. Confined concrete was modelled using a confinement factor determined based on the expression proposed by Kent, *et al.* (1971) associated with the Concrete01 model. Steel reinforcement bars were modelled using the uniaxial Giuffre-Menegotto-Pinto model (Menegotto*, et al.*, 1973) with isotropic hardening, termed Steel02 in OpenSees, with the default parameters proposed by the software. For the beam-column joints, a rigid end-offset joint model was used (Mondal, *et al.*, 2008). The lengths of the rigid parts were considered to be half of the depth of the perpendicular element.

To complement the description of the models, the fundamental periods of the bare frame models were determined from modal analyses. Table 6.3 presents the periods of the first and second modes of the four- and eight-storey bare frames.

Table 6.3 First and second periods of the considered structures (bare frames)

No. of storeys	Acronym	T_1 (s)	T_2 (s)
Four storeys	BF-4	0.68	0.22
Eight storeys	BF-8	1.05	0.35

6.3.2 Modelling of the masonry infills

The infills were modelled using a single compressive strut element connected to the RC frame at the corner nodes. The properties of the strut element were determined using the stiffness-based approach presented in the previous chapter. As referred before, a set of masonry infilled structures were simulated using strut elements with properties based on experimental data and a second set replicated these structures using strut elements with properties now based on numerical data. The mechanical properties of the strut were determined based on the scaled experimental data and on the scaled numerical model. The extracted responses of the infill were then scaled according to the ratio between the tested panel and the panel considered in the numerical models which has the same aspect ratio of the scaled panel (CEB, 1996, Petry*, et al.*, 2014). Models where the single strut was calibrated based on experimental data were used as reference models, first to perform a comparative assessment

of the performance of the different infilled frames, and then to assess differences in the performance of the frames when the infills are modelled based on numerical data.

The data of specimen S and specimen WO3 were used to calibrate the single strut model to simulate the fully and partially infilled panels, respectively (see previous chapters for details on the specimens). To illustrate the differences between the experimental and numerical data, the positive envelope of the extracted masonry components of the responses of the experimental and numerical data are plotted in Figure 6.4 for both the fully and the partially infilled panels. The area of the struts and the main parameters of the masonry materials are shown in Table 6.4. It is recalled that when defining the strut parameters using the stiffness-based approach, the fundamental parameters are the maximum compressive strength of the infill and the residual stress, along with their corresponding strains. Therefore, when analysing Figure 6.4 a), the differences between the experimental and numerical curves are not found to be excessive since points A and B are relatively close. On the other hand, for the case of Figure 6.4 b), the strain difference between point B and point A is more significant. It is noted that no specific value for the strain level corresponding to the maximum strength (ε_m) of the masonry material can be found in the literature and several researchers suggest the use of different values. For example (Al-Chaar*, et al.*, 2008) used 0.0031 and (Dolšek*, et al.*, 2008) suggest values within the range 0.0015~0.002, depending on the infill aspect ratio. In order to analyse the importance of the pre-peak stiffness of the masonry infill, two sets of strut models were defined for the partially infilled frames: one set where the infill parameters are based on point A and a second set where the infill parameters are based on point B. The former is considered to be the reference set while the latter is only considered to examine the differences that are obtained in the fragility curves as a result of using a lower stiffness for the struts. In the numerical models, the previously referred masonry parameters were used to define the masonry material with zero tensile strength which is simulated by the Concrete01 constitutive model of OpenSees.

To complement the description of the models, the fundamental periods of the infilled frame models with different configurations were determined from modal analyses Table 6.5 presents the periods of the first and second modes of the infilled models with their different configurations (the suffixes -Exp and –Num in the identification of the structures stand for models where the infills were defined based on experimental data and for models where the infills were defined based on data from refined finite element analyses). By comparing these values with those in Table 6.3, it is clear that considering the infill contributions introduces a significant reduction of the fundamental periods of

the structures and, therefore, a significant change of their dynamic characteristics, as will be presented in detail throughout this chapter.

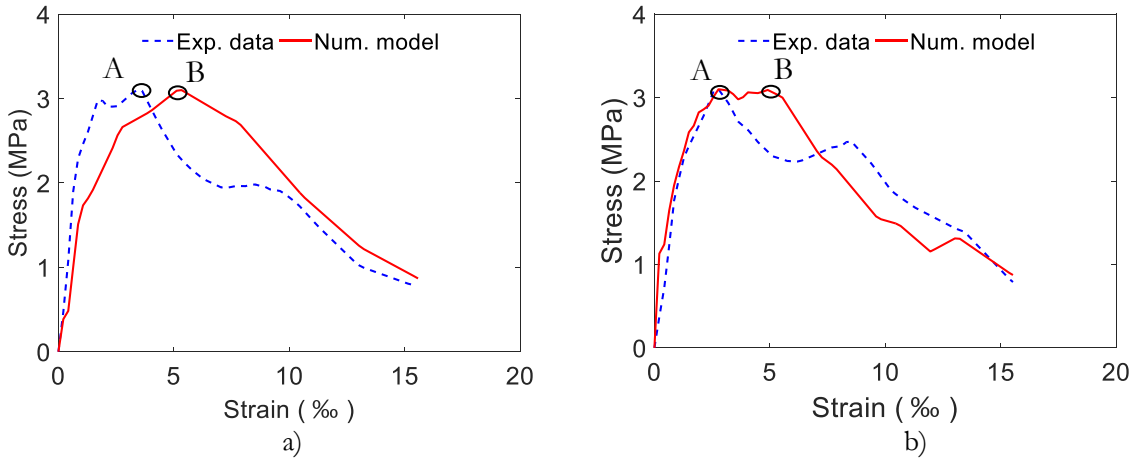

Figure 6.4 Experimental and numerical responses for the masonry component: a) fully infilled specimen; b) partially infilled specimen

Table 6.4 Main parameters of the struts and their materials based on experimental data and numerical data

Parameter	Fully infilled			Partially infilled		
	experimental	numerical	Ratio	experimental	numerical A/B	Ratio A/B
Area of the strut (m^2)	0.195	0.22	**1.13**	0.127	0.116/0.114	**0.91/0.90**
Maximum strength (MPa)	3.10	3.10	**1.00**	3.10	3.10/3.10	**1.00/1.00**
Strain at maximum strength (‰)	3.42	5.3	**1.55**	2.78	2.78/5.1	**1.00/1.83**
Residual strength (MPa)	0.31	0.31	**1.00**	0.31	0.31/0.31	**1.00/1.00**
Ultimate Strain (‰)	23.2	23.38	**1.01**	23.31	23.31/23.31	**1.00/1.00**

Table 6.5 First and second periods of the considered infilled structures

No. of storeys	Experimental based				Numerical based			
	model	Acronym	T_1(s)	T_2(s)	model	Acronym	T_1(s)	T_2(s)
Four storeys	Fully infilled	FF-4-Exp	0.21	0.07	Fully infilled	FF-4-Num	0.23	0.08
	Soft storey infilled	SF-4-Exp	0.44	0.9	Soft storey infilled	SF-4-Num	0.44	0.10
	Partially frame	PF-4-Exp	0.23	0.08	Partially frame	PF-4-Num	0.24	0.08
Eight storeys	Fully infilled	FF-8-Exp	0.45	0.15	Fully infilled	FF-8-Num	0.50	0.16
	Soft storey infilled	SF-8-Exp	0.57	0.19	Soft storey infilled	SF-8-Num	0.59	0.19
	Partially frame	PF-8-Exp	0.47	0.17	Partially frame	PF-8-Num	0.49	0.16

6.4 Description of the analysis procedure

6.4.1 Incremental dynamic analysis

The seismic behaviour of the considered structures was analysed using IDA, a computational analysis procedure for performing a comprehensive assessment of the behaviour of structures under seismic loading. The procedure involves subjecting a structural model to one or more ground motions, each scaled to multiple levels of intensity, to produce one or more curves of structural response versus the ground motion intensity levels (Vamvatsikos, *et al.*, 2002). Therefore, performing a multi ground motion IDA that will capture the response uncertainty coming from the record-to-record variability requires a series of nonlinear dynamic analyses under a multiply scaled suite of adequate ground motion records. The scaling levels need to be appropriately selected to obtain the structure's response throughout its entire range of behaviour. Furthermore, the ground motion scaling levels reflect increasing levels of an intensity that is defined by a parameter usually termed intensity measure (IM).

The structure's response (or demand) can be defined by any type of structural or non-structural parameter, local or global (e.g. maximum interstorey drift over the height, peak storey drifts, peak floor accelerations, shear force, etc). In this study, the maximum interstorey drift over the height is considered as the structural demand parameter representing the behaviour of the structures. This demand parameter was selected due to its good correlation with structural losses and with a large part of the non-structural losses. With respect to the selected IM, even though the 5%-damped spectral acceleration for the first-mode period of the structure is one of the most widely used IMs, due to the variability of the first mode period of the structures during its range of behaviour (e.g. depending on whether the infill is active or not, or depending on the level of ductility demand), the peak ground acceleration (PGA) was considered instead. Furthermore, considering PGA also allows for a more direct comparison of the fragility curves between the structures since the same IM is common to all.

6.4.2 Ground motion record selection

The IDAs of each structure were carried out using fifty real ground motion records that match the selected target response spectrum. The selected target response spectrum defining the reference seismic scenario corresponds to that of Zone 3 of the Portuguese territory considering the interplate

seismic action (type 1) and a soil of type B according to the Portuguese National Annex of Eurocode 8 (EC8-1, 2010). The PGA considered for this scenario was 0.15*g*, corresponding to a return period of 475 years. The records were selected from the NGA database (Chiou, *et al.*, 2008) using the software *SelEQ* platform (Macedo*, et al.*, 2013, Araújo*, et al.*, 2016). Table 6.6 provides the general characteristics of the selected ground motions. The records are characterized by magnitudes higher than 5.5 and epicentral distances larger than 10 km. These records were obtained from the NGA database by enforcing that the average response spectrum of the selected records matches the target spectrum in the range of periods between 0.15s and 1.5s, which cover all fundamental periods of the selected structures (Ricci*, et al.*, 2016). Furthermore, the ground motion record selection process also ensures that, for this period range, the spectral values of each individual ground motion are within a bound defined by ±50% of the target spectral values. Figure 6.5 shows the elastic response spectrum for the fifty ground motion records along with their mean spectrum and the target response spectrum. As referred before, the selected IM was PGA and each ground motion was scaled to several intensities starting from 0.05g until leading to global dynamic instability (i.e. "numerical failure").

Table 6.6 Characteristics of the selected ground motions

Name	Year	M	Depth km	Name	Year	M	Depth km
Imperial Valley-06	1979	6.53	33.73	**Chi-Chi, Taiwan**	1999	7.62	41.2
Imperial Valley-02	1940	6.95	12.99	**Imperial Valley-06**	1979	6.53	43.15
Northridge-01	1994	6.69	25.44	**Chi-Chi, Taiwan**	1999	7.62	25.57
Chi-Chi, Taiwan	1999	7.62	63.29	**Imperial Valley-06**	1979	6.53	31.99
Chi-Chi, Taiwan-04	1999	6.2	50.36	**Chi-Chi, Taiwan**	1999	7.62	32.67
Coalinga-01	1983	6.36	55.67	**Superstition Hills-02**	1987	6.54	19.51
Northridge-01	1994	6.69	16.99	**Landers**	1992	7.28	75.2
Chi-Chi, Taiwan	1999	7.62	21.8	**Imperial Valley-06**	1979	6.53	31.99
Northridge-01	1994	6.69	24.13	**Chi-Chi, Taiwan**	1999	7.62	38.53
Landers	1992	7.28	75.2	**Chi-Chi, Taiwan**	1999	7.62	45.37
Taiwan SMART1(40)	1986	6.32	65.48	**Kocaeli, Turkey**	1999	7.51	47.03
Chi-Chi, Taiwan	1999	7.62	43.31	**Northridge-01**	1994	6.69	31.73
Loma Prieta	1989	6.93	51.2	**Northridge-01**	1994	6.69	33.25
Loma Prieta	1989	6.93	35.47	**Northridge-01**	1994	6.69	29.59
Chi-Chi, Taiwan	1999	7.62	26.67	**Chi-Chi, Taiwan**	1999	7.62	81.1
Loma Prieta	1989	6.93	18.46	**Taiwan SMART1(45)**	1986	7.3	71.35
Manjil, Iran	1990	7.37	77.84	**Northridge-01**	1994	6.69	32.72
Superstition Hills-02	1987	6.54	29.91	**Northridge-01**	1994	6.69	25.42
Loma Prieta	1989	6.93	55.16	**Imperial Valley-06**	1979	6.53	27.47
Coyote Lake	1979	5.74	23.24	**Chi-Chi, Taiwan**	1999	7.62	79.2
Chi-Chi, Taiwan-03	1999	6.2	32.39	**Chi-Chi, Taiwan-04**	1999	6.2	39.86
Chi-Chi, Taiwan	1999	7.62	55.23	**Chi-Chi, Taiwan**	1999	7.62	24.41
Imperial Valley-06	1979	6.53	27.13	**Chi-Chi, Taiwan**	1999	7.62	25.57
Chi-Chi, Taiwan	1999	7.62	101.62	**Imperial Valley-06**	1979	6.53	27.23
Chalfant Valley-02	1986	6.19	31.25	**Northridge-01**	1994	6.69	12.35

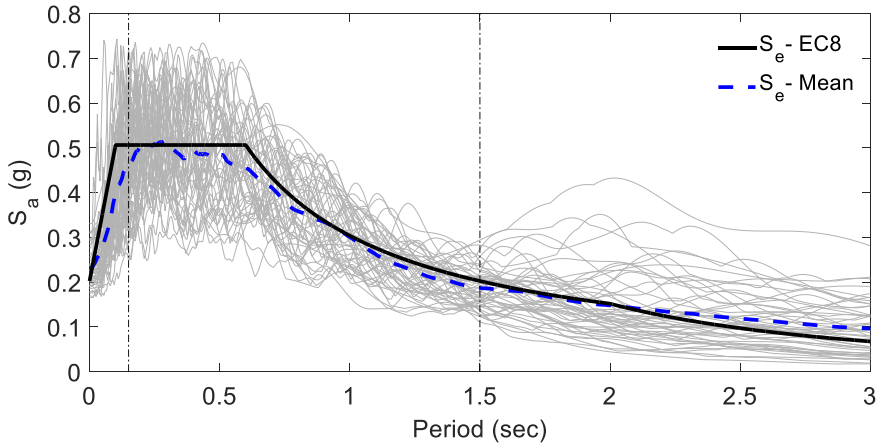

Figure 6.5 Scaled response spectra for the fifty ground motions with their mean response spectrum and the target elastic response spectrum for Zone 3 of the Portuguese territory (type 1 earthquake and soil B)

6.4.3 Definition of the limit states

Limit states are a measure to describe the state of the structure according to predefined levels of damage, e.g. onset of cracking, yielding, collapse. A significant amount of research has been carried out over the years to define performance limit states for RC building (e.g. see (FEMA-273, 1997, FEMA-356, 2000, Rossetto*, et al.*, 2003, Ghobarah, 2004, Rossetto*, et al.*, 2005) among several others). In the present study, since structural demand and performance is defined in terms of maximum interstorey drifts over the height of the structure (IDR_{max}), the limit states shown in Table 6.7 were used, which correspond to those proposed by (Rossetto*, et al.*, 2005). The performance of the structures was evaluated considering to two types of limit states: deterministic limit states and nondeterministic (variable) limit states. For the first case, the performance is established for each ground motion by determining the IM value for which the deterministic value of a given limit state is reached, as shown in Figure 6.6 a). For the second case, the performance is established for each ground motion by determining the IM values for which a sample of limit state values (compatible with the variability conditions that were considered) is reached, as shown in Figure 6.6 b).

Table 6.7 Threshold values for the considered damage limit states defined in terms of IDR_{max}

Damage state	Slight damage	Light damage	Moderate damage	Extensive damage	Partial collapse	Collapse
IDR (%)	0.05	0.08	0.30	1.15	2.80	>4.36

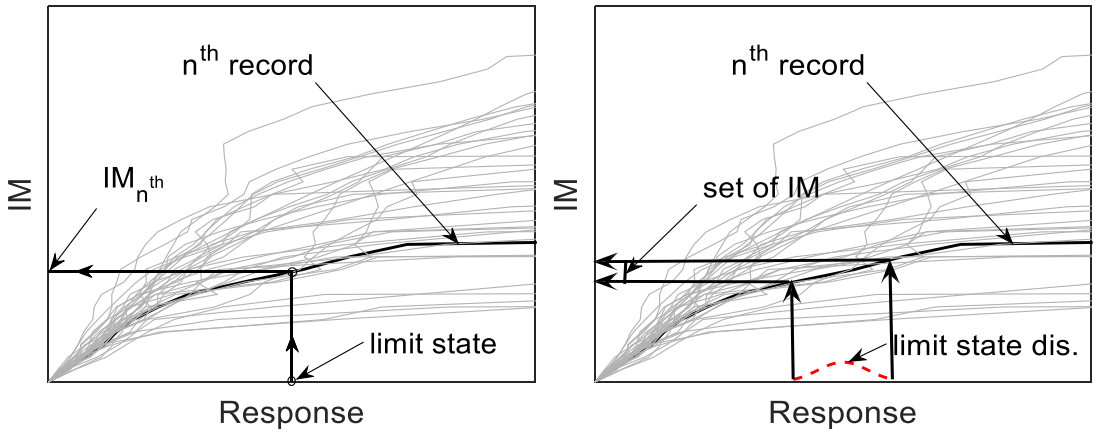

Figure 6.6 Performance analysis based on the IDA curves for a) a deterministic limit states and b) a nondeterministic limit states

In this study, the variability of the limit state values was considered to be defined by a triangular distribution for simplicity and to have bounded distributions. Two distribution scenarios were defined, as shown in Figure 6.7, where the first distribution uses a predefined coefficient of variation (CV) of 20% representing the dispersion of the limit state value. In this case, the range of the several limit states may overlap, as shown in Figure 6.7. To analyse also a situation where each limit state is assigned with a range that does not overlap with others, a second distribution was defined based on dividing the range between two consecutive deterministic limit state values in two equal ranges, each one assigned to consecutive limit state values (see Figure 6.7). It is noted that the limit state distributions that are represented in Figure 6.7 are not to scale. For each distribution, the corresponding deterministic limit state value is the most likely value of the distribution (i.e. the mode). The parameters of the considered limit state distributions for the two scenarios are presented in Table 6.8 for each limit state where a, b, c and μ are the minimum, the mode, the maximum and the mean values of the distributions, respectively.

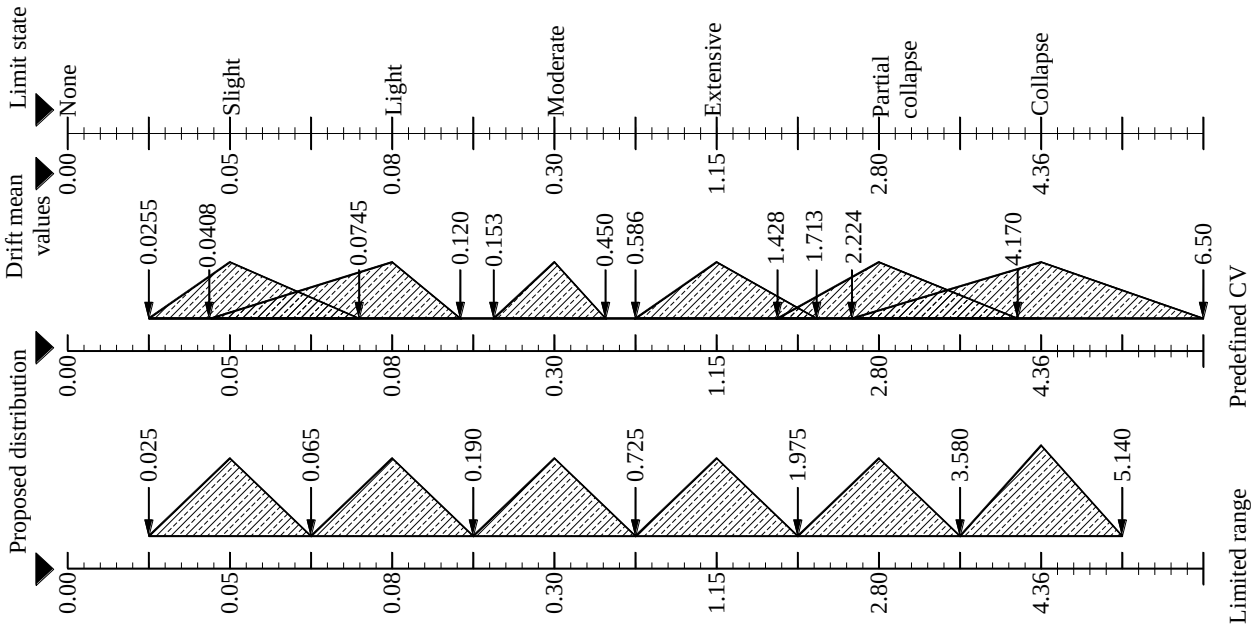

Figure 6.7 Proposed distributions for the nondeterministic limit states (the represented limit state distributions are not to scale)

Table 6.8 Parameters of the selected triangular distributions representing nondeterministic limit states

Limit state	With predefined CV (NDLSCV)					Width predefined range (NDLSR)				
	a	b	c	μ	CV (%)	a	b	c	μ	CV (%)
Slight damage	0.0255	0.05	0.0745	0.05	20	0.025	0.05	0.065	0.047	17.68
Light damage	0.0408	0.08	0.120	0.08	20	0.065	0.08	0.19	0.112	24.95
Moderate damage	0.153	0.30	0.450	0.30	20	0.19	0.30	0.725	0.405	28.48
Extensive damage	0.586	1.15	1.713	1.15	20	0.725	1.15	1.975	1.283	20.22
Partial collapse	1.428	2.80	4.170	2.80	20	1.975	2.80	3.58	2.785	11.77
Collapse	2.224	4.36	6.50	4.36	20	3.58	4.36	5.14	4.360	7.30

6.5 Results of the IDAs

Fourteen structures with different configurations were analysed using the procedures and modelling features previously described. These involve seven four-storey structures which are one bare frame, three infilled fames with different configurations and infill parameters based on experimental data and three infilled fames with different configurations and infill parameters based on numerical data, and seven eight-storey structures similar to the four-storey ones. The incremental dynamic

analyses were performed for all models due to the selected ground motions records. The results shown in Figure 6.8 to Figure 6.11 illustrate the IDA curves that were obtained for the different structures. Each curve represents the evolution of IDR_{max} for increasing values of the PGA. To facilitate reading the results, the bare frame results of each case are shown with the results of all the infilled structures.

It can be seen that, for all cases, the SF structures always exhibit higher values of IDR_{max} for low IMs, even when compared to those of the bare frame. This is due to the soft-storey failure mechanism that occurs very early as a result of the structural configuration that is considered for these structures. On the other hand, for a given IM level, the fully infilled structure, followed then by the partially infilled structure, generally exhibit lower IDR_{max} values than the corresponding bare frame structure. For a better comparison between the results obtained when the infill properties are defined based on numerical or experimental data, the mean IDA curves (the IDA curves obtained by computing the mean demand of all IM values) obtained for both cases and for a given structure are shown in Figure 6.12. Generally, both infill models yield similar mean IDA curves. Larger differences are only found for the fully infilled structures for larger demand values (i.e. above 3%).

In order to assess quantitatively the differences between the IDA curves resulting from using different infill models, Figure 6.13 shows the absolute differences between the mean IDA curves of the several structures. For the FF models, the maximum absolute differences are 0.049g and 0.087g for the four- and eight-storey structures, respectively. On the other hand, for the PF models, these differences are 0.036g and 0.026g for the four- and eight-storey structures, respectively. As expected, for the SF structures these differences are lower than for the other cases and amount to 0.006g and 0.010g for the four- and eight-storey structures, respectively. Therefore, the differences in the strut parameters are seen to have a minor effect on the mean IDA curve but the effect of these different modelling parameters will also be analysed in further steps of the performance assessment of the structures, namely on the fragility curves obtained for different limit states.

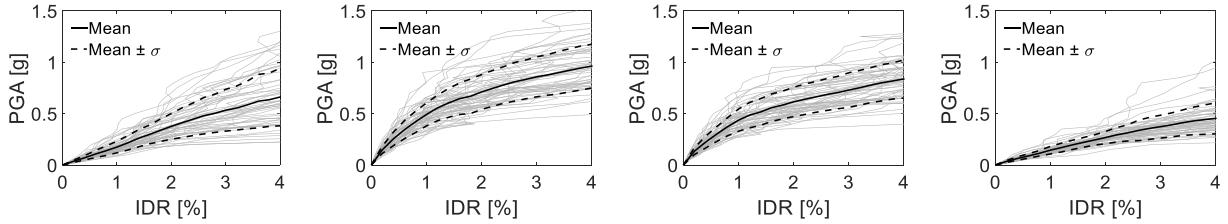

a) BF-4 b) FF-4-Exp c) PF-4-Exp e) SF-4-Exp

Figure 6.8 IDA results for the four-storey structures with different structural configurations and when the infill model is based on experimental data.

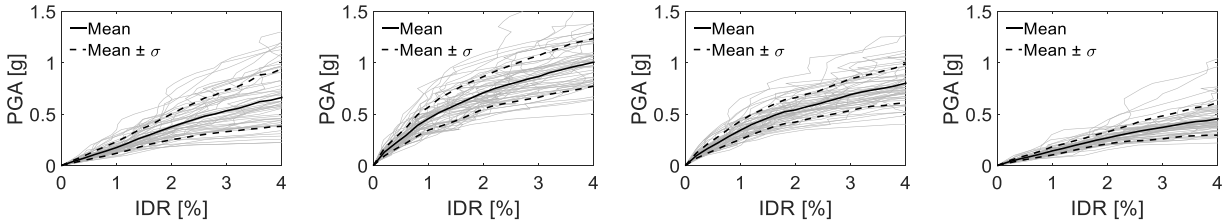

a) BF-4 b) FF-4-Num c) PF-4-Num e) SF-4-Num

Figure 6.9 IDA results for the four-storey structures with different structural configurations and when the infill model is based on numerical data.

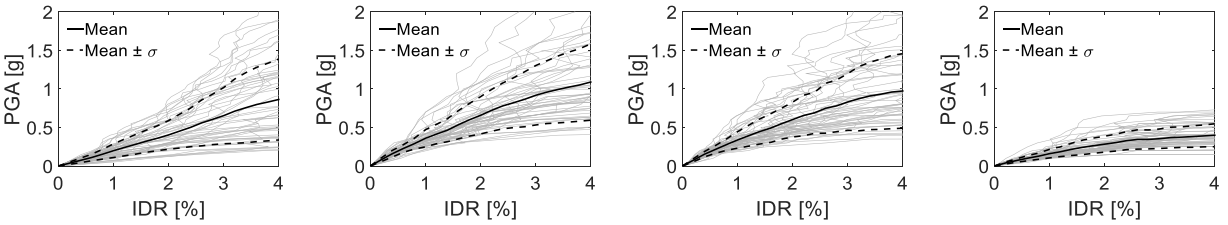

a) BF-8 b) FF-8-Exp c) PF-8-Exp e) SF-8-Exp

Figure 6.10 IDA results for the eight-storey structures with different structural configurations and when the infill model is based on experimental data.

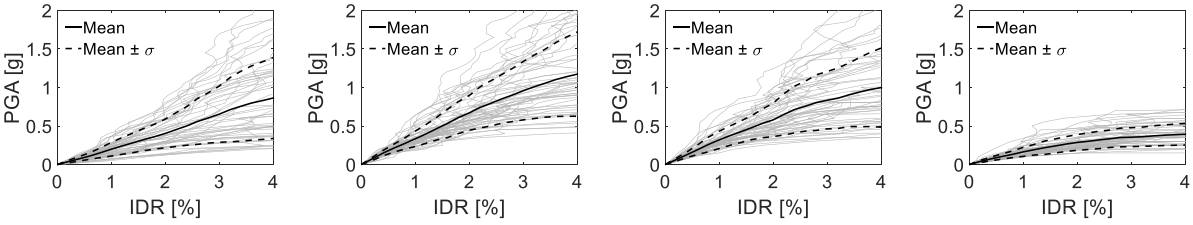

a) BF-8 b) FF-8-Num c) PF-8-Num e) SF-8-Num

Figure 6.11 IDA results for the eight-storey structures with different structural configurations and when the infill model is based on numerical data.

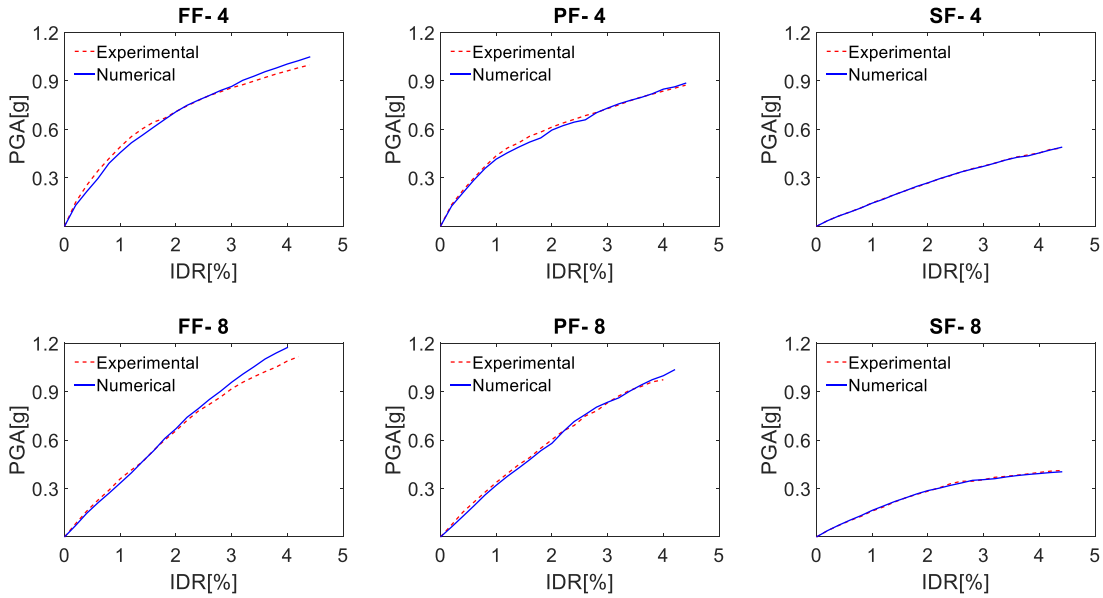

Figure 6.12 Comparison of the mean IDA curves obtained for the different structures when the infill model is based on numerical or experimental data

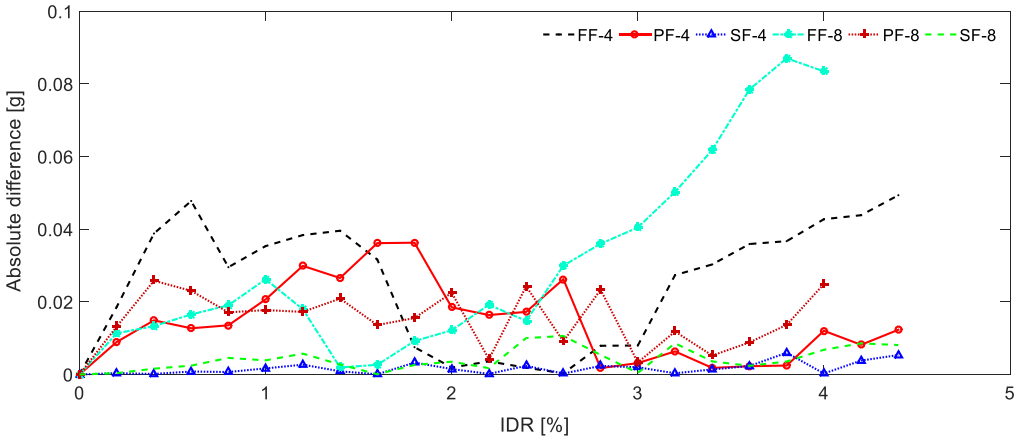

Figure 6.13 Absolute differences in terms of IMs for fixed values of IDR between the mean IDA curves of the several structures when the infill models are based on numerical and experimental data.

6.6 Statistical analysis of the fragility datasets

As referred before, IDA results combined with the limit state values are able to provide a set of IM values associated with the exceedance of a given limit state. By using deterministic limit states, each IDA curve yields one IM value corresponding to the ground motion intensity for which the limit state

under analysis occurs (see Figure 6.6 a). The statistical distribution of these IM values defines the fragility curve representing the probability of exceeding a given limit state conditional to a certain value of the IM which accounts for the record-to-record variability. This formulation of the fragility curve is similar in nature to the IM-based approach referred by Ibarra*, et al.* (2002) but it is used herein for limit states other than collapse. For the case on nondeterministic limit states, random samples of 1000 limit state values were extracted from each of the previously defined limit state distributions. For each limit state, all the corresponding sample estimates were combined with all the IDA curves. Therefore, each IDA curve yields 1000 IM values corresponding to the ground motion intensities for which the limit state values occur (see Figure 6.6 b) and the total distribution of IM values for each limit state has 50000 values. The statistical distribution of these IM values defines the fragility curve of the limit state which now also accounts for the uncertainty in the limit state definition. The analytical definition of the fragility curves is normally expressed by a theoretical statistical distribution model and the lognormal distribution is typically the selected model (Shinozuka*, et al.*, 2000). To analyse the validity of this assumption, the empirical IM datasets obtained for the different structures, limit states and limit state definitions were carefully examined.

The statistical analysis of the fragility datasets was first carried out for the cases where deterministic limit states were considered. To illustrate the general characteristics of the data, Table 6.9 provides some descriptive statistics (i.e. mean μ, standard deviation σ and the coefficient of variation CV) for each dataset. As expected the variability of the datasets increases as the severity of the limit state also increases. As referred before, the fitting of the datasets to a theoretical statistical distribution model was analysed and, in particular, the validity of the lognormal distribution model for that purpose was examined. Goodness-of-fit techniques such as hypothesis tests are usually the most powerful approaches to determine the validity of fitting a dataset with a certain theoretical distribution. However, adequate hypothesis tests are only available for a few types of distributions (e.g. see(D'Agostino*, et al.*, 1986)) and their sensitivity to deviations between the empirical data and the theoretical distribution under analysis becomes excessive when the size of the dataset is very large. Therefore, since both factors are relevant for the statistical analyses that were carried out, the choice was made to analyse the goodness-of-fit of the datasets using statistical quantile-quantile (*Q-Q*) plots and by analysing their coefficients of determination R^2 (which represents the agreement of the linear fit between the empirical quantile data and the theoretical quantile data, for the distribution under analysis).

The statistical analysis that was carried out at this stage had the dual purpose of examining the performance of the lognormal distribution in fitting the several datasets and of determining if other

statistical models could perform better or as good as the lognormal model. Aside from the lognormal distribution, the normal, the Weibull, the extreme value, the generalized extreme value, the Gamma and the Rayleigh distributions were also considered. To illustrate graphically some of the results that were obtained, Figure 6.14 and Figure 6.15 show the *Q-Q* plots for the lognormal distribution for the FF-8-exp and SF-4-exp structures, respectively, for the different limit states. These cases were selected because they represent extreme situations in terms of fitting: for the FF-8-exp structure all distributions exhibit higher performance while for the SF-4-exp most distributions exhibit a lower performance. As can be seen, the lognormal model exhibits a reasonable fit to the empirical data of all the limit states. Still, the fits are seen to be better for the eight-storey structure than for the four-storey structure, as referred, and their quality is seen to reduce as the limit state severity increases. Additionally, Figure 6.16 and Figure 6.17 show the *Q-Q* plots for the generalized extreme value distribution for the same structures. The fits obtained with this distribution are presented because, of the other tested distributions, it is the one that exhibits the best fitting performance for the generality of the datasets. This can be seen in particular for the case of the more severe limit states.

The fitting results obtained for the all the tested distributions involving fragility datasets of the four- and eight-storey structures are presented in in Table 6.10 and Table 6.11, respectively. The fitting results are expressed in terms of the coefficient of determination R^2. For the sake of brevity, results for structures with masonry infills are only presented for the cases where the infill models are based on experimental data. In those tables, the results obtained for the lognormal model are always presented in bold. As can be seen, the normal, Weibull, extreme value and Rayleigh distributions provide fits of lower quality for several datasets. On the other hand, the lognormal, Gamma and generalized extreme value distributions provide a better and more regular performance in terms of fitting quality for all sets. Even though, in some individual cases, the Gamma or the generalized extreme value distributions exhibit slightly higher coefficients of determination than those obtained for the lognormal distribution, the differences were not found to be significant to favour the Gamma distribution or the generalized extreme value distribution instead of the lognormal distribution. To illustrate this, it is noted that the average and the CV of the R^2 value obtained with the generalized extreme value distribution over all the datasets corresponding to structures with infills is 0.98 and 1.2%, respectively. For the lognormal distribution, these statistics are 0.98 and 1.7% instead. On average, these differences are not seen to be large enough to lead to significant changes in a risk or loss analysis that would be carried using these different fragility curves. Therefore, for the fragility data obtained

when the limit state values were considered to be deterministic, the lognormal model is selected to represent the fragility curves of the structures.

Table 6.9 Statistical parameters of the fragility datasets for different structures and different limit states.

Model	Limit state	Four storeys						eight storeys					
		Experimental			Numerical			Experimental			Numerical		
		μ[g]	σ[g]	CV [%]	μ [g]	σ [g]	(CV) [%]	μ[g]	σ[g]	CV [%]	μ [g]	σ [g]	(CV) [%]
Bare frame BF	Slight	0.009	0.003	**28.52**	0.009	0.003	**28.52**	0.009	0.004	**40.22**	0.009	0.004	**40.22**
	Light	0.015	0.004	**28.52**	0.015	0.004	**28.52**	0.015	0.006	**40.22**	0.015	0.006	**40.22**
	Moderate	0.054	0.015	**27.80**	0.054	0.015	**27.80**	0.055	0.022	**40.07**	0.055	0.022	**40.07**
	Extensive	0.206	0.068	**33.29**	0.206	0.068	**33.29**	0.230	0.104	**45.11**	0.230	0.104	**45.11**
	Partial collapse	0.511	0.190	**37.22**	0.511	0.190	**37.22**	0.620	0.340	**54.91**	0.620	0.340	**54.91**
	Collapse	0.698	0.298	**42.67**	0.698	0.298	**42.67**	0.911	0.551	**60.48**	0.911	0.551	**60.48**
Fully infilled FF	Slight	0.041	0.011	**27.08**	0.036	0.009	**24.17**	0.021	0.006	**27.81**	0.017	0.004	**24.68**
	Light	0.064	0.016	**25.27**	0.057	0.013	**23.56**	0.033	0.009	**27.81**	0.027	0.007	**24.68**
	Moderate	0.200	0.047	**23.22**	0.173	0.045	**25.97**	0.123	0.036	**29.27**	0.112	0.029	**25.55**
	Extensive	0.540	0.119	**22.09**	0.499	0.130	**26.10**	0.402	0.121	**30.15**	0.387	0.122	**31.54**
	Partial collapse	0.840	0.191	**22.70**	0.847	0.196	**23.18**	0.881	0.373	**42.36**	0.906	0.354	**39.09**
	Collapse	0.995	0.213	**21.44**	1.043	0.233	**22.36**	1.127	0.519	**46.03**	1.209	0.567	**46.93**
Partially infilled PF	Slight	0.037	0.008	**22.42**	0.036	0.008	**22.22**	0.018	0.004	**21.35**	0.015	0.004	**27.13**
	Light	0.059	0.014	**23.49**	0.056	0.013	**23.21**	0.028	0.006	**21.35**	0.024	0.007	**27.13**
	Moderate	0.177	0.044	**24.90**	0.168	0.043	**25.59**	0.117	0.029	**24.91**	0.095	0.027	**28.16**
	Extensive	0.474	0.120	**25.32**	0.450	0.120	**26.66**	0.380	0.127	**33.40**	0.363	0.122	**33.67**
	Partial collapse	0.712	0.160	**22.54**	0.714	0.150	**21.00**	0.795	0.341	**42.88**	0.814	0.370	**45.49**
	Collapse	0.870	0.195	**22.42**	0.889	0.204	**22.95**	1.010	0.509	**50.42**	1.062	0.580	**54.62**
Soft storey SF	Slight	0.009	0.002	**27.29**	0.009	0.003	**28.91**	0.010	0.003	**33.62**	0.010	0.003	**34.39**
	Light	0.014	0.004	**27.29**	0.014	0.004	**28.91**	0.016	0.005	**33.62**	0.016	0.005	**34.39**
	Moderate	0.051	0.013	**26.55**	0.051	0.013	**26.38**	0.056	0.017	**30.73**	0.057	0.019	**33.97**
	Extensive	0.163	0.041	**24.92**	0.160	0.042	**26.06**	0.179	0.059	**32.89**	0.188	0.074	**39.67**
	Partial collapse	0.361	0.108	**29.94**	0.358	0.106	**29.58**	0.350	0.126	**35.97**	0.358	0.128	**35.71**
	Collapse	0.481	0.167	**34.73**	0.485	0.170	**34.96**	0.411	0.163	**39.53**	0.402	0.146	**36.27**

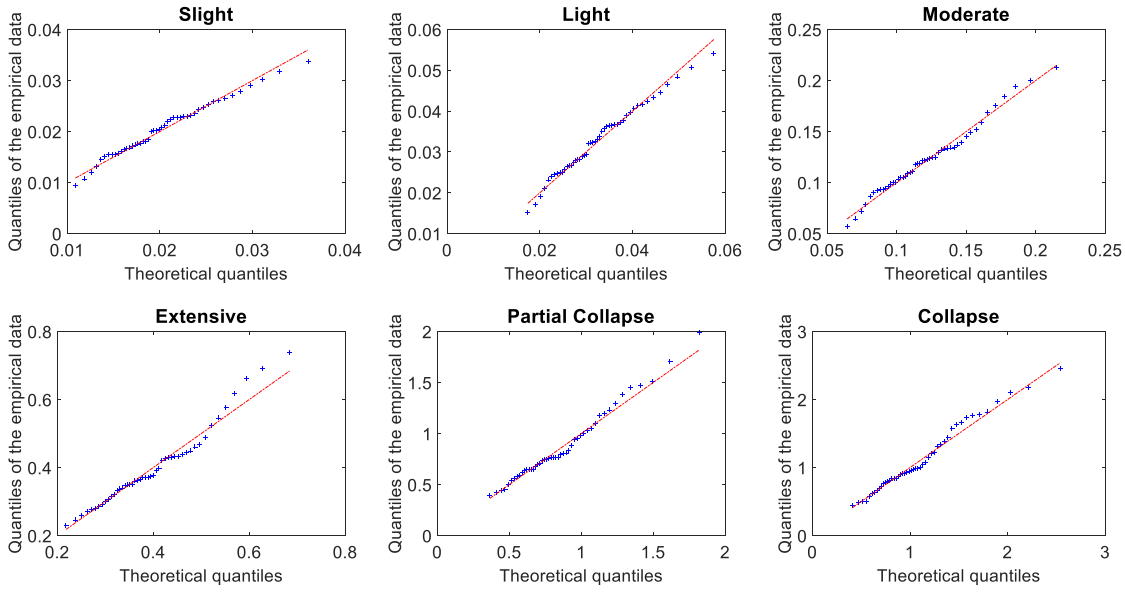

Figure 6.14 *Q-Q* plots for the lognormal distribution for the IM datasets of different limit states of the structure FF-8-Exp

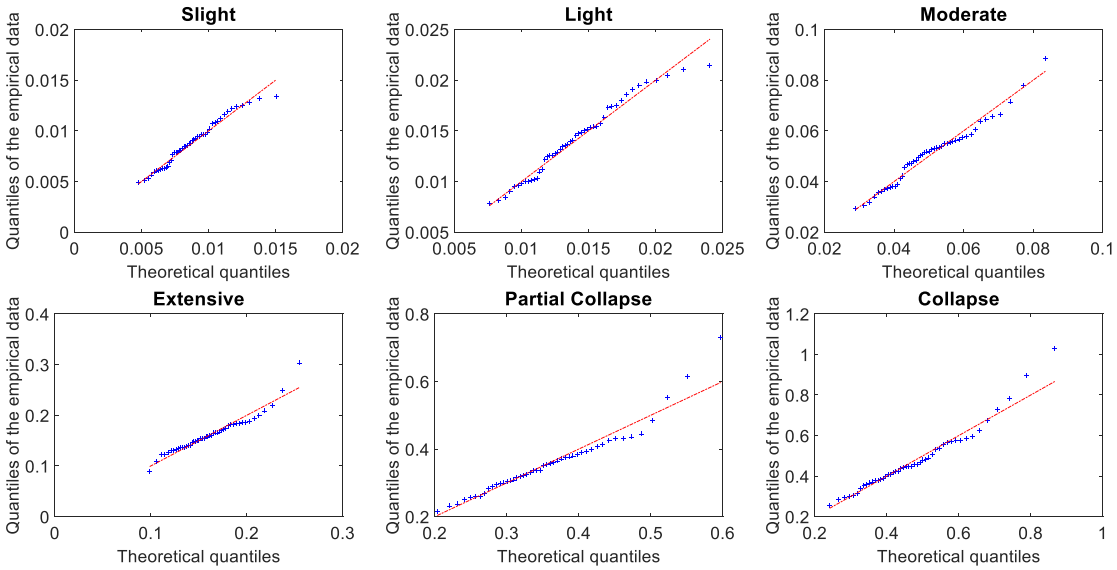

Figure 6.15 *Q-Q* plots for the lognormal distribution for the IM datasets of different limit states of the structure SF-4-Exp

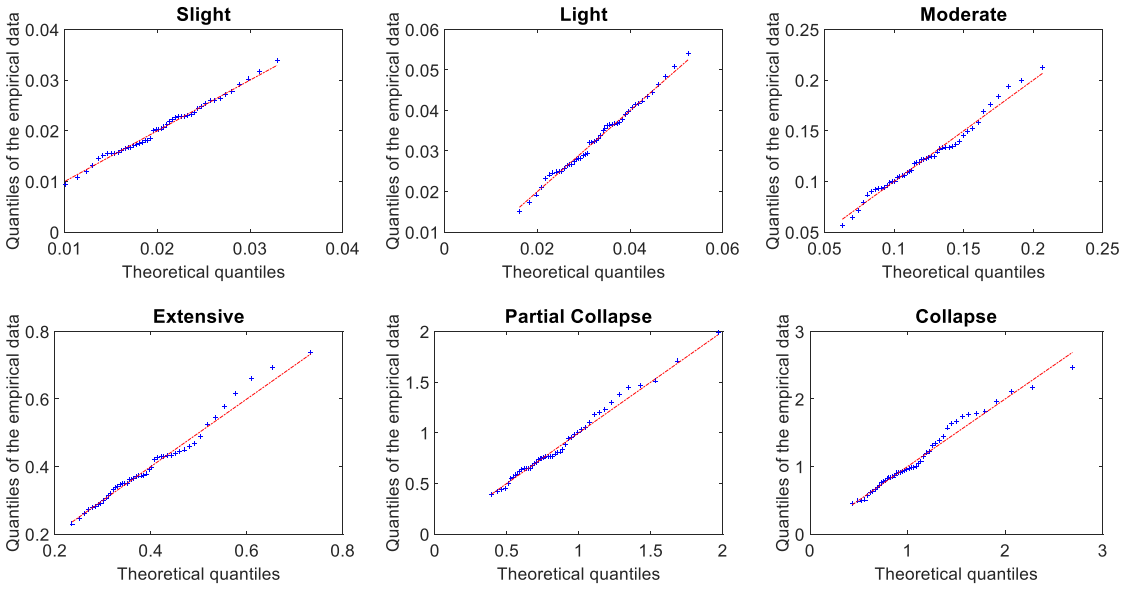

Figure 6.16 *Q-Q* plots for the generalized extreme value distribution for the IM datasets of different limit states of the structure FF-8-Exp

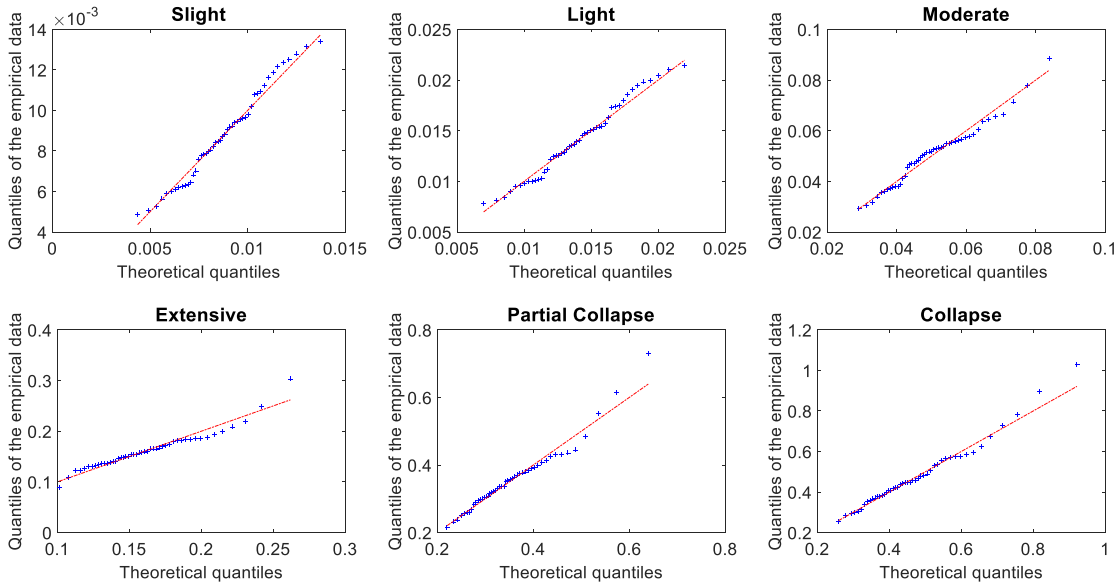

Figure 6.17 *Q-Q* plots for the generalized extreme value distribution for the IM datasets of different limit states of the structure SF-4-Exp

Table 6.10 Coefficients of determination R^2 obtained from the *Q-Q* plots for the four-storey structures

Limit state		Slight	Light	Moderate	Extensive	Partial collapse	Collapse
Distribution	**model**						
Normal	BF-4	0.981	0.981	0.975	0.895	0.970	0.972
	FF-4-Exp	0.942	0.945	0.974	0.978	0.981	0.985
	PF-4-Exp	0.984	0.980	0.961	0.952	0.969	0.989
	SF-4-Exp	0.979	0.979	0.952	0.865	0.848	0.869
Lognormal	BF-4	**0.972**	**0.972**	**0.984**	**0.969**	**0.989**	**0.958**
	FF-4-Exp	**0.984**	**0.980**	**0.993**	**0.992**	**0.995**	**0.989**
	PF-4-Exp	**0.984**	**0.993**	**0.992**	**0.986**	**0.992**	**0.973**
	SF-4-Exp	**0.975**	**0.975**	**0.971**	**0.926**	**0.929**	**0.952**
Gamma	BF-4	0.983	0.983	0.986	0.952	0.992	0.985
	FF-4-Exp	0.974	0.971	0.989	0.990	0.993	**0.992**
	PF-4-Exp	0.988	0.992	0.984	0.978	0.987	0.985
	SF-4-Exp	0.983	0.983	0.969	0.912	0.911	0.931
Weibull	BF-4	0.980	0.980	0.967	0.882	0.979	0.986
	FF-4-Exp	0.921	0.915	0.953	0.953	0.960	0.966
	PF-4-Exp	0.972	0.963	0.934	0.927	0.936	0.983
	SF-4-Exp	0.977	0.977	0.918	0.757	0.789	0.865
Extreme Value	BF-4	0.859	0.859	0.726	0.096	0.733	0.808
	FF-4-Exp	0.545	0.539	0.764	0.729	0.778	0.811
	PF-4-Exp	0.809	0.760	0.603	0.613	0.659	0.880
	SF-4-Exp	0.862	0.862	0.382	N/a	N/a	0.077
Generalized Extreme Value	BF-4	0.985	0.985	0.986	0.985	0.991	0.984
	FF-4-Exp	0.990	0.984	0.991	0.992	0.994	0.992
	PF-4-Exp	0.988	0.992	0.993	0.990	0.991	0.988
	SF-4-Exp	0.984	0.984	0.970	0.934	0.962	0.976
Rayleigh	BF-4	0.447	0.447	0.332	0.604	0.869	0.956
	FF-4-Exp	0.259	0.000	N/a	N/a	N/a	N/a
	PF-4-Exp	N/a	N/a	N/a	0.061	N/a	N/a
	SF-4-Exp	0.357	0.357	0.043	N/a	0.254	0.663

Table 6.11 Coefficients of determination R^2 obtained from the *Q-Q* plots for the eight-storey structures

Limit state		Slight	Light	Moderate	Extensive	Partial collapse	Collapse
Distribution	**model**						
Normal	BF-8	0.976	0.976	0.981	0.975	0.941	0.941
	FF-8-Exp	0.988	0.988	0.957	0.905	0.900	0.921
	PF-8-Exp	0.992	0.992	0.987	0.881	0.929	0.912
	SF-8-Exp	0.941	0.941	0.921	0.875	0.920	0.961
Lognormal	BF-8	**0.928**	**0.928**	**0.945**	**0.952**	**0.928**	**0.908**
	FF-8-Exp	**0.983**	**0.983**	**0.985**	**0.965**	**0.980**	**0.983**
	PF-8-Exp	**0.969**	**0.969**	**0.984**	**0.949**	**0.987**	**0.985**
	SF-8-Exp	**0.988**	**0.988**	**0.966**	**0.954**	**0.979**	**0.990**
Gamma	BF-8	0.974	0.974	0.984	0.988	0.969	0.972
	FF-8-Exp	0.992	0.992	0.980	0.950	0.961	0.975
	PF-8-Exp	0.983	0.983	0.991	0.932	0.977	0.974
	SF-8-Exp	0.978	0.978	0.960	0.935	0.965	0.991
Weibull	BF-8	0.982	0.982	0.988	0.990	0.974	0.979
	FF-8-Exp	0.982	0.982	0.946	0.888	0.931	0.958
	PF-8-Exp	0.990	0.990	0.977	0.880	0.958	0.961
	SF-8-Exp	0.935	0.935	0.871	0.869	0.929	0.975
Extreme Value	BF-8	0.856	0.856	0.837	0.786	0.714	0.712
	FF-8-Exp	0.830	0.830	0.665	0.395	0.338	0.495
	PF-8-Exp	0.920	0.920	0.823	0.402	0.504	0.463
	SF-8-Exp	0.373	0.373	N/a	0.186	0.531	0.621
Generalized Extreme Value	BF-8	0.981	0.981	0.988	0.988	0.940	0.930
	FF-8-Exp	0.992	0.992	0.983	0.984	0.989	0.977
	PF-8-Exp	0.990	0.990	0.991	0.969	0.983	0.972
	SF-8-Exp	0.988	0.988	0.967	0.993	0.981	0.992
Rayleigh	BF-8	0.914	0.914	0.918	0.975	0.973	0.962
	FF-8-Exp	0.358	0.358	0.460	0.486	0.902	0.953
	PF-8-Exp	N/a	N/a	N/a	0.660	0.933	0.966
	SF-8-Exp	0.672	0.672	0.328	0.622	0.791	0.900

After analysing the fragility datasets for the cases involving deterministic limit states, a similar statistical analysis was performed for the fragility datasets involving nondeterministic limit states. As referred before, these cases involve two datasets: one where the limit state variability was defined by setting a value of the CV (NDLSCV) and another where the limit state variability was defined by setting a range for the limit state values (NDLSR). To illustrate the general characteristics of these new datasets, Table 6.12 and Table 6.13 provide descriptive statistics (i.e. mean μ, standard deviation σ and the coefficient of variation CV) for these datasets. By analysing these statistics and comparing them with those presented in Table 6.9, it can be seen that the variability of the datasets increases in about 80% of the cases and that a shift of the left of the mean value is also found in about 40% of the cases. It is also noted that unlike for the case of deterministic limit states, an increase in the severity of the limit state does not imply a direct increase in the variability of the IM values. In some cases, due to the flatness of the IDA curves for larger IM values, combining different limit state values in the range of the IDA curve where it is flat or close-to-flat will lead to very small changes in the actual IM values leading to that limit state. This effect combined with that of the record-to-record variability leads to a lower value of the CV, in some cases.

Table 6.12 Statistical parameters of the NDLSR fragility datasets for different structures and limit states

Model	Limit state	Four storeys						eight storeys					
		Experimental			Numerical			Experimental			Numerical		
		μ[g]	σ[g]	CV [%]	μ [g]	σ [g]	(CV) [%]	μ[g]	σ[g]	CV [%]	μ [g]	σ [g]	(CV) [%]
Bare frame BF	Slight	0.009	0.003	**33.84**	0.009	0.003	**33.84**	0.009	0.004	**44.16**	0.009	0.004	**44.16**
	Light	0.021	0.008	**38.38**	0.021	0.008	**38.38**	0.021	0.010	**48.10**	0.021	0.010	**48.11**
	Moderate	0.071	0.030	**41.66**	0.071	0.030	**41.66**	0.074	0.037	**49.34**	0.074	0.037	**49.34**
	Extensive	0.234	0.093	**39.51**	0.234	0.093	**39.51**	0.257	0.129	**49.99**	0.257	0.129	**50.0**
	Partial collapse	0.502	0.192	**38.36**	0.502	0.192	**38.36**	0.585	0.316	**54.02**	0.585	0.316	**54.03**
	Collapse	0.700	0.304	**43.37**	0.700	0.304	**43.37**	0.715	0.371	**51.82**	0.715	0.371	**51.83**
Fully infilled FF	Slight	0.038	0.012	**32.39**	0.034	0.010	**29.97**	0.019	0.006	**33.18**	0.016	0.005	**30.50**
	Light	0.088	0.029	**33.50**	0.078	0.027	**34.58**	0.046	0.017	**37.79**	0.038	0.014	**36.63**
	Moderate	0.254	0.086	**33.84**	0.217	0.074	**34.31**	0.161	0.059	**36.62**	0.147	0.053	**35.90**
	Extensive	0.566	0.147	**25.97**	0.532	0.153	**28.69**	0.439	0.163	**37.12**	0.430	0.167	**38.72**
	Partial collapse	0.828	0.192	**23.12**	0.838	0.198	**23.64**	0.862	0.360	**41.76**	0.898	0.358	**39.90**
	Collapse	0.995	0.216	**21.72**	1.039	0.231	**22.20**	1.060	0.454	**42.82**	1.131	0.506	**44.72**
Partially infilled PF	Slight	0.034	0.010	**28.72**	0.033	0.010	**29.97**	0.016	0.005	**27.76**	0.016	0.005	**29.73**
	Light	0.081	0.027	**33.44**	0.076	0.026	**33.89**	0.040	0.014	**35.37**	0.038	0.014	**35.49**
	Moderate	0.221	0.073	**33.17**	0.208	0.071	**34.24**	0.153	0.053	**34.97**	0.145	0.052	**36.01**
	Extensive	0.494	0.131	**26.59**	0.480	0.129	**26.96**	0.413	0.162	**39.17**	0.394	0.155	**39.18**
	Partial collapse	0.705	0.162	**22.95**	0.686	0.160	**23.39**	0.780	0.346	**44.40**	0.768	0.336	**43.78**
	Collapse	0.869	0.195	**22.47**	0.858	0.193	**22.47**	0.975	0.484	**49.65**	0.973	0.473	**48.66**
Soft storey SF	Slight	0.008	0.003	**32.66**	0.008	0.003	**34.00**	0.009	0.004	**38.01**	0.009	0.004	**38.78**
	Light	0.020	0.007	**37.50**	0.019	0.007	**38.48**	0.022	0.009	**42.55**	0.022	0.010	**44.77**
	Moderate	0.064	0.022	**34.63**	0.064	0.022	**34.29**	0.072	0.029	**40.59**	0.074	0.031	**41.72**
	Extensive	0.181	0.054	**29.79**	0.180	0.055	**30.63**	0.198	0.079	**40.17**	0.202	0.084	**41.33**
	Partial collapse	0.353	0.107	**30.29**	0.352	0.105	**29.87**	0.346	0.125	**36.01**	0.347	0.126	**36.25**
	Collapse	0.483	0.167	**34.62**	0.485	0.171	**35.26**	0.409	0.154	**37.64**	0.402	0.145	**36.05**

Table 6.13 Statistical parameters of the NDLSCV fragility datasets for different structures and limit states

Model	Limit state	Four storeys						eight storeys					
		Experimental			Numerical			Experimental			Numerical		
		μ[g]	σ[g]	CV [%]	μ [g]	σ [g]	(CV) [%]	μ[g]	σ[g]	CV [%]	μ [g]	σ [g]	(CV) [%]
Bare frame BF	Slight	0.009	0.003	**35.23**	0.009	0.003	**35.23**	0.009	0.004	**45.19**	0.009	0.004	**45.19**
	Light	0.015	0.005	**35.16**	0.015	0.005	**35.16**	0.015	0.007	**45.35**	0.015	0.007	**45.35**
	Moderate	0.054	0.018	**34.35**	0.054	0.018	**34.35**	0.055	0.025	**44.94**	0.055	0.025	**44.94**
	Extensive	0.208	0.082	**39.50**	0.208	0.082	**39.50**	0.228	0.114	**49.87**	0.228	0.114	**49.87**
	Partial collapse	0.500	0.208	**41.58**	0.500	0.208	**41.58**	0.567	0.316	**55.73**	0.567	0.316	**55.73**
	Collapse	0.673	0.299	**44.34**	0.673	0.299	**44.34**	0.704	0.366	**52.00**	0.704	0.366	**52.00**
Fully infilled FF	Slight	0.041	0.014	**33.25**	0.036	0.011	**31.25**	0.021	0.007	**34.44**	0.017	0.005	**31.86**
	Light	0.064	0.020	**31.49**	0.057	0.017	**30.71**	0.033	0.011	**34.58**	0.027	0.009	**31.96**
	Moderate	0.202	0.058	**28.88**	0.173	0.052	**30.02**	0.123	0.042	**34.51**	0.111	0.036	**32.84**
	Extensive	0.531	0.140	**26.44**	0.495	0.145	**29.20**	0.398	0.141	**35.29**	0.385	0.144	**37.42**
	Partial collapse	0.825	0.201	**24.34**	0.836	0.211	**25.21**	0.856	0.378	**44.11**	0.894	0.386	**43.15**
	Collapse	0.965	0.208	**21.61**	1.001	0.216	**21.59**	1.010	0.425	**42.11**	1.062	0.423	**39.84**
Partially infilled PF	Slight	0.037	0.011	**30.35**	0.036	0.011	**31.09**	0.018	0.005	**29.47**	0.017	0.005	**31.31**
	Light	0.059	0.018	**30.99**	0.056	0.017	**30.46**	0.028	0.008	**29.58**	0.027	0.009	**31.12**
	Moderate	0.178	0.052	**29.44**	0.167	0.051	**30.40**	0.116	0.037	**31.86**	0.110	0.034	**31.08**
	Extensive	0.466	0.127	**27.35**	0.456	0.129	**28.21**	0.378	0.145	**38.42**	0.384	0.147	**38.42**
	Partial collapse	0.706	0.170	**24.11**	0.680	0.181	**26.69**	0.779	0.365	**46.85**	0.790	0.370	**46.85**
	Collapse	0.855	0.200	**23.35**	0.849	0.213	**25.05**	0.953	0.447	**46.91**	0.968	0.454	**46.91**
Soft storey SF	Slight	0.009	0.003	**34.29**	0.009	0.003	**35.60**	0.010	0.004	**39.48**	0.010	0.004	**40.13**
	Light	0.014	0.005	**34.14**	0.014	0.005	**35.71**	0.016	0.006	**39.47**	0.016	0.006	**40.06**
	Moderate	0.050	0.016	**31.31**	0.050	0.016	**31.83**	0.056	0.020	**35.75**	0.057	0.022	**38.38**
	Extensive	0.163	0.050	**30.57**	0.161	0.051	**31.42**	0.179	0.071	**39.35**	0.184	0.077	**41.76**
	Partial collapse	0.352	0.117	**33.22**	0.352	0.116	**32.93**	0.359	0.122	**34.03**	0.356	0.128	**36.01**
	Collapse	0.481	0.175	**36.30**	0.481	0.179	**37.13**	0.445	0.145	**32.50**	0.437	0.140	**32.00**

As for the previous goodness-of-fit analyses, the quality of the fitting between these datasets and several theoretical distributions was also examined using *Q-Q* plots. Like for the previous analyses, the lognormal, normal, Weibull, extreme value, generalized extreme value, Gamma and Rayleigh distributions were considered. To illustrate graphically some of the results that were obtained, Figure 6.18 and Figure 6.19 show the *Q-Q* plots for the lognormal distribution for the FF-4 and SF-4-exp structures, respectively, for the different limit states. As can be seen, the fitting scenario is significantly different than the one where the limit state values were considered deterministically. None of the selected theoretical models is now able to capture the evolution of the data for any of the limit states. Since these fitting examples are representative of what was found for all the datasets, a different approach was considered in this case to define the fragility curves of the structures. To be able to compare the effect of considering the variability of the limit state values, two types of fragility curves were defined: one where the lognormal model is used (given the popularity of this model, it will provide a direct comparison with the curves obtained when the limit state values are deterministic) and another where the fragility is directly defined by the empirical cumulative distribution function of the datasets. Since the NDLSCV and NDLSR datasets have a size of 50000, they have enough data to adequately represent the real fragility curve. Furthermore, based on these empirical fragility curves, it is possible to determine the level of error involved when using the lognormal model to approximate the fragility curves.

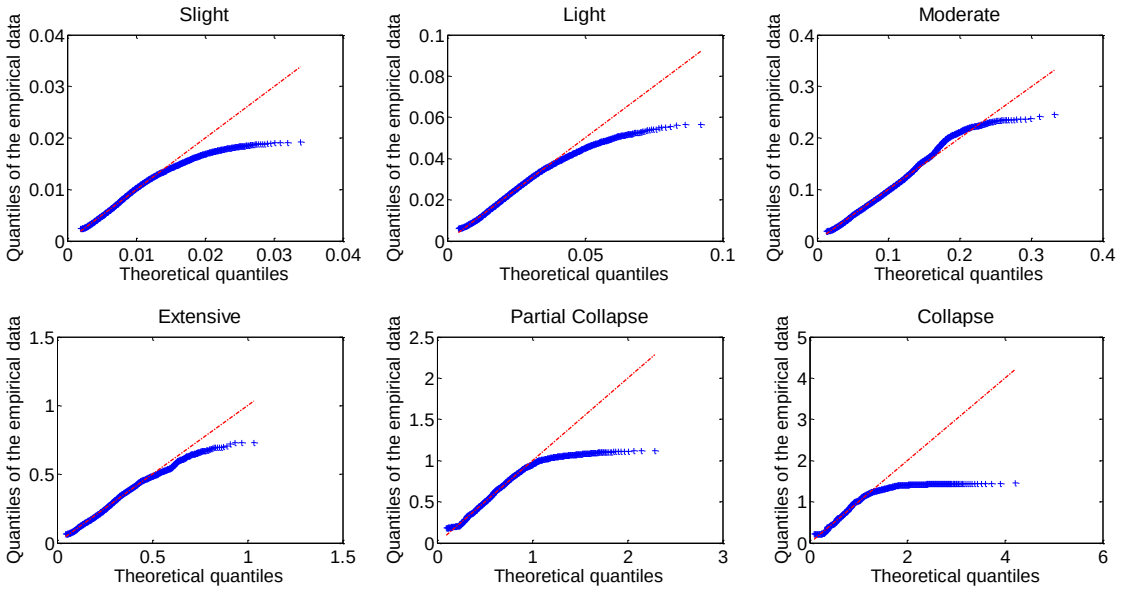

Figure 6.18 *Q-Q* plots for the lognormal distribution for the IM datasets of different limit states of the structure FF-4

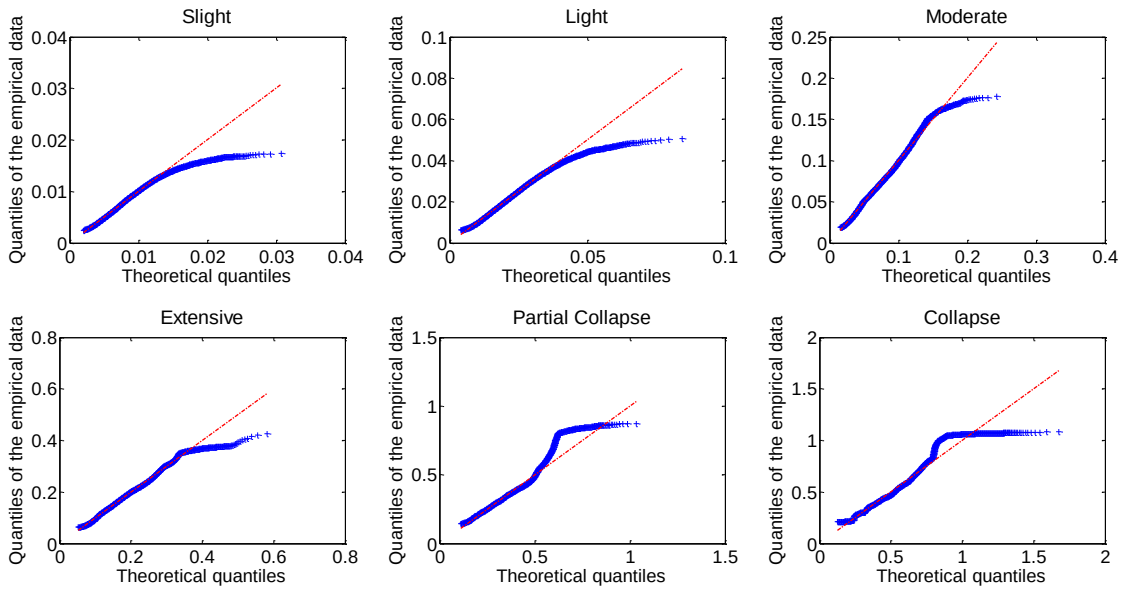

Figure 6.19 *Q-Q* plots for the lognormal distribution for the IM datasets of different limit states of the structure SF-4-Exp.

6.7 Seismic vulnerability assessment: influence of the limit state definition

Based on the fragility curves obtained for the different structures when considering the experimental data to define behaviour of the infills, a vulnerability analysis of the infilled structures with different configurations was performed for different performance levels, using the performance of the corresponding bare frames as a reference. The fragility curves that were developed using different nondeterministic definitions for the limit states were then also compared to analyse the importance of the variability of the limit state threshold value in the vulnerability analysis of RC structures. As referred before, both empirical and theoretical fragility curves are presented when analysing the case of nondeterministic limit states.

6.7.1 Fragility curves obtained for the deterministic limit states

The fragility curves based on the lognormal distribution and the corresponding empirical data obtained for the several four-storey structures and for the six different limit states are presented in Figure 6.20. As can be seen, the PF and FF structures exhibit better performance for all the limit states. Furthermore, the SF structure can be seen to be the one exhibiting the worst performance among all configurations, especially for higher damage limit states. The fact that the BF and SF structures reach almost any level of damage for lower intensities can be explained by the non-seismically designed RC elements controlling their behaviour combined with the fact that the infills act as behaviour modifiers for the PF and FF structures for the less severe limit states. As can be seen, for the first limit states (i.e. slight, light and moderate), structures BF and SF have a close performance while the performance of the PF structure is closer to that of the FF structure. After reaching the extensive limit state, the BF structure exhibits a better performance than the SF structure due to its higher capacity to spread plasticity. The higher vulnerability of the SF structure for the more severe limit states is a direct result of the soft-storey failure mechanism that is easily reached due to the structural configuration that has a weak ground storey. Furthermore, it is also noted that for the more severe limits states (i.e. the partial collapse and collapse limit states), the performance of the PF and FF structures is closer to that of the BF structure as a result of losing a significant part of the strength after the failure of the infills. For those levels of seismic demand, the behaviour of the PF and FF structures approaches that of the BF structure since most of the infills are inactive.

In a more quantitative analysis, structures SF and BF can be seen to reach the slight and light limit states for PGA values lower than 0.05g while the FF and PF structures require excitation levels higher than 0.15g. Analysing the moderate limit state yield similar results as the BF and SF structures reach this limit state for PGA values lower than 0.13 g while the PF and FF structures exhibit a capacity that can go up to 0.44g. For the extensive limit state, the behaviour of the four structures begins to spread and the limit state capacities of the SF, BF, PF and FF structures can now go up to 0.39g, 0.45g, 1.10g, and 1.25g, respectively. For partial collapse limit state, the two groups of structures with a distinct behaviour are now much closer as well as their capacities. In this case, the limit state capacities of the SF, BF, PF and FF structures can go up to 0.9g, 1.4g, 1.6g, and 1.8g, respectively. Finally, for the collapse limit state the limit states capacities of structures BF, SF, PF, and FF can go up to 2.7g, 1.2g, 2.1g, and 2.5g, respectively. In this case, it can be seen that the BF structure appears to be able to support higher levels of excitation in some cases. However, it can also be seen that its fragility curve

for this limit state exhibits a much larger variability. With respect to this parameter, it can be seen that, as the severity of the limit state increases, the variability of the performance of the structures also increases, as expected. However, this increases in the variability is more regular for the PF and FF structures than for the SF structure which exhibits a significant increase in the variability of its performance after reaching the extensive limit state.

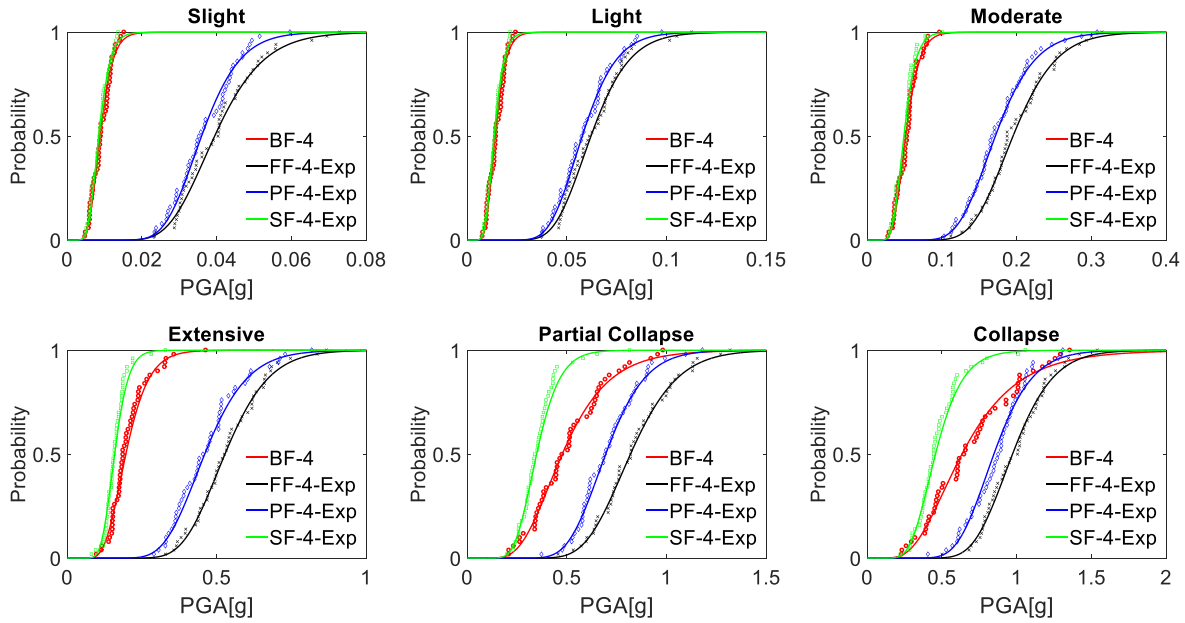

Figure 6.20 Fragility curves of the several four-storey structures for different limit states considering deterministic limit state values (DLS)

As for the four-storey structures, Figure 6.21 presents the fragility curves based on the lognormal distribution and the corresponding empirical data obtained for the several eight-storey structures and for the six different limit states. As can be seen, the fragility curves for these structures exhibit a trend similar to that of the four-storey structures: for the lower severity limit states, structures BF and SF exhibit a higher vulnerability than the PF and FF structures while for limit states of larger severity (i.e. from extensive onwards), the PF and FF structures start to exhibit a behaviour closer to that of the BF structure. As referred before, the influence of the infills and of their level of damage introduces a behaviour modifier that changes the behaviour of the PF and FF structures as the ground moiton intensity increases. When comparing the maximum PGA involved in the first four limit states (i.e. slight, light, moderate and extensive damage) for the eight-storey structure with those obtained for the

four-storey structures, it can be seen that the latter exhibit a higher capacity than the former. On the other hand, for the remaining limit states the trend is opposite. Furthermore, it is also noted that, on average, the variability of the fragility curves of the eight-storey structures (other than the SF structure) is larger than that of the four-storey structures (other than the SF structure), irrespective of the limit state. The larger redistribution capacity and ability to spread the nonlinear behaviour across a larger number of members of the eight-storey structures with respect to that of the four-storey structures may be a factor leading in this situation.

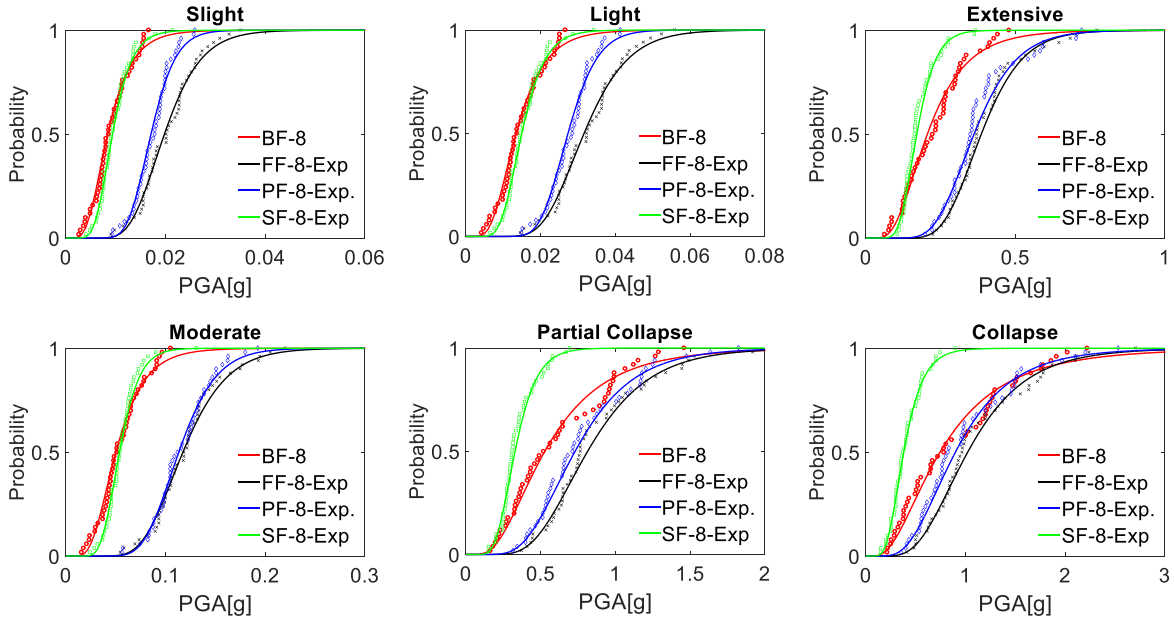

Figure 6.21 Fragility curves of the several eight-storey structures for different limit states considering deterministic limit state values (DLS)

6.7.2 Fragility curves obtained for the nondeterministic limit states and comparison with those obtained for the deterministic limit states

As referred before, the fragility curves developed for the cases where nondeterministic limit states are considered involve both theoretical distributions defined by the lognormal model (to compare with those defined in the previous section) and the real empirical distributions (to determine the level of error involved with the lognormal assumption). Furthermore, these fragility curves also involve two different forms of simulating the nondeterministic limit states: one where a constant CV

was considered (the NDLSCV case) and one establishing a predefined range of variation (the NDLSR case). The empirical and theoretical fragility curves that were obtained for the NDLSCV case are presented in Figure 6.22 (for both the four- and eight-storey structures) while those of the NDLSR case are presented in Figure 6.23 (for both the four- and eight-storey structures). As can be seen, the use of nondeterministic limit states does not change the relative global performance of the structures with respect to the cases where deterministic limit states were considered. However, these fragility curves are now seen to exhibit a larger variability which is translated in the larger range of IM values that each curve involves. Moreover, the curves obtained for the NDLSR case can be seen to be slightly less conservative than those of the NDLSCV case for limit states between slight and extensive (i.e. they are slightly more shifted to the left). For the more severe limit states, both approaches yield very similar fragility curves. Finally, it also noted that relevant differences between the empirical and theoretical fragility curves can only be seen for the more severe limit states, i.e. from the extensive onwards, but especially for the partial collapse and collapse limit states. Nevertheless, the lognormal model provides fragility estimates that are more conservative than the empirical values when those differences become larger (this conservativeness of the lognormal model can be seen from the *Q-Q* plots of Figure 6.18 and Figure 6.19).

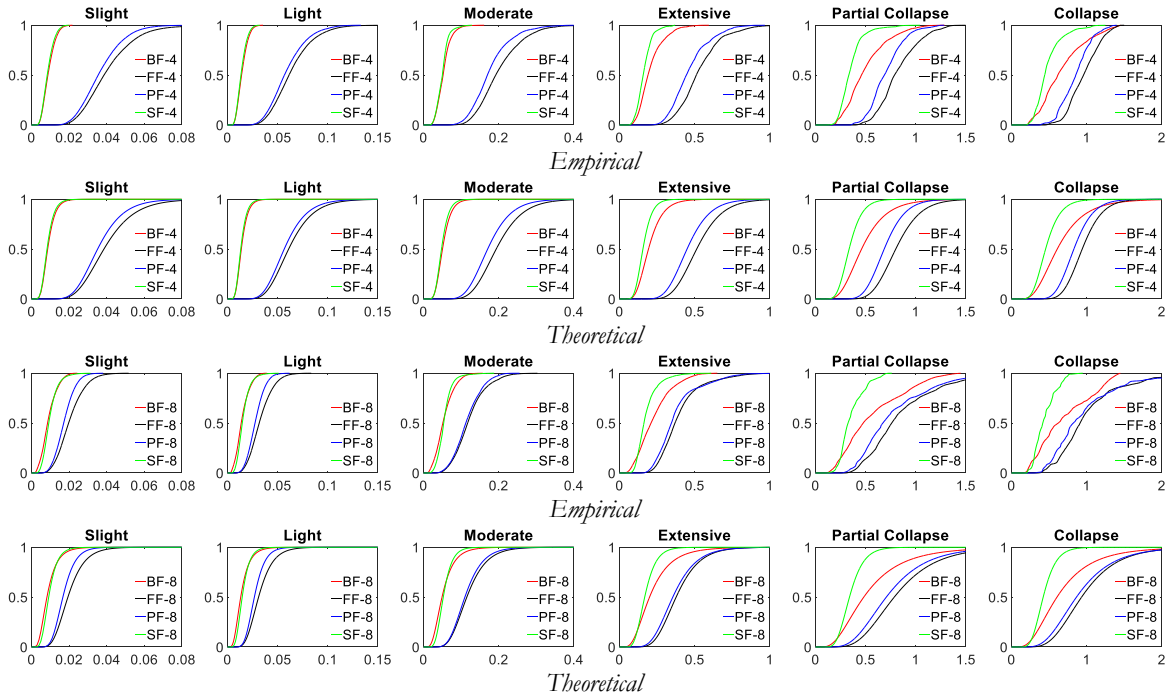

Figure 6.22 Fragility curves of different structures for different limit states using the NDLSCV datasets; the vertical axis is the probability of exceedance and the horizontal axis is the PGA in [g]

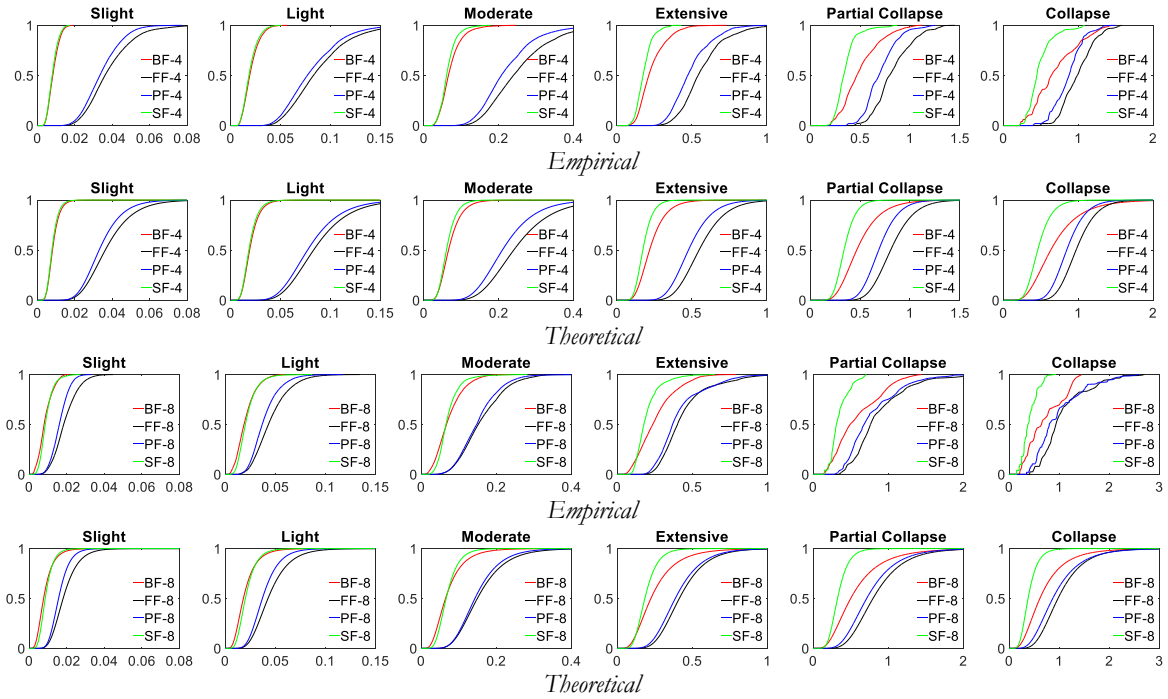

Figure 6.23 Fragility curves of different structures for different limit states using the NDLSR datasets; the vertical axis is the probability of exceedance and the horizontal axis is the PGA in [g]

To be able to perform a more detailed comparison between the fragility curves obtained for the NDLSCV and the NDLSR cases and those obtained for the case where deterministic limit states were considered (the DLS case), Figure 6.24 and Figure 6.25 show these fragility curves for the different limit states and for the several infilled four- and eight-storey structures, respectively. It is noted that for the NDLSCV and the NDLSR cases only the lognormal fragility curves are presented. As can be seen, the effect of the limit state variability is almost non-existent for the partial collapse and collapse limit states. This effect is mostly due to the previously referred flatness of the IDA curves for larger IM values given that combining different limit state values in the range of the IDA curve where it is flat or close-to-flat leads to very small changes in the actual IM values leading to that limit state. Since this effect leads to a reduction in the variability of the fragility curve, it can be seen that it starts to affect different structures at different limit states. For example, for the FF and PF structures this effect starts to be noticeable for the extensive limit state. However, for the SF structures the effect starts to be noticeable for the moderate limit state. This indicates that the SF structures develop their failure mechanism an start to have flat IDAs much earlier than the others, as expected due to their structural configuration.

For the less severe limit states, it can be seen that the influence of the nondeterministic limit states increase as the severity of the limit state also increases. However, the effect of considering nondeterministic limit states depends on how their variability is simulated. It can be seen that the main difference of the NDLSCV case with respect to the DLS case is that it increases the variability of the fragility curve while maintaining the median of the curve more or less constant. On the contrary, the NDLSR case increases the variability of the fragility curve (in some cases more than the NDLSCV case) but also shifts the median of the curve to the right. The reason for these differences is directly connected to the way the limit state variability was defined: the NDLSCV scenario leads to a symmetric variation of the limit state value around the value considered by the DLS case while the NDLSR scenario leads to asymmetric limit state distributions maintaining the value considered by the DLS case as the mode of the distribution.

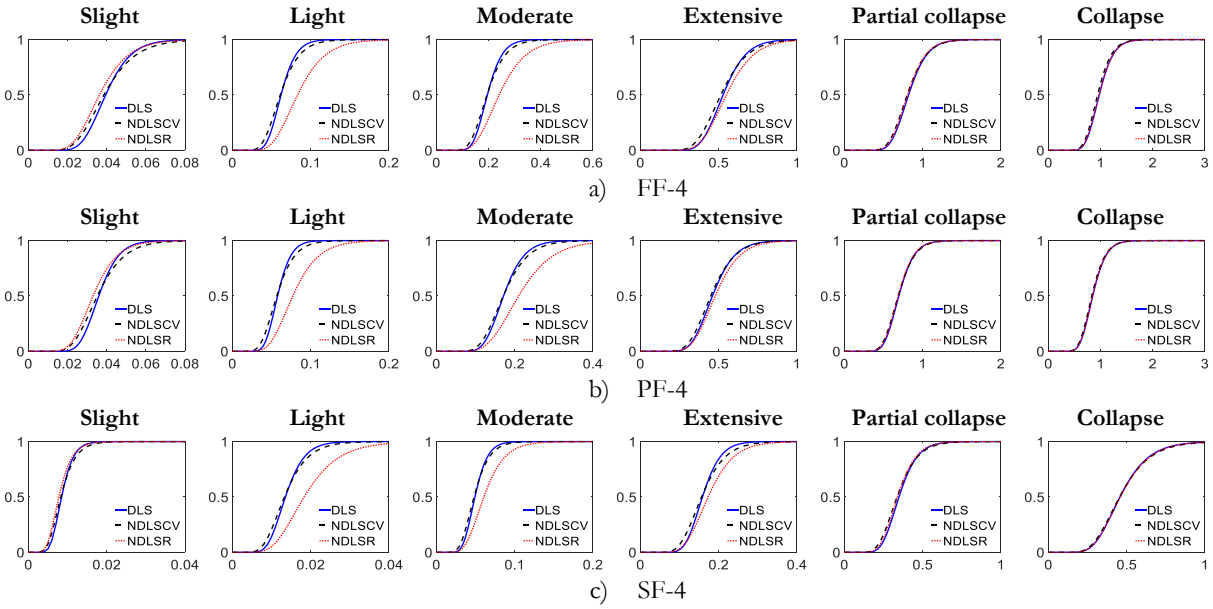

a) FF-4

b) PF-4

c) SF-4

Figure 6.24 Comparison between the fragility curves involving different limit state definitions for the several four-storey structures and for the six different limit states; the vertical axis is the probability of exceedance and the horizontal axis is the PGA in [g]

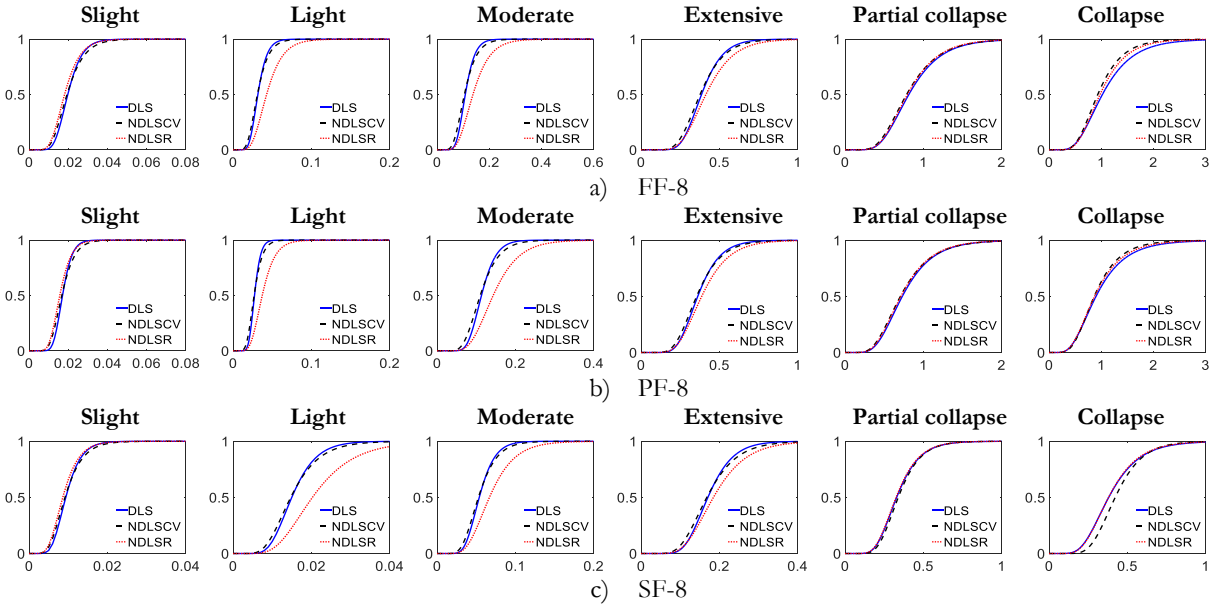

Figure 6.25 Comparison between the fragility curves involving different limit state definitions for the several eight-storey structures and for the six different limit states; the vertical axis is the probability of exceedance and the horizontal axis is the PGA in [g]

6.8 Seismic vulnerability assessment: influence of the data considered to define the infill models

The fragility curves presented in the previous section are based on IDA results obtained from numerical models where the infill modelling was defined using experimental data. In this section, a comparison is made between these fragility curves and those obtained when the infill modelling was defined using data obtained from refine finite element models. Therefore, the fragility analysis presented in the previous section is repeated herein for those corresponding IDA results.

As referred in Section 6.3.2, the numerical properties of the strut models for the partially infilled structures were defined using two different scenarios: one based on Point A of Figure 6.4 b), considered to be the reference scenario, and another based on Point B of Figure 6.4 b). As mentioned before, the latter scenario is only considered to examine the differences that are obtained in the fragility curves as a result of using a lower stiffness for the struts.

6.8.1 Qualitative comparison of fragility curves obtained using different infill models

The fragility curves obtained for the several four-storey infilled structures when the infill models are defined using numerical data are presented in Figure 6.26 to Figure 6.28 against those obtained when the infill models are defined using experimental data. Fragility curves involving both deterministic and nondeterministic limit states are presented for the several limit states. As can be seen, two fragility curves are always presented for the partially infilled structures: one curve termed num^{a}, corresponding to the case where Point A of Figure 6.4 b) was used to define the infill parameters, and another termed num^{b}, corresponding to the case where Point B of Figure 6.4 b) was used instead.

According to the results presented for the fully infilled FF-4 structures, the fragility curves obtained using numerical data to define the infills are seen to be more conservative than those obtained using experimental data to define the infills. These differences are the result of the larger sensitivity of the model to the pre-peak properties of the infill models, mainly the stiffness. However, the referred differences between the "experimentally-based" and "numerically-based" fragility curves reduce significantly as the severity of the limit state increases. Furthermore, these differences are also seen to be smaller when nondeterministic limit states are considered.

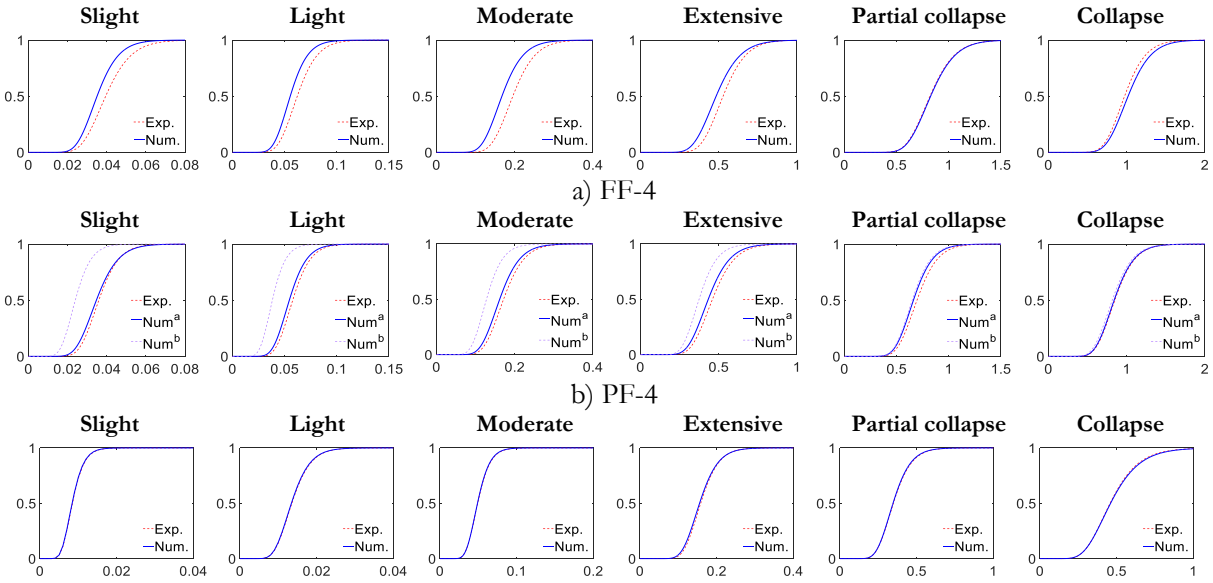

a) FF-4

b) PF-4

c) SF-4

Figure 6.26 "Experimentally-based" and "numerically-based" fragility curves of the four-storey structures for the DLS datasets; vertical axis is the probability of exceedance and the horizontal axis is the PGA in [g]

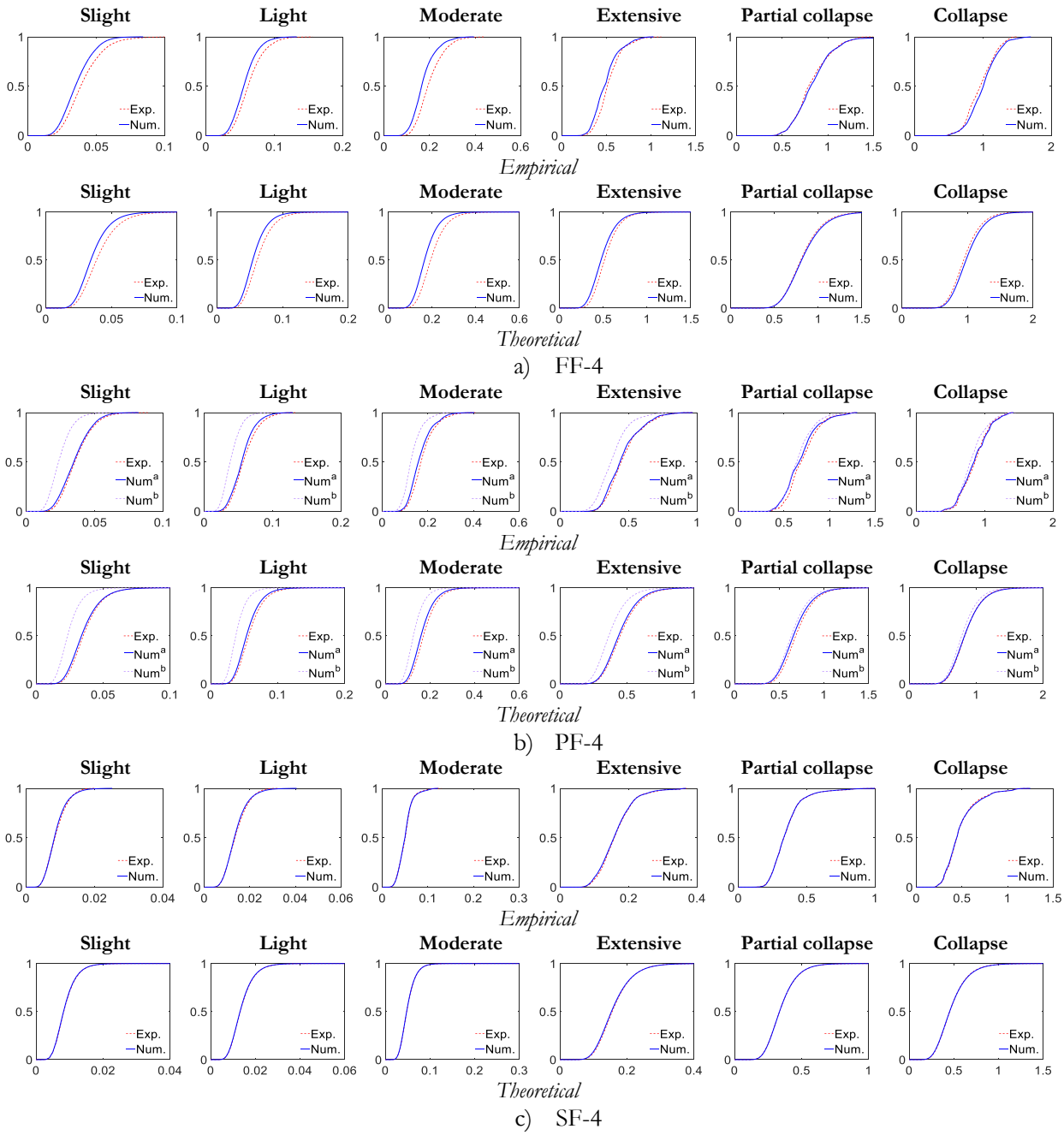

a) FF-4

b) PF-4

c) SF-4

Figure 6.27 "Experimentally-based" and "numerically-based" fragility curves of the four-storey structures for the NDLSCV datasets; vertical axis is the probability of exceedance and the horizontal axis is the PGA in [g]

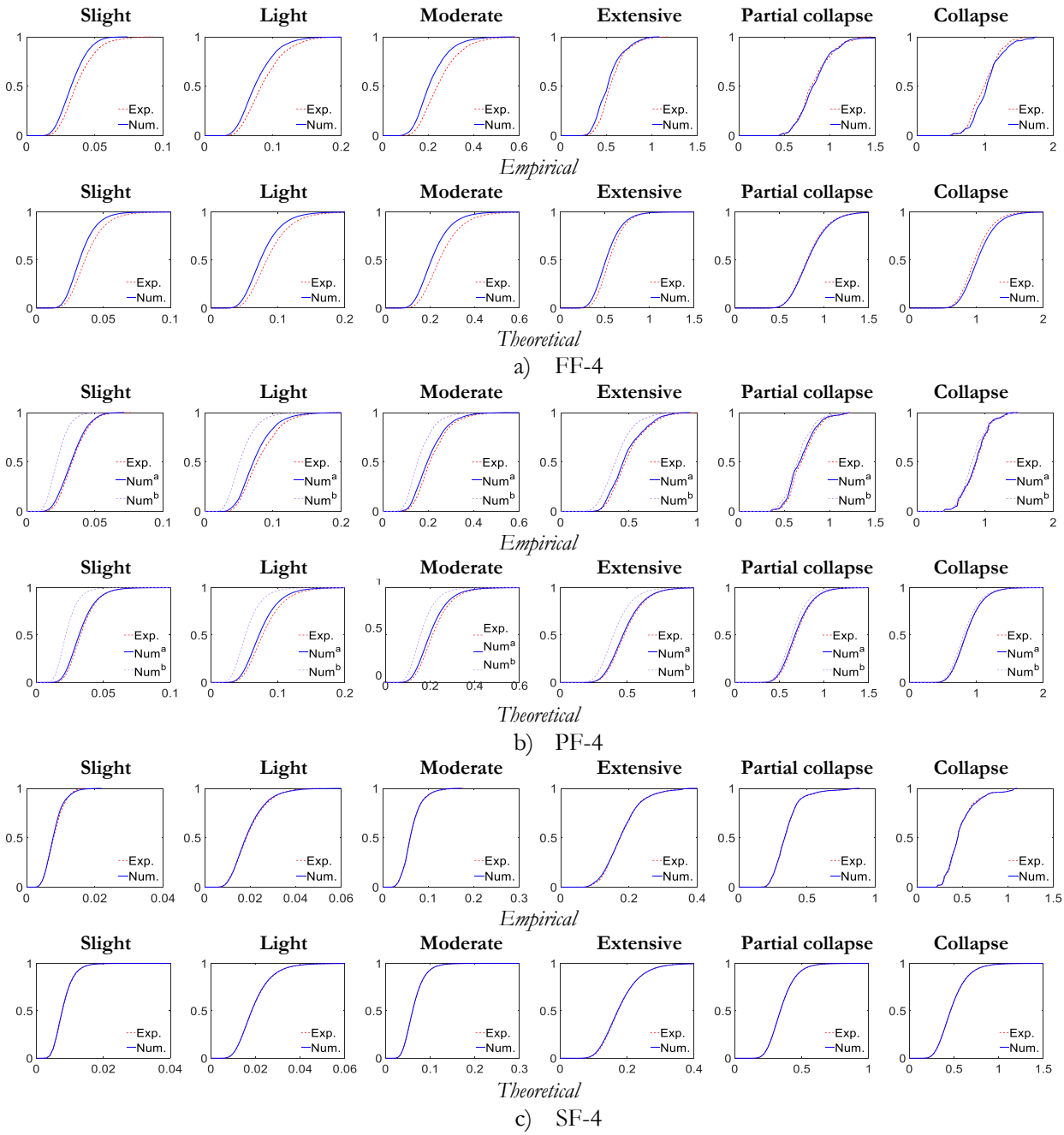

Figure 6.28 "Experimentally-based" and "numerically-based" fragility curves of the four-storey structures for the NDLSR datasets; vertical axis is the probability of exceedance and the horizontal axis is the PGA in [g]

For the partially infilled PF-4 structures, the trend of the fragility curves is similar to that of the fully infilled structures. However, when infills are defined according to the num^b model, the level of conservativeness of the "numerically-based" fragility curves increases significantly. This result reflects directly the effect of considering the strut model with a lower initial stiffness. As the severity of the

limit state increases, these differences reduce gradually, reflecting the level of infill damage that lowers the infill contribution to the overall behaviour. Finally, it is noted that the soft-storey SF-4 structures have a lower sensitivity to the way the infill model is defined. As can be seen, "experimentally-based" and "numerically-based" fragility curves exhibit an almost perfect match, which indicates that the overall behaviour is governed by the RC elements of the ground storey and not by the infill, as expected.

The fragility curves obtained for the several eight-storey infilled structures when the infill models are defined using numerical data are presented in Figure 6.29 to Figure 6.31 against those obtained when the infill models are defined using experimental data. As can be seen, the trends observed for the eight-storey structures are similar to those found for the four-storey structures. Still, the overall differences between the "experimentally-based" and "numerically-based" fragility curves are found to be smaller in this case. This is particularly clear when analysing the fragility curves obtained for the partially infilled structures when infills are defined according to the num^b model. Unlike for the four-storey structures, the influence of the way the partial infill model is defined is now much smaller.

To obtain a more comprehensive understanding about the effect of the infill modelling approach in the overall performance, a quantitative analysis of the differences between the presented fragility curves is carried out in the next section.

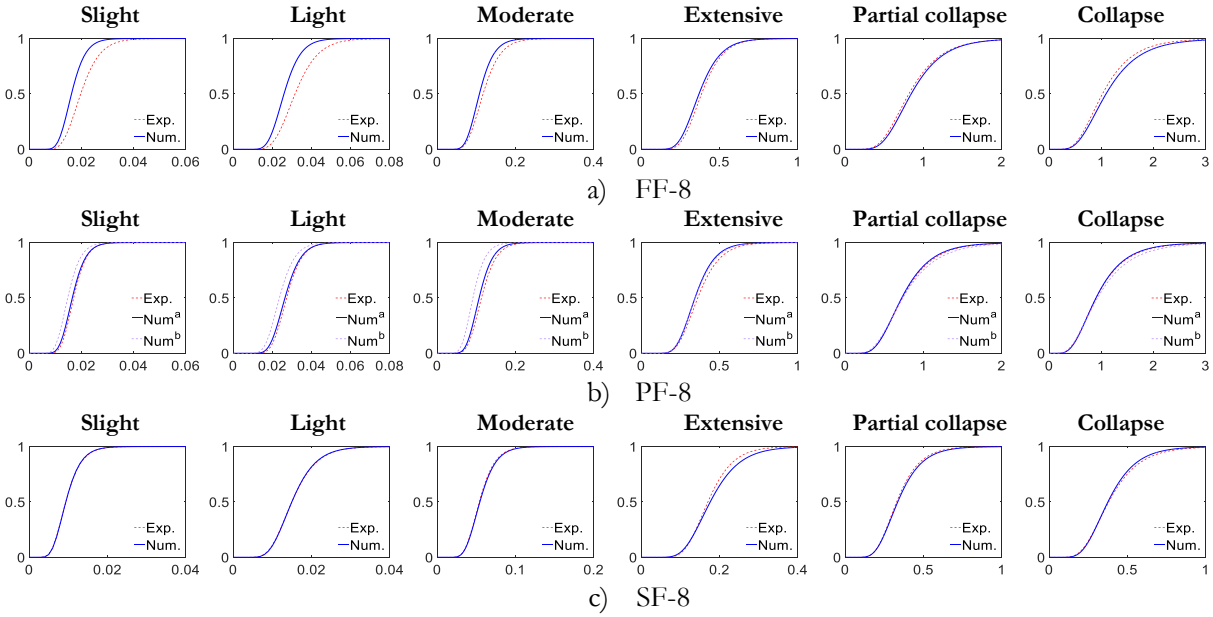

Figure 6.29 "Experimentally-based" and "numerically-based" fragility curves of the eight-storey structures for the DLS datasets; vertical axis is the probability of exceedance and the horizontal axis is the PGA in [g]

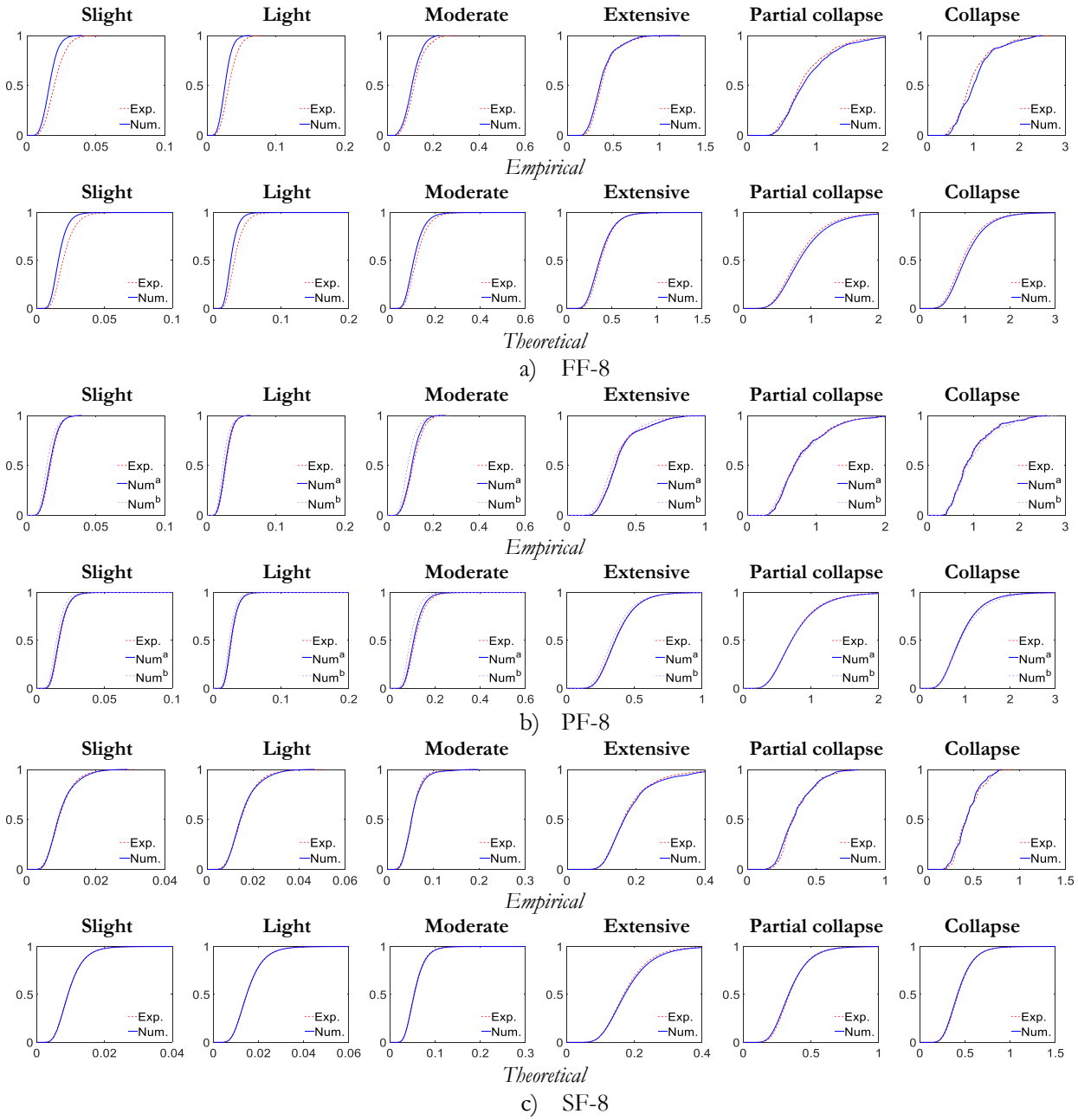

Figure 6.30 "Experimentally-based" and "numerically-based" fragility curves of the eight-storey structures for the NDLSCV datasets; vertical axis is the probability of exceedance and the horizontal axis is the PGA in [g]

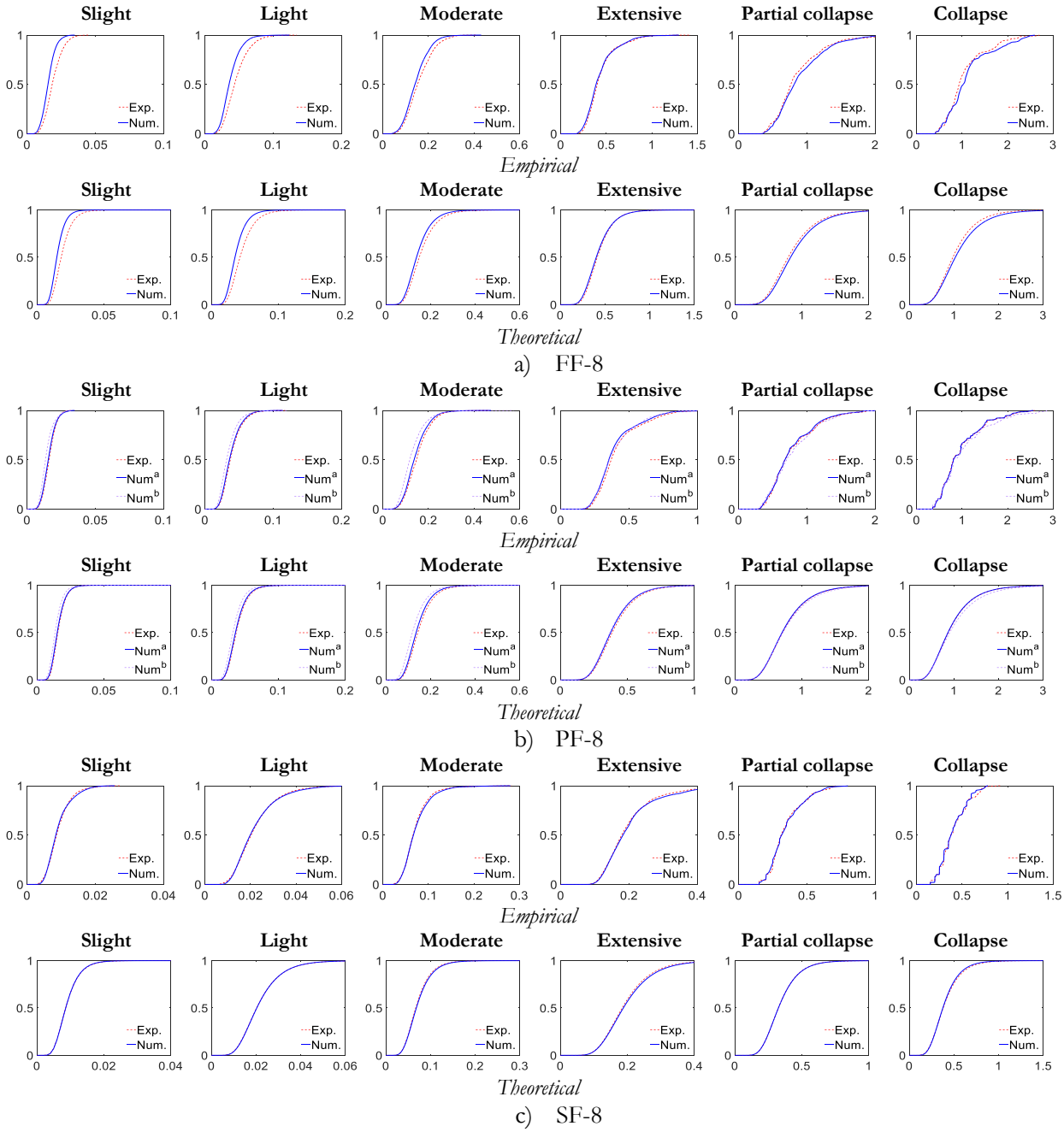

a) FF-8

b) PF-8

c) SF-8

Figure 6.31 "Experimentally-based" and "numerically-based" fragility curves of the eight-storey structures for the NDLSR datasets; vertical axis is the probability of exceedance and the horizontal axis is the PGA in [g]

6.8.2 Quantitative comparison of fragility curves obtained using different infill models

In order to quantify the differences between the fragility curves obtained for the several infilled structures when the infill models are defined using numerical data and experimental data, two indicators are determined and presented in this section. One of the indicators represents the maximum absolute difference measured vertically between two fragility curves (i.e. the difference in terms of the probability of exceedance of the two curves for a given IM value) representing the same structure and limit state. The second indicator is the normalized Wasserstein distance (*WD*) between two fragility curves defined by the following expression:

$$WD = \frac{\int_0^a \left| F_{comp}(x) - F_{\text{ref}}(x) \right| dx}{\int_0^{a_{\max}} F_{\text{ref}}(x)\, dx} \tag{6.2}$$

where F_{comp} is the cumulative distribution function representing the fragility curve that is going to be compared with F_{ref} which is the cumulative distribution function representing the fragility curve that is used as the reference, and a is an IM value of interest. In the current analysis, F_{comp} is defined by a fragility curve obtained using an infill model defined from numerical data, F_{ref} is the corresponding fragility curve where the infill model was defined from experimental data and a_{max} is the value of IM where F_{ref} reaches 1. These two indicators were determined for all the infilled structures, for all the limit states and for the cases where both deterministic and nondeterministic limit states were considered. It is noted that, for these comparisons, the empirical fragility data for the cases where the limit states are deterministic was also used. This way the fitting error between the theoretical lognormal model and the real data can also be singled out.

To illustrate quantitatively the overall differences between "experimentally-based" and "numerically-based" fragility curves before determining the first indicator, the evolution of those differences for the range of IM values of interest for each limit state is presented in Figure 6.32 and Figure 6.33 for all the cases involving the four- and eight-storey structures, respectively. For the partially infilled structures, only the results of structures involving the previously referred num[a] model are considered. Based on the presented results, it is possible to observe that, on average, the differences

decrease when the severity of the limit state increases. Furthermore, the cases where nondeterministic limit states are considered usually involve smaller differences. On average, the maximum level of difference does not exceed 20%-25% (although a few exceptions are seen).

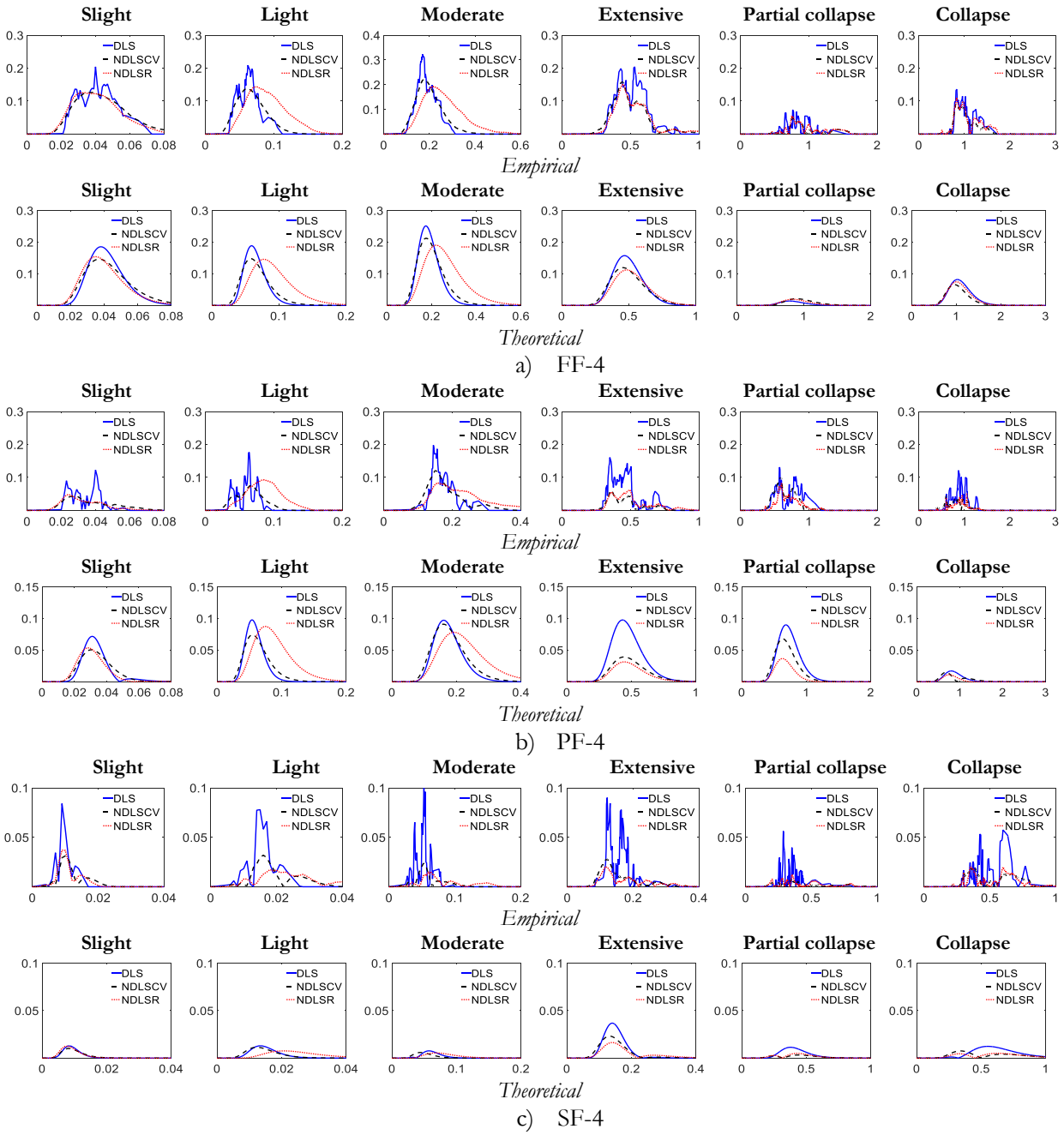

Figure 6.32 Absolute difference between "experimentally-based" and "numerically-based" fragility curves for the four-storey structures and the several limit states; vertical axis is the difference in the probability of exceedance and the horizontal axis is the PGA in [g]

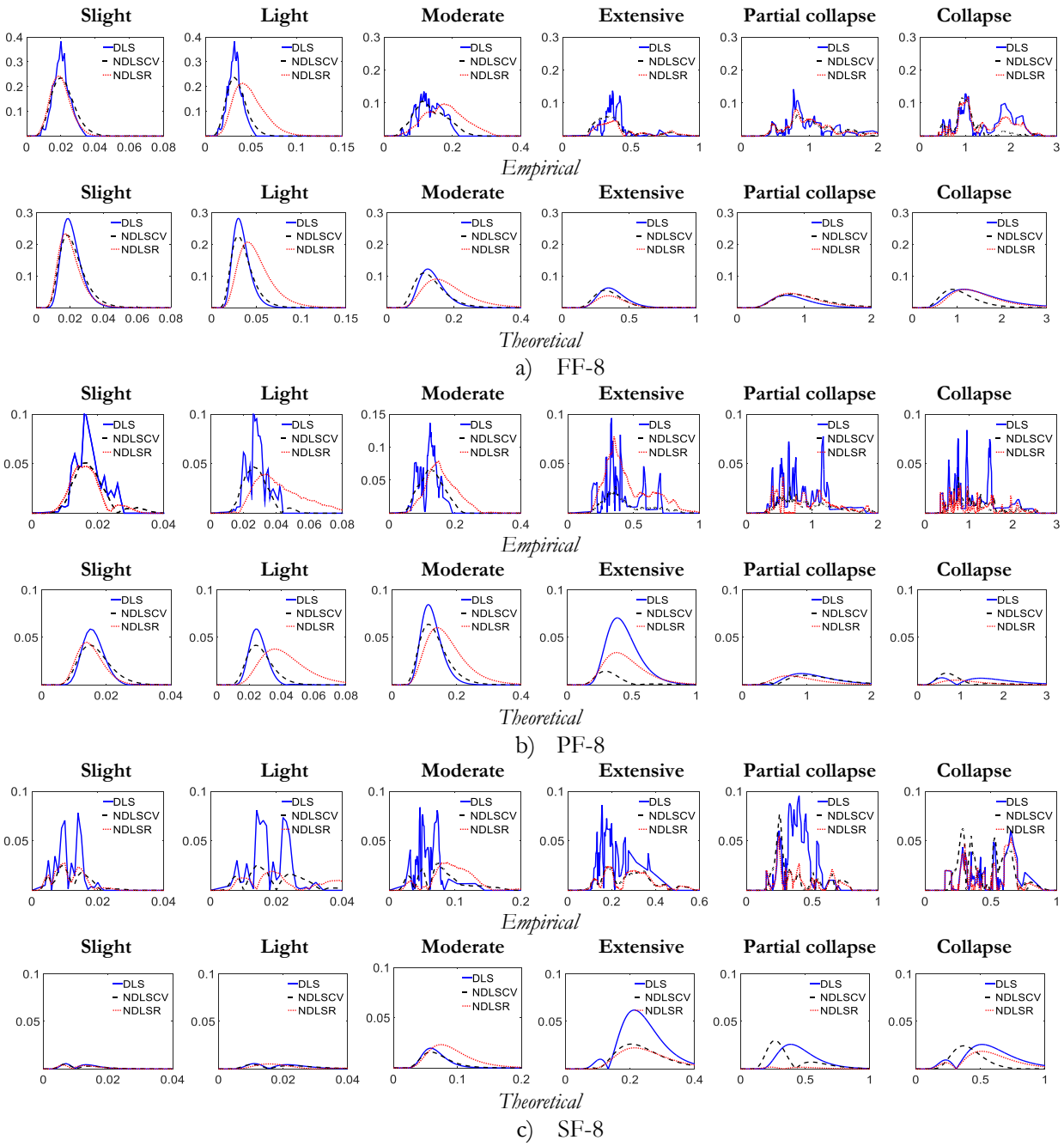

Figure 6.33 Absolute difference between "experimentally-based" and "numerically-based" fragility curves for the eight-storey structures and the several limit states; vertical axis is the difference in the probability of exceedance and the horizontal axis is the PGA in [g]

The exact results obtained for the first indicator, i.e. the maximum absolute difference between the fragility curves under comparison, are presented in Table 6.14 for the empirical fragility curves and in Table 6.15 for the theoretical (lognormal) fragility curves. The results clearly show that the larger

differences are found for the cases involving deterministic limit states. Given the differences between the cases involving nondeterministic and deterministic limit states, it is believed that the differences found for the latter reflect differences in the fitting or in the empirical data mostly due to the smaller sample size involved in these cases. As such, they are not found to be representative of the true differences between "experimentally-based" and "numerically-based" fragility curves and the differences obtained for nondeterministic limit states are suggested instead for this purpose. As mentioned also before, larger differences are found for less severe limit states and the size of those differences reduces with the increase of the limit state severity.

The values found for these maximum differences, however, do not allow to define the validity of the "experimentally-based" and "numerically-based" fragility curves to represent the same case. Such analysis would require a statistical test to compare the two distributions. Even though the two-sample Kolmogorov–Smirnov test (Zwillinger*, et al.*, 2000) could be used for this purpose, meaningful results are not expected to be obtained for the cases involving nondeterministic limit states due to their very large sample size and the previously referred sensitivity issue of statistical tests for such large sample sizes. Still, for illustrative purposes, the two-sample Kolmogorov–Smirnov test was applied for the cases where deterministic limit states were considered. The test establishes that the null hypothesis that two one-dimensional distributions can be accepted to be the same with a 5% confidence level if the maximum absolute difference between their corresponding cumulative distribution functions is not larger than (Zwillinger*, et al.*, 2000).

$$T_{crit} = 1.36\sqrt{\frac{2}{n}} \tag{6.3}$$

where n is the sample size. For a value of n equal to fifty, T_{crit} is then 0.272. By comparing this limit with the maximum absolute differences presented in Table 6.14 and Table 6.15 for the cases involving deterministic limit states, it can be seen that only a few cases do not comply with this limit value and that all of them occur for low severity limit states. Given that these limit states involve very low values of interstorey drift, the structures, and in particular the infills, are still expected to be elastic and almost undamaged; thus, in a behaviour state prior to that corresponding to an immediate occupancy level (FEMA-356, 2000). Therefore, since these limit states are not expected to play a fundamental role in a loss assessment scenario, the level of differences found in these few cases is not seen to be relevant.

Table 6.14 Maximum absolute difference between "experimentally-based" and "numerically-based" empirical fragility curves for all the structures and the several limit states

Structure	Limit state	Slight	Light	Moderate	Extensive	Partial collapse	Collapse
Fully infilled							
FF-4	DLS	20.42%	20.87%	**32.30**%	20.36%	7.32%	13.60%
	NDLSCV	12.65%	13.85%	22.06%	15.76%	4.82%	9.01%
	NDLSR	12.56%	14.33%	19.26%	15.03%	5.63%	10.81%
FF-8	DLS	**38.26**%	**38.26**%	13.49%	13.69%	14.14%	12.84%
	NDLSCV	23.46%	23.71%	10.62%	5.99%	6.49%	11.74%
	NDLSR	24.28%	21.35%	9.74%	4.72%	8.17%	11.87%
Partially infilled configuration							
PF-4[a]	DLS	12.27%	17.63%	**19.78**%	16.06%	13.13%	12.11%
	NDLSCV	4.33%	7.48%	12.08%	6.12%	9.83%	4.37%
	NDLSR	4.80%	9.31%	8.32%	6.16%	8.38%	5.04%
PF-8[a]	DLS	10.63%	10.81%	**13.67**%	9.59%	7.76%	8.38%
	NDLSCV	5.09%	4.71%	6.80%	2.66%	2.66%	3.65%
	NDLSR	4.82%	3.97%	7.88%	7.71%	3.70%	2.77%
Soft storey configuration							
SF-4	DLS	8.41%	7.80%	**10.23**%	9.01%	5.63%	5.74%
	NDLSCV	3.12%	3.19%	2.36%	2.79%	0.72%	1.91%
	NDLSR	3.70%	1.73%	1.51%	2.02%	1.22%	2.03%
SF-8	DLS	7.80%	8.09%	**8.38**%	8.61%	9.53%	6.02%
	NDLSCV	2.52%	2.55%	2.75%	2.39%	7.63%	6.22%
	NDLSR	2.74%	1.94%	2.84%	2.44%	5.48%	5.27%

Table 6.15 Maximum absolute difference between "experimentally-based" and "numerically-based" theoretical fragility curves for all the structures and the several limit states

Structure	Limit state	Slight	Light	Moderate	Extensive	Partial collapse	Collapse
Fully infilled							
FF-4	DLS	18.6%	18.9%	**25.1%**	15.7%	1.4%	8.2%
	NDLSCV	14.6%	14.8%	21.2%	11.9%	2.1%	6.6%
	NDLSR	15.4%	14.6%	19.0%	11.2%	1.9%	7.5%
FF-8	DLS	**28.2%**	**28.2%**	12.2%	6.3%	4.0%	5.8%
	NDLSCV	22.9%	22.6%	11.0%	5.5%	4.3%	5.8%
	NDLSR	23.4%	20.7%	9.1%	3.8%	4.6%	5.8%
Partially infilled configuration							
PF-4[a]	DLS	7.2%	**9.8%**	9.7%	**9.8%**	9.0%	1.7%
	NDLSCV	5.1%	7.4%	9.1%	3.9%	6.8%	1.5%
	NDLSR	5.4%	8.7%	7.8%	3.1%	3.7%	1.1%
PF-8[a]	DLS	5.9%	5.9%	**8.4%**	7.0%	1.2%	0.8%
	NDLSCV	4.2%	4.2%	6.4%	1.4%	1.0%	1.2%
	NDLSR	4.5%	3.8%	6.0%	3.4%	1.0%	0.5%
Soft storey configuration							
SF-4	DLS	1.3%	1.3%	0.8%	**3.7%**	1.1%	1.2%
	NDLSCV	1.0%	1.1%	0.6%	2.3%	0.3%	0.8%
	NDLSR	1.3%	0.8%	0.5%	1.6%	0.5%	0.5%
SF-8	DLS	0.6%	0.6%	2.0%	**6.2%**	2.6%	2.6%
	NDLSCV	0.5%	0.5%	1.6%	2.6%	3.0%	2.4%
	NDLSR	0.4%	0.5%	2.3%	2.2%	0.2%	1.9%

Since the maximum absolute difference between the "experimentally-based" and "numerically-based" fragility curves does not fully indicate the overall difference between the curves, the normalized Wasserstein distance (*WD*) was also analysed. Based on the expression of this indicator, it can be seen that it measures the accumulated difference between the two fragility curves normalized by the area of the reference fragility curve, thus providing a measure of the global relative difference between the two curves. The evolution of the values of *WD* obtained for the different structures for the several limit states are presented in Figure 6.34 and Figure 6.35 for the four- and eight-storey structures, respectively. As can be seen, *WD* increases until the moderate/extensive limit states, after which it either decreases or remains rather constant. The larger values of *WD* found for the limit states of lower severity are consistent with the previously shown results in terms of maximum absolute difference. However, the *WD* are larger for the limit states of lower severity because of two factors: first, because the larger pointwise differences between the two fragility curves are larger for these limit states (as seen for the results in terms of maximum absolute difference), and second, because the area of the reference fragility curve is smaller for these limit states (i.e. the IM range covered by the fragility curve is usually smaller for low severity limit states). Furthermore, as also found when analysing the maximum absolute differences, the largest *WD* values are obtained for the fragility curves involving deterministic limit states. As referred before, this reflects differences in the fitting or in the empirical data mostly due to the smaller sample size involved in these cases.

From the curves represented in Figure 6.34 and Figure 6.35, it can also be seen that the largest values of *WD* are obtained when comparing "experimentally-based" and "numerically-based" empirical fragility curves. These reflect the true fragility data without any masking effect from distribution fitting. Also, the largest contributions to the maximum value of *WD* are obtained for the first half of the IM range of the fragility curves of a given limit state. This means that for a given limit state and probability level above 50%, the "experimentally-based" and "numerically-based" fragility curves provide a similar probability of exceedance of the limit state for a given IM value. When analysing the actual maximum values of *WD*, it can be seen that the largest value are in the range of 20%-25%, but only occur for a handful of cases. On average, the largest values of *WD* are around 10%. In order to determine the maximum values of the presented *WD* evolutions, Table 6.16 and Table 6.17 present those maximum values for all structures and for all the considered limit states. As can be seen, the overall highest value is 27.37% and was found for a low severity limit state as referred. On the other hand, it found the lowest *WD* values are always obtained for the SF structures because

their fragility curves are governed by the soft-storey mechanism which is less influenced by the ype of infill model.

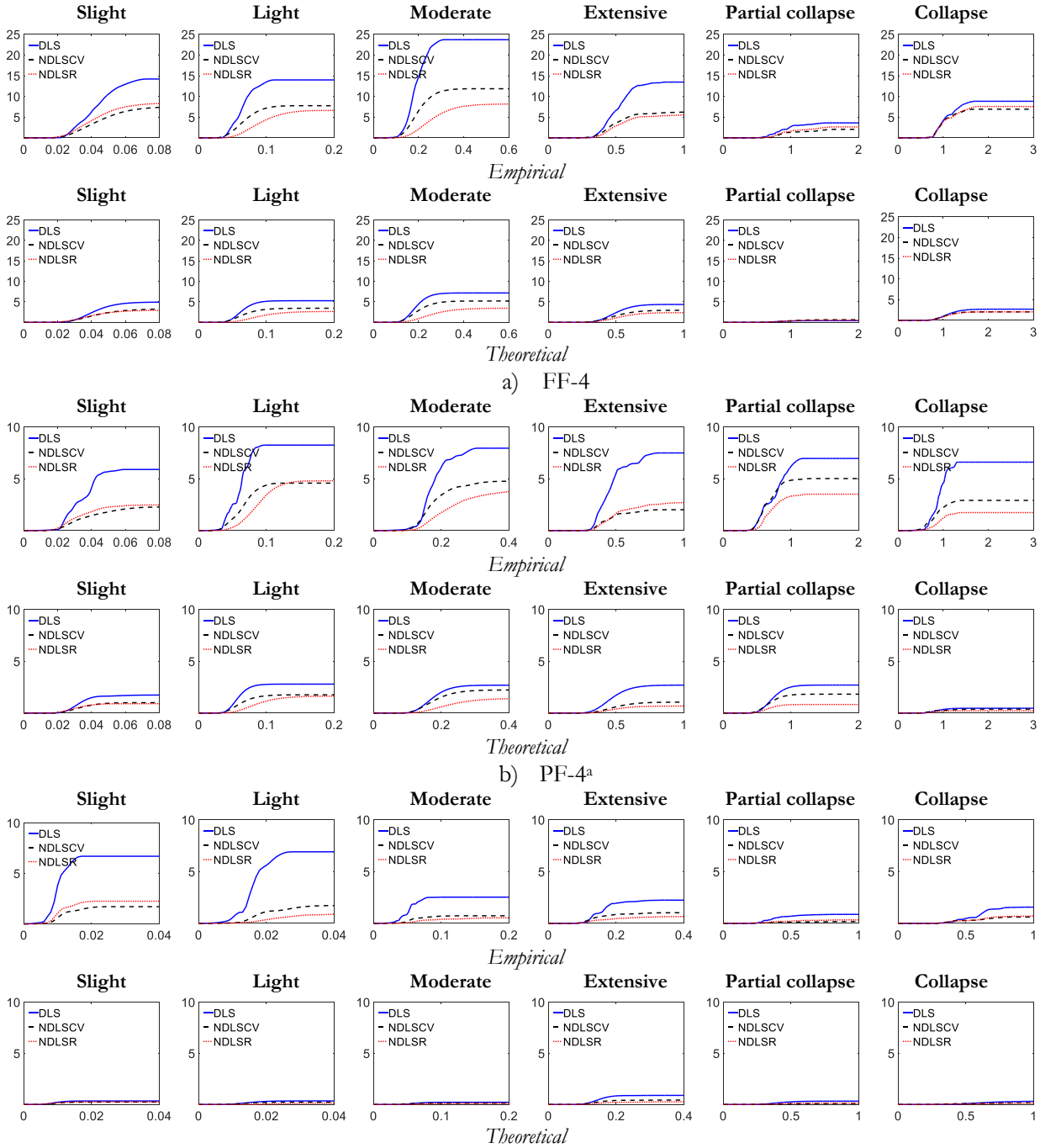

a) FF-4

b) PF-4[a]

c) SF-4

Figure 6.34 Normalized Wasserstein distance between the "experimentally-based" and "numerically-based" fragility curves for different limit states for the four-storey structures; the vertical axis is *WD in* [%] and the horizontal axis is the PGA in [g]

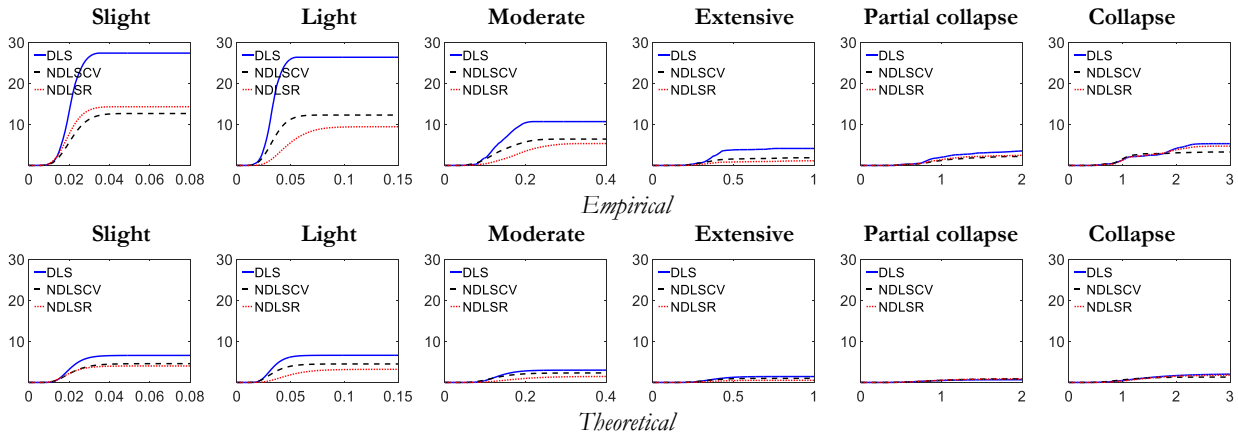

a) FF-8

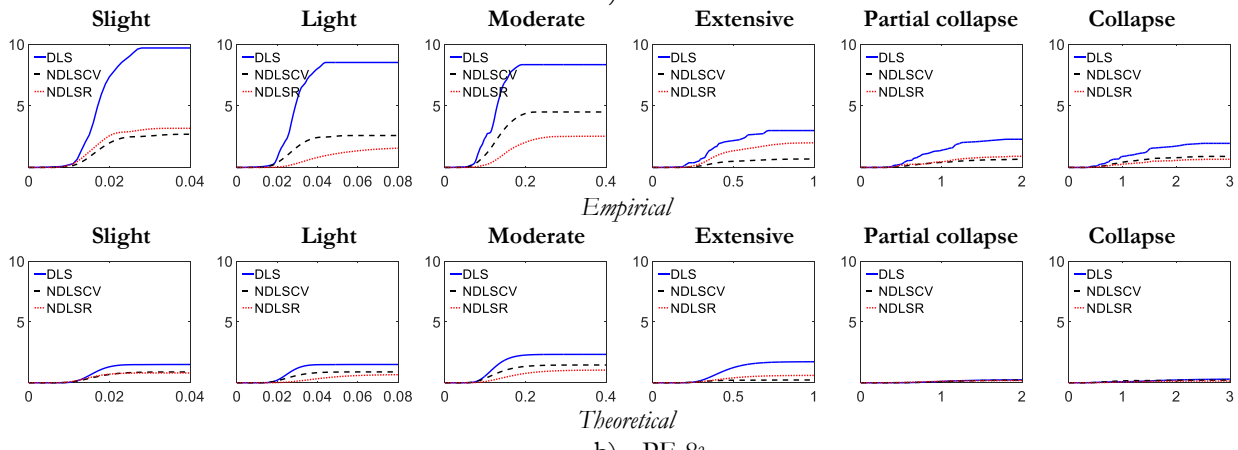

b) PF-8[a]

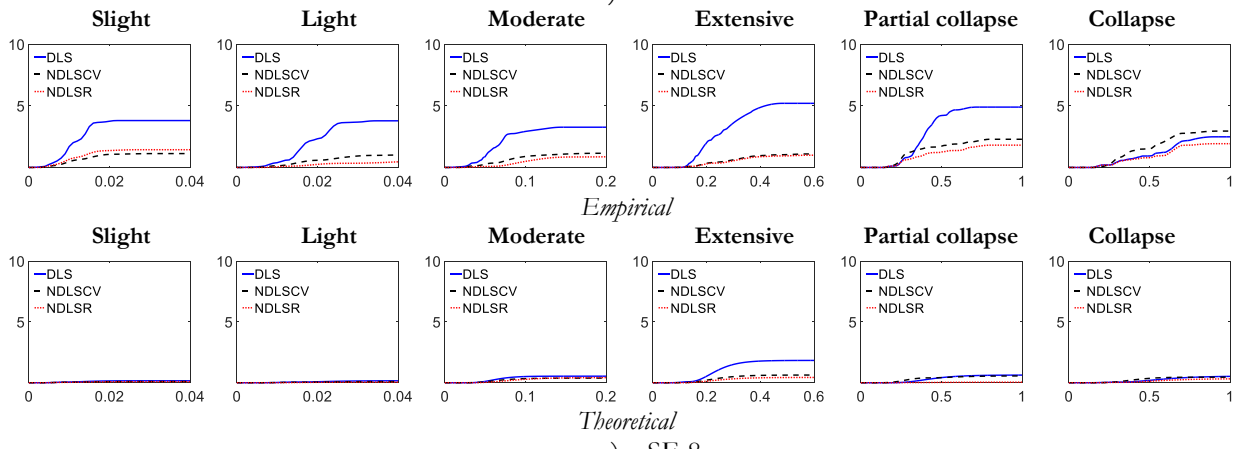

c) SF-8

Figure 6.35 Normalized Wasserstein distance between the "experimentally-based" and "numerically-based" fragility curves for different limit states for the eight-storey structures; the vertical axis is *WD* in [%] and the horizontal axis is the PGA in [g]

Table 6.16 Maximum values of the normalized Wasserstein distance between the "experimentally-based" and "numerically-based" fragility curves for different structures and limit states for empirical fragility curves

Structure	Limit state	Slight	Light	Moderate	Extensive	Partial collapse	Collapse
			Fully infilled				
FF-4	DLS	14.21%	13.99%	23.70%	13.47%	3.62%	8.84%
	NDLSCV	7.53%	7.77%	11.86%	6.24%	2.07%	6.92%
	NDLSR	8.35%	6.63%	8.18%	5.63%	2.65%	7.57%
FF-8	DLS	27.37%	26.36%	10.68%	4.14%	3.56%	5.31%
	NDLSCV	12.65%	12.28%	6.42%	1.90%	2.27%	3.28%
	NDLSR	14.30%	9.43%	5.34%	1.18%	2.58%	4.70%
			Partially infilled configuration				
PF-4[a]	DLS	5.91%	8.26%	7.96%	7.50%	6.97%	6.61%
	NDLSCV	2.29%	4.59%	4.77%	2.02%	5.03%	2.92%
	NDLSR	2.48%	4.82%	3.92%	2.70%	3.52%	1.74%
PF-8[a]	DLS	9.70%	8.52%	8.35%	3.00%	2.29%	1.95%
	NDLSCV	2.70%	2.59%	4.50%	0.69%	0.68%	0.90%
	NDLSR	3.18%	1.60%	2.54%	2.03%	0.91%	0.66%
			Partially infilled configuration				
SF-4	DLS	6.70%	6.91%	2.54%	2.25%	0.87%	1.58%
	NDLSCV	1.71%	1.72%	0.74%	1.03%	0.19%	0.66%
	NDLSR	2.25%	1.08%	0.54%	0.66%	0.34%	0.74%
SF-8	DLS	3.81%	3.79%	3.27%	5.21%	4.90%	2.49%
	NDLSCV	1.13%	1.04%	1.15%	1.10%	2.29%	2.95%
	NDLSR	1.44%	0.64%	0.88%	1.00%	1.81%	1.93%

Table 6.17 Maximum values of the normalized Wasserstein distance between the "experimentally-based" and "numerically-based" fragility curves for different structures and limit states for theoretical fragility curves

Structure	Limit state	Slight	Light	Moderate	Extensive	Partial collapse	Collapse
			Fully infilled				
FF-4	DLS	4.95%	5.28%	7.18%	4.37%	0.40%	2.71%
	NDLSCV	3.29%	3.44%	5.22%	2.94%	0.64%	2.06%
	NDLSR	2.96%	2.67%	3.46%	2.36%	0.52%	2.06%
FF-8	DLS	6.58%	6.61%	3.00%	1.44%	0.66%	2.11%
	NDLSCV	4.58%	4.50%	2.32%	1.01%	0.94%	1.31%
	NDLSR	4.01%	3.20%	1.47%	0.53%	0.89%	1.81%
			Partially infilled configuration				
PF-4[a]	DLS	1.75%	2.80%	2.70%	2.71%	2.71%	0.47%
	NDLSCV	1.01%	1.77%	2.24%	1.07%	1.83%	0.39%
	NDLSR	0.92%	1.65%	1.43%	0.68%	0.83%	0.23%
PF-8[a]	DLS	1.50%	1.50%	2.33%	1.73%	0.25%	0.32%
	NDLSCV	0.89%	0.89%	1.46%	0.23%	0.23%	0.22%
	NDLSR	0.81%	0.68%	1.04%	0.61%	0.18%	0.14%
			Partially infilled configuration				
SF-4	DLS	0.34%	0.35%	0.22%	0.89%	0.32%	0.32%
	NDLSCV	0.23%	0.23%	0.13%	0.43%	0.10%	0.18%
	NDLSR	0.24%	0.14%	0.11%	0.27%	0.13%	0.14%
SF-8	DLS	0.16%	0.16%	0.54%	1.84%	0.63%	0.55%
	NDLSCV	0.10%	0.11%	0.38%	0.63%	0.56%	0.46%
	NDLSR	0.09%	0.06%	0.43%	0.44%	0.05%	0.34%

As referred before, the numerical properties of the strut models for the partially infilled structures were defined using two different scenarios: one based on Point A of Figure 6.4 b) (the

reference scenario considered in the previous comparisons) and another based on Point B of Figure 6.4 b). To analyse the influence of using a lower stiffness for the struts (i.e. when Point B is considered) the differences that are found when comparing the fragility curves of the two scenarios are examined in the following. Figure 6.36 shows the absolute differences between the "experimentally-based" and the two cases of "numerically-based" fragility curves considering deterministic limit states. The fragility data obtained when using a lower stiffness (i.e. Point B) are termed Num^b while the data obtained when using Point a is termed Num^a. It can be seen that considering a lower stiffness for the struts leads to large errors. For example, for the slight limit state and the four-storey structure, the differences obtained when using Point B go up to 59.7% while those obtained when using Point A are just 7.2%. On the contrary, the eight-storey structure is seen to be less sensitive to this parameter. Further analyses and different structures should be examined to confirm this finding.

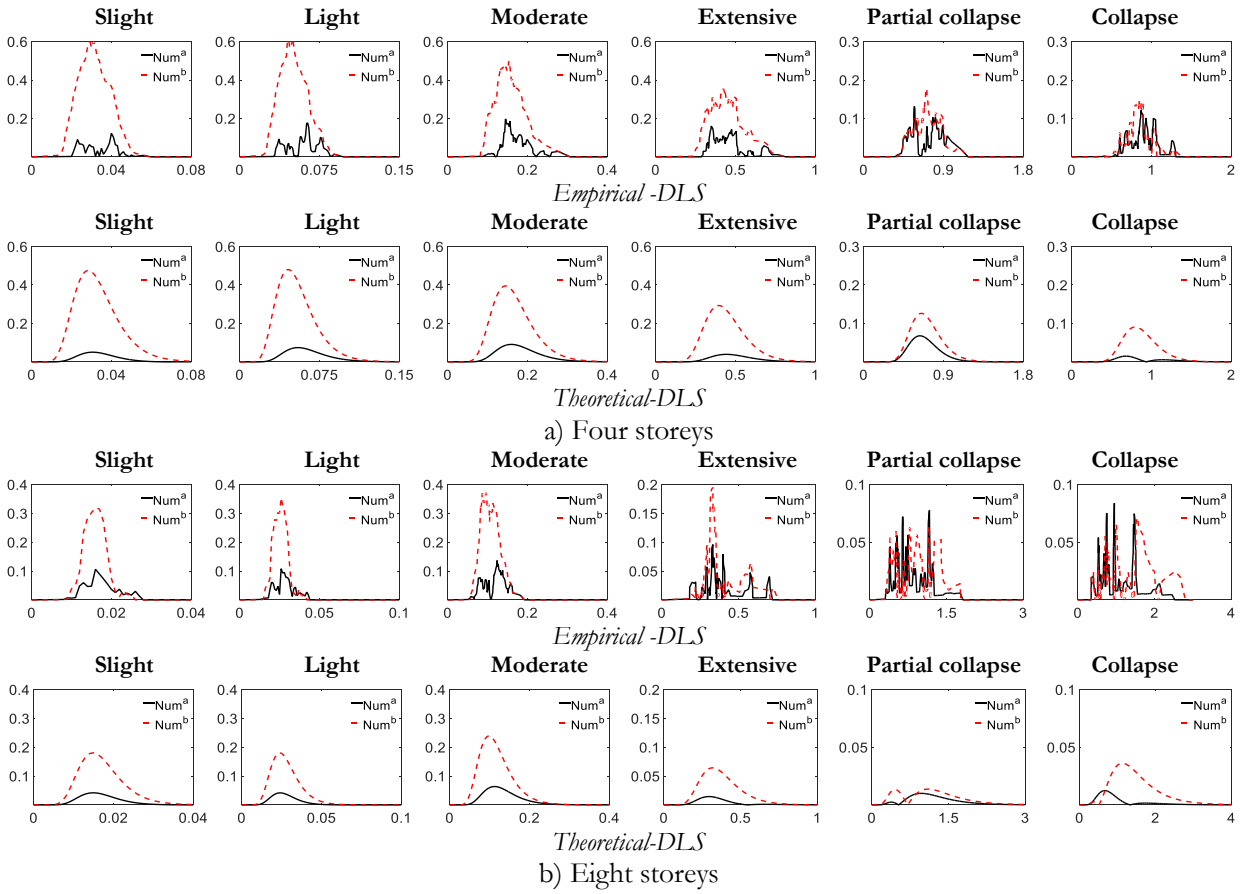

a) Four storeys

b) Eight storeys

Figure 6.36 Absolute error between "experimentally-based" and "numerically-based" fragility curves using two different initial stiffnesses for the strut model; vertical axis is the difference in the probability of exceedance and the horizontal axis is the PGA in [g]

To complement the data presented in Figure 6.36, Table 6.18 and Table 6.19 show the maximum values of the absolute error for each case, considering both deterministic and nondeterministic limit states. These results confirm that much larger differences are obtained in most cases (particularly for the four-storey structures) when using Point B to define the strut parameters, irrespective of the limit state and limit state definition. Therefore, having an adequate value for the initial stiffness of the strut model is seen to be fundamental to ensure the reliability of the structural behaviour and safety analysis results.

Table 6.18 Maximum absolute error between "experimentally-based" and "numerically-based" empirical fragility curves using two different initial stiffnesses for the strut model for the four storeys building

Limit state	Slight (A/B)	Light (A/B)	Moderate (A/B)	Extensive (A/B)	Partial collapse(A/B)	Collapse (A/B)
			Four storeys			
DLS	12.27/61.21	17.63/62.22	19.78/49.93	16.06/35.32	13.13/17.76	12.11/14.84
NDLSCV	4.33/46.33	7.48/46.6	12.08/41.68	6.12/26.65	9.83/14.31	4.37/13.28
NDLSR	4.8/47.87	9.31/42.56	8.32/35.23	6.16/25.33	8.38/15.25	5.04/14.95
			Eight storeys			
DLS	10.63/31.93	10.81/35.4	13.67/37.13	9.59/19.5	7.76/6.37	8.38/7.14
NDLSCV	5.09/21.33	4.71/21.05	6.8/26.86	2.66/8.57	2.66/4.48	3.65/6.91
NDLSR	4.82/22.89	3.97/17.75	7.88/21.89	7.71/7.18	3.7/5.57	2.77/6.66

Table 6.19 Maximum absolute error between "experimentally-based" and "numerically-based" empirical fragility curves using two different initial stiffnesses for the strut model for the eight storeys building

Limit state	Slight (A/B)	Light (A/B)	Moderate (A/B)	Extensive (A/B)	Partial collapse(A/B)	Collapse (A/B)
			Four storeys			
DLS	7.2/59.7	9.8/59.6	9.7/44.8	9.8/32.9	9/12.3	1.7/6.7
NDLSCV	5.1/47.5	7.4/48	9.1/39.5	3.9/29.3	6.8/12.6	1.5/9.1
NDLSR	5.4/49.5	8.7/44.6	7.8/34.9	3.1/27	3.7/12.8	1.1/7.8
			Eight storeys			
DLS	5.9/23.9	5.9/23.9	8.4/31.6	7/6.1	1.2/2.6	0.8/3.6
NDLSCV	4.2/18.1	4.2/18	6.4/23.9	1.4/6.4	1/1.4	1.2/3.6
NDLSR	4.5/19	3.8/16.7	6/19.7	3.4/5.2	1/1.7	0.5/4.2

6.9 Conclusion

The seismic vulnerability of RC frames with different configurations of masonry infills was analysed. Configurations involving fully infilled (FF), partially infilled (PF) and soft-storey (SF) structures with four and eight storeys were considered, in addition of the corresponding bare frame model used as a reference case. The infill panels were modelled using single strut elements and their parameters were defined for two analysis scenarios: one where the strut parameters were defined using experimental data and another where they were defined using numerical data from the results of detailed finite element analyses. The behaviour of the structures was analysed by incremental dynamic analysis using fifty real ground motions records. The performance of the structures was then examined for different limit states, considering both deterministic and nondeterministic limit state definitions. Performance and vulnerability was then represented by fragility curves obtained using an IM-based approach.

The fragility datasets obtained for the different structures and the several limit states were analysed from a statistical point of view to determine which theoretical distribution model would perform better at fitting the data. Of the several the theoretical distribution models that were considered, it was seen that the generalized extreme value distribution performed slightly better, in some cases, than the commonly considered lognormal distribution, for datasets involving deterministic limit states. However, the differences were not found to be significant and the lognormal distribution was considered to represent the fragility curves for these datasets. On the other hand, for datasets involving nondeterministic limit states, none of the considered theoretical distribution models was able to perform adequately in fitting the data. Therefore, for these datasets, fragility curves were represented using the empirical fragility curve and the lognormal distribution model. The former represents the true fragility curve while using the latter provides the level of error that would be obtained when using the most commonly considered distribution model.

Based on the fragility curves, the performance of the several structures was analysed for the different limit states. For the first limit states (i.e. slight, light and moderate), structures BF and SF have a close performance while the performance of the PF structure is closer to that of the FF structure. After reaching the extensive limit state, the BF structure exhibits a better performance than the SF structure due to its higher capacity to spread plasticity. The higher vulnerability of the SF structure for the more severe limit states is a direct result of the soft-storey failure mechanism that is easily reached due to its weak ground storey. Furthermore, for the more severe limits states (i.e. the

partial collapse and collapse limit states), the performance of the PF and FF structures is closer to that of the BF structure as a result of losing a significant part of the strength after the failure of the infills.

By comparing the fragility curves obtained when using nondeterministic and deterministic limit states, it was found that, for the less severe limit states, the influence of the nondeterministic limit states increase as the severity of the limit state also increases. On the other hand, the effect of the limit state variability is almost non-existent for the partial collapse and collapse limit states, as the result of the flatness of the IDA curves for larger IM values. However, considering nondeterministic limit states does not change the relative global performance of the structures with respect to the cases where deterministic limit states were considered. Furthermore, for the cases involving nondeterministic limit states, it is also noted that relevant differences between the empirical and theoretical fragility curves can only be seen for the more severe limit states, i.e. from the extensive onwards, but especially for the partial collapse and collapse limit states. Nevertheless, the lognormal model was seen to provide fragility estimates that are more conservative than the empirical values when those differences become larger.

Finally, when comparing the "numerically-based" and "experimentally-based" fragility curves, the former were generally seen to be more conservative than the latter. These differences are due to the larger sensitivity of the model to the pre-peak properties of the infill models, mainly the stiffness. However, the referred differences between the "experimentally-based" and "numerically-based" fragility curves reduce significantly as the severity of the limit state increases. Furthermore, these differences are also seen to be smaller when nondeterministic limit states are considered. For the particular cases of the SF structures, a lower sensitivity to the way the infill model was observed, which indicates that the overall behaviour is governed by the RC elements of the ground storey and not by the infill. Additional analyses examining the influence of how the initial stiffness of the numerical infill model is defined indicated that having a suitable value for the initial stiffness of the strut model is fundamental to ensure the reliability of the structural behaviour and safety analysis results. Nevertheless, performing detailed finite element analyses to represent the behaviour of infilled structures as an alternative to experimental tests can be seen to provide suitable data to define the parameters of simplified strut models with an adequate level of reliability.

Chapter 7.
Closure

7.1 Conclusions

The present thesis addressed the numerical modelling of reinforced concrete (RC) frames with masonry infills to develop adequate approaches for seismic performance and seismic risk assessment analyses. Several aspects of the infill modelling were addressed ranging from the use of detailed finite element models to the calibration of simplified macro-models. Although the main findings and remarks regarding each of the topics addressed by the research were presented in each chapter, the most relevant remarks and conclusions are highlighted in the following.

Since masonry infills have a non-negligible contribution to the global structural behaviour, many simplified approaches were proposed in the literature to model the structural contributions of masonry infill walls to the global structure response. The use of these approaches is normally suggested when relevant experimental data is unavailable and they have been categorized into two main groups: stiffness-based procedures and strength-based procedures. The research that was carried out analysed the reliability of several empirical procedures by comparing their strength and stiffness predictions with available experimental data. The main principle of the stiffness-based approach that an infill panel works as a constant area member under compression loads throughout the entire loading history leads to large errors in predicting both the maximum lateral strength and the initial stiffness of the infill. Therefore, due to the large variability of the performance of the tested stiffness-based procedures, none of them is recommended to establish the parameters needed to simulate the behaviour of masonry infills using the single strut modelling approach. With respect to the empirical strength-based

procedures that were analysed (that include several procedures suggested by standards) these were seen to provide better predictions of the maximum lateral strength and the initial stiffness of the infill. However, the large variability of the predictions obtained for the several experimental specimens that were considered renders the applicability of these models highly uncertain. In the overall, all the strength-based procedures that were analysed exhibit a large variability of their performance. Even if some procedures provided reasonable predictions for part of the specimens, their significant underestimation or overestimation of the parameters analysed for other specimens is a clear reflection of their empirical nature and uncertain performance.

With respect to the modelling of partially infilled walls, the use of reduction factors for the strength and stiffness of the full infill was seen to be a more efficient approach when compared to the use of a new configuration of struts which requires adding several elements, thus involving a higher computational cost. In this context, the performance of several existing empirical expressions proposing reduction factors was analysed. By comparing the strength predicted by these expressions with those measured experimentally for several experimental specimens, most expressions were seen to exhibit a reasonable error.

Since the use of existing empirical stiffness-based or strength-based procedures is not recommended to define the parameters of simplified strut models in a general situation, a more reliable framework was proposed to obtain the necessary data. This framework is proposed for cases where experimental data is unavailable and analysed the possibility of using refined finite element models to simulate experimental data as an alternative for the actual experimental tests. The results obtained from the use of the detailed finite element modelling strategy that was proposed show that it is able to represent the behaviour of masonry infilled RC frames adequately and can be used to simulate this type of structural system using only the essential mechanical properties of the materials involved (i.e. without the need to test an entire specimen). This conclusion was supported by the ability of the modelling strategy to adequately account for the more common masonry failure mechanisms, as well as to represent the strength and stiffness envelopes with a reasonable accuracy when compared to experimental results. The numerical results that were obtained also indicate there is no clear increase in their accuracy when the longitudinal reinforcement of RC members is modelled using a discrete steel modelling approach. Given the significant computational effort required by this approach, the use of a smeared steel modelling approach is recommended instead.

Since macro-models such as the single strut element are seen to be reliable tools to represent the structural contribution of an infill panel and their parameters should not be defined by uncalibrated

empirical proposals, robust data is needed (e.g. from experimental data or results obtained by refined finite element simulations) to determine such parameters. Still, assuming that such data is available, specific procedures are required to establish the parameters of the macro-model. In this context, calibration procedures were proposed to determine the parameters of macro models, first for single strut models, and then extended for multi-strut systems and for another macro-model with a special configuration. The proposed procedures for defining the parameters of strut models uses the capacity curve of the masonry infill which is extracted by combining the capacity curves of the bare and the infilled frames. Specific procedures were developed to define the parameters of strut models for both stiffness- and strength-based approaches. For the particular case of the stiffness-based approach, it is noted that the proposed procedure does not simulate a reduction in the cross-section area of the strut element to overcome the highlighted limitations of the usual way this approach is used. Instead, the proposed approach uses a constitutive model that accounts for stress degradation to simulate a similar overall effect. The proposed procedures were tested for fully and partially infilled specimens with different configurations and using both experimental and numerical data from detailed finite element models. When comparing the experimental results of the specimens analysed with the global behaviour obtained from the simplified models involving single-strut elements with parameters defined by the proposed procedures (either the stiffness- or the strength-based approach), a good agreement was found, thus validating those procedures. After extending the proposed procedures for two multi-strut models and for the model proposed by (Rodrigues*, et al.*, 2010), the behaviour of several RC frames with masonry also seen to exhibit a good agreement with the corresponding experimental data, thus validating also the proposed procedures for these macro-models.

Even though the presented macro-models were seen to be able to capture the global behaviour of the physical specimens, analysing the local structural demand they yield led to different conclusions. When analysing the shear force distribution in columns of masonry infilled frames simulated using different macro-models, it was seen that compression-only macro-models were able to provide more realistic shear force distributions in columns, when compared to models involving elements active in both loading directions.

The seismic vulnerability of RC frames with four and eight storeys and with different configurations of masonry infills was then analysed using calibrated single strut models based on both experimental and numerical data from the refined finite element model. After performing incremental dynamic analyses using a suite of fifty real ground motions, fragility datasets were obtained for the different structures and the several deterministic and nondeterministic limit states that were

considered. The fragility datasets were analysed from a statistical point of view to determine which theoretical distribution model would perform better at fitting the data. Of the several the theoretical distribution models that were considered, it was seen that the generalized extreme value distribution performed slightly better, in some cases, than the commonly considered lognormal distribution, for datasets involving deterministic limit states. However, the differences were not found to be significant and the lognormal distribution was considered to represent the fragility curves for these datasets. On the other hand, for datasets involving nondeterministic limit states, none of the considered theoretical distribution models was able to perform adequately in fitting the data.

By comparing the fragility curves obtained when using nondeterministic and deterministic limit states, it was found that, for the less severe limit states, the influence of the nondeterministic limit states increase as the severity of the limit state also increases. On the other hand, the effect of the limit state variability was almost non-existent for the partial collapse and collapse limit states. However, considering nondeterministic limit states does not change the relative global performance of the structures with respect to the cases where deterministic limit states were considered. Furthermore, for the cases involving nondeterministic limit states, it was also noted that relevant differences between the empirical and theoretical fragility curves can only be seen for the more severe limit states. Nevertheless, the lognormal model was seen to provide fragility estimates that are more conservative than the empirical values when those differences become larger.

Finally, when comparing the "numerically-based" and "experimentally-based" fragility curves, the former were generally seen to be more conservative than the latter. These differences are due to the larger sensitivity of the model to the pre-peak properties of the infill models, mainly the stiffness. However, the referred differences between the "experimentally-based" and "numerically-based" fragility curves reduce significantly as the severity of the limit state increases. Furthermore, these differences were also seen to be smaller when nondeterministic limit states are considered. Additional analyses examining the influence of how the initial stiffness of the numerical infill model is defined indicated that having a suitable value for the initial stiffness of the strut model is fundamental to ensure the reliability of the structural behaviour and safety analysis results. Nevertheless, performing detailed finite element analyses to represent the behaviour of infilled structures as an alternative to experimental tests was seen to provide suitable data to define the parameters of simplified strut models with an adequate level of reliability.

7.2 Recommendations for future research

Three main topics were addressed in this thesis and each one raised additional questions that were not able to be addressed in this dissertation. In order to answer those questions, further research should be conducted according to the main research points referred in the following:

- With respect to the use of refined finite element models, further analysis should be carried out to account for the shear failure which may occur in RC columns or for the discrete cracking that may occur through the bricks. Furthermore, debonding effects that may occur between the reinforcement and the concrete should be considered in further research work.
- A parametric study about the sensitivity of the refined finite element modelling strategy to the parameters of the infill panel should be carried out. This includes further research to analyse the performance of existing empirical expressions that can be used to estimate the parameters of contact elements, in case the necessary experimental data is unavailable. In this context, further studies analysing the use of such expressions in the context of the simplified framework proposed in the Annex D are also required in order to examine its ability to simulate experimental tests.
- Further research should address the possibility of analysing the out-of-plane behaviour of masonry infill panels using refined finite element models. Such analyses would provide important data to establish interaction curves between the in-plane and out-of-plane capacity curves.
- Further research should be carried out to analyse the influence of the connection between the infill wall and the surrounding RC frame. This aspect is mentioned briefly in Chapter 5 when analysing the local demand of the structural elements and not only the global response.
- It was found that the fragility curves of the infilled RC frames are sensitive to the stiffness value considered for the strut model. Further research should be carried out to assess if other parameters or combinations of parameters also lead to significant variations in the fragility curves.
- In Chapter 6, the variability of the limit states was assumed. Further research should be carried out to determine more objectively how to represent such dispersion to accommodate the variability in the materials and construction techniques.

- The methodology considered in Chapter 6 to analyse the seismic performance of infilled frames should be extended to also consider limit states defined for acceleration-sensitive non-structural components.
- The RC structures considered in the case studies that were analysed in Chapter 6 were non-seismically designed structures. A replication of these analyses should be carried out for seismically designed structures to determine if the conclusions that were found can be generalized.
- The performance analysis carried out in Chapter 6 should be extended to analyse risk and loss values to determine if there are significant changes in the conclusions that were established when analysing the fragility curves.
- The vulnerability analyses that were performed should be extended to 3D structures that include the out-of-plane behaviour of infills.

Annex

A. Experimental data selected for the validation of the proposed modelling approach

A set of specimens from ten different experimental campaigns (Pires, 1990, Mehrabi, 1994, Mehrabi*, et al.*, 1996, Crisafulli, 1997, Bergami, 2007, Kakaletsis*, et al.*, 2008, Kakaletsis*, et al.*, 2009, Kakaletsis, 2009, Misir*, et al.*, 2012, Sigmund*, et al.*, 2013, Bergami*, et al.*, 2015, Misir, 2015, Basha*, et al.*, 2016, Zhai*, et al.*, 2016) were selected to validate the numerical models in this study. Table 3.1 provides the notations of the selected specimens from these experimental campaigns. The specimens were tested under increasing cyclic lateral loading. The common aspect between these tests is that all specimens were scaled models and are one-bay one-storey frames.

Table A.1 Experimental tests and specimens that were considered in the comparative analyses

campaign (Reference)	Specimen scale	Bare frame Specimen ID	Fully infilled Specimen ID
(Zhai, *et al.*, 2016)	1:1	Specimen 1	Specimen 2
(Pires, 1990)	2:3	Specimen M1	Specimen M2
(Sigmund, *et al.*, 2013)	2:5	Specimen III/1	Specimen III/2
(Kakaletsis, 2009)	1:3	Specimen B	Specimen S
(Bergami, 2007, Bergami, *et al.*, 2015)	1:2	Specimen Fn1	Specimen FT1
(Basha, *et al.*, 2016)	1:2	Specimen DB	Specimen DFS
(Stylianidis, 2012)	1:3	Specimen FB	Specimen F1
(Misir, 2015)	1:2	Specimen BaF	Specimen SBF
(Mehrabi, *et al.*, 1996)	1:2	Na	Specimen 6
(Mehrabi, *et al.*, 1996)	1:2	Na	Specimen 11
(Mehrabi, *et al.*, 1996)	1:2	Na	Specimen 12
(Mehrabi, *et al.*, 1996)	1:2	Na	Specimen 7
(Mehrabi, *et al.*, 1996)	1:2	Specimen 1	Specimen 4
(Mehrabi, *et al.*, 1996)	1:2	Specimen 1	Specimen 5
(Kakaletsis, 2009)	1:3	Specimen B	Specimen IS
(Crisafulli, 1997)	3:4	Na	Specimen unit1

The reinforcement details of the reinforced concrete (RC) elements which are part of these specimens are presented in Figure A.1 to Figure A.3. Since experimental campaigns do not include a separate test on a bare frame, the properties of the RC frames were considered to be those of the corresponding fully infilled specimens. The mechanical properties of the materials involved are summarized in Table A.2.

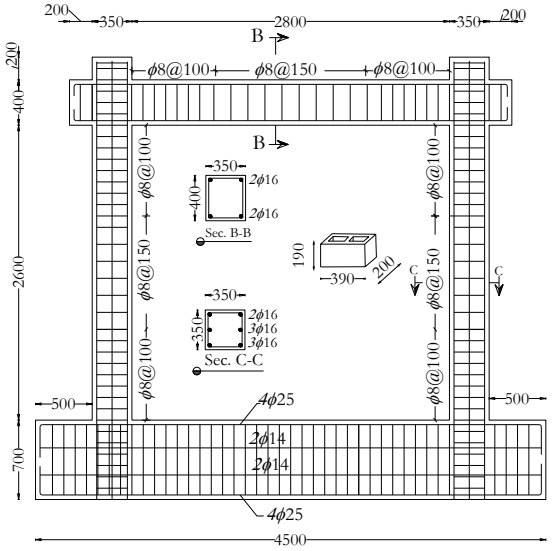

Specimen 2 (Zhai, *et al.*, 2016)

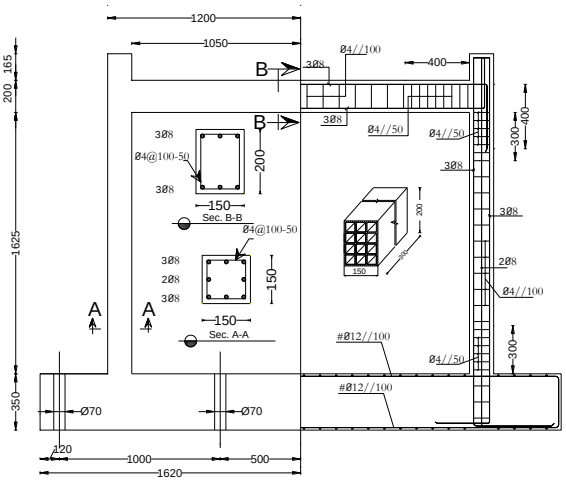

Specimen M2 (Pires, 1990)

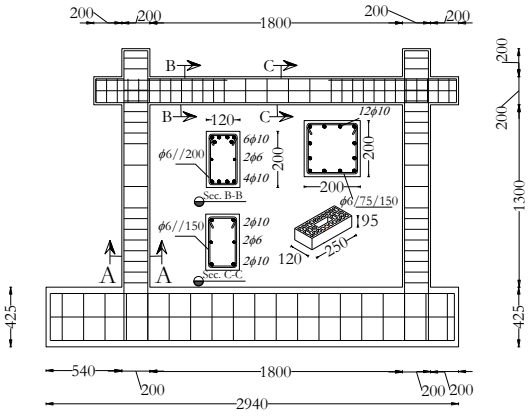

Specimen III/2 (Sigmund, *et al.*, 2013)

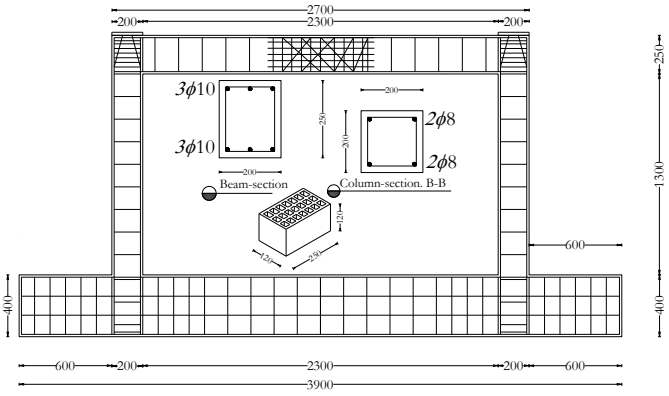

Specimen Ft1(Bergami, 2007, Bergami, *et al.*, 2015)

Figure A.1 Geometry and reinforcement details of the specimens (All dimensions are in millimetre)

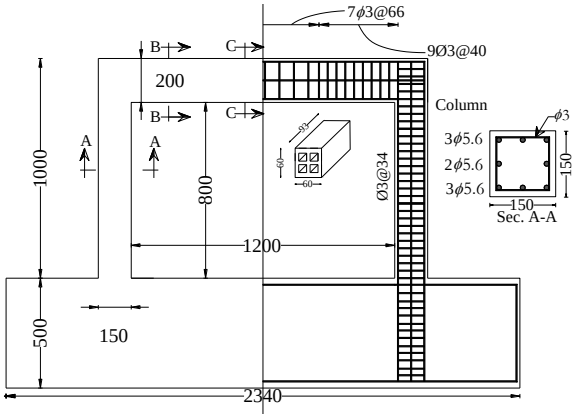

Specimen S (Kakaletsis, 2009)

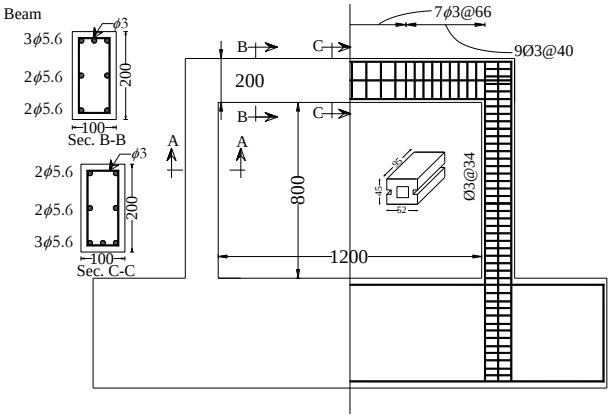

Specimen IS(Kakaletsis, 2009)

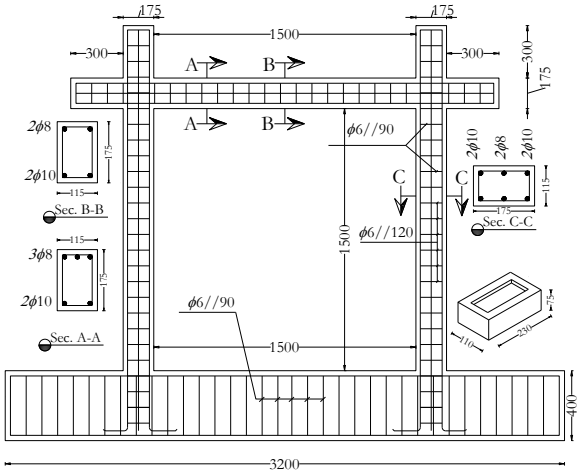

Specimen DFS (Basha, *et al*., 2016)

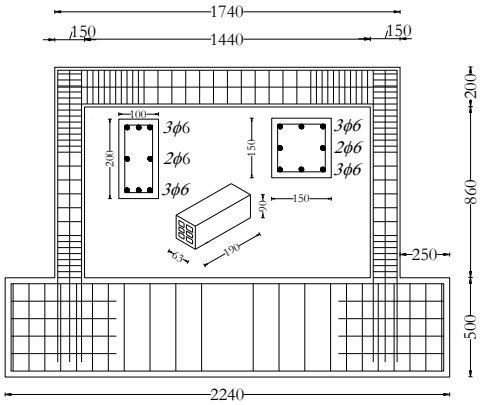

Specimen F1(Stylianidis, 2012)

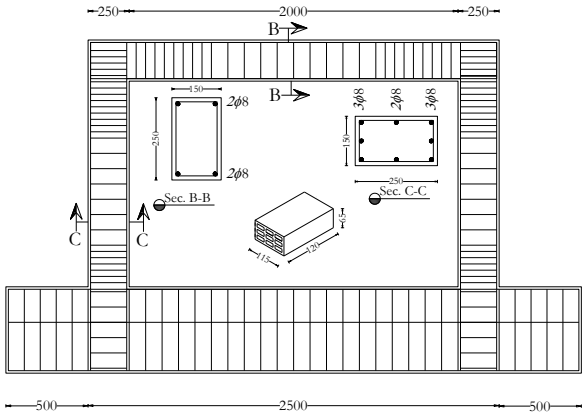

Specimen SBF (Misir, 2015)

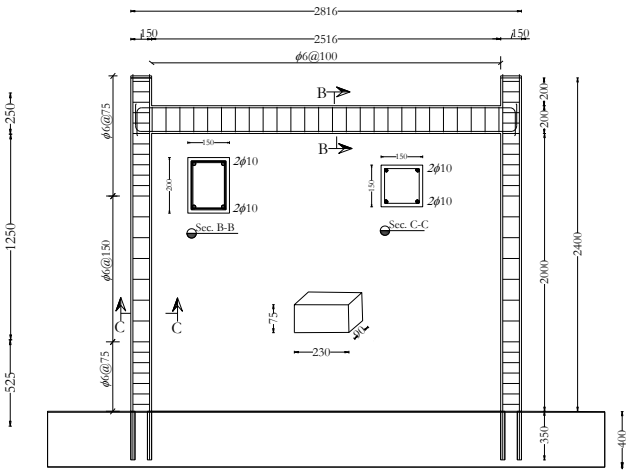

Specimen unit 1(Crisafulli, 1997)

Figure A.2 Geometry and reinforcement details of the specimens (All dimensions are in millimetre).

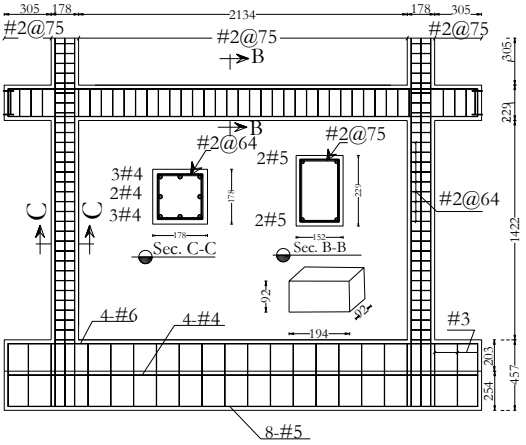

Specimen 5(Mehrabi, *et al.*, 1996)

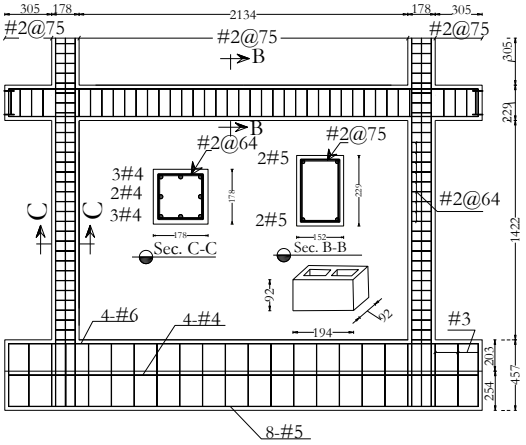

Specimen 4 (Mehrabi, *et al.*, 1996)

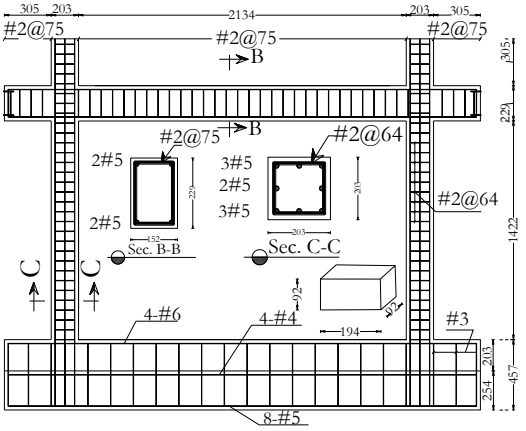

Specimen 7 (Mehrabi, *et al.*, 1996)

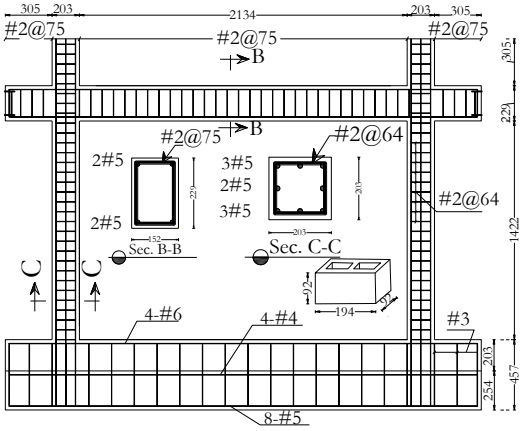

Specimen 6 (Mehrabi, *et al.*, 1996)

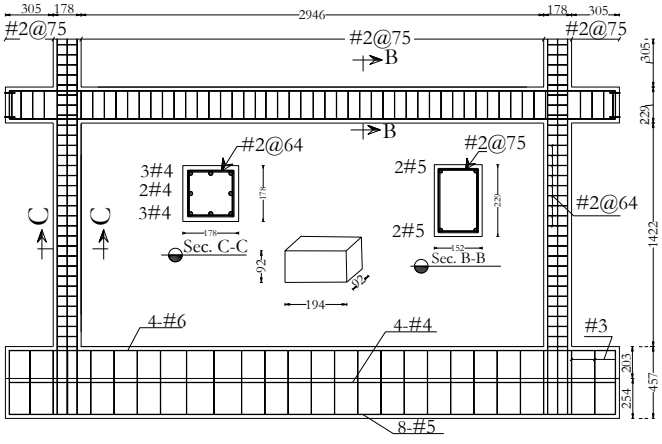

Specimen 11,12 (Mehrabi, *et al.*, 1996)

Figure A.3 Geometry and reinforcement details of the specimens (All dimensions are in millimetre).

Table A.2 Mechanical properties of the materials involved in the experimental specimens

Specimen ID	Concrete		Steel reinforcement				Infill panel			Vertical loading (kN)
			main		stirrups		Brick unit	Mortar	Masonry	
	f_c (MPa)	f_t (MPa)	σ_y	σ_u	σ_y	σ_u	f_m (MPa)	f_{mo} (MPa)	f_m	
Specimen 2	27.74	n/a	472	456	308	464	2.8/1.34	4.56	1.90	700
Specimen M2	23.5*/28.3**	n/a	434.3	519.3	522.7	552.3	4.8	6.2*/6.4**	2.20	220
Specimen III/2	45	n/a	600	700	600	700	15.9/2.6	5.15	2.70	365
Specimen S	28.5	n/a	390.47	516.27	212.2	321.07	3.10	1.53	2.63/5.11	100
Specimen FT1	25.9	n/a	564.00	n/a	n/a	n/a	n/a	n/a	5.29/2.67	159
Specimen DFS	22.4	n/a	460	530	265	520	5.7	17.3	3.9	140
Specimen F1	26.5	n/a	340	467	271	395	6.0	10.7	4.20	0
Specimen SBF	20.1	n/a	472	538	n/a	n/a	19.1	5.3	n/a	365
Specimen 6	25.9	4.91	413.8	622.1	367.6	449.6	16.48	16.76	10.14	294
Specimen 11	25.7	4.26	420.7	622.1	367.6	449.6	15.58	13.03	11.45	294
Specimen 12	26.9	4.75	420.7	622.1	367.6	449.6	15.58	17.86	13.29	294
Specimen 7	33.4	2.26	413.8	622.1	367.6	449.6	15.59	15.52	13.59	294
Specimen 4	26.8	2.77	420.7	622.1	367.6	449.6	16.48	11.17	10.62	294
Specimen 5	20.9	4.38	420.7	622.1	367.6	449.6	15.59	13.38	13.86	294
Specimen IS	28.5	n/a	390.47	516.27	212.2	321.07	26.4	1.75	15.18/17.68	100
Specimen unit1	14.6*/22.5**	2.4	323	441	353	466	26.4	8.0	19.30	200

- f_c is the compressive strength of concrete, f_t is the tensile strength of concrete, σ_y is the steel yield stress and σ_u is the ultimate strength of steel
[1] cubic strength which was converted to cylinder strength.
* at 28 days, ** when the specimen was tested

B. Real constant values of the different models

As referred in Chapter 4, for the smeared modelling approach, the cross sections of the columns, beam and their connections are meshed such that longitudinal rebars are merged with a limited number of elements at the appropriate reinforcement locations, as shown in Figure B.1. The real constants for these particular elements are defined in the following sections according to the notations defined in Table B.1. Regarding the real constants, it is noted that parameter cstif was always considered to be 0.01.

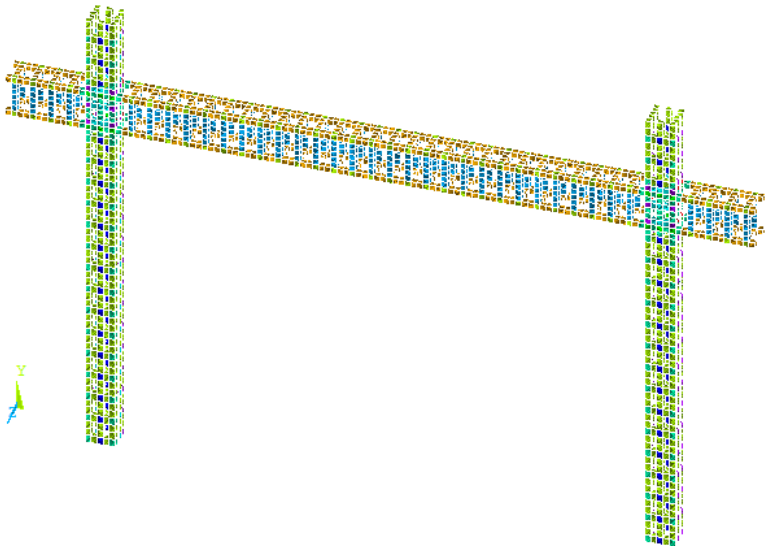

Figure B. 1 The smeared rebar elements in Specimens 1 and 9, Mehrabi's test

Table B.1 Notation of the real constants

Notation	Description
mat1	The material number for the first rebar
vr1	The ratio between the first rebar size and the element size
theta1	The inclination angle θ_1 with respect to the plane oxy of the first rebar
phi1	The inclination angle ϕ_1 with respect to the plane oxz of the first rebar
mat2	The material number for the second rebar
vr2	The ratio between the second rebar size and the element size
theta2	The inclination angle θ_2 with respect to the plane oxy of the second rebar
phi2	The inclination angle ϕ_2 with respect to the plane oxz of the second rebar
mat3	The material number for the third rebar
vr3	The ratio between the third rebar size and the element size
theta3	The inclination angle θ_3 with respect to the plane oxy of the third rebar
phi3	The inclination angle ϕ_3 with respect to the plane oxz of the third rebar
cstif	Stiffness multiplier factor which is used across a cracked face or for a crushed element; the default value is 1.0E-6.

B.1 Specimen 1 and Specimen 9

Figure B.2 shows the RC frame configuration of Specimen 1 and Specimen 9. Columns were meshed with equal meshes with an in-plane size 25.4*25.4 mm^2 and a 32.32 mm height while the beam element size is 24.8*25.4*25.4 mm^3. The beam-column connections were meshed to be consistent with the beam and column mesh sizes in order to accommodate the connection rebars. Tables B.1 to B.3 show the real constants assigned to the columns, beams and beam-column connections, respectively, for the RC frames of Specimen 1 and Specimen 9. Also, the locations for these real constants in columns sections, beam sections, left column-beam connection and right column-beam connection are illustrated in Figure B.3, Figure B.4, Figure B.5 and Figure B.6, respectively, which are in correspondence with Table B.1, Table B.2 and Table B.3, respectively. The extensions of the beam and columns have the same real constants as the main beam and columns, respectively. It is worth noting that the elements that are not assigned with a real constant take the default real constant value corresponding to a full concrete-only section.

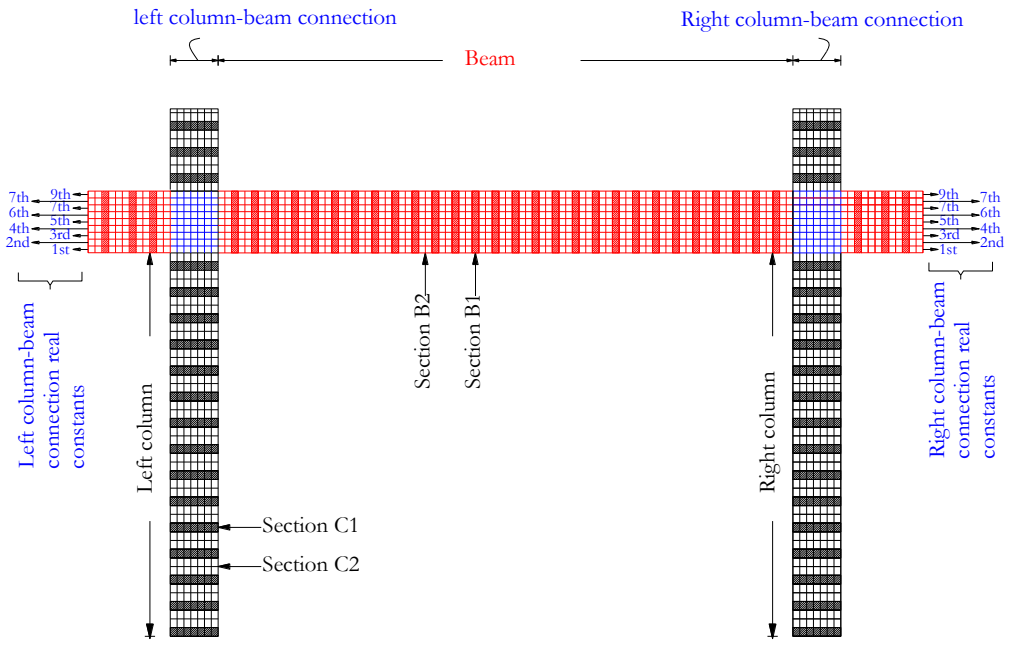

Figure B. 2 General description of Specimen 1, illustrating the different parts of the specimen's real constants and their notations.

Table B.2 Real constants for columns

Number	mat1	vr1	theta	phi	mat1	vr2	theta	phi	mat3	vr3	theta	phi
R22	11	0.039	0	0	1	0.196	90	0	11	0.039	0	90
R20	0	0	0	0	1	0.196	0	0	0	0	0	90
R21	11	0.039	0	0	1	0.196	90	0	11	0	90	0
R12	11	0	0	1	0.196		90	0	11	0.039	0	90
R31	11	0.039	0	0	1		90	0	11	0	90	0
R13	11	0	0	1			90	0	11	0.039	0	90

Table B.3 Real constants for beams

Number	mat1	vr1	theta	phi	mat1	vr2	theta	phi	mat3	vr3	theta	phi
R42	1	0.307	0	0	11	0.049	90	0	11	0.049	0	90
R40	1	0.307	0	0	11	0	90	0	11	0	0	90
R51	1	0	0	11	0	0	90	0	11	0.049	0	90
R15	1	0	0	11	0.049	0	90	0	11	0	90	0

Table B.4 Real constants for beam-column connections

Number	mat1	vr1	theta	phi	mat1	vr2	theta	phi	mat3	vr3	theta	phi
R220	1	0	0	1	0.196	0	90	0	11	0	90	0
R222	11	0.049	0	0	1	0.196	90	0	11	0.049	0	90
R221	11	0.049	0	0	1	0.196	90	0	11	0	90	0
R112	11	0	0	1	0.196	0	90	0	11	0.049	0	90
R331	11	0.049	0	0	1	0	90	0	11	0	90	0
R113	11	0	0	1	0	0	90	0	11	0.049	0	90
R501	1	0.307	0	0	1	0.196	90	0	1	0	90	0
R440	1	0.307	0	0	1	0	90	0	1	0	90	0

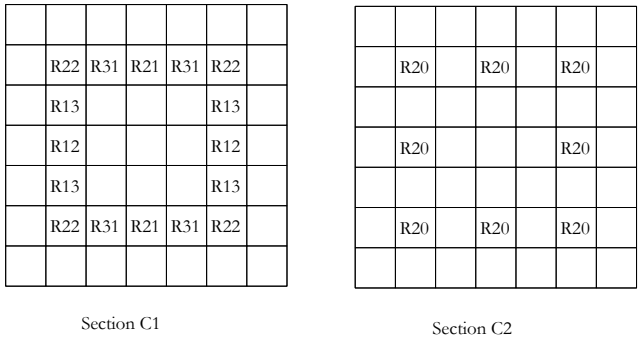

Figure B.3 Specimen 1 real constants for the column according to Table B.2

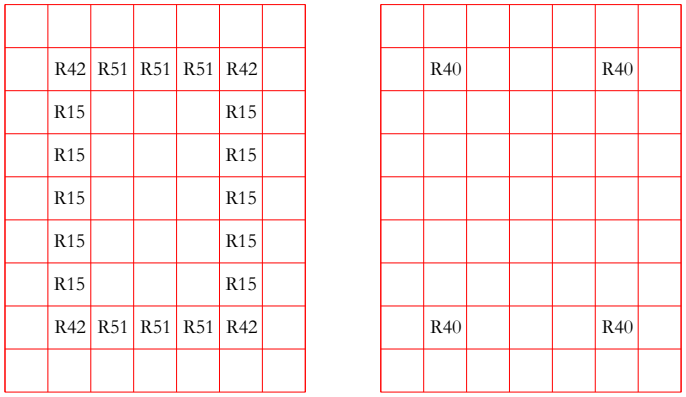

Figure B.4 Specimen 1 real constants for the beam according to Table B.3

Left column-beam connection

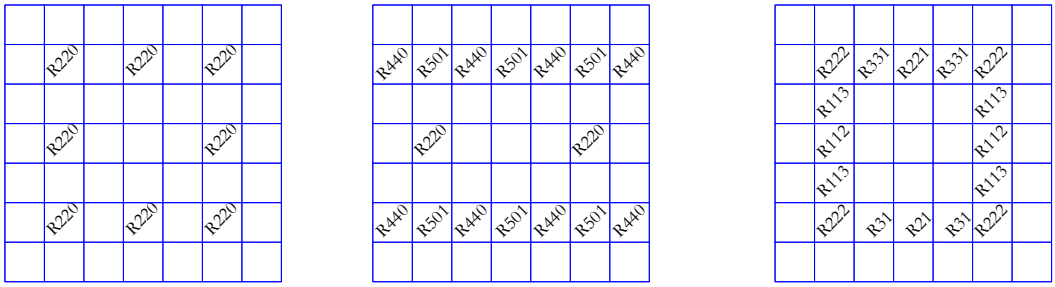

Figure B.5 Specimen 1 real constants for the left column-beam connection according to Table B.4

Right column-beam connection

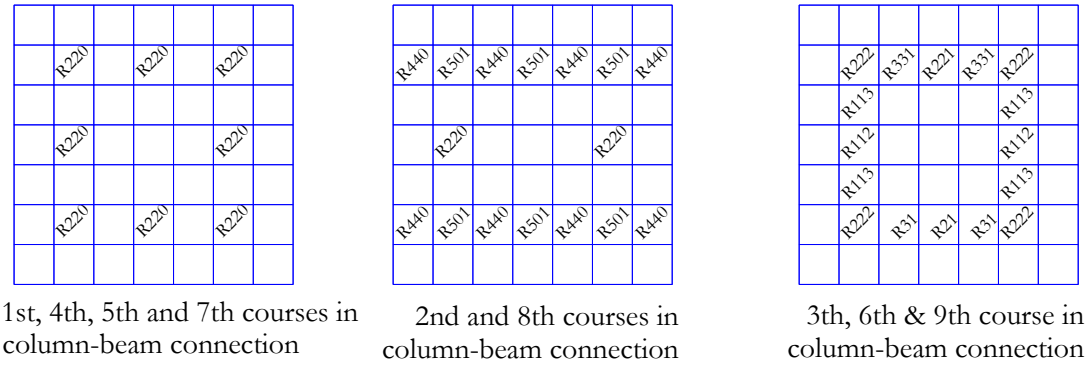

Figure B.6 Specimen 1 real constants for the right column-beam connection according to Table B.4

B.1 Specimen M1 and Specimen M2

Figure B.7 shows the RC frame configuration of specimen M1 and specimen M2. Columns were meshed with equal meshes with an in-plane size of 30*30 mm^2 and a 50.78 mm height, while the beam element size is 50*30*30 mm^3. The beam-column connections were meshed to be consistent with the beam and column mesh sizes in order to accommodate the connection rebars. The column extensions were meshed using the same column mesh and were assigned with the same column real constants. Tables B.4 to B.6 show the real constants assigned to the columns, beam and beam-column connections, respectively, for the RC frame of specimen M1 and specimen M2. Also, the locations for these real constants in columns and beam sections, left column-beam connection and right column-beam connection are illustrated in Figure B.8, Figure B.9 and Figure B.11, respectively, which are in correspondence with Table B.4, Table B.5 and Table B.6, respectively.

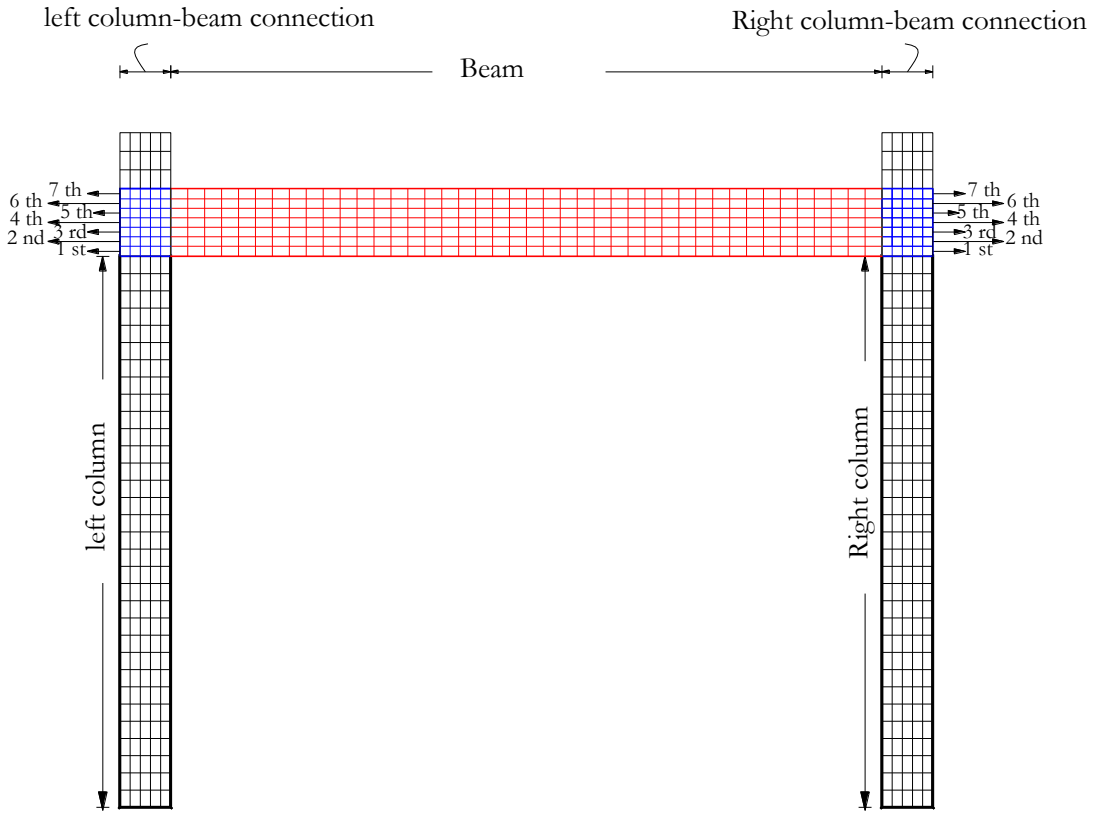

Figure B. 7 General description of the RC frame of specimens M1 and M2, illustrating the different parts of the specimen's real constants and their notations.

Table B.5 Real constants for columns

Number	mat1	vr1	theta	phi	mat1	vr2	theta	phi	mat3	vr3	theta	phi
R20	1	0	0	0	1	0.056	90	0	11	0	0	90
R22	11	0.017	0	0	1	0.056	90	0	11	0.017	0	90
R21	11	0.017	0	0	1	0.056	90	0	0	0	0	0
R12	0	0	1	0.056			90	0	11	0.017	0	90
R31	11	0.017	0	0			0	0	0	0	0	0
R13	0	0					11	0.017	0	90	0	0

Table B.6 Real constants for the beam

Number	mat1	vr1	theta	phi	mat1	vr2	theta	phi	mat3	vr3	theta	phi
R40	1	0.056	0	0	11	0	90	0	11	0	0	90
R42	1	0.056	0	0	11	0.017	90	0	11	0.017	0	90
R402	1	0.056	0	0	11	0.017	0	90	0	0	0	0
R51	11	0.017	0	90			0	0	0	0	0	0
R15	11	0.017	90	0			0	0	0	0	0	0

Table B.7 Real constants for beam-column connections

Number	mat1	vr1	theta	phi	mat1	vr2	theta	phi	mat3	vr3	theta	phi
R501	1	0.056	0	0	1	0.056	90	0	0	0	0	0
R440	1	0.056	0	0			0	0	0	0	0	0
R80	1	0.056	0	0	1	0.112	90	0	0	0	0	0
R202	1	0.112	90	0								
R222	11	0.015	0	0	1	0.056	90	0	11	0.015	0	90
R221	11	0.015	0	0	1	0.056	90	0	11	0	90	0
R331	11	0.015	0	0								
R533	11	0.015	0	0	1	0.112	90	0	0	0	0	0
R113	11	0.015	0	90								
R112	1	0.015	90	0	11	0.015	0	90	0	0	0	0

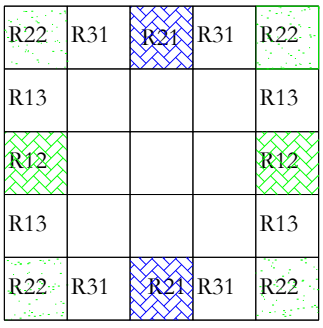

a)

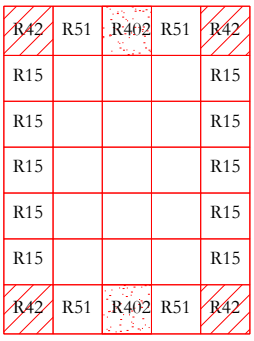

b)

Figure B.8 Specimen M1 real constants: a) column real constants; b) beam real constants

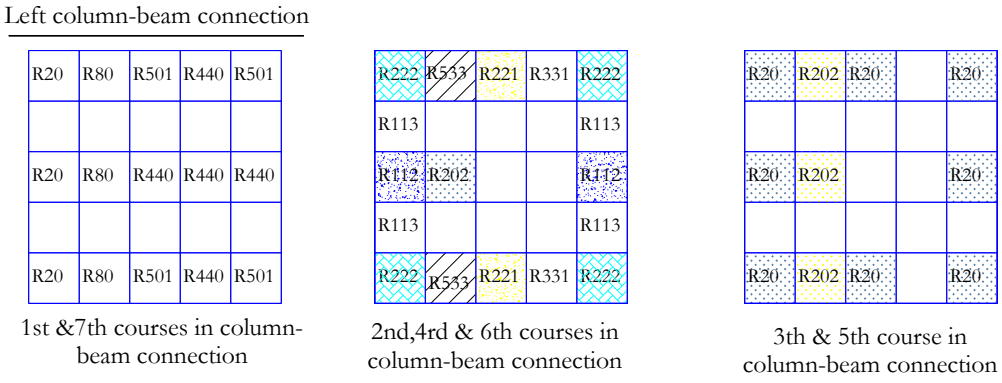

Figure B.9 Specimen M1 real constants for the left column-beam connection

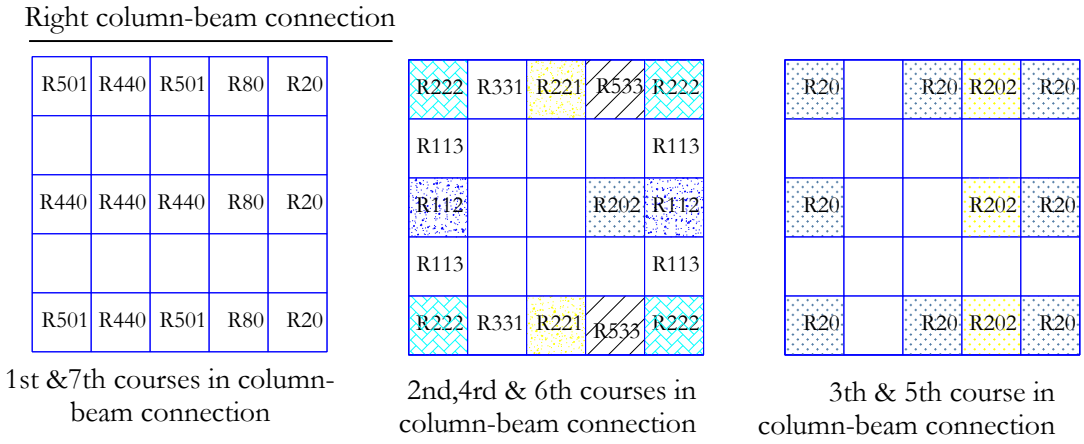

Figure B.10 Specimen M1 real constants for the right column-beam connection

B.3 Specimen B

Figure B.11 shows the RC frame configuration of specimen B. Columns were meshed with equal meshes with an in-plane size of 30*30 mm2 and a 34.8 mm height while the size of the elements in the beam was 40*25*35 mm3 for the core elements and 25*40*37.5 mm3 for the elements of the first and last course of the beam. The beam-column connections were meshed to be consistent with beam and column mesh sizes in order to accommodate the connection rebars. Table B.8 to Table B.10 show the real constants assigned to the columns, beam and beam-column connections, respectively, for the RC frame of specimen B. Also, the locations for these real constants in the column and beam sections, left

column-beam connection and right column-beam connection are illustrated in Figure B.12, Figure B.13 and Figure A.14, respectively, which are in correspondence with Table B.7, Table B.8 and Table B.9, respectively.

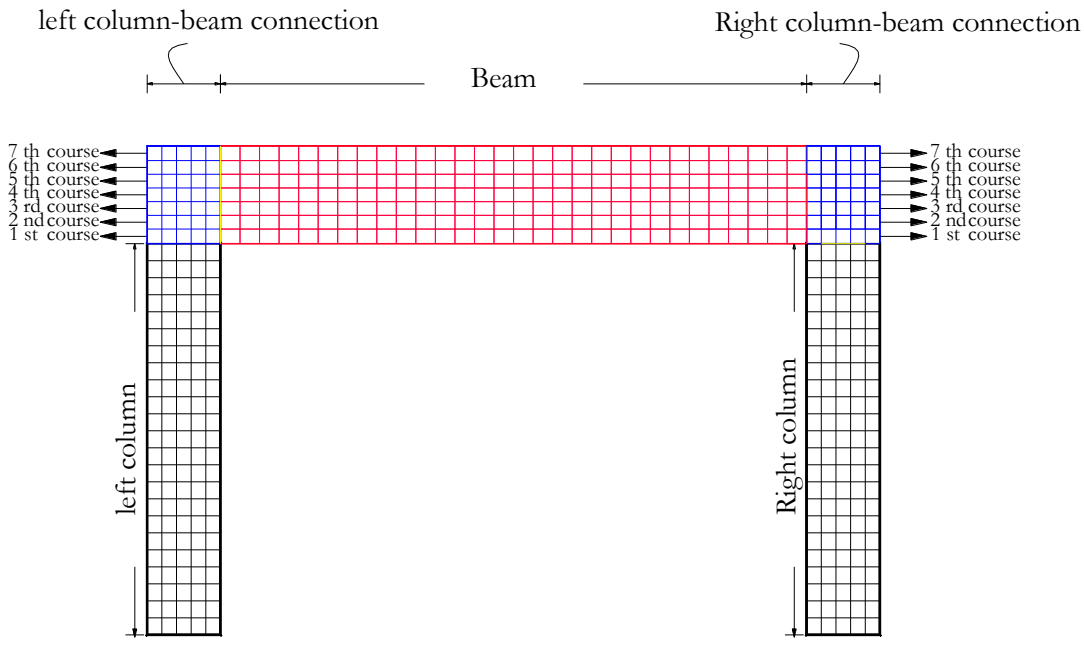

Figure B. 11 General description of the RC frame of specimen B, illustrating the different parts of the specimen's real constants and their notations.

Table B.8 Real constants for columns

Number	mat1	vr1	theta	phi	mat1	vr2	theta	phi	mat3	vr3	theta	phi
R22	11	0.008	0	0	1	0.033	90	0	11	0.007	0	90
R31	11	0.008	0	0			0	0	0	0	0	0
R21	11	0.008	0	0	1	0.033	90	0	0	0	0	0
R13	11	0.007	0	90			0	0	0	0	0	0
R12	11	0.007	0	90	1	0.041	0	0	0	0	0	0

Table B.9 Real constants for beam

Number	mat1	vr1	theta	phi	mat1	vr2	theta	phi	mat3	vr3	theta	phi
R42	1	0.041	0	0	11	0.009	90	0	11	0.006	0	90
R51	11	0.006	0	90	0	0	0	0	0	0	0	0
R402	1	0.041	0	0	11	0.006	0	90	0	0	0	0
R15	11	0.009	90	0	0	0	0	0	0	0	0	0
R105	1	0.044	0	0	11	0.009	90	0	0	0	0	0

Table B.10 Real constants for beam-column connections

Number	mat1	vr1	theta	phi	mat1	vr2	theta	phi	mat3	vr3	theta	phi
R440	1	0.041	0	0	0	0	0	0	0	0	0	0
R44	1	0.044	0	0			0	0	0	0	0	0
R400	1	0.041	0	0	11	0.008	0	90	0	0	0	0
R40	1	0.044	0	0	11	0.008	0	90	0	0	0	0
R112	1	0.041	0	0	1	0.041	90	0	11	0.008	0	90

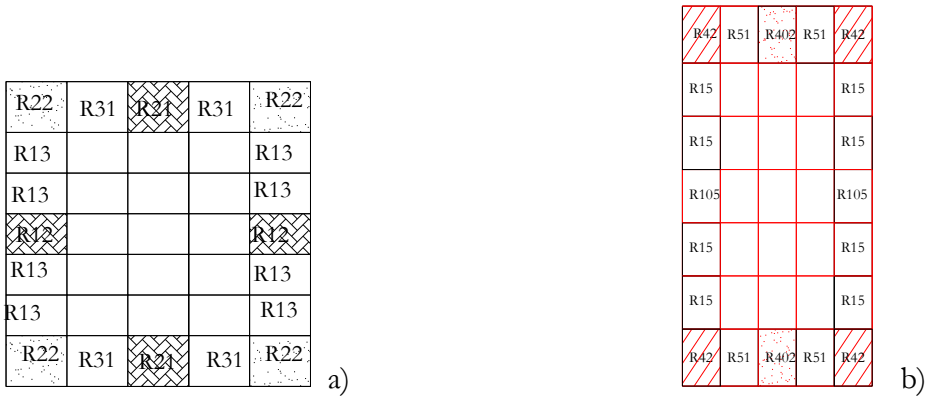

Figure B.12 Specimen B real constants: a) for the column; b) for the beam

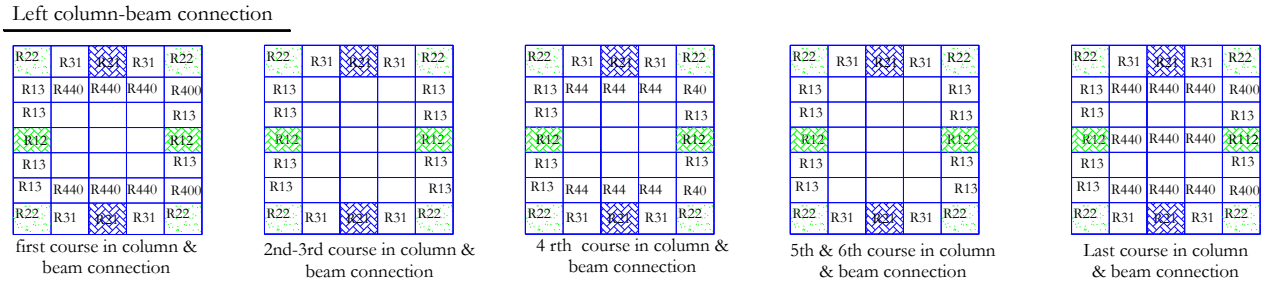

Figure B.13 Specimen B real constants for the left column-beam connection

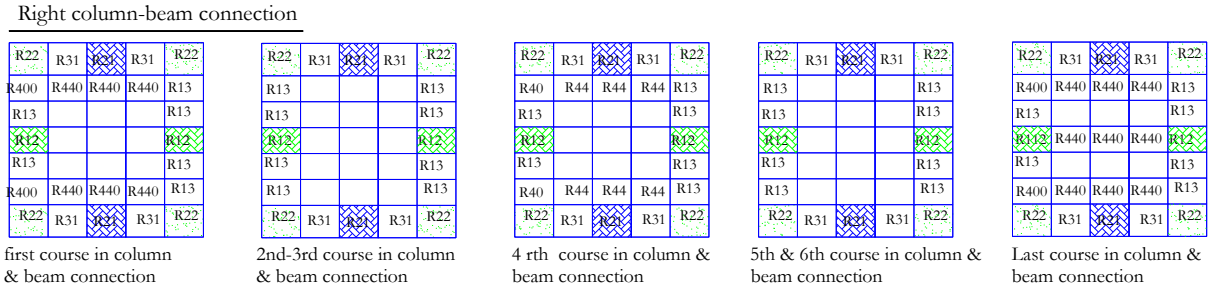

Figure B.14 Specimen B real constants for the right column-beam connection

C. The real constant and the key-options for the interface elements

The definition of contact elements in ANSYS involves a set of options (i.e. real constants and key-options). This annex presents the real constants and key-options which were used to define the interface elements. The real constants for the contact element (CONTA174) are presented in Table C.1. Table C.2 presents the key-options for the CONTA174 element. Each key-option has several options in order to enable the user to adapt the behaviour of the contact element for the structural problem under analysis. It is worth noting that the options highlighted in bold represent the options considered for the proposed model.

Table C.1 Real constants of the contact element (CONTA174)

No.	Name	Description
1	R1	Target radius for cylinder, cone, or sphere
2	R2	Target radius at second node of cone
3	FKN	Normal penalty stiffness factor
4	FTOLN	Penetration tolerance factor
5	ICONT	Initial contact closure
6	PINB	Pinball region
7	PMAX	Upper limit of initial allowable penetration
8	PMIN	Lower limit of initial allowable penetration
9	TAUMAX	Maximum friction stress
10	CNOF	Contact surface offset
11	FKOP	Contact opening stiffness
12	FKT	Tangent penalty stiffness factor
13	COHE	Contact cohesion

Table C.2 Key-options for the contact element (CONTA174).

Keyoption	Description	Available options
1	Selection of degree of freedom	***0 -- UX, UY, UZ*** 1 -- UX, UY, UZ, TEMP 2 -- TEMP 3 -- UX, UY, UZ, TEMP, VOLT 4 -- TEMP, VOLT 5 -- UX, UY, UZ, VOLT 6 -- VOLT 7 -- MAG
2	Contact algorithm:	***0 -- Augmented Lagrangian (default)*** 1 -- Penalty function 2 -- Multipoint constraint (MPC 3 -- Lagrange multiplier on contact normal and penalty on tangent 4 -- Pure Lagrange multiplier on contact normal and tangent
4	Location of contact detection point:	***0 -- On Gauss point (for general cases)*** 1 -- On nodal point - normal from contact surface 2 -- On nodal point - normal to target surface 3 -- On nodal point - normal from contact surface (projection-based method)
5	CNOF/ICONT Automated adjustment:	0 -- No automated adjustment 1 -- Close gap with auto CNOF 2 -- Reduce penetration with auto CNOF 3 -- Close gap/reduce penetration with auto CNOF ***4 -- Auto ICONT***
6	Contact stiffness variation	***0 -- Use default range for stiffness updating*** 1 -- Make a nominal refinement to the allowable stiffness range 2 -- Make an aggressive refinement to the allowable stiffness range
7	Element level time incrementation control / impact constraints:	***0 -- No control,*** 1 -- Automatic bisection of increment 2 -- Change in contact predictions made to maintain a reasonable time/load increment 3 -- Change in contact predictions made to achieve the minimum time/load increment whenever a change in contact status occurs 4 -- Use impact constraints for standard or rough contact (KEYOPT(12) = 0 or 1) in a transient dynamic analysis with automatic adjustment of time increment
8	Asymmetric contact selection:	***0 -- No action*** 2 -- ANSYSinternally selects which asymmetric contact pair is used at the solution stage (used only when symmetry contact is defined).
9	Effect of initial penetration or gap:	0 -- Include both initial geometrical penetration or gap and offset ***1 -- Exclude both initial geometrical penetration or gap and offset*** 2 -- Include both initial geometrical penetration or gap and offset, but with ramped effects 3 -- Include offset only (exclude initial geometrical penetration or gap) 4 -- Include offset only (exclude initial geometrical penetration or gap), but with ramped effects 5 -- Include offset only (exclude initial geometrical penetration or gap) regardless of the initial contact status (near-field or closed) 6 -- Include offset only (exclude initial geometrical penetration or gap), but with ramped effects regardless of the initial contact status (near-field or closed)
10	Contact stiffness update:	0 -- Each load step if FKN is redefined during load step (pair based). ***2 -- Each iteration based on current mean stress of underlying elements (pair based)***
11	Shell thickness effect:	***0 -- Exclude*** 1 -- Include
12	Behavior of contact surface:	0 – Standard 1 – Rough 2 -- No separation (sliding permitted) ***3 – Bonded*** 4 -- No separation (always) 5 -- Bonded (always) 6 -- Bonded (initial contact)

D. Generalized procedure for the calibration of the properties of simplified macro-models

Based on the results presented throughout Chapter 5, it is concluded that using a strut element with properties defined based on experimental data is able to reproduce the real behaviour of the physical masonry infilled specimens. In case experimental data is unavailable or unobtainable, using detailed finite element models was seen as an affordable and efficient alternative to simulate the experimental data. However, the refined finite element modelling approach that was presented in Chapter 4 still a large modelling effort to represent all the components of the specimen with real geometric and mechanical characteristics. Therefore, a revised modelling approach still involving refined finite element models is proposed herein. This approach follows the same strategy followed in Chapter 4 to model the bare frames and the infilled frames, but simplifies some of the modelling aspects namely to simulate a situation where very little data about the real material characteristics of the masonry is available.

The several simplifications considered in the revised modelling strategy proposed herein are presented throughout this section. It is noted that regarding the modelling of the interfaces between masonry units and between the masonry and the surrounding frame, no changes were made to the approach described in Chapter 4. Moreover, in case experimental data about the mechanical properties of the masonry panel components is unavailable, empirical expressions are recommended to estimate the necessary mechanical properties. Finally, the revised modelling strategy for bare frames and infilled frames is implemented in a framework that uses Matlab as a platform to estimate the parameters of the simplified strut model for any specimen. The framework only requires one input file that is handled by Matlab which then compiles the bare frame and masonry infilled frame models, runs ANSYS to analyse the models, and determines the parameters of the strut model. The results obtained from this proposed framework were compared to the experimental data in order to verify the reliability of the proposed procedure.

D.1 Revised model for the RC frame

The procedure described in Chapter 4 was followed introducing a modification in order to simplify the model of the bare frame model. The column cross sections were meshed with an odd

number of elements in the two in-plan directions with an equal mesh size while the vertical mesh size was defined in order to be compatible to the mesh size assigned to the beam in the vertical direction. The exterior elements were assigned with real constants with a steel ratio equal to the total steel area divided by the number elements. The material of the exterior elements was defined as unconfined concrete while the interior elements were defined with a confined concrete as shown in Figure D.1. The same procedure was followed for the beam section. The cross-section was meshed according to the column meshing size in the horizontal and vertical directions as shown in Figure D.2. The upper and lower reinforcements As1 and As2 are equally distributed along the top and bottom elements, respectively, and the middle reinforcement is lumped in the two exterior middle elements as shown in Figure D.2 also. Two different beam-column connections, shown in Figure D.3, are considered in this revised modelling procedure. For the beam-column connection in Figure D.3 a), where the beam width and the column width are equal, the real beam width is kept. For the beam-column connection in Figure D.3 In the case of the beam-column connection in Figure D.3 b), where the beam width is smaller than the column width, the beam width is modified to match the horizontal mesh size of the column. The horizontal reinforcement of the beam in the column that is part of the anchorage length is counted for both connections but the horizontal component of the column reinforcement anchorage length in the beam or the vertical component of the beam reinforcement anchorage length in the column are not considered in this simplified modelling approach.

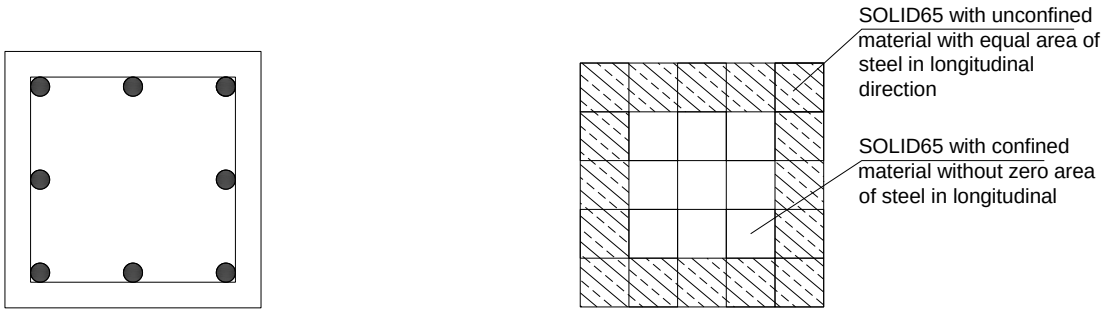

a) Column cross-section b) Cross-section mesh

Figure D.1 Description of the column cross-section considered in the proposed modelling approach

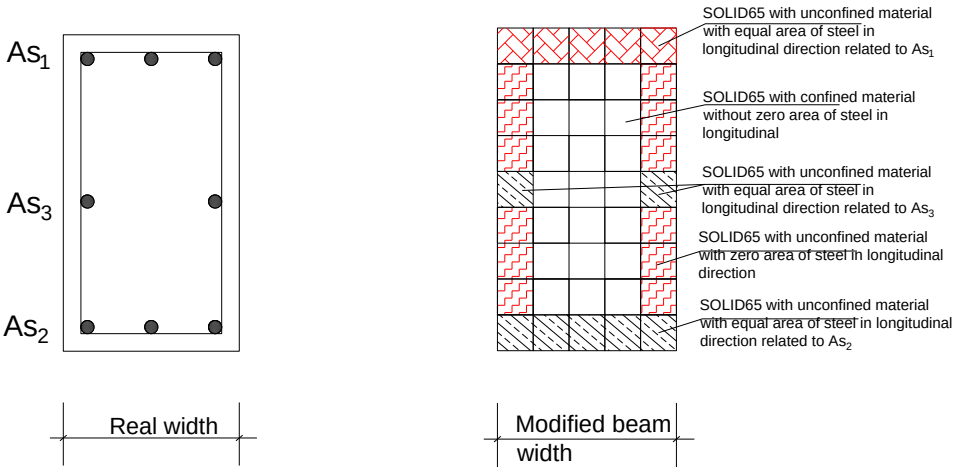

a) Beam cross-section b) Generalized beam cross section

Figure D.2 Description of the beam cross-section considered in the proposed modelling approach

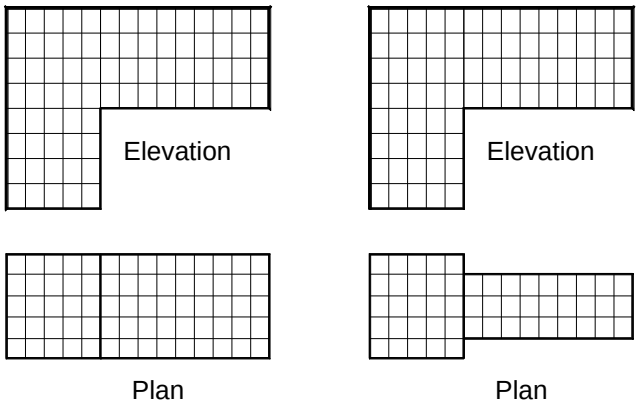

a) b)

Figure D.3 Description of the beam-column connections considered in the proposed modelling approach: a) when the beam width is equal to the column width; b) when the beam width is smaller than the column width

D.2 Generalized model for the infill panel

The modelling approach developed in Chapter 4 for the brick units, where the brick unit was modelled using it is real geometry, requires additional effort during the modelling process and also during the analysis. Therefore, the approximation shown in Figure D.4 is proposed instead for the case

of masonry units with perforations. The material of the new section of the masonry wall is assigned with the compressive strength of the masonry. Consequently, using an effective width, the shear strength and tensile strength of the mortar joints were modified according to the effective area. In order to define the mechanical properties of the infill panel components, empirical expressions found in the literature can be used to overcome the situation where experimental data on these properties are unavailable. However, the compressive strength of the brick unit and of the mortar are essential data. The compressive strength of the brick unit can be assessed using manufacturer information while the mortar strength can by assessed using expert judgment or other alternative approaches. For the determination of the compressive strength of the masonry, Eurocode 6 (EN6-1, 2005) (EC6) defines the following expression:

$$f_{k,m} = K f_{mo}^{\beta} f_{br}^{\alpha} \tag{D.1}$$

where f_{mo} and f_{br} are the mortar and brick compressive strength, respectively, and K, α and β are parameters defined by the national annexes of EC6. If no values are available in the annexes, EC6 refers that K ranges from 0.20 to 0.80, and that α and β can be set as 0.7 and 0.3, respectively. For the shear strength, the expression proposed by Crisafulli (1997) can be used;

$$\tau = k_1 \sqrt{f_{k,m}} \tag{D.2}$$

where k_1 is an empirical parameter that varies from 0.17 to 0.38.

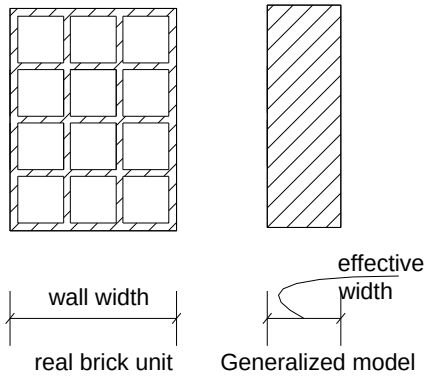

Figure D.4 Description of the brick unit which used in the proposed modelling approach

D.3 Framework to establish the infill capacity curve and preliminary applications

The proposed modelling procedures and the overall characterization of the infill capacity curve can be summarized in the flowchart shown in Figure D.5, which involves two series of analyses controlled using Matlab as the platform to create the models and call the finite element solver (Ansys). This procedure saves time in creating the model that now only requires the compressive strengths of the mortar, brick and concrete along with the steel yield strength to be defined. Three different experimental tests were used to evaluate the performance of this procedure. The results obtained for bare frames and fully infilled specimens of those tests are presented in Figure D.6 and Figure D.7, respectively. As can be seen, the results obtained from this procedure are not entirely satisfactory since their agreement with the experimental data is not as good as the one obtained using the modelling strategy proposed in Chapter 4. However, several aspects have room from improvement. As an example, the effect of using an equivalent cross-section for the masonry units changes the connection, and therefore the behaviour, these elements have with the surrounding contact elements. The current approach is not entirely equivalent to the modelling strategy proposed in Chapter 4 regarding this aspect and further research should be carried out to improve this feature in the simplified modelling approach.

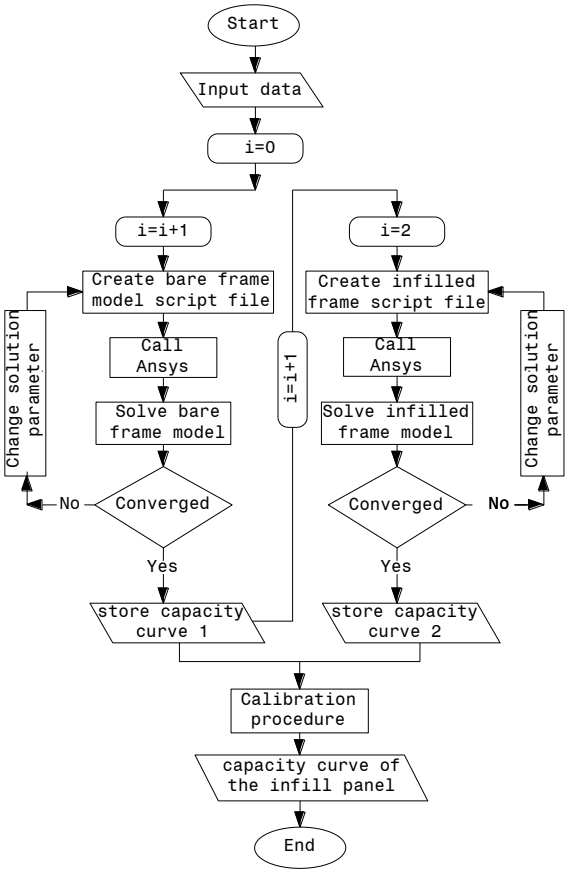

Figure D.5 Flowchart for the proposed procedure to establish the infill capacity curve based on refined finite element models

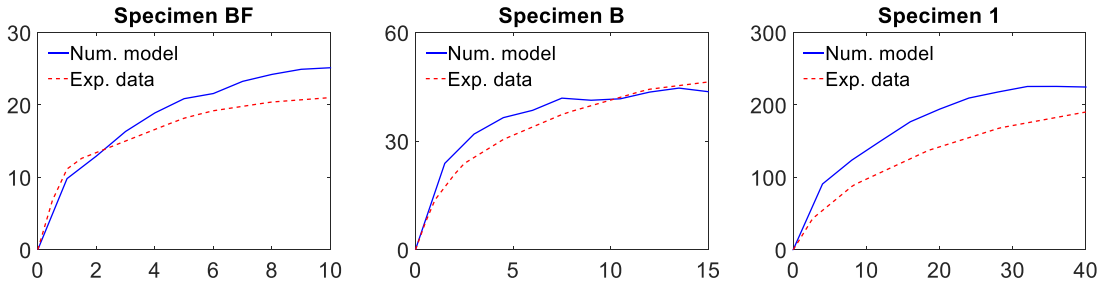

Figure D.6 Capacity curves obtained from modelling three different bare RC frames using the proposed simplified modelling approach

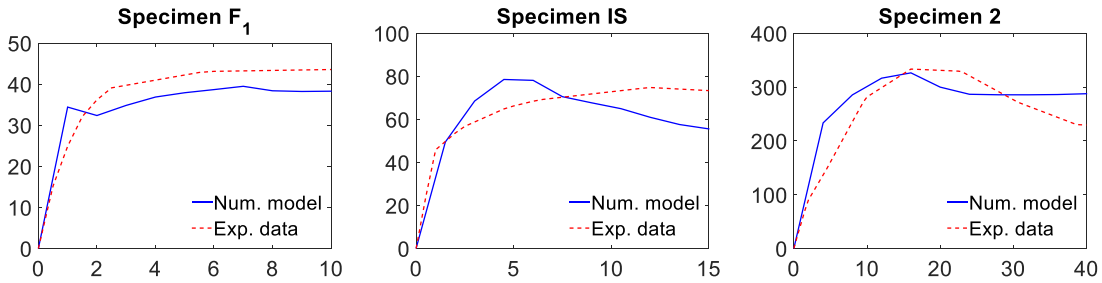

Figure D.7 Capacity curves obtained from modelling three different fully infilled frames using the proposed simplified modelling approach

References

ABAQUS, A. S. (2011). User's manual, Version 6.11. 1. Dassaults Systemes Inc.

ACI 318-14 (2014) Building Code Requirements for Standard Concrete (ACI 318-14) and Commentary (ACI 318R-14). American Concrete Institute, Farmington Hills, Michigan,USA.

ACI 530/530.1-08 (2011) Building code requirements and specification for masonry structures and related commentaries. . American Concrete Institute, Masonry Standards Joint Committee Farmington Hills, Michgan,USA.

Ahmed, H. and Romão, X. (2017) Finite element micro-modelling as a proxy for experimental tests on masonry-infilled RC frames. *16th. World Conference on Earthquake Engineering 16wcee*, Santiago, Chile

Al-Chaar, G. (2002) Evaluating strength and stiffness of unreinforced masonry infill structures. *Construction Engineering Research Laboratory, US Army Corps of Engineers*, Washington, USA.

Al-Chaar, G., Issa, M. and Sweeney, S. (2002) Behavior of masonry-infilled nonductile reinforced concrete frames. *Journal of Structural Engineering* **128**(8), 1055-1063.

Al-Chaar, G. L. and Mehrabi, A. (2008) Constitutive models for nonlinear finite element analysis of masonry prisms and infill walls. *Construction Engineering Research Laboratory, US Army Corps of Engineers* Washington, USA.

Alemdar, F. (2010) Plastic hinging behavior of reinforced concrete bridge columns. *PhD Thesis*,University of Kansas, Kansas.

Alfano, G. and Crisfield, M. (2001) Finite element interface models for the delamination analysis of laminated composites: mechanical and computational issues. *International Journal for Numerical Methods in Engineering* **50**(7), 1701-1736.

Andreaus, U., Cerone, M., D'Asdia, P. and Iannozzi, F. (1985) A finite element model for the analysis of masonry structures under cyclic actions. *Proceeding of the Seventh Internacional Brick and Masonry Conference,* Melbourne, Australia, 479-88.

Angel, R. (1994) Behavior of reinforced concrete frames with masonry infill walls. *PhD Thesis*,University of Illinois, Champaign, USA.

Anil, Ö. and Altin, S. (2007) An experimental study on reinforced concrete partially infilled frames. *Engineering Structures* **29**(3), 449-460.

ANSYS (2012) Theory reference for the mechanical APDL and mechanical applications Release 14.5. *Company, A. I.,*Release 14.5,Canonsburg, PA, USA.

Anthoine, A. (1992) In-plane behaviour of masonry: a literature review. *Commission of the European Communities, Joint Research Centre,Institute for Safety Technology* Ispra,Italy.

Araújo, M., Macedo, L., Marques, M. and Castro, J. M. (2016) Code-based record selection methods for seismic performance assessment of buildings. *Earthquake Engineering & Structural Dynamics* **45**(1), 129-148.

ASCE (2007) Seismic rehabilitation of existing buildings (ASCE/SEI 41-06). American Society of Civil Engineers,Reston, Virginia, USA.

ASCE (2013) Seismic Evaluation and Retrofit of Existing Buildings (ASCE/SEI 41-13). American Society of Civil Engineers,Reston, Virginia, USA.

Asteris, P. G., Antoniou, S. T., Sophianopoulos, D. S. and Chrysostomou, C. Z. (2011a) Mathematical Macromodeling of Infilled Frames: State of the Art. *Journal of Structural Engineering* **137**(12), 1508-1517.

Asteris, P. G., Cavaleri, L., Di Trapani, F. and Sarhosis, V. (2016) A macro-modelling approach for the analysis of infilled frame structures considering the effects of openings and vertical loads. *Structure and Infrastructure Engineering* **12**(5), 551-566.

Asteris, P. G., Chrysostomou, C. Z., Giannopoulos, I. P. and Smyrou, E. (2011b) Masonry infilled reinforced concrete frames with openings. *Proc. 3rd International Conference on Computational Methods in Structural Dynamics and Earthquake Engineering (Compdyn 2011),* 26-28.

Asteris, P. G., D.J., K., Chrysostomou, C. Z. and E.E., S. (2011c) Failure Modes of In-filled Frames *Electronic Journal of Structural Engineering* **11(1)**, 11-20.

Axley, J. W. and Bertero, V. V. (1979) Infill Panels: Their Influence on Seismic Response of Buildings. *Earthquake Engineering Research Center (EERC), University of California, Berkeley*, report no. EERC 79-28, California, USA.

Basha, S. H. and Kaushik, H. B. (2016) Behavior and failure mechanisms of masonry-infilled RC frames (in low-rise buildings) subject to lateral loading. *Engineering Structures* **111**, 233-245.

Bazan, E. and Meli, R. (1980) Seismic analysis of structures with masonry walls. *Proceeding of the Seventh World Conference on Earthquake Engineering,* Istanbul, Turkey, 633-640.

Benjamin, J. R. and Williams, H. A. (1958) The behavior of one-story brick shear walls. *Journal of Structural Division, Asce, Proceedings*.

Bennett, R. M., Fischer, W., Flanagan, R. and Tenbus, M. (1996) Evaluation and analysis of the performance of masonry infills during the Northridge earthquake. *Oak Ridge National Laboratory*, Tennessee, USA.

Bergami, A. V. (2007) Implementation and experimental verification of models for nonlinear analysis of masonry infilled RC frames. *PhD Thesis*,Università degli studi ROMA TRE.

Bergami, A. V. and Nuti, C. (2015) Experimental tests and global modeling of masonry infilled frames. *Earthquakes and Structures* **9**(2), 281-303.

Bertoldi, S., Decanini, L. and Gavarini, C. (1993) Telai tamponati soggetti ad azioni sismiche, un modello semplificato, confronto sperimentale e numerico. *Atti Del 6 Conv. Naz. Ing. Sism. It* **2**, 815-824.

Beyhan, B. and Polat, G. (2011) Buildings Subjected to Recurring Earthquakes: A Tale of Three Cities. *Earthquake Spectra* **27**(3), 635-659.

Blackard, B., Willam, K. and Mettupalayam, S. (2009) Experimental observations of masonry infilled RC frames with openings. *ACI Structural Journal* **265**, 199–222.

Bolis, V., Stavridis, A. and Preti, M. (2016) Numerical Investigation of the In-Plane Performance of Masonry-Infilled RC Frames with Sliding Subpanels. *Journal of Structural Engineering* (04016168).

Buch, S. H. and Bhat, D. M. (2015) Book section title "*Comparative Modelling of Infilled Frames: A Descriptive Review and Analysis*" book title" Advances in Structural Engineering: Materials" Matsagar, V. Springer, New Delhi, India.

Buonopane, S. and White, R. (1999) Pseudodynamic testing of masonry infilled reinforced concrete frame. *Journal of Structural Engineering* **125**(6), 578-589.

Burton, H. and Deierlein, G. (2014) Simulation of Seismic Collapse in Nonductile Reinforced Concrete Frame Buildings with Masonry Infills. *Journal of Structural Engineering* **140**(8), A4014016.

Calvi, G. M. and Santini, S. (1996) Experimental and numerical investigations on the seismic response of RC infilled frames and recommendations for code provisions. *Laboratório Nacional de Engenharia Civil (LNEC)*, Lisbon, Portugal

Catherin, J. M., Jayalekshmi, B. R. and Katta, V. (2013) Modeling of Masonry infills-A review. *American Journal of Engineering Research (AJER)* **2**, 59-63.

CCMPA (2009) Seismic design guide for masonry buildings. Canadian Concrete Masonry Producers Association CCMPA,Toronto,Ontario, Canada.

CEB (1996) RC frames under earthquake loading: state of the art. *Comité Euro-International du Béton (CEB)*, Telford, T., London, England, UK.

Celarec, D., Ricci, P. and Dolšek, M. (2012) The sensitivity of seismic response parameters to the uncertain modelling variables of masonry-infilled reinforced concrete frames. *Engineering Structures* **35**, 165-177.

Chansawat, K., Kachlakev, D., Miller, T. and Yim, S. (2001) FE Modeling and Experimental Verification of an FRP Strengthened Bridge. *Sem Annual Conference on Experimental and Applied Mechanics,* Portland, Oregon, USA, 624-627.

Chen, X. and Liu, Y. (2016) A finite element study of the effect of vertical loading on the in-plane behavior of concrete masonry infills bounded by steel frames. *Engineering Structures* **117**, 118-129.

Chethan, K., Babu, R., Venkataramana, K. and Sharma, A. (2009) Study on Dynamic Characteristics of 3D Reinforced Concrete Frame with Masonry Infill. *Journal of CPRI* **5**(2), 11-18.

Chiou, B., Darragh, R., Gregor, N. and Silva, W. (2008) NGA Project Strong-Motion Database. *Earthquake Spectra* **24**(1), 23-44.

Chrysostomou, C. Z. (1991) Effects of degrading infill walls on the nonlinear seismic response of two-dimensional steel frames. *PhD Thesis*,Cornell University, New York, USA.

Chrysostomou, C. Z., Gergely, P. and Abel, J. F. (1992) Non-linear seismic response of infilled steel frames. *Proceedings Tenth World Conference on Earthquake Enginerring, Madrid, Spain*, 4435-4437.

Crisafulli, F. (1997) Seismic behaviour of reinforced concrete structures with masonry infills. *PhD Thesis*,University of Canterbury, Christchurch, New Zealand.

Crisafulli, F. and Carr, A. (2007) Proposed macro-model for the analysis of infilled frame structures. *Bulletin of the New Zealand Society for Earthquake Engineering* **40**(2), 69-77.

Crisafulli, F., Carr, A. and Park, R. (2000) Analytical modelling of infilled frame structures-a general review. *Bulletin-New Zealand Society for Earthquake Engineering* **33**(1), 30-47.

D'Agostino, R. and Stephens, M. (1986) Goodness-of-Fit Techniques Marcel Dekker New York. Marcel Dekker, Inc.,New York, USA.

Dawe, J. and Seah, C. (1988) Lateral load resistance of masonry panels in flexible steel frames. *Brick and Block Masonry(8 Th Ibmac) London, Elsevier Applied Science* **2**, 606-616.

Dean, R. A. and Yanev, P. (2008) Peace of mind in earthquake country. JSTOR.

Decanini, L. D. and Fantin, G. E. (1987) Modelos simplificados de la mampostería incluida en porticos. Características de rigidez y resistencia lateral en astado límite. *Jornadas Argentinas De Ingeniería Estructural Iii Asociacion De Ingenieros Estructurales* **2**, 817-836.

Decanini, L. D., Liberatore, L. and Mollaioli, F. (2014) Strength and stiffness reduction factors for infilled frames with openings. *Earthquake Engineering and Engineering Vibration* **13**(3), 437-454.

Dhanasekhar, M. and Page, A. (1986) The influence of brick masonry infill properties on the behaviour of i nfilled frames. *ICE Proceedings* **81**(4), 593-605.

DIANA (2011) Finite Element Analysis: User's Manual. *Research, T. B. a. C.,* Finite Element Analysis, Delft, Netherlands, https://support.tnodiana.com/manuals/d96/Diana.html.

Dolšek, M. and Fajfar, P. (2008) The effect of masonry infills on the seismic response of a four-storey reinforced concrete frame — a deterministic assessment. *Engineering Structures* **30**(7), 1991-2001.

Doudoumis, I. N. and Mitsopoulou, E. N. (1986) Non-linear analysis of multistorey infilled frames for unilateral contact conditions. *Proceedings of 8th European Conference on Earthquake Engineering, European Association for Earthquake Engineering (Eaee), Istanbul, Turkey*, 63 –70.

Durrani, A. J. and Luo, Y. H. (1994) Seismic retrofit of flat-slab buildings with masonry infills. *Proceedings Nceer Workshop on Seismic Response of Masonry Infills*.

EC8-1 (2010) NP ENV Portuguese National Annex to Eurocode 8: Design of structures for earthquake resistance—part 1: General rules, seismic actions and rules for buildings. Instituto Português da Qualidade.

El-Dakhakhni, W. W., Elgaaly, M. and Hamid, A. A. (2003) Three-Strut Model for Concrete Masonry-Infilled Steel Frames. *Journal of Structural Engineering* **129**(2), 69-77.

EN6-1 (2005) Eurocode 6: Design of Masonry Structures - Part 1: General Rules for Reinforced and Unreinf. Masonry Structures. European Committee for Standardization Brussels, Belgium

Faison, H., Comartin, C. and Elwood, K. (2004) Reinforced concrete moment frame building without seismic details.

FEMA-273 (1997) NEHRP Guidelines for the seismic rehabilitation of buildings. Washigton D.C., Maryland, USA.

FEMA-356 (2000) Prestandard and commentary for seismic rehabilitation of buildings. Federal Emergency Management Agency Washigton D.C., Maryland, USA.

Fenves, G. and Scott, M. (2006) Plastic Hinge Integration Methods for Force-Based Beam–Column Elements. *Journal of Structural Engineering* **32**(2), 244-252.

Fiorato, A. E., Sozen, M. A. and Gamble, W. L. (1970) An Investigation of the Interaction of Reinforced Concrete Frames with Masonry Filler Walls. *Department of civil engineering, Illinois university Urbana*, Illinois, USA.

Flanagan, R. D. and Bennett, R. M. (1999) Arching of masonry infilled frames: Comparison of analytical methods. *Practice Periodical on Structural Design and Construction* **4**(3), 105-110.

Furtado, A., Rodrigues, H., Arêde, A. and Varum, H. (2016) Simplified macro-model for infill masonry walls considering the out-of-plane behaviour. *Earthquake Engineering & Structural Dynamics* **45**(4), 507-524.

Ghobarah, A. (2004) On drift limits with different damage levels. *Proceedings of International Workshop on Performance-Based Seismic Design Concepts and Implementation, June 28th–July 1st*.

Hamburger, R. O., Chakradeo, A. S. and Consortium, U. C. U. S. E. (1993) Book section title "*Methodology for seismic capacity evaluation of steel-frame buildings with infill unreinforced masonry*" book title" Mitigation and Damage to the Built Environment" US Central United States Earthquake Consortium (CUSEC).

Haselton, C. B. (2008) Beam-column element model calibrated for predicting flexural response leading to global collapse of RC frame buildings. *Pacific Earthquake Engineering Research Center*.

Hashemi, A. and Mosalam, K. M. (2006) Shake-table experiment on reinforced concrete structure containing masonry infill wall. *Earthquake Engineering & Structural Dynamics* **35**(14), 1827-1852.

Hendry, A. (1990) Structural masonry. Scholium International, Macmillan Education Ltd,London, UK.

Holmes, M. (1961) Steel frames with brickwork and concrete infilling. *ICE Proceedings* **19**(4), 473-478.

Hu, J., Chen, B., Smith, D., Flewitt, P. and Cocks, A. (2016) On the evaluation of the Bauschinger effect in an austenitic stainless steel—The role of multi-scale residual stresses. *International Journal of Plasticity* **84**, 203-223.

Ibarra, L., Medina, R. and Krawinkler, H. (2002) Collapse assessment of deteriorating SDOF systems. *Proceedings of the 12th European Conference on Earthquake Engineering,* London, England, UK., 9-13.

Imai, H. and Miyamoto, M. (1989) Seismic Behavior of Reinforced Masonry Walls with Small Opening. *Proceedings of 5 Jornadas Chilenas De Sismología E Ingeniería Antisísmica* **2**, 965-973.

Induprabha, S. and Dilrukshi, K. (2011) Contribution to numerical modelling of concrete-masonry interface In concrete framed structures with masonry infill. *In: International Conference on Structural Engineering Construction and Management*, Kandy, Central, Sri Lanka

Kakaletsis, D. and Karayannis, C. (2008) Influence of Masonry Strength and Openings on Infilled R/C Frames Under Cycling Loading. *Journal of Earthquake Engineering* **12**(2), 197-221.

Kakaletsis, D. and Karayannis, C. (2009) Experimental investigation of infilled reinforced concrete frames with openings. *ACI Structural Journal* **106**(2), 132-141.

Kakaletsis, D. J. (2009) Masonry infills with window openings and influence on reinforced concrete frame constructions. *Earthquake Resistant Engineering Structures Vii* **104**, 445-455.

Kent, D. C. and Park, R. (1971) Flexural members with confined concrete. *Journal of the Structural Division* **97**(7), 1969-1990.

Khaja, M., Chethan, K. and Ramesh, B. (2013) Earthquake analysis on 2d RC frames with different aspect ratios of masonry infill and monolithic panel. *International Journal of Research in Engineering and Technology*, 18-23.

Klingner, R. E. and Bertero, V. V. (1978) Earthquake resistance of infilled frames. *Journal of the Structural Division* **104**(6), 973-989.

Koutromanos, I., Stavridis, A., Shing, P. B. and Willam, K. (2011) Numerical modeling of masonry-infilled RC frames subjected to seismic loads. *Computers & Structures* **89**(11), 1026-1037.

Kwan, A., Dai, H. and Cheung, Y. (1999) Non-linear seismic response of reinforced concrete slit shear walls. *Journal of Sound and Vibration* **226**(4), 701-718.

Lee, H. S. and Woo, S. W. (2002) Effect of masonry infills on seismic performance of a 3-storey R/C frame with non-seismic detailing. *Earthquake Engineering & Structural Dynamics* **31**(2), 353-378.

Leuchars, J. M. and Scrivener, J. C. (1976) Masonry infill panels subjected to cyclic in-plane loading. *Bulletin of the New Zealand National Society for Earthquake Engineering* **9 n 2** 122-131.

Li, B., Wang, Z., Mosalam, K. M. and Xie, H. (2008) Wenchuan Earthquake Field Reconnaissance on Reinforced Concrete Framed Buildings With and Without Masonry Infill Walls. *The 14th World Conference on Earthquake Engineering October 12-17, 2008, Beijing, China*.

Lotfi, H. and Shing, P. (1991) An appraisal of smeared crack models for masonry shear wall analysis. *Computers & Structures* **41**(3), 413-425.

Lotfi, H. R. and Shing, P. B. (1994) Interface model applied to fracture of masonry structures. *Journal of Structural Engineering* **120**(1), 63-80.

Lourenço, P. and Rots, J. (1997) Multisurface Interface Model for Analysis of Masonry Structures. *Journal of Engineering Mechanics* **123**(7), 660-668.

Lourenço, P. B., Barros, J. O. and Oliveira, J. T. (2004) Shear testing of stack bonded masonry. *Construction and Building Materials* **18**(2), 125-132.

Macedo, L., Araújo, M. and Castro, J. (2013) Assessment and calibration of the harmony search algorithm for earthquake record selection. *Proceedings of the Vienna Congress on Recent Advances in Earthquake Engineering and Structural Dynamics*.

Madan, A., Reinhorn, A., Mander, J. and Valles, R. (1997) Modeling of masonry infill panels for structural analysis. *Journal of Structural Engineering* **123**(10), 1295-1302.

Mainstone, R. J. (1971) On The stiffness and strengths of infilled frames. *ICE Proceedings* **49**(2), 230.

Mainstone, R. J. (1974) Supplementary note on the stiffness and strengths of infilled frames. *Building Research Station,* .

Mainstone, R. J., Weeks, G. A. and Building Research, S. (1972) The influence of a bounding frame on the racking stiffness and strengths of brick walls. Building Research Station,Garston, Eng.

Mallick, D. and Severn, R. (1967) The behaviour of infilled frames under static loading. *ICE Proceedings* **38**(4), 639-656.

Mansouri, A., Marefat, M. S. and Khanmohammadi, M. (2014) Experimental evaluation of seismic performance of low-shear strength masonry infills with openings in reinforced concrete frames with deficient seismic details. *The Structural Design of Tall and Special Buildings* **23**(15), 1190-1210.

McKenna, F., Fenves, G. and Scott, M. (2000) Open system for earthquake engineering simulation. *University of California, Berkeley, Ca*.

Mehrabi, A. and Shing, P. (1997) Finite Element Modeling of Masonry-Infilled RC Frames. *Journal of Structural Engineering* **123**(5), 604-613.

Mehrabi, A. B. (1994) Behavior of masonry-infilled reinforced concrete frames subjected to lateral loadings. *PhD Thesis*,University of Colorado,Colorado,USA.

Mehrabi, A. B. and Shing, P. B. (1996) Experimental evaluation of masonry infilled RC. frames. *Journal of Structural Engineering* **122**, 228-237.

Menegotto, M. and Pinto, P. (1973) Method of Analysis for Cyclically Loaded RC Frames Including Changes in Geometry and Non-elastic Behaviour of Elements Under Combined Normal Force and Bending. *Proc., Iabse Symp. Of Resistance and Ultimate Deformability of Structures Acted on by Welldefined Repeated Loads,* Libson, Portugal, 15-22.

Mises, R. v. (1913) Mechanics of solid bodies in the plastically-deformable state. *Nachrichten Von Der Gesellschaft Der Wissenschaften Zu Gottingen. Mathematisch-Physikalische Klasse* **1**, 582-592.

Misir, I. S. (2015) Potential Use of Locked Brick Infill Walls to Decrease Soft-Story Formation in Frame Buildings. *Journal of Performance of Constructed Facilities* **29**(5), 04014133.

Misir, S., Ozcelik, O., Girgin, S. C. and Kahraman, S. (2012) Experimental work on seismic behavior of various types of masonry infilled RC frames. *Structural Engineering and Mechanics* **44**(6), 763-774.

Moghaddam, H. and Dowling, P. (1988) Earthquake resistant design of brick infilled frame. *Proceedings of the Eighth International Brick and Block Masonry Conference*, 774-784.

Mohammadi, M. and Nikfar, F. (2012) Strength and stiffness of masonry-infilled frames with central openings based on experimental results. *Journal of Structural Engineering* **139**(6), 974-984.

Mohyeddin, A., Goldsworthy, H., Gad, E. F. and (2013a) FE modelling of RC frames with masonry infill panels under in-plane and out-of-plane loading. *Engineering Structures* **51**(1), 73-87.

Mohyeddin, A., Goldsworthy, H. M. and Gad, E. F. (2013b) Sensitivity Analysis of Nonlinear Behaviour of Infill-Frames Under In-Plane and Out-of-Plane Loading. *Advances in Structural Engineering* **16**(10), 1729-1748.

Mondal, G. and Jain, S. K. (2008) Lateral stiffness of masonry infilled reinforced concrete (RC) frames with central opening. *Earthquake Spectra* **24**(3), 701-723.

Mortezaei, A. and Ronagh, H. R. (2012) Plastic hinge length of FRP strengthened reinforced concrete columns subjected to both far-fault and near-fault ground motions. *Scientia Iranica* **19**(6), 1365-1378.

Mosalam, K. M., White, R. N. and Ayala, G. (1998) Response of infilled frames using pseudo-dynamic experimentation. *Earthquake Engineering & Structural Dynamics* **27**(6), 589-608.

NOAA, N. O. a. A. A. (2003). Damage to an apartment building with a soft first story in Bordj-El-Kiffan city, Algeria.

NZS 4230 (2004) The New Zealand masonry Code: Design of Reinforced Concrete Masonry Structures Authority, Building Industry New Zealand.

NZSEE (2006) New Zealand Society for Earthquake Engineering (Assessment and Improvement of the Structural Performance of Buildings in Earthquakes, Study Group on Earthquake Risk Buildings).

NZSEE (2016) The Seismic Assessment of Existing Buildings. Technical Guidelines for Engineering Assessments, Revised Draft section C7: Moment Resisting Frames with Infill Panels.

Ohsumi, T., Mukai, Y. and Fujitani, H. (2016) Investigation of Damage in and Around Kathmandu Valley Related to the 2015 Gorkha, Nepal Earthquake and Beyond. *Geotechnical and Geological Engineering* **34**(4), 1223-1245.

Oliveira, D. V. and Lourenço, P. B. (2004) Implementation and validation of a constitutive model for the cyclic behaviour of interface elements. *Computers & Structures* **82**(17–19), 1451-1461.

Panagiotakos, T. and Fardis, M. (1994) Proposed nonlinear strut models for infill panels. *Note for the Prec8 Network*.

Panagiotakos, T. and Fardis, M. (1996) Seismic response of infilled RC frames structures. *11th World Conference on Earthquake Engineering, Acapulco*.

Paulay, T. and Priestley, M. J. N. (1992) Seismic design of reinforced concrete and masonry buildings. John Wiley & Sons, Inc.,Toronto, Ontario, Canada.

Petry, S. and Beyer, K. (2014) Scaling unreinforced masonry for reduced-scale seismic testing. *Bulletin of Earthquake Engineering* **12**(6), 2557-2581.

Pinto, A. V. and Taucer, F. (2006) Book section title "*Assessment and retrofit of full-scale models of existing RC frames*" book title" Advances in Earthquake Engineering for Urban Risk Reduction" Springer, Netherlands.

Pires, F. M. G. (1990) Influence of masonry walls over the behavior of reinforced concrete frames under horizontal actions. . *PhD Thesis (in Portuguese)*, *Laboratório Nacional de Engenharia Civil (LNEC)*, Lisbon, Portugal

Polyakov, S. V. (1956) Masonry in Framed Buildings : An Investigation into the Strength and Stiffness of Masonry Infilling. "Gosudarstvennoe izdatel'stvo Literatury po stroitel'stvu i arkhitekture", Moscow Russia. *(English translation by G. L. Cairns, National Lending Library for Science and Technology, Boston, Yorkshire, England, 1963).*

Pradhan, P. M., Pradhan, P. L. and Maskey, R. K. (2012) A review on partial infilled frames under lateral loads. *Kathmandu University Journal of Science, Engineering and Technology* **8**(1), 142-152.

Reflak, J. and Fajfar, P. (1991) Elastic analysis of infilled frames using substructures. *Proceeding of the Sixth Canadian Conference on Earthquake Engineering,* Ontario, Canada, 285-292.

Ricci, P., De Risi, M. T., Verderame, G. M. and Manfredi, G. (2013) Influence of infill distribution and design typology on seismic performance of low- and mid-rise RC buildings. *Bulletin of Earthquake Engineering* **11**(5), 1585-1616.

Ricci, P., De Risi, M. T., Verderame, G. M. and Manfredi, G. (2016) Procedures for calibration of linear models for damage limitation in design of masonry-infilled RC frames. *Earthquake Engineering & Structural Dynamics*.

Rodrigues, H., Varum, H. and Costa, A. (2010) Simplified Macro-Model for Infill Masonry Panels. *Journal of Earthquake Engineering* **14**(3), 390-416.

Romão, X., Costa, A. A., Paupério, E., Rodrigues, H., Vicente, R., Varum, H. and Costa, A. (2013) Field observations and interpretation of the structural performance of constructions after the 11 May 2011 Lorca earthquake. *Engineering Failure Analysis* **34**, 670-692.

Rossetto, T. and Elnashai, A. (2003) Derivation of vulnerability functions for European-type RC structures based on observational data. *Engineering Structures* **25**(10), 1241-1263.

Rossetto, T. and Elnashai, A. (2005) A new analytical procedure for the derivation of displacement-based vulnerability curves for populations of RC structures. *Engineering Structures* **27**(3), 397-409.

Sachanski, S. (1960) analysis of the earthquake resistance of frame buildings taking into consideration the carrying capacity of the filling maosnry. *Proc. 2nd World Conference on Earthquake Engineering & Structural Dynamics*, 2127-2141.

Saneinejad, A. and Hobbs, B. (1995) Inelastic design of infilled frames. *Journal of Structural Engineering* **121**(4), 634-650.

Sattar, S. (2013) Influence of masonry infill walls and other building characteristics on seismic collapse of concrete frame buildings. *PhD Thesis*,University of Colorado Boulder, Colorado,USA

Sattar, S. and Liel, A. B. (2010) Seismic performance of reinforced concrete frame structures with and without masonry infill walls. *9th Us National and 10th Canadian Conference on Earthquake Engineering*.

Sattar, S. and Liel, A. B. (2016a) Seismic Performance of Nonductile Reinforced Concrete Frames with Masonry Infill Walls: I. Development of a Strut Model Enhanced by Finite Element Models. *Earthquake Spectra* **32**(2), 795-818.

Sattar, S. and Liel, A. B. (2016b) Seismic Performance of Nonductile Reinforced Concrete Frames with Masonry Infill Walls: II. Collapse Assessment. *Earthquake Spectra* **32**(2), 819-842.

Schierle, G. (2003) Northridge earthquake field investigations: Statistical analysis of woodframe damage. Consortium of Universities for Research in Earthquake Engineering.

Schmid, B., Kariotis, J. and Schwartz, E. (1973) Tentative Los Angeles ordinance and testing program for unreinforced masonry buildings. *Department of Building and Safety, City of Los Angeles*, Los Angeles,California, USA.

Scott, B., Park, R. and Priestley, M. (1982) Stress-strain behavior of concrete confined by overlapping hoops at low and high strain rates. *ACI Structural Journal* **79**(1), 13-27.

Scott, M. H. and Ryan, K. L. (2013) Moment-Rotation Behavior of Force-Based Plastic Hinge Elements. *Earthquake Spectra* **29**(2), 597-607.

Shakya, M. and Kawan, C. K. (2016) Reconnaissance based damage survey of buildings in Kathmandu valley: An aftermath of 7.8 Mw, 25 April 2015 Gorkha (Nepal) earthquake. *Engineering Failure Analysis* **59**, 161-184.

Shan, S., Li, S., Xu, S. and Xie, L. (2016) Experimental study on the progressive collapse performance of RC frames with infill walls. *Engineering Structures* **111**, 80-92.

Shing, P. B. and Mehrabi, A. B. (2002) Behaviour and analysis of masonry-infilled frames. *Progress in Structural Engineering and Materials* **4**(3), 320-331.

Shinozuka, M., Feng, M., Lee, J. and Naganuma, T. (2000) Statistical analysis of fragility curves. *Journal of Engineering Mechanics* **126**(12), 1224-1231.

Sigmund, V. and Penava, D. (2013) Assessment of masonry infilled reinforced-concrete frames with openings. *Tehnicki Vjesnik/Technical Gazette* **20**(3), 459-466.

Smith, B. S. and Carter, C. (1969) A method of analysis for infilled frames. *ICE Proceedings* **44**(1), 31-48.

Smyrou, E., Blandon, C., Antoniou, S., Pinho, R. and Crisafulli, F. (2011) Implementation and verification of a masonry panel model for nonlinear dynamic analysis of infilled RC frames. *Bulletin of Earthquake Engineering* **9**(5), 1519-1534.

Soroushian, P., Obaseki, K. and Choi, K. (1988) Nonlinear Modeling and Seismic Analysis of Masonry Shear Walls. *Journal of Structural Engineering* **114**(5), 1106-1119.

Stafford-Smith, B. (1962) Lateral stiffness of infilled frames. *Journal of Structural Division* **88**(6), 183 – 199.

Stavridis, A. (2009) Analytical and experimental study of seismic performance of reinforced concrete frames infilled with masonry walls. *PhD Thesis*,University of California San Diego.

Stavridis, A., Koutromanos, I. and Shing, P. B. (2012) Shake-table tests of a three-story reinforced concrete frame with masonry infill walls. *Earthquake Engineering & Structural Dynamics* **41**(6), 1089-1108.

Stavridis, A. and Shing, P. (2010) Finite-element modeling of nonlinear behavior of masonry-infilled RC frames. *Journal of Structural Engineering* **136**(3), 285-296.

Stylianidis, K. (2012) Experimental investigation of masonry infilled RC frames. *Open Constr Build Technol J* **6**(1), 194-212.

Surendran, S. and Kaushik, H. B. (2012) Masonry Infill RC Frames with Openings: Review of In-plane Lateral Load Behaviour and Modeling Approaches. *Open Construction and Building Technology Journal* **6**(Special issue 1), 126-154.

Süsoy, M. (2004) Seismic strengthening of masonry infilled reinforced concrete frames with precast concrete panels. *M.Sc. Thesis*,Middle east technical university

Syrmakezis, C. A. and Vratsanou, V. Y. (1986) Influence of infill walls to RC frames Response. *Proc., 8th European Conf. On Earthquake Engineering, European Association for Earthquake Engineering (Eaee). Istanbul, Turkey*, 47-53.

Tasnimi, A. and Mohebkhah, A. (2011) Investigation on the behavior of brick-infilled steel frames with openings, experimental and analytical approaches. *Engineering Structures* **33**(3), 968-980.

Tassios, T. P. (1984) Masonry infill and RC walls (an invited state of the art report). *Third international Symposium: On Wall Structures, Centre for Buildingsystems, Research and Development*.

Taucer, F., Spacone, E. and Filippou, F. C. (1991) A fiber beam-column element for seismic response analysis of reinforced concrete structures. Earthquake Engineering Research Center, College of Engineering, University of California,California, USA.

Te-Chang, L. and Kwok-Hung, K. (1984) Nonlinear behaviour of non-integral infilled frames. *Computers & Structures* **18**(3), 551-560.

TEC (2007) Turkish Code for Buildings in Seismic Zones Turkish Seismic Code, The Ministry of Public Works and Settlement, Ankara, Turkey Cengelkoy, Istanbul, Turkey.

Thiruvengadam, V. (1985) On the natural frequencies of infilled frames. *Earthquake Engineering & Structural Dynamics* **13**(3), 401-419.

Tucker, C. J. (2007) Predicting the in-plane capacity of masonry infilled frames. *PhD thesis*,University of Tennessee.

Turgay, T., Durmus, M. C., Binici, B. and Ozcebe, G. (2014) Evaluation of the Predictive Models for Stiffness, Strength, and Deformation Capacity of RC Frames with Masonry Infill Walls. *Journal of Structural Engineering* **140**(10).

Uva, G., Raffaele, D., Porco, F. and Fiore, A. (2012) On the role of equivalent strut models in the seismic assessment of infilled RC buildings. *Engineering Structures* **42**, 83-94.

Vamvatsikos, D. and Cornell, C. A. (2002) Incremental dynamic analysis. *Earthquake Engineering & Structural Dynamics* **31**(3), 491-514.

Varum, H. (2003) Seismic assessment, strengthening and repair of existing buildings. *PhD Thesis* Aveiro, Aveiro.

Velasquez, C. A., Ginestar, M. H., Jofre, F. R., Oyandenel, H. S. M. and Jara, D. H. (2016) The World Housing Encyclopedia

Vijaya, S., Shivakumaraswamy, B. and Ravikiran, K. (2014) Numerical modelling on behaviour of reinforced concrete exterior beam-column joint retrofitte with externally bonded Fiber Reinforced Polymere (FRP). *Ijret: International Journal of Research in Engineering and Technology* **3** (Special Issue: 06), 247-252.

William, K. J. and Warnke, E. D. (1975) Constitutive model for the triaxial behavior of concrete. *In: Proceedings of the Int. Association for Bridge and Structural Engineering, Ismes,* **19**, 174.

Xiaohan, W. and Xilin, L. (1996) Nonlinear Finite Element Analysis of Reinforced Concrete Slit Shear Wall under Cyclic Loading [J]. *Journal of Tongji University* **2**.

Yuen, T. Y. P., Kuang, J. S. and Ali, B. S. M. (2016) Assessing the effect of bi-directional loading on nonlinear static and dynamic behaviour of masonry-infilled frames with openings. *Bulletin of Earthquake Engineering* **14**(6), 1721-1755.

Žarnić, R. and Gostič, S. (1997) Book section title "*Masonry infilled frames as an effective structural sub-assemblage*" book title" Seismic design methodologies for the next generation of codes" Fajfar, P. and Krawinkler, H.

Zarnic, R. and Tomazevic, M. (1988) An experimentally obtained method for evaluation of the behaviour of masonry infilled RC frames. *Proceedings of the 9th World Conference on Earthquake Engineering,* Tokyo-Kyoto, Japan, 163–168.

Zhai, C., Kong, J., Wang, X. and Chen, Z. (2016) Experimental and Finite Element Analytical Investigation of Seismic Behavior of Full-Scale Masonry Infilled RC Frames. *Journal of Earthquake Engineering*, 1-28.

Zhao, X., Wu, Y.-F., Leung, A. Y. and Lam, H. F. (2011) Plastic Hinge Length in Reinforced Concrete Flexural Members. *Procedia Engineering* **14**, 1266-1274.

Zwillinger, D. and Kokoska, S. (2000) Standard Probability and Statistics Tables and Formulae. CHAPMAN & HALL/CRC,Boca Raton London New York Washington, D.C.